

Technical University of Crete
School of Environmental Engineering



Postgraduate Program "Environmental Health and
Engineering"

**MATHEMATICAL AND COMPUTATIONAL
MODELING FOR THE GENERATION AND
PROPAGATION OF WAVES IN MARINE AND
COASTAL ENVIRONMENTS**

A Dissertation submitted for the degree of Doctor of
Philosophy

by Maria Kazolea

September 2013



Contents

1 Introduction	15
1.1 Numerical modeling	17
1.2 Wave breaking	21
1.3 Outline of the thesis	23
2 Shallow water and Boussinesq-type (BT) equations	27
2.1 The shallow water system of equations	28
2.1.1 Derivation of the non-linear shallow water equations	28
2.2 Derivation of Madsen and Sørensen’s (MS) Boussinesq formulation	32
2.2.1 Linear dispersion properties and shoaling	37
2.3 Derivation of Nwogu’s Boussinesq formulation	39
2.3.1 Formulation of Nwogu’s BT equation in conservation-like form	42
2.3.2 Linear dispersion properties and shoaling	44
2.4 Steady state solutions	49
3 Numerical method in One Dimension	51
3.1 One-Dimensional systems	51
3.2 FV spatial discretization	53
3.2.1 Brief review	53
3.2.2 Topography source term discretization	59
3.2.3 Wet/dry front treatment	61
3.2.4 Higher order reconstruction	64
3.3 FD discretization of the dispersion terms	66
3.3.1 Discretization of the dispersion terms for Nwogu’s equations	66
3.3.2 Discretization of the dispersion terms for MS equations	67
3.4 Time integration	68

3.5	Evaluation of the velocities	69
3.6	Boundary conditions and wave generator	70
3.7	Wave breaking modeling	73
3.7.1	Eddy Viscosity Models	75
3.7.2	Hybrid wave breaking models	77
4	Numerical test and results in one dimension	83
4.1	The Carrier and Greenspan (1958) solutions	83
4.1.1	Carrier and Greenspan periodic wave solution	84
4.1.2	The Carrier and Greenspan transient solution	85
4.2	Solitary wave propagation	87
4.3	Head on collision of two solitary waves	90
4.4	Solitary wave run-up on a plane beach	92
4.4.1	Case I	94
4.4.2	Case II	95
4.5	Regular wave propagation over a submerged bar	100
4.6	Solitary wave propagation over fringing reefs	105
4.6.1	Dry reef	105
4.6.2	Submerged reef	107
5	Finite Volume methods on unstructured meshes	115
5.1	Grid terminology	115
5.2	Finite Volume (FV) approaches to conservation laws	118
5.2.1	Node-centered FV scheme on triangles	120
5.2.2	Cell-centered schemes on triangles	129
5.3	Topography source term discretizations	137
5.4	Wet-dry front treatment and mass conservation	139
5.5	Friction term discretization	141
5.6	Time integration	142
5.7	Comparison of CCFV and NCFV discretization for the NSW equations . . .	143
5.7.1	The traveling vortex solution	144
5.7.2	Thacker's planar solution	149
5.7.3	A 2D potential solution with topography	152
5.7.4	Discussion	157

6 An unstructured FV scheme for BT equations	159
6.1 Higher-order reconstruction	160
6.2 Divergence edge-based formula	162
6.3 Discretization of the dispersion terms	162
6.4 Time integration and velocity field recovery	164
6.4.1 Solution of the linear system	167
6.5 Boundary conditions and the internal source function	171
6.6 Wave breaking treatment	173
6.6.1 Eddy viscosity wave breaking treatment of Kennedy et al.[93] . . .	173
6.6.2 Hybrid wave breaking treatment	175
7 Numerical test and results in two dimensions	179
7.1 2D Solitary wave propagation in a channel	179
7.2 Spatial accuracy and efficiency	181
7.3 Solitary interaction with a vertical circular cylinder	183
7.4 2D run-up of a solitary wave on a conical island	185
7.5 Wave propagation over a semicircular shoal	193
7.6 Wave propagation over an elliptic shoal	198
7.7 Solitary wave run-up on a plane beach	201
7.8 Breaking waves on a sloping beach	204
7.9 Regular wave propagation over a submerged bar	209
7.10 Solitary wave propagation over a two dimensional reef	212
7.11 Solitary wave propagation over a three-dimensional reef	220
7.11.1 Case I.	220
7.11.2 Case II.	223
8 Conclusions	231
8.1 Summary and concluding remarks	231
8.2 Future Work/Recommendations	233
A Initial conditions	235

List of Figures

2.1	Definition sketch. One horizontal dimension.	28
2.2	Comparison of normalized phase speeds	47
2.3	Comparison of normalized group velocities	48
2.4	Linear shoaling properties	48
3.1	Computational cells and piecewise constant distribution for 1D problems.	55
3.2	Snapshots of surface elevation at $t = 20s$. $T = 1.27s$ (up), $T = 2.02s$ (down).	73
3.3	Definition sketch for a broken wave and the switching zones from BT to NSWE	80
4.1	The Carrier and Greenspan periodic wave solution: comparison between analytical (solid line) and numerical (red dashed line) results for the free surface elevation at different times $t^* \in [2T^*, 2T^* + T^*/2]$	84
4.2	The Carrier and Greenspan periodic wave solution: comparison between analytical and numerical results for the shoreline position (left) and shore- line velocity (right)for $t^* \in [T^*, 2T^*]$	85
4.3	The Carrier and Greenspan transient solution: comparison between an- alytical (solid line) and numerical (red dashed line) results for the free surface elevation at different times t^*	86
4.4	The Carrier and Greenspan transient solution: comparison between ana- lytical and numerical results for the shoreline position (left) and shoreline velocity (right) for $t^* \in [0, 20]$	87
4.5	Solitary wave propagation ($A/h = 0.1, 0.2, 0.3$ from top to bottom) at times $t = 0, 50, 100, 150, 200s$ for Nwogu's (left) and MS (right) formulations . .	89
4.6	Amplitude variations of solitary waves for $\epsilon = 0.1, 0.2, 0.3$ from top to bottom	90

4.7	The solitary wave's ($A/d = 0.1, 0.2, 0.3$ from top to bottom) shape at $t = 50s$ and $t = 150s$ for Nwogu's (left) and MS (right) formulations	91
4.8	Conservation of mass	92
4.9	Surface profiles of solitary waves at times $t\sqrt{g/d} = 0, 101.2, 200$ (from top to bottom) with $A/d = 0.3$ propagating in opposite directions in a channel of constant depth.	93
4.10	Set up for the numerical test of the solitary wave run-up on a plane beach.	94
4.11	Free surface elevation of solitary wave run-up on a plane beach for $A/h = 0.04$	96
4.12	Free surface elevation of solitary wave run-up on a plane beach for $A/h = 0.28$. Comparison of eddy viscosity models (left) and Hybrid models (right)	98
4.13	Free surface elevation of solitary wave run-up on a plane beach for $A/h = 0.28$. Comparison of eddy viscosity models (left) and Hybrid models (right)	99
4.14	Free surface elevation of solitary wave run-up on a plane beach for $A/h = 0.28$. Hybrid models.	99
4.15	Regular wave propagation over a submerged bar: definition of bed topography and wave gauges.	100
4.16	Time series of surface elevation at wave gauges for periodic wave propagation over a submerged bar for case (a).	101
4.17	Time series of surface elevation at wave gauges for periodic wave propagation over a submerged bar for case (b).	103
4.18	Time series of surface elevation at wave gauges for periodic wave breaking over a submerged bar for case (c)	104
4.19	Spatial snapshot of breaking wave propagation over a bar for the New Hybrid model (left) and the Hybrid(ϵ) model (right). Between two consecutive vertical lines, the flow is governed by NSW equations	105
4.20	Schematics of flume experiments over fringing reefs. (a) 48.8-m flume. (b) 104-m flume. Figure is obtained from [142]	106
4.21	Evolution of the water surface profile for the test case of solitary wave propagation over a dry reef (cont. in Fig. 4.19)	108
4.22	Evolution of the water surface profile for the test case of solitary wave propagation over a dry reef.	109

4.23	Time series of free surface elevation at wave gauges for the submerged reef case.	110
4.24	Evolution of normalized surface profile and wave transformation over an exposed reef for $A/h = 0.3$ and $1/12$ slope (continued in Fig 4.25.	112
4.25	Evolution of normalized surface profile and wave transformation over an exposed reef for $A/h = 0.3$ and $1/12$ slope.	113
4.26	Time series of free surface elevation at wave gauges for the submerged reef case.	114
5.1	Representative grid types	117
5.2	Distribution of Grids Metrics	118
5.3	Control cell definitions, for an internal mesh node (left) and a boundary node (right), for the NCFV scheme	120
5.4	Definition of the region where the gradient for the NCFV scheme is computed	125
5.5	Control cell definition, for an internal mesh node, for the CCFV scheme .	129
5.6	Linear representation for the CCFV schemes	130
5.7	CCFV compact (top) and wide (bottom) stencils used for gradient reconstruction	133
5.8	Ghost cells for CCFV schemes, general formulation (top) and for periodic boundary conditions (bottom)	135
5.9	Schematic representation for the location of D and M on the different grid types	136
5.10	Relative positions between M and the gradient volume for the compact stencil	137
5.11	Traveling vortex: Contour plots for h (left) and at $y = 0$ (right), $t = 1/6$. . .	146
5.12	Traveling vortex: Convergence results for the NCFV scheme at $t = 1/6$. .	146
5.13	Traveling vortex: Convergence results for the CCFVc1 scheme at $t = 1/6$.	147
5.14	Traveling vortex: Convergence results for the CCFVc2 scheme at $t = 1/6$.	147
5.15	Traveling vortex: Convergence results for the CCFVw1 scheme at $t = 1/6$	148
5.16	Traveling vortex: Convergence results for the CCFVw2 scheme at $t = 1/6$	148
5.17	Traveling vortex: Convergence comparisons for h in all grids for all schemes	

5.18	Thacker's Planar: Numerical results for the CCFVw2 scheme using the distorted type-IV grid for time $t = 4T$, 3D view (left) and contour plots for h between the analytical (dashed line) and numerical solution	152
5.19	Thacker's Planar: Shoreline and velocities at $t = 4T$ on the type-IV grid ($h_N^* = 0.0308$) for the NCVF scheme (top), the CCFVc2 (middle) and the CCFVw2 scheme (bottom) with $h_N = 0.0219$	153
5.20	Thacker's Planar: Shoreline and velocities at $t = 4T$ on the type-IV grid ($h_N^* = 0.0154$) for the NCVF scheme (top), the CCFVc2 (middle) and the CCFVw2 scheme (bottom) with $h_N = 0.0110$	154
5.21	Thacker's Planar: Convergence comparisons for h in grid type-IV.	155
5.22	2D potential solution: h residual convergence for the NCFV and the CCFVw2 schemes	156
5.23	2D potential solution: Convergence results for the NCFV and the CCFVw2 schemes	156
6.1	Computational cells for the gradient of the divergence: internal cell (left) and boundary cell (right)	163
7.1	Solitary wave profiles along a channel of constant depth	180
7.2	Convergence rates for the propagation of a solitary wave	182
7.3	CPU times as a function of accuracy in the L_2 norm	182
7.4	Non-zero elements as a function of N (left) and CPU times as a function of N (right)	183
7.5	Mesh and wave gauge locations for the solitary wave-cylinder interaction .	184
7.6	Solitary wave-cylinder interaction: 3D view of the free surface at different time instances	185
7.7	Solitary wave-cylinder interaction: numerical and experimental results for η at WG1-WG6 (from top to bottom)	186
7.8	Runup of solitary waves on a conical island: mesh and wave gauge locations	188
7.9	Evolution of the solitary wave around the conical island for $A/h = 0.09$ (case B)	190
7.10	Evolution of the solitary wave around the conical island for $A/h = 0.18$ (case C)	191

7.11 Time series of surface elevation at wave gauges around the conical island: (a) $A/h = 0.09$; (b) $A/h = 0.18$	192
7.12 Experimental measurements and numerical runoff around the conical is- land with (a) $A/h = 0.09$ and (b) $A/h = 0.181$	193
7.13 Shoaling of regular waves: semicircular bottom topography	194
7.14 Shoaling of regular waves: perspective view of the free surface (top) and surface elevation along the centerline at $t = 40s$ for $T = 1s$	195
7.15 Shoaling of regular waves: comparison of the computed and experimental results for the wave amplitudes for the first and second harmonics along the centerline for $T = 1s$	196
7.16 Shoaling of regular waves: perspective view of the free surface (top) and surface elevation along the centerline at $t = 48.5s$ for $T = 2s$	197
7.17 Shoaling of regular waves: comparison of the computed and experimental results for the wave amplitudes for the first, second and third harmonics along the centerline for $T = 2s$	198
7.18 Shoaling of regular waves: perspective view of the free surface (top) and surface elevation along the centerline at $t = 48s$ for $T = 3s$	199
7.19 Shoaling of regular waves: comparison of the computed and experimental results for the wave amplitudes for the first, second and third harmonics along the centerline for $T = 3s$	200
7.20 Bottom topography and position of experimental sections for the wave propagation over an elliptic shoal test case	200
7.21 Wave diffraction over an elliptic shoal. Comparison of the computed av- erage wave height with the experimental data [16] in sections 1-5 and 7	202
7.22 Free surface elevation of solitary wave run-up on a plane beach for $A/d =$ 0.28 (cont)	204
7.23 Free surface elevation of solitary wave runoff on a plane beach for $A/d = 0.28$	205
7.24 The normalized maximum runoff of solitary waves up a 1:19.85 beach versus the normalized wave height. Solid line and circles denote computed and measured data. Dashed line denote the runoff law.	205
7.25 Definition sketch of the numerical domain for the test cases of Hansen and Svendsen [79]	206

7.26 Spatial snapshots, along the centerline, of regular waves over a sloping beach with the flow between two consecutive vertical lines governed by the NSW equations	207
7.27 Computed and measured wave heights(top) and set-up (bottom) for the Hansen and Svendsen plunging breaker 031041	208
7.28 Computed and measured wave heights(top) and set-up (bottom) for the Hansen and Svendsen spilling breaker 051041	209
7.29 Time series of surface elevation at wave gauges for periodic wave propagation over a submerged bar	211
7.30 Spatial snapshots along the centerline of regular waves breaking over a bar with the flow between two consecutive vertical lines governed by the NSW equations	213
7.31 Time series of surface elevation at wave gauges for periodic wave breaking over a bar	214
7.32 Evolution of surface profiles and wave transformations over an exposed reef for $A/h = 0.3$ and $1/12$ slope	216
7.33 Evolution of surface profiles and wave transformations over an exposed reef for $A/h = 0.3$ and $1/12$ slope	217
7.34 Spatial snapshots along the centerline of a solitary wave propagation over a two-dimensional reef with the flow between two consecutive vertical lines governed by the NSW equations	218
7.35 Time series of the normalized free surface at the wave gauges before the reef	219
7.36 Time series of the normalized free surface at the wave gauges on top and after the reef	220
7.37 Water surface for solitary wave propagation on a 3D reef at different times	222
7.38 Time series of surface elevation for solitary wave propagation on a 3D reef along the centerline	224
7.39 Time series of surface elevation for solitary wave propagation on a 3D reef along $y = 5m$	225
7.40 Time series of surface elevation for solitary wave propagation on a 3D reef for the wave gauges located at the edge of the reef flat.	226
7.41 Time series of cross-shore and long-shore velocity for benchmark1.	226

7.42 Three-dimensional reef problem geometry along with wave gauges's and
ADVs's locations 227

7.43 Water surface for solitary wave propagation on a 3D reef at different times 228

7.44 Time series of surface elevation for solitary wave propagation on a 3D reef 229

7.45 Time series of velocity components at the different ADVs for solitary wave
propagation on a 3D reef 230

List of Tables

4.1	Experimental wave characteristics for Beji and Battjes [19] Tests.	100
5.1	Typical grid values for characteristic length and degrees of freedom	118
5.2	Summary and description of the Finite Volume schemes	144
6.1	Non-zero elements for two different still water levels (type IV).	168
6.2	Number of iterations for the linear systems produced using $h = 1m$	168
6.3	Number of iterations for the linear systems produced using $h = 1m$, the ILUT preconditioner with $lfil = 300$ and $dpt = 10^{-5}$	169
6.4	Number of iterations for the linear systems produced using $h = 1m$, the ILU0 preconditioner	169
6.5	Number of iterations for the linear systems produced using $h = 1m$, the ILUk preconditioner with $lfil = 300$	169
6.6	Number of iterations for the linear systems produced using $h = 1m$ (up) $h = 100m$ (down) and the ILUT preconditioner.	170
6.7	Number of iterations for the linear systems produced using $h = 100m$ and the ILUk preconditioner.	170
7.1	Propagation of a solitary wave: L_2 and L_∞ error norms and convergence rates (\mathcal{R}) for η	181
7.2	Experimental wave characteristics for Hansen and Svendsen Tests.	206

Acknowledgements

I would like to thank my thesis advisor prof. Costas. E. Synolakis along with my Reading and Supervisory Committee A.I.Delis and N. Kampanis. I owe special thanks to prof. A.I.Delis for his guidance and patience. I would also like to express gratitude to Professors I.Nikolos for his support and advice. I would like to thank the director of the Applied Mathematics and Computer Laboratory Pr. Y. Saridakis, as well as all Lab members, for providing me with all necessary equipment, help and support. I would like to especially thank Dr. M. Papadomanolaki and Dr T. Sifalakis.

I would like to thank Dr. Volker Roeber for his helpful discussions during the course of this work, as well as for providing relevant experimental data.

Last but not least, I would like to thank my family and friends, and Nikolas and his family for patience and encouragement.

The author has been co-financed by the European Union (European Social Fund-ESF) and Greek national funds through the Operational Program "Education and Lifelong Learning" of the National Strategic Reference Framework (NSRF)-Research Funding Program: Heracleitus II. Investing in knowledge society through the European Social Fund.

Extended Abstract (in Greek)

Στο θαλάσσιο περιβάλλον εξελίσσεται ταυτόχρονα ένα πλήθος κυματικών φαινομένων, αρκετά από τα οποία βρίσκονται σε ουσιώδη σύζευξη μεταξύ τους. Το θαλασσινό νερό είναι ένα ελαφρά συμπιεστό, ανομοιογενές και αγώγιμο ρευστό, το οποίο εδράζεται πάνω σε ένα πολυστρωματικό παραμορφώσιμο στερεό πυθμένα και περατώνεται σε μια ελεύθερη επιφάνεια. Η προσομοίωση της γένεσης και διάδοσης των κυματισμών και η ακριβής περιγραφή των μετασχηματισμών που υφίστανται στις παράκτιες περιοχές είναι απαραίτητη σε σχέση με τον σχεδιασμό των θαλάσσιων κατασκευών, την ασφάλεια καθώς και την πρόβλεψη της εξέλιξης του προφίλ της ακτογραμμής.

Ένα από τα πιο ενδιαφέροντα και ενεργά πεδία έρευνας, τις τελευταίες δεκαετίες είναι η μαθηματική και αριθμητική μοντελοποίηση των επιφανειακών κυματισμών βαρύτητας. Αυτό αποτελεί και το αντικείμενο μελέτης της παρούσας εργασίας. Σημαντικά θέματα που πρέπει να ληφθούν υπόψη είναι η εγκυρότητα του μαθηματικού μοντέλου στις παράκτιες περιοχές και σε βαθύτερα νερά, μεταβάσεις της ροής από υπερκρίσιμη σε υποκρίσιμη, η ακριβής διακριτοποίηση της τοπογραφίας όπως και η εμφάνιση υγρών-στεγανών κινούμενων συνόρων. Πολύ σημαντικά θέματα μοντελοποίησης είναι επίσης οι φυσικές διαδικασίες των κυμάτων στην παράκτια ζώνη, όπου παρουσιάζεται το μεγαλύτερο ενδιαφέρον εξέτασης. Στην περιοχή αυτή συναντώνται όλα τα χαρακτηριστικά κυματικά φαινόμενα όπως η ανάκλαση η διάθλαση καθώς και η τροποποίηση του πλάτους λόγω ρήχωσης. Σημαντικά είναι επίσης και τα μη γραμμικά φαινόμενα όπως η τριβή λόγω του πυθμένα, οι μη-γραμμικές αλληλεπιδράσεις μεταξύ διαφορετικών κυματικών συνιστωσών και η μεταφορά ενέργειας καθώς και η θραύση των κυμάτων.

Τα μοντέλα που χρησιμοποιούνται ευρέως τα τελευταία χρόνια είναι τα μοντέλα μέσου βάθους, με το πιο γνωστό από αυτά να είναι οι μη γραμμικές εξισώσεις ρηχών υδάτων (Non Linear Shallow Water Equations- NSWE). Οι εξισώσεις αυτές είναι ικανές να μοντελοποιήσουν μερικά σημαντικά φαινόμενα όπως η αναρρίχηση των κυμάτων σε ακτές αλλά δεν είναι κατάλληλες για νερά μέσου ή μεγαλύτερου βάθους όπου τα φαινόμενα διασποράς

είναι ισχυρότερα από τα μη-γραμμικά φαινόμενα. Για αυτόν τον λόγο εισάγονται οι εξισώσεις τύπου Boussinesq (BT) οι οποίες περιέχουν όρους διασποράς. Αρκετά εκτεταμένα BT μοντέλα, εφαρμόσιμα και σε βαθύτερα νερά, έχουν προταθεί τα τελευταία χρόνια όπως για παράδειγμα [170,113,116, 120]. Από τα πιο γνωστά είναι αυτά των Nwogu [127] και των Madsen και Sørensen [114]. Παρόλο που τα δύο αυτά μοντέλα έχουν διαφορετική μορφή είναι και τα δύο εφαρμόσιμα σε νερά μέχρι $kh \approx 3$, όπου k ο κυματαριθμός και h το βάθος του νερού σε ισορροπία.

Μέχρι πρόσφατα, τα αριθμητικά σχήματα που χρησιμοποιούνταν για την επίλυση των BT μοντέλων, ήταν βασισμένα στην μέθοδο πεπερασμένων διαφορών (ΜΠΔ) [1,20,67,68,114, 110,178]. Βασικό περιοριστικό κριτήριο αυτών, είναι η χρησιμοποίηση μόνο δομημένων υπολογιστικών πλεγμάτων στα δισδιάστατα (2Δ) προβλήματα, ακόμα και για μη ομαλά χωρία, το οποίο μπορεί να οδηγήσει σε μείωση της τάξης ακρίβειας των αριθμητικών σχημάτων. Για αυτού του είδους τα προβλήματα υιοθετήθηκαν οι μέθοδοι πεπερασμένων στοιχείων (ΜΠΣ) και οι μέθοδοι πεπερασμένων όγκων (ΜΠΟ). Οι ΜΠΟ μέθοδοι συνήθως απαιτούν λιγότερη υπολογιστική προσπάθεια σε σχέση με αυτήν των ΜΠΣ και μπορούν να διαχειριστούν καλύτερα τους μη-γραμμικούς όρους και τους όρους τοπογραφίας από τις ΜΠΔ. Τα τελευταία χρόνια η ΜΠΟ είναι η πιο ευρέως χρησιμοποιούμενη μέθοδος για την αριθμητική επίλυση των 2Δ NSWE.

Σε σχέση με τις BT εξισώσεις, ο Nwogu [127] χρησιμοποίησε ένα ήμι-πεπλεγμένο σχήμα Grank-Nicolson για την χρονική διακριτοποίηση των εξισώσεών του εφαρμόζοντας κεντρικές διαφορές για την χωρική διακριτοποίηση ίδιας τάξης με την τάξη των παραγώγων στις εξισώσεις. Οι Wei και Kirby [179] δημιούργησαν ένα τέταρτης τάξης σχήμα ΠΔ χρησιμοποιώντας για προώθηση στον χρόνο ένα σχήμα πρόβλεψης τρίτης τάξης Adams-Bashforth ακολουθούμενο από ένα σχήμα διόρθωσης τέταρτης τάξης Adams-Moulton. Το αριθμητικό αυτό σχήμα βελτιώθηκε από τους Shi κ.ά. [147] εφαρμόζοντας το κατάλληλα σε εναλλασσόμενα υπολογιστικά πλέγματα (staggered grids). Η εφαρμογή των μεθόδων πεπερασμένων όγκων στην επίλυση εξισώσεων τύπου Boussinesq δεν μπορεί να γίνει άμεσα, λόγω των υπάρχοντων όρων διασποράς οι οποίοι πρέπει να διακριτοποιηθούν με υψηλό βαθμό ακρίβειας. Για αυτό το λόγο σχετικά πρόσφατα αναπτύχθηκαν υβριδικού τύπου σχήματα σύζευξης πεπερασμένων διαφορών και πεπερασμένων όγκων, [150,62,61, 24,148,163,142], όπου αντιμετωπίζουν το πρόβλημα είτε στη μία χωρική διάσταση είτε στις δύο χωρικές διαστάσεις χρησιμοποιώντας μόνο δομημένα πλέγματα. Επίσης δεν αντιμετωπίζουν πλήρως και συνολικά τα τρία προς μελέτη στάδια της γένεσης, διάδοσης και

αναρρίχησης των κυματισμών σε σύνθετη τοπογραφία, που αποτελεί κεντρικό στόχο στην παρούσα εργασία. Μοναδική εξαίρεση είναι η εργασία των Asmar και Nwogu [59] όπου παρουσιάζεται μια πρώτη προσπάθεια εφαρμογής της μεθόδου πεπερασμένων όγκων στις εξισώσεις του Nwogu χρησιμοποιώντας μη δομημένα πλέγματα όπου χρησιμοποιείται ένα χαμηλής τάξης σχήμα.

Στόχος της παρούσας εργασίας είναι η υλοποίηση και παρουσίαση μιας νέας αριθμητικής μεθόδου για την επίλυση ενός 2D BT μοντέλου αναπτύσσοντας μια υψηλής τάξης ακρίβειας μέθοδο πεπερασμένων όγκων εφαρμόσιμη σε μη δομημένα υπολογιστικά πλέγματα. Η εργασία αυτή θα μπορούσαμε να πούμε ότι χωρίζεται σε τρεις ενότητες. Στην πρώτη ενότητα διακριτοποιούνται (με χρήση πεπερασμένων όγκων και διαφορών) και συγκρίνονται στη μια διάσταση δυο BT μοντέλα. Αυτά του Nwogu [127] και αυτά των MS [114] έτσι ώστε να επιλέξουμε το μοντέλο που θα διακριτοποιήσουμε στις δυο διαστάσεις. Στη συνέχεια διακριτοποιούνται οι 2D NSWΕ με δυο διαφορετικά σχήματα πεπερασμένων όγκων σε μη δομημένα πλέγματα. Ένα κεντροθετημένο ανα κέντρο βάρους, όπου οι άγνωστοι "τοποθετούνται" στο κέντρο βάρους των υπολογιστικών κελιών και ένα κεντροθετημένο ανά κόμβο, όπου οι άγνωστοι "τοποθετούνται" στον κόμβο των υπολογιστικών κελιών. Γίνεται σύγκριση αυτών, υλοποιώντας υπολογιστικά προβλήματα με αναλυτική λύση που προσομοιώνουν σύνθετες διδιάστατες επιφανειακές ροές. Στη συνέχεια και μετά από επιλογή των εξισώσεων του Nwogu και του κεντροθετημένου ανά κόμβο σχήματος πεπερασμένων όγκων, γίνεται υλοποίηση και παρουσίαση ενός νέου υπολογιστικού μοντέλου για την διακριτοποίηση των επιλεγμένων εξισώσεων σε δυο διαστάσεις.

Πιο συγκεκριμένα στο δεύτερο κεφάλαιο της παρούσας εργασίας παρουσιάζονται τα μαθηματικά μοντέλα που χρησιμοποιούνται. Γίνεται εξαγωγή των εξισώσεων ρηχών υδάτων, των BT εξισώσεων MS και των εξισώσεων του Nwogu. Οι BT εξισώσεις ξαναγράφονται σε συντηρητική μορφή η οποία είναι ιδανική για την σωστή αντιμετώπιση των εμφανιζόμενων ασυνεχειών και την σωστή διαχείριση των πηγαίων όρων τοπογραφίας (βαθυμετρίας). Αυτή η προσέγγιση των υβριδικών σχημάτων είναι αρκετά χρήσιμη δεδομένου ότι μπορούμε εύκολα να μεταπηδήσουμε στις μη γραμμικές εξισώσεις ρηχών υδάτων, αγνοώντας κατάλληλα τους όρους διασποράς στα μαθηματικά μοντέλα. Πιο συγκεκριμένα :

$$\mathbf{U}_t + \nabla \cdot \mathcal{H}(\mathbf{U}^*) = \mathbf{S}(\mathbf{U}^*) \quad \text{on} \quad \Omega \times [0, t] \subset \mathbb{R}^2 \times \mathbb{R}^+, \quad (1)$$

με \mathbf{U} να δηλώνει το διάνυσμα των νέων μεταβλητών, \mathbf{U}^* το διάνυσμα των μεταβλητών των NSWΕ, $\mathcal{H} = [\mathbf{F}, \mathbf{G}]$ οι μη γραμμικοί όροι ροής και $\mathbf{S} = \mathbf{S}_b + \mathbf{S}_f + \mathbf{S}_d$ οι πηγαίοι όροι. Με $H = H(x, t) \geq 0$ δηλώνεται το ολικό βάθος του νερού και $\mathbf{u} = [u, v]^T$ είναι το πεδίο

ταχυτήτων. $\eta = \eta(x, t)$ είναι η μεταβολή της ελεύθερης επιφάνειας και $h = h(x)$ η απόσταση της τοπογραφίας από την στάθμη του νερού όταν βρίσκεται σε ηρεμία. Για τις εξισώσεις των MS έχουμε:

$$\mathbf{U} = \begin{bmatrix} H \\ \tilde{P}_1^* \\ \tilde{P}_2^* \end{bmatrix}, \quad \mathbf{F}(\mathbf{U}^*) = \begin{bmatrix} Hu \\ Hu^2 + \frac{1}{2}gH^2 \\ Huv \end{bmatrix}, \quad \mathbf{G}(\mathbf{U}^*) = \begin{bmatrix} Hv \\ Hv^2 + \frac{1}{2}gH^2 \\ Huv \end{bmatrix},$$

$$\mathbf{S}(\mathbf{U}^*) = \mathbf{S}_b + \mathbf{S}_f + \mathbf{S}_d = \begin{bmatrix} 0 \\ -gHb_x \\ -gHb_y \end{bmatrix} + \begin{bmatrix} 0 \\ -\tau_1 \\ -\tau_2 \end{bmatrix} + \begin{bmatrix} 0 \\ -\psi_1 \\ -\psi_2 \end{bmatrix} \quad (2)$$

όπου,

$$\mathbf{P}^* = \begin{bmatrix} P_1^* \\ P_2^* \end{bmatrix} = \begin{bmatrix} Hu - \left(B + \frac{1}{3}\right)h^2(P_{xx} + Q_{xy}) - hh_x\left(\frac{1}{3}P_x + \frac{1}{6}Q_y\right) - hh_y\left(\frac{1}{6}Q_x\right) \\ Hv - \left(B + \frac{1}{3}\right)h^2(Q_{yy} + P_{xy}) - hh_y\left(\frac{1}{3}Q_y + \frac{1}{6}P_x\right) - hh_x\left(\frac{1}{6}P_y\right) \end{bmatrix}, \quad (3)$$

$$\boldsymbol{\psi} = \begin{bmatrix} \psi_1 \\ \psi_2 \end{bmatrix} = \begin{bmatrix} -Bgh^3(\eta_{xxx} + \eta_{xyy}) - hh_x(2Bgh\eta_{xx} + Bgh\eta_{yy}) - hh_y(Bgh\eta_{xy}) \\ -Bgh^3(\eta_{yyy} + \eta_{xxy}) - hh_y(2Bgh\eta_{yy} + Bgh\eta_{xx}) - hh_x(Bgh\eta_{xy}) \end{bmatrix}. \quad (4)$$

Οι πηγαίοι όροι συμπεριλαμβάνουν τους όρους τοπογραφίας \mathbf{S}_b , τους όρους τριβής \mathbf{S}_f και ένα μέρος των όρων διασποράς \mathbf{S}_d . Ο όρος P^* περιέχει όλους τους όρους με χρονικές παραγώγους ενώ ο όρος $\boldsymbol{\psi}$ περιέχει όρους διασποράς με χωρικές παραγώγους.

Για τις εξισώσεις του Nwogu έχουμε:

$$\mathbf{P}^* = \begin{bmatrix} P_1^* \\ P_2^* \end{bmatrix} = H \left[\frac{z_a^2}{2} \nabla(\nabla \cdot \mathbf{u}) + z_a \nabla(\nabla \cdot h\mathbf{u}) + \mathbf{u} \right], \quad \mathbf{S}_d = \begin{bmatrix} -\psi_c \\ -u\psi_c + \psi_{M_x} \\ -v\psi_c + \psi_{M_y} \end{bmatrix}, \quad (5)$$

$$\psi_c = C + \mathcal{D} = \nabla \cdot \left[\left(\frac{z_a^2}{2} - \frac{h^2}{6} \right) h \nabla(\nabla \cdot \mathbf{u}) + \left(z_a + \frac{h}{2} \right) h \nabla(\nabla \cdot h\mathbf{u}) \right] \quad (6)$$

και

$$\boldsymbol{\psi}_M = \begin{bmatrix} \psi_{M_x} \\ \psi_{M_y} \end{bmatrix} = \begin{bmatrix} H_t \mathcal{A} \\ H_t \mathcal{B} \end{bmatrix} = H_t \frac{z_a^2}{2} \nabla(\nabla \cdot \mathbf{u}) + H_t z_a \nabla(\nabla \cdot h\mathbf{u}). \quad (7)$$

με όλους τους υπόλοιπους όρους να είναι όπως και παραπάνω.

Για την διακριτοποίηση των παραπάνω στη 1Δ χρησιμοποιούμε ένα υβριδικό σχήμα πεπερασμένων όγκων / πεπερασμένων διαφορών. Πιο συγκεκριμένα και για τους μη γραμμικούς όρους μεταφοράς όπως και για την διακριτοποίηση των όρων τοπογραφίας χρησιμοποιούμε ένα σχήμα πεπερασμένων όγκων τύπου Godunov , ενώ για την διακριτοποίηση των όρων διασποράς χρησιμοποιούμε το σχήμα πεπερασμένων διαφορών. Για την κατασκευή της αριθμητικής ροής χρησιμοποιούμε τον προσεγγιστικό επιλυτή Riemann του Roe [139]. Οι όροι τοπογραφίας διακριτοποιούνται και αυτοί με ανάντι (upwind) τρόπο έτσι ώστε να διατηρείται το νερό σε ισορροπία ακόμα και με την ύπαρξη υγρών/στεγανών μετώπων. Ένας πολύ σημαντικός παράγοντας στην κατασκευή των αριθμητικών σχημάτων είναι η διατήρηση της ισορροπίας ανάμεσα στην διακριτή αριθμητική ροή και την διακριτοποίηση των πηγαιών όρων. Τα σχήματα που ικανοποιούν αυτήν την ισορροπία είναι γνωστά με την ονομασία καλώς ισορροπημένα (well-balanced) σχήματα [87,123,135,118,50,73]. Επιπρόσθετα προβλήματα τα οποία αντιμετωπίζονται είναι η διαχείριση του υγρού/στεγανού συνόρου, εφόσον είναι προφανές ότι οι εξισώσεις ορίζονται για τις υγρές περιοχές και χρειάζεται ιδιαίτερη αντιμετώπιση για την μετάβαση από τις στεγανές στις υγρές περιοχές. Όπως έχει δειχθεί στα [136,51,91] προβλήματα που πρέπει να αντιμετωπιστούν είναι: (1) *Η αναγνώριση των στεγανών κεφιών*, (2) *Διατήρηση της ροής σε ισορροπία όταν συμπεριλαμβάνονται στεγανές περιοχές*, (3) *Ροή σε έναντι κλίση*, (4) *Διατήρηση μάζας και υπολογισμός θετικών τιμών βάθους*.

Για την επέκταση του σχήματος σε υψηλότερης τάξης χωρική ακρίβεια χρησιμοποιούμε ένα τέταρτης τάξης MUSCL (Monotone Upstream-centered Schemes for Conservation Laws) σχήμα παρεμβολής [185], πριν την αποτίμηση των αριθμητικών ροών [62,163,148]. Η αναπαράσταση της λύσης μέσω της παρεμβολής MUSCL γίνεται στις ποσότητες του βάθους H της ταχύτητας u και της τοπογραφίας b . Και τα δυο μοντέλα που εξετάζουμε περιέχουν χωρικές παραγώγους, μέχρι τρίτης τάξης. Έχει δειχθεί ότι για να είναι το σφάλμα αποκοπής μικρότερο από τους όρους διασποράς των εξισώσεων, θα πρέπει να εφαρμοστεί τέταρτης τάξης ακρίβειας διακριτοποίηση στους όρους πρώτης παραγώγου. Για αυτόν τον λόγο τους διακριτοποιούμε χρησιμοποιώντας ένα σχήμα κεντρικών διαφορών, τέταρτης τάξης για τους όρους πρώτης παραγώγου, ένα σχήμα κεντρικών διαφορών τρίτης τάξης για τους όρους τρίτης παραγώγου και ένα σχήμα δεύτερης τάξης για τους όρους δεύτερης παραγώγου. Για την χρονική διακριτοποίηση των σχημάτων χρησιμοποιούμε την μέθοδο διακριτοποίησης τέταρτης τάξης των Adams-Moulton η οποία είναι ένα σχήμα πρόβλεψης-διόρθωσης. Στη συνέχεια, και για κάθε χρονικό βήμα, εφόσον έχουμε λάβει

τις νέες μεταβλητές, χρειάζεται η ανάκτηση της ταχύτητας για κάθε υπολογιστικό κελί. Διακριτοποιώντας τις σχέσεις (3) για τις εξισώσεις των MS και (5) για αυτές του Nwogu, με την μέθοδο πεπερασμένων διαφορών καταλήγουμε σε ένα προς επίλυση τριδιαγώνιο γραμμικό σύστημα. Χρησιμοποιούμε τον αλγόριθμο του Thomas για την επίλυσή του. Οι συνοριακές συνθήκες που εφαρμόστηκαν είναι ανάκλασης και ελεύθερης ροής, σε συνδυασμό με ένα "στρώμα απορρόφησης" (sponge layer) το οποίο διαχέει την ενέργεια των εισερχόμενων κυμάτων έτσι ώστε να περιοριστούν οι μη φυσικές ταλαντώσεις. Επίσης υλοποιήθηκε η γεννήτρια κυματισμών των Wei και Kirby [179] για τις εξισώσεις του Nwogu και υλοποιήθηκε μια νέα μορφή της γεννήτριας κυματισμών που περιγράφεται στο [138] για τις εξισώσεις των MS.

Στη συνέχεια έγινε μελέτη και εξέλιξη μηχανισμών θραύσης. Η θραύση των κυματισμών είναι ένα πολύπλοκο φαινόμενο. Οι BT εξισώσεις δεν δέχονται μη ομαλές λύσεις και έτσι, τα φυσικά μοντέλα που μελετάμε δεν είναι ικανά να περιγράψουν την παραπάνω φυσική διαδικασία αφού η διακριτοποίηση των πεπερασμένων διαφορών που έχει γίνει στους όρους διασποράς προκαλεί την γέννηση μη φυσικών ταλαντώσεων κατά την παρουσία ισχυρών κλίσεων. Εφαρμόστηκαν και μελετήθηκαν τέσσερις μηχανισμοί θραύσης. Δυο μοντέλα τύπου eddy viscosity, των Roeber [142] και Kennedy κ.α [93] το οποία προσθέτουν έναν όρο διάχυσης, στην εξίσωση ορμής, που βασίζεται στην τυρβώδη συνεκτικότητα (eddy viscosity). Η διαφορά τους έγκειται τόσο στον τρόπο υπολογισμού της τυρβώδους συνεκτικότητας αλλά και στο κριτήριο εισαγωγής του όρου. Τα υπόλοιπα δύο μοντέλα που μελετήθηκαν είναι αυτό των Tonelli κ.ά. [163] και ένα νέο υβριδικό μοντέλο που παρουσιάζεται στην παρούσα εργασία για πρώτη φορά. Είναι και τα δυο υβριδικού τύπου και βασίζονται στην απλή ιδέα ότι οι BT εξισώσεις εκφυλίζονται στις μη-γραμμικές εξισώσεις ρηχών υδάτων (NSWE) καθώς οι όροι διασποράς γίνονται αμελητέοι συγκριτικά με τους μη-γραμμικούς όρους. Πιο συγκεκριμένα, λύνουμε στο υπολογιστικό χωρίο είτε με εξισώσεις Boussinesq είτε με τις μη-γραμμικές εξισώσεις ρηχών υδάτων σύμφωνα με συγκεκριμένο κριτήριο. Επίσης παρουσιάζεται ένας νέος τρόπος απενεργοποίησης των όρων διασποράς όποτε αυτό είναι αναγκαίο. Εκτεταμένα υπολογιστικά προβλήματα και σύγκριση των αριθμητικών μοντέλων μπορούν να βρεθούν στο τέταρτο κεφάλαιο.

Στο πέμπτο κεφάλαιο γίνεται παρουσίαση της μεθόδου πεπερασμένων όγκων για την επίλυση των 2D μη γραμμικών εξισώσεων ρηχών υδάτων. Δυο σχήματα εφαρμόζονται και συγκρίνονται με στόχο την επιλογή του καλύτερου ως προς την εφαρμογή και απόδοση. Ένα κεντροθετημένο ανά κέντρο βάρους και ένα κεντροθετημένο ανά κόμβο. Στην πρώτη

προσέγγιση οι όγκοι ελέγχου που προκύπτουν είναι ίδιοι με τα υπολογιστικά κελιά και οι άγνωστοι "τοποθετούνται" στα βαρύκεντρα των τριγώνων. Στο κεντροθετημένο ανά κόμβο σχήμα τα δεδομένα είναι κεντροθετημένα ανά κόμβο και οι όγκοι ελέγχου που προκύπτουν στην παραπάνω διακριτοποίηση σχηματίζουν ένα υπολογιστικό πλέγμα δυικό του αρχικού. Πιο συγκεκριμένα το σύνορο ενός όγκου ελέγχου, γύρο από ένα κόμβο, σχηματίζεται ενώνοντας τα βαρύκεντρα των τριγώνων που έχουν το κόμβο ως μια κορυφή τους. Η δομή αυτή είναι βασισμένη στις ακμές (edge-based structure). Ολοκληρώνοντας τις εξισώσεις πάνω σε κάθε όγκο ελέγχου καταλήγουμε στην αριθμητική μορφή του νόμου διατήρησης την οποία καλούμαστε να διακριτοποιήσουμε. Υποθέτοντας ότι η λύση είναι σταθερή σε κάθε υπολογιστικό κελί λαμβάνουμε το πρώτης τάξης, χωρικά, σχήμα. Για τον υπολογισμό της αριθμητικής ροής σε κάθε πλευρά του τριγώνου, για το κεντροθετημένο ανα κέντρο βάρους σχήμα, και κατά μήκος της ακμής για το κεντροθετημένο ανα κόμβο σχήμα, καλούμαστε να επιλύσουμε ένα πρόβλημα Riemann. Χρησιμοποιούμε και εδώ τον προσεγγιστικό επιλυτή Riemann του Roe. Το διάνυσμα της αριθμητικής ροής υπολογίζεται θεωρώντας ομοιόμορφη κατανομή της ροής πάνω στο σύνορο του κελιού και ίση με την τιμή της στο μέσο της ακμής.

Η χρονική διακριτοποίηση επιτυγχάνεται με την άμεση μέθοδο Runge-Kutta τεσσάρων βημάτων και χρησιμοποιείται λόγω της εκτεταμένης περιοχής ευστάθειας που έχει. Τα πλέγματα τα οποία χρησιμοποιούνται για την διακριτοποίηση του χωρίου είναι όλα μη δομημένα. Επίσης γίνεται επέκταση του σχήματος έτσι ώστε να είναι δεύτερης τάξης χωρικής ακρίβειας. Αυτό επιτυγχάνεται με γραμμική ανακατασκευή της λύσης σε κάθε υπολογιστικό κελί. Η ανακατασκευή της λύσης γίνεται χρησιμοποιώντας ένα σχήμα τύπου MUSCL σε 2D όπου η μέση τιμή της λύσης παραμένει σταθερή σε κάθε κελί.

Οι ανακατασκευασμένες τιμές εκατέρωθεν κάθε συνόρου κελιών, υπολογίζονται στο μέσο αυτών, προτείνοντας και μια νέα μεθοδολογία, έτσι ώστε να μην υπάρχει ασυμβατότητα με τον υπολογισμό της αριθμητικής ροής. Για να βρούμε τα παραπάνω για το κεντροθετημένο ανά κέντρο βάρους σχήμα, επιβάλλεται ο υπολογισμός των κλίσεων σε κάθε τρίγωνο. Έχουν υλοποιηθεί δύο περιπτώσεις. Στην πρώτη υπολογίζονται οι κλίσεις χρησιμοποιώντας μόνο τα τρία γειτονικά κελιά κάθε τριγώνου ενώ στην δεύτερη χρησιμοποιούμε ένα πιο εκτεταμένο σύνολο τριγώνων. Για το κεντροθετημένο ανά κόμβο σχήμα οι κλίσεις υπολογίζονται σε κάθε υπολογιστικό κελί.

Στην συνέχεια έγινε κατάλληλη διαχείριση των συνοριακών συνθηκών. Για αυτόν τον λόγο υιοθετήσαμε την προσέγγιση των φανταστικών κελιών (ghost cells) για το κεντρο-

θετημένο ανά κέντρο βάρους σχήμα. Τα φανταστικά κελιά είναι επιπρόσθετα στρώματα κελιών έξω από το φυσικό μας πεδίο. Τα παραπάνω κελιά είναι ιδεατά παρόλο που έχουν γεωμετρικές ποσότητες οι οποίες λαμβάνονται από τα εσωτερικά κελιά στο σύνορο. Στην παρούσα εργασία τα βαρύκεντρα των φανταστικών κελιών είναι ο καθρέφτης των βαρυκέντρων των συνοριακών κελιών. Για να καταλήξουμε σε ένα σωστό αριθμητικό σχήμα πρέπει να επιτύχουμε μια σωστή διακριτοποίηση για τις διαφορικού τύπου συνοριακές συνθήκες. Η ιδέα είναι να χρησιμοποιήσουμε την ασθενή μορφή για τον υπολογισμό των ροών σε κάθε συνοριακή πλευρά τριγώνου. Σύμφωνα με την θεωρία των χαρακτηριστικών αλλά και αναλόγως την ροή επιβάλλουμε στο σύνορο την τιμή του βάθους ή των ταχυτήτων. Ο τρόπος αντιμετώπισης των συνοριακών συνθηκών διατηρεί την τάξη ακρίβειας του σχήματος. Η διακριτοποίηση του πηγαίου όρου γίνεται με τέτοιο τρόπο έτσι ώστε να διατηρείται η ισορροπία ανάμεσα στην αριθμητική ροή και τον πηγαίο όρο για συνθήκες ισορροπίας. Για να ισχύει το ίδιο και για το δεύτερης τάξης σχήμα ένας όρος διόρθωσης πρέπει να προστεθεί. Στην συνέχεια έγινε κατάλληλη διαχείριση για το κινούμενο σύνορο που εμφανίζεται ανάμεσα σε υγρές και στεγανές περιοχές λόγω αλλαγής του ύψους του νερού. Τα ζητήματα που αντιμετωπίζονται και επιλύονται είναι όμοια με αυτά της μιας διάστασης. Εκτός από τα ζητήματα (1)-(4) που προαναφέρθηκαν, επιβάλλεται και η συνεπής ανακατασκευή της λύσης σε περιοχές υγρού/στεγανού λαμβάνοντας υπόψη ότι πρέπει να ισχύει $\nabla H = -\nabla b$.

Ακόμα υλοποιήθηκε και η διακριτοποίηση του όρου της τριθής χρησιμοποιώντας μια έμμεση μέθοδο. Η σύγκριση των δυο σχημάτων επιτυγχάνεται υλοποιώντας προβλήματα αναφοράς που διαθέτουν αναλυτική λύση.

Μετά την υλοποίηση των παραπάνω και την επιλογή των εξισώσεων του Nwogu έναντι αυτών των MS όπως και την επιλογή του κεντροθετημένου ανά κόμβου σχήματος πεπερασμένων όγκων, παρουσιάζεται μια νέα μέθοδος διακριτοποίησης των 2Δ εξισώσεων του Nwogu (1), (3)-(7). Μετά την ολοκλήρωση των παραπάνω στο υπολογιστικό χωρίο λαμβάνουμε τις εξισώσεις που ισχύουν σε κάθε υπολογιστικό κελί. Σε αυτές οι όροι μεταφοράς και οι όροι τοπογραφίας διακριτοποιούνται με τον ίδιο τρόπο που περιγράψαμε παραπάνω για τις μη-γραμμικές εξισώσεις ρηχών υδάτων.

Για την επέκταση της ακρίβειας στο χώρο και μάλιστα σε ένα τρίτης τάξης σχήμα έτσι ώστε να μην ακυρώνονται οι όροι διασποράς από το χωρικό σφάλμα διακριτοποίησης, χρησιμοποιούμε, όπως έχει προαναφερθεί ένα MUSCL σχήμα, ανακατασκευάζοντας τις τιμές του βάθους H των ταχυτήτων $\mathbf{U} = [u, v]^T$ και της τοπογραφίας b στο μέσον της κάθε ακμής. Για την ανακατασκευή των παραπάνω ποσοτήτων χρησιμοποιείται ένας συνδυ-

ασμός κεντρικών και ανάντι κλίσεων έτσι ώστε να αυξήσουμε την ακρίβεια της βασικής MUSCL ανακατασκευής [173]. Το σχήμα είναι ακριβώς τρίτης τάξης ακρίβειας για γραμμικά προβλήματα [7,51,149]. Παρόλα αυτά, η παραπάνω ανακατασκευή μειώνει την αριθμητική διάχυση που εισάγεται στους μη γραμμικούς όρους ροής και παρέχει ακριβείς λύσεις για ομαλές ροές όπως δείχνουν τα αριθμητικά αποτελέσματα των προβλημάτων που παρουσιάζονται στο κεφάλαιο επτά αυτής της εργασίας. Σε περιπτώσεις όπου η συνεισφορά των όρων διασποράς είναι αμελητέα, δηλαδή όταν επιλύονται μόνο οι μη γραμμικές εξισώσεις ρηχών υδάτων, η παραπάνω ανακατασκευή μπορεί να δημιουργήσει ακρότατα κυρίως όταν παρουσιάζονται ασυνέχειες στην λύση. Σε αυτές τις περιπτώσεις, και για να μειώσουμε τις ταλαντώσεις στην λύση εφαρμόζεται ένας περιοριστής κλίσεων. Για να περιορίσουμε την εμφάνιση των ταλαντώσεων στην αριθμητική λύση, επιβάλλεται στην ανακατασκευή αυστηρή μονοτονία χρησιμοποιώντας τον μη-γραμμικό περιοριστή κλίσεων Van Albada-Van Leer [7,51,173,176,75]. Οι όροι διασποράς διακριτοποιούνται χρησιμοποιώντας το θεώρημα απόκλισης όπως και μια τύπου-ακμής μέθοδο υπολογισμού του διανύσματος απόκλισης. Επιπρόσθετα για τους όρους διασποράς της εξίσωσης μάζας είναι απαραίτητος ο ορισμός ενός νέου υπολογιστικού κελιού το οποίο αποτελείται από δυο τρίγωνα που έχουν μια κοινή ακμή. Σε αυτό το τρίγωνο υπολογίζεται η κλίση της απόκλισης η οποία αποτιμάται στο μέσον της κοινής πλευράς των δυο τριγώνων.

Όπως και στην 1Δ σε κάθε βήμα της RK είναι απαραίτητη η επίλυση ενός γραμμικού συστήματος για την ανάκτηση του πεδίου ταχυτήτων. Ο πίνακας που προκύπτει από την διακριτοποίηση του (5) είναι αραιός και εξαρτάται από το πλέγμα που χρησιμοποιούμε. Για αυτόν τον λόγο ο πίνακας υπολογίζεται πριν αρχίσει η χρονική επαναληπτική διαδικασία και αποθηκεύεται σε συμπιεσμένη κατα γραμμές αραιή μορφή. Το γεγονός ότι ο πίνακας δεν αλλάζει ανά χρονικό βήμα είναι υψίστης σημασίας για τον μηχανισμό θραύσης που περιγράφεται παρακάτω. Το γραμμικό σύστημα, μετά από μελέτη του πίνακα, επιλύεται χρησιμοποιώντας την επαναληπτική μέθοδο BiCGSTAB. Οι συνοριακές συνθήκες που υλοποιούνται είναι συνοριακές συνθήκες ανάκλασης και συνοριακές συνθήκες απορρόφησης. Για τις δεύτερες και μπροστά από αυτό το σύνορο ορίζεται ένα απορροφητικό στρώμα. Σε αυτό το στρώμα η ελεύθερη επιφάνεια του νερού αποσβένεται πολλαπλασιάζοντάς την με ένα συντελεστή. Ακόμα υλοποιείται η γεννήτρια κυμάτων των [179]. Τέλος επεκτείνονται στις 2Δ οι μηχανισμοί θραύσης των Kennedy [93], των Tonelli κ.ά. [163] όπως και ο νέος υβριδικός μηχανισμός θραύσης. Επίσης επεκτείνεται στις 2Δ ο νέος τρόπος απενεργοποίησης των όρων διασποράς, που παρουσιάστηκε στην 1Δ. Ο τρόπος

αυτός είναι συμβατός με το γεγονός ότι ο πίνακας του γραμμικού συστήματος παραμένει αμετάβλητος. Στο έβδομο κεφάλαιο παρουσιάζονται τα αριθμητικά προβλήματα σε δυο διαστάσεις για το μοντέλο που περιγράφηκε παραπάνω. Τα αριθμητικά προβλήματα έχουν χωριστεί σε δύο κατηγορίες, σε μη θραυόμενους και θραυόμενους κυματισμούς.

Συμπερασματικά και αρχικά για την 1Δ, αναπτύσσεται ένα υβριδικό συντηρητικό αριθμητικό μοντέλο ΠΟ/ΠΔ για την επίλυση και την σύγκριση των ΒΤ εξισώσεων του Nwogu και των Madsen και Sørensen. Παρατηρούμε ότι για μη θραυόμενους, μακρείς κυματισμούς οι διαφορές ανάμεσα στις λύσεις που παράγονται από τις NSWΕ και από τις ΒΤ εξισώσεις είναι πολύ μικρές. Παρόλο που οι NSWΕ επαρκούν σε κάποιες περιπτώσεις όπως στον υπολογισμό της αναρρίχησης των κυμάτων και κάποιων γενικότερων χαρακτηριστικών των διαδιδόμενων κυματισμών, τα αποτελέσματα των ΒΤ εξισώσεων είναι ακριβέστερα σε διασπειρόμενους κυματισμούς και σε μεγαλύτερου βάθους νερό. Τα δυο ΒΤ μοντέλα παρουσίασαν παρόμοια αποτελέσματα συγκρινόμενα με πειραματικά δεδομένα. Οι εξισώσεις του Nwogu υπερτερούν ελαφρώς και για αυτόν τον λόγο επιλέχθηκαν για την διακριτοποίηση τους στις 2Δ.

Στην δεύτερη ενότητα της παρούσας εργασίας γίνεται σύγκριση των δυο βασικών τρόπων υλοποίησης των μεθόδων πεπερασμένων όγκων για μη δομημένα υπολογιστικά πλέγματα που προέρχονται από τριγωνισμούς. Συγκρίνουμε, μέσα σε ένα ελεγχόμενο υπολογιστικό περιβάλλον, ένα κεντροθετημένο ανά κέντρο βάρους υπολογιστικού κελιού και ένα κεντροθετημένο ανά κόμβο σχήμα, με στόχο την επιλογή του βέλτιστου για την διακριτοποίηση των ΒΤ εξισώσεων σε 2Δ. Και τα δύο σχήμα συγκρίνονται με αναλυτικές λύσεις καταλήγοντας στο γεγονός ότι για την κεντροθετημένη μέθοδο ανά κέντρο βάρους υπολογιστικού κελιού προσέγγιση, η συμπεριφορά σύγκλισης εξαρτάται από το υπολογιστικό πλέγμα που χρησιμοποιούμε, κάτι που δεν συμβαίνει στο κεντροθετημένο ανά κόμβο σχήμα. Επίσης η χρησιμοποίηση φανταστικών κελιών για τον υπολοισμό οριακών συνθηκών, στο κεντροθετημένο ανά κέντρο βάρους σχήμα μπορεί να οδηγήσει σε μείωση ακρίβειας.

Στην συνέχεια, και χρησιμοποιώντας τις ΒΤ εξισώσεις του Nwogu και το κεντροθετημένο ανά κόμβο σχήμα ΠΟ, υλοποιείται ένα νέο 2Δ μη δομημένο αριθμητικό μοντέλο ΠΟ για τις προαναφερθείς εξισώσεις. Από όσο γνωρίζουμε είναι η πρώτη φορά που μια προσέγγιση ΠΟ εφαρμόζεται σε ΒΤ εξισώσεις. Στη συνέχεια υλοποιήθηκαν διαφορετικού τύπου μηχανισμοί θραύσης και παρουσιάστηκε για πρώτη φορά ένα νέο υβριδικό μοντέλο θραύσης το οποίο χρησιμοποιεί ένα συνδυασμό κριτηρίων για την ενεργοποίηση του όπου

μόνο μια παράμετρος χρειάζεται να βαθμονομηθεί. Το μοντέλο αποδείχθηκε αποτελεσματικό και ακριβές, συγκρινόμενο με τα υπάρχοντα μοντέλα θραύσης που υπάρχουν την βιβλιογραφία και που επίσης υλοποιήθηκαν στην παρούσα εργασία.

Το αριθμητικό μοντέλο βαθμονομείται χρησιμοποιώντας πειραματικά αποτελέσματα προβλημάτων που μελετούν πληθώρα κυματικών φαινομένων. Σε όλα τα προβλήματα παρατηρήθηκε πολύ καλή συμφωνία των αριθμητικών αποτελεσμάτων με πειραματικά δεδομένα καθώς και με λύσεις μοντέλων που μπορούν να βρεθούν στην βιβλιογραφία.

Chapter 1

Introduction

In the last two decades mathematical and numerical modeling of free surface flows in realistic environments has been one of the most interesting and active research fields in coastal engineering, where accurate simulations of nonlinear and dispersive water waves are important and have largely replaced laboratory experiments for the design of coastal structures. Important issues one has to consider include, the validity of a mathematical model in near-shore zones as well as in deeper waters, transitions between sub and super-critical flows, frequency dispersion and accurate numerical treatment of natural topographies and wetting/drying processes. Significant research effort has been expanded into advancing important simulation issues which include representation of near-shore wave processes such as, shoaling, run-up, diffraction, refraction and wave breaking. To this end, depth averaged models have gained a lot of popularity, in terms of applicability and development, with the nonlinear shallow water equations (NSWE) being one of the most applied models falling in this category. The NSWE have been employed widely to model wave propagation and runup, see for example [161, 162, 86, 32, 118, 27, 58, 50, 125, 91] among many others. The NSWE model is currently accepted to mathematically describe a wide variety of free surface flows under the effect of gravity and that it can be very useful for simulating long wave hydrodynamics when the vertical acceleration of water particles can be neglected and the flow can reasonably assumed to be nearly horizontal. In general, the NSWE constitute a hyperbolic system of conservation laws with source terms present due to the bed topography and friction (if other effects like Coriolis forces, are omitted).

Although the models utilizing the NSWE appear to be able to model important aspects of the flow and the general characteristics of the runup process they are not ap-

propriate for deeper waters where frequency dispersion effects become more important than nonlinearity. On the other hand, Boussinesq-type (BT) equations introduce dispersion terms and are more suitable in water where dispersion begins to have an effect on the free surface. Under the assumption that nonlinearity and frequency dispersion are weak, and in the same order of magnitude, Peregrine [133] derived the so called standard Boussinesq equations for variable depth using the free surface displacement and the depth averaged velocity as dependent variables. The standard Boussinesq equations, written in terms of the depth averaged velocity, break down when the depth is greater than one fifth of the equivalent deep water wavelength and as such are limited to relative shallow water. In addition the weakly nonlinear assumption limits the largest wave height that can be accurately modeled. The linear dispersion characteristics of the BT equations of Peregrine, rapidly diverge from the true behavior in deeper water rendering the model invalid in these situations.

In recent years, many researchers have proposed a number of extended BT systems for which the dispersion relationship is valid up to the deep water limit, making the BT models applicable in deeper water regions. Some widely used equations among others are [183, 124, 113, 127, 20] and possess equivalent dispersion properties. These extended models give a more accurate representation of the phase and group velocities in intermediate water with water depth to wave length ratio up to $1/2$, and sometimes are referred as low-order enhanced BT equations. Witting [183] expressed the depth-averaged momentum equations in terms of the velocity at the free surface and dispersion was added using a fourth order Taylor expansion. Madsen et al. [113] added extra dispersion terms to the original equations in order to improve the linear dispersion characteristics and extended the procedure including a variable bottom topography [114]. Nwogu [127] derived an extended system of equations, from the full fluid equations, by using the velocity at an arbitrary depth and Beji and Nadaoka [20] produced a BT system using Peregrine's BT model. The most popular among the aforementioned BT models are those of Nwogu [127] and Madsen and Sørensen (MS) [114]. Each model is different in the form and arrangement of the dispersive terms but they both lead to dispersion relationships that could become Padé approximants to the exact linear relationship, which give good results from shallow water up to a dimensionless wavenumber of $kh \approx 3$. In recent years, progress was made in advancing the nonlinear and the dispersion terms and multiple BT models were proposed. We refer for

example [179, 74, 68, 107, 21, 110, 111, 112, 106] among others which in turn are more difficult to integrate and thus require more computational effort in their numerical integration.

1.1 Numerical modeling

Many numerical schemes have been developed to solve BT equations. Until recently most of them were based on the finite difference (FD) method, please refer for example in [1, 20, 67, 68, 114, 110, 179]. The popularity of the FD schemes can be attributed to the ease in which higher order derivatives can be approximated and to the well structured resulted linear systems, which can be efficiently solved (e.g. tridiagonal ones). Nwogu [127] used central differences of the same order as the derivatives in his equations for the spatial discretisation and Madsen et al. [114, 113] used a straight forward mid-centering finite difference approximation. A simpler method was suggested by [179] where all first-order spatial derivatives were approximated using a fourth order finite difference scheme to ensure that the truncation error of the numerical scheme was less than that of the dispersion in the governing equations. Recently, Shi et al. [146] used a spatially staggered scheme. Operational models such as FUNWAVE [147] and COULWAVE [108, 94] are based on the finite-difference methodology. The earliest application of the FD method [1, 179] showed that the truncation errors of low-order approximation significantly affect the accuracy of the solution. This is because the truncation errors of the FD approximations are of the same form as the dispersive terms in the BT equations. Hence, these errors lead to the prediction of non-physical dispersion or "numerical diffusion", hence a careful treatment of truncation errors is necessary. The major limitation of the FD methods is that, for 2D formulations, one has to use structured spatial meshes, even for irregular domains, which can lead to loss of accuracy. Some negative aspects of this shortcoming can be avoided using curvilinear coordinates [146], but considerable work may be needed to generate such grids for arbitrary geometries and accuracy may be limited due to mapping problems. Another problem with the FD method is the correct treatment of the boundary conditions.

The use of unstructured spatial meshes for 2D complex geometries, where the mesh size can be adapted to local features such as, depth profile and complex boundaries, has been put forward as a strategy to obtain more cost-effective models. In Sørensen et

al. [152] it was estimated that the potential reduction factor, compared to structured meshes, is of the order of 10 – 20. The most natural candidates for unstructured methods are finite element (FE) methods and finite volume (FV) methods. The use of FE methods in the solution of extended BT models has increased in the last ten years (see [56] for a review) with promising results in terms of accuracy and efficiency, see for example [4, 103, 178, 152, 184, 63, 64, 60, 190, 105]. Walkley et al. [178] showed, using Nwogu's equations, that the solution can produce non-physical dispersion, the degree of which depends on the selected mesh size. Hence, the variation of mesh size needs to be suitably controlled. The main disadvantage of the FE methodology is that usually higher-order spatial derivatives present even in the low-order extended Boussinesq equations must be reduced. For example, third-order derivatives in low-order extended models are usually reduced by introducing auxiliary variables to the system of equations, resulting in additional equations to be solved. Although relatively efficient schemes with higher-order accuracy can be derived within the FE framework, significant complexities and stability issues may also arise, especially on arbitrary grids.

FV methods usually require significantly less computational effort than FE ones, while non-linear advection terms and topography source terms can be more easily treated when compared to FD methods. The advantages of the FV method for numerically approximating the NSWE are well known also in terms of the topography and wet/dry front treatment, we refer to [167, 51] and references therein for comprehensive reviews. The FV formulation is probably, now days the most applied modeling strategy for the numerical approximation of the 2D NSWE. The FV formalism can be applied to both structured and unstructured computational meshes and as such the physical domain under study can be divided into a certain number of finite control volumes, and the equations, cast in integral form, can be applied individually to each one of them. This procedure guarantees, a priori, the conservation of physical quantities like mass and momentum, is extremely flexible and conceptually simple. FV schemes have been applied to solve the non-dispersive NSWE for a wide range of applications, like flood propagation, dam-break flows, bore propagation as well as to long wave propagation and runup, see for example [161, 162, 34, 86, 170, 78, 30, 118, 27, 50, 125, 91] among many others. Specifically, Godunov-type FV schemes based on Riemann solvers have the advantage of solving the integral form of the nonlinear equations as fully conservative schemes with intrinsic shock capturing properties as well as with correctly

incorporating the bed topography and treating accurately advancing wet/dry fronts [170, 30, 86, 102, 167, 118, 51, 50, 91]. FV schemes can be categorized, in the main, as of the cell-centered (CCFV) or the node-centered (NCFV) (also referred as vertex-centered) type [9, 84, 75, 22, 119, 121]. A third approach also exists, the so called FV of the edge-type, introduced in [17]. For the CCFV approach, the (finite) control volumes used to satisfy the integral form of the equation are the mesh elements themselves, for example triangles. For the NCFV approach, the control volumes are elements of the mesh dual to the computational mesh. In a NCFV layout three possible definitions of the control volumes exist; the *centroid dual*, created by connecting the centroids of the triangular elements which are jointed to the concerned node; the *Dirichlet tessellation* which is formed by connecting the centers of the circum-circles of the same element; and finally the *median dual* obtained by linking the centroids of the elements and mid-points of the edges around the node [9]. In the edge-type control volumes the nodes are placed on the edges of an original triangulation, see [17, 41, 42] for details. Both cell-centered and node-centered of the median dual type FV discretizations will be presented in this work and will be used to simulate complex 2D free surface water flows by approximating the NSWE model. One of these formulations will be chosen in order to be used for the discretization of a 2D Boussinesq-type model.

For most problems of practical interest the numerical treatment of the source terms is a relatively standard procedure. For computing the topography source term within the FV framework, considerable progress has been made and as such several numerical and mathematical treatments have been proposed for balancing the flux gradient and the source term, in order to properly compute stationary or almost stationary solutions. This property is known as *well-balancing* and is currently a very active subject of research, we refer to [51] and references therein. An other important problem, arising in engineering applications is the appearance of dry areas, due to initial conditions or as a result of the water motion. As such, the necessity to handle wetting and drying moving boundaries (e.g. shoreline motion [27]) is a challenge that has attracted much attention. Several approaches have been proposed in different models and numerical schemes, using the NSWE equations [161] and, for Boussinesq-type equations, [108, 68] have used an extrapolation technique to allow the models to handle moving boundaries. Other techniques have been developed as to avoid dealing with wet/dry interfaces by excluding the dry cells from the computational domain [30, 32], by artificially wetting

dry cells [86] and by modeling the shore as porous or slotted [93].

Very recently, and in one spatial dimension, classical FV schemes (of the Godunov type) have been modified to solve enhanced BT equations. In these modifications the BT equations are re-written in a vector conservative like form and the FV method is used to solve the nonlinear shallow water part of the equations, while the dispersive terms are discretized by FD schemes resulting in hybrid FV/FD schemes. Frazao et al. [66] were the first to introduce the hybrid modeling for the BT equations and concluded that the hybrid solution produces more accurate results than the FD solution for wave profiles that are initially steep. Erduran et al. [62, 61] developed a new fourth-order hybrid FV/FD model for the 1D MS equations, by employing a MUSCL-type scheme with Roe's Riemann solver on the FV part of the equation. In addition, the a fourth-order predictor corrector time stepping was used and the topography slopes were discretized using the surface gradient method (SGM)[191]. Wet/dry fronts and wave breaking treatment have not been considered in [62]. The application of the hybrid scheme requires the governing equations to be recast to obtain a conservative part that suits the FV discretization. MS equations have been also used by Borthwick et al. [24] where the HLL Riemann solver was used and a wave breaking treatment was introduced. Lynett et al. [108] used the equations from [104] while Cienfuegos et al. [46, 47] developed a high-order FV scheme for the so-called Serre equations [11] which are recasted in a convenient quasi conservative form. Both the MS and Nwogu's models, but in non conservative form, were numerically solved and compared in [148] utilizing again the HLL solver along with the SGM. In [142] a fifth-order in space and fourth-order in time scheme was used for the equations of Nwogu. More, recent works, that use hybrid FV/FD schemes are those in [150, 57, 91, 109, 147, 141, 94]. These hybrid schemes, which combine the FV and FD methodology have been introduced for Boussinesq-type equations as to incorporate the flexibility and shock-capturing capabilities of the FV approach into dispersive wave models. This approach is particularly useful for short and long wave interactions as the solution can be easily turned into entirely FV solution of the NSWE by removing the higher-order Boussinesq terms, if needed.

Further, this hybrid approach has been extended to two space dimensions but for uniform structured grids [163, 94, 164]. Although for structured grids hybrid FV/FD schemes are relatively simple to implement, they can severely restrict the modeling when dealing with 2D irregular geometries, similar to the FD method. For coastal flood-

ing over complex topography and wave interaction with coastal structures, this leads to a loss of accuracy or to the use of excessively refined grids. One approach to reduce the effect of a structured grid was presented in [126], where the cut-cell approach was used to solve the 2D Madsen and Sørensen [114] equations by a Godunov-type second order FV scheme. The use of unstructured meshes provides geometrical flexibility and, in addition, mesh resolution can be more easily refined where needed, for example in shallow regions or near structures. A first attempt to apply the unstructured FV methodology on Nwogu's extended equations was presented in [59], where a low order staggered FV scheme was presented. The scheme does not account for topography sources neither for accurate wet/dry front treatment. Additionally is of low order, imposing questions in deeper waters where dispersive effects are predominant. Furthermore, important flow problems such as run-up and wave breaking were not included.

1.2 Wave breaking

Wave breaking in the nearshore environment becomes an important modeling issue. As a wave's amplitude increases and reaches a critical level the wave crest steepens, the front of the wave becomes vertical and then the crest of the wave overturns. It should be noted that, wave breaking is a complex phenomenon, with substantial air entrainment, turbulence that causes energy dissipation. At this point BT models are unable to describe the physical procedure since the FD discretization of the dispersive terms causes the generation of spurious oscillations if steep gradients are present. Thus, a wave breaking mechanism has to be considered. A wave breaking model for the BT equations requires two mechanisms to simulate the breaking process numerically. The first one is a trigger mechanism related to the initiation and, possibly the termination, of the breaking process. The second mechanism is an energy dissipation mechanism.

Three types of additional momentum dissipation methods for wave breaking exist: *The surface roller model* [144, 115, 116, 151], *the vorticity model* and *the eddy viscosity model* [93, 189, 142, 48, 90]. The last few years, a new approach has been used which simply (under certain conditions) turns off the dispersive terms in the region where breaking occurs [163, 164, 141, 91, 24].

In *eddy viscosity* models dissipation due to turbulence generated by wave breaking and bore propagation is treated by a diffusion term in the momentum conservation

equation in order to prevent numerical instabilities resulting from frequency and amplitude dispersion. The amount of dissipation is governed by the value of the eddy viscosity coefficient, which is calibrated with experimental data. A breaking criterion is used to decide exactly where and when the dissipation becomes active [49]. Heitner and Housner [83] proposed an eddy viscosity model to dissipate energy for breaking waves. Energy loss is limited to the front face of waves where the change of wave properties exceeds a certain criteria. Zelt [189] treated wave breaking similarly in a Lagrangian Boussinesq model to simulate solitary wave breaking and run-up. The same model used from Wei et al. [180]. Karambas and Koutitas [90] used also an eddy viscosity mechanism with the limitation that the formulation was not momentum preserving and the setup prediction in the inner surf zone (in the investigation of the performance for periodic waves) was very poor. Kennedy et al. [93] followed [83] and [189] but with extensions to provide a more realistic description of the initiation and cessation of wave breaking and were able to adequately reproduce wave height and setup for regular waves breaking on planar beaches. The largest disadvantage in that formulation is that, in some special cases, such as stationary hydraulic jumps, wave breaking initiation is not recognized. Additionally, Cienfuegos et al.[47] showed that Kennedy et al.'s eddy viscosity breaking model could hardly predict simultaneously accurate wave height and asymmetry along the surf zone. Lynett [106] used the eddy viscosity model of Kennedy et al. [93] with some modifications which regards the manner in which a breaking event is initiated and reformulations of the models thresholds in terms of the total water depth H . Nwogu and Demirbilek [128] present a more sophisticated eddy viscosity model in which the eddy viscosity is expressed in terms of turbulent kinetic energy and a length scale. Recently, Roeber et al. [142] adapt the approach of [83, 93] and presented an eddy viscosity approach consistent with the conservative formulation of the Boussinesq-type equations of Nwogu [127] in 1D, to account for breaking waves in the surf zone.

Other methods are based on the surface roller concept introduced by Svendsen [154]. These methods, like the eddy viscosity ones, add a flux gradient to the BT momentum equation [144, 151] but this approach stems on different hypothesis and ideas than those on the eddy viscosity ones. The added term depends on the dynamically determined roller thickness, the mean front slope of the breaker and other parameters which must be tuned during the numerical implementation. The roller approach has

been improved by [115, 116] and by [175, 89]. Recently Cienfuegos et al. [46, 47, 48] considered the wave breaking energy dissipation through extra terms written both in mass and momentum equations.

A relatively new approach, based on the assumption that Boussinesq equations automatically degenerate into NSWE as dispersive terms become negligible compared to nonlinear terms, developed the last few years. The idea introduced by [163, 164], for the equations of MS [114], is to exploit the shock-capturing advantages of the FV scheme within the framework of BT equations in order to model discontinuous phenomena such as wave breaking and runup. These models take advantage of the fact that in shallow water, the NSWE (under the FV framework) have the ability to naturally embody bore propagation and the related energy dissipation. This feature is interesting because of the similarity between spilling breakers and bores [134, 12]. Borthwick et. al. [24] introduced the above idea using as an indicator criterion, one similar to the criterion used by Kennedy et al. [93]. Tonelli et al. [163, 164] introduced a simple criterion (developed on a physical basis) in the numerical scheme to establish which set of equations should be solved in each computational cell and recently they applied an extended version of their hybrid model, including an additional criterion for the switch back to the BT equations, to describe the transformation of irregular waves [165]. Roeber et al. [141] utilize the local momentum gradients as an indicator for deactivation of the dispersive terms. The above treatment has been developed for 1D and 2D BT equations on structure meshes. Among the researchers that have followed the same idea are also [160, 23, 147, 24, 130]. In all aforementioned works it is not clear the way that wave breaking technique is implemented, with a concern about method's sensitivity to grid spacing [147].

1.3 Outline of the thesis

The existing discretizations for the BT models, as discussed so far, consist of FD or hybrid FV/FD methods which are either for 1D BT equations or for 2D equations using only structured meshes. No one has discussed the the study of the generation, propagation and runup of the waves including complex topography holistically, which is one of this thesis targets. With the exemption of [59] and to the best of our knowledge, this is the first attempt to numerically solve enhanced BT equations on unstructured

meshes by a higher- order FV scheme which exploits the advantages of the FV approach and incorporates state of the art discretization for the topography and for the treatment of wet/dry fronts

Hence, the aim of the present work is to present the development, application and potentials of a novel higher-order FV scheme for the numerical integration of extended BT equations on unstructured triangular meshes. The model should handle multiple flow problems such as propagation in deeper water, shoaling, runup, wet/dry processes, wave breaking etc. This work consist of three parts. The first part describes the derivation and discretization of two 1D BT equations (Nwogu's [127] and Madsen and Sørensen's equations [114]) through a hybrid FV/FD model. The second part of this thesis presents the discretization of the NSWE, specifically two FV schemes are implemented under the same framework and compared in order to find the one more appropriate for the discretization of a 2D BT model. The last part describes the derivation of a novel unstructured FV scheme for the 2D Nwogu's equations. The outline of the remaining chapters of this thesis is as follows.

In Chapter 2, both Nwogu's [127] and Madsen and Sørensen's [114] models are formulated in a conservative form of the NSWE. Nwogu's extended BT equations are formulated in a conservative like form, incorporating the time derivative component of the dispersion terms into the vector of conserved variables with a flux term that is identical to that of the NSWE. Both models are numerically solved, in one spatial dimension, using a hybrid FV/FD scheme.

The numerical solution is described in Chapter 3 where a fourth-order Godunov-type FV technique is used, based on the approximate Riemann solver of Roe with the topography source term discretized in an upwind manner as to provide a well-balanced scheme. As such, no special algorithms need to be implemented, e.g. extrapolation or exclusion of dry cells, to accurately compute shoreline movements. Additionally four wave breaking mechanisms are implemented and tested with one of them having a novel approach.

These two models are compared in Chapter 4, as to determine their differences and help us choose the BT equations that will be used for the 2D formulation. Suitable numerical tests in one spatial dimension are implemented, to highlight the model differences and compare the numerical results with analytic solution and/or benchmark data.

In Chapter 5 a brief review of FV schemes is described. Two FV approaches for unstructured meshes (a NCFV and a CCFV approach) are implemented and compared for the 2D NSWE. A controlled environment for a fair and extensive comparison between the two approaches is provided. The behavior of each approach is numerically tested, individually, equipped with proposed modifications and improvements and their relative behavior is compared in order to choose the FV framework in which we will discretize the BT equations.

Chapter 6 presents the development of a NCFV scheme for the numerical integration of the extended BT equations of Nwogu, on unstructured triangular meshes. The equations are numerically solved employing a third order, node centered, Godunov type FV technique that utilizes the approximate Riemann solver of Roe with the topography source term discretized again in an upwind manner. Temporal accuracy is achieved using a strong stability preserving Runge-Kutta time stepping. Furthermore two of the wave breaking treatments presented in Chapter 3 are extended for 2D formulations.

Numerical tests for the 2D formulation are presented in Chapter 7. This the first attempt (with the exemption of [59]) to numerically solve enhanced BT equations on unstructured meshes by a higher-order FV scheme wich exploits the advantages of the FV approach and incorporates state of the art discretizations for the topography and for the treatment of wet/dry fronts.

Chapter 2

Shallow water and Boussinesq-type (BT) equations

In the last few decades mathematical modeling of free surface flows has been one of the most interesting fields in coastal engineering. The modeling of free surface flows is usually described, in the classical fluid mechanics framework, using the three dimensional Navier-Stokes (NS) equations, assuming the fluid to be Newtonian, viscous and incompressible. However, the NS equations are computationally onerous thus the depth-averaging assumption has been used to simplify the equations so that numerical models can be of practical use. Depth-averaged models (or depth-integrated) are derived using mass and momentum conservation under the assumption that the velocity in the vertical direction is negligible. The most popular among these models is that of the nonlinear shallow water equations (NSWE). This set of equations is particularly well-suited for the study and numerical simulations of a large class of geophysical flow phenomena, such as river flow, ocean circulation and coastal processes like, wave propagation and runup. A large limitation of the NSWE model is that they are not applicable in deeper waters where frequency dispersion effects become more important than nonlinearity. On the other hand, Boussinesq-type (BT) equations introduce dispersion terms and are more suitable in waters where dispersion begins to have an effect on the free surface, and thus have become an increasingly important predictive tool in coastal engineering. As described in Chapter 1 a large number of BT equations exists. The extended BT equations presented next are applicable for irregular wave propagation on slowly varying bathymetry from deeper to shallow water.

In this chapter the mathematical models used in this work are presented. In Section

2.1 the NSWE are derived in one and two dimensions. Sections 2.3 and 2.4 presents the BT equations of Madsen and Sørensen (MS) [114] and Nowgu [127] respectively, along with their dispersion properties. Both set of equations are re-written here in a conservation like form in order to be numerically approximated by conservative FV schemes and to able to handle shock-wave modeling. The last Section 2.5 presents an important solution for the NSWE as well as for the BT models, the steady state solution.

2.1 The shallow water system of equations

The shallow water equations constitute a system of non-linear hyperbolic partial differential equations that fall in the category of conservation laws. They are derived from the physical laws of the mass and momentum conservation and they are also called balance laws due to significant source terms e.g. topography and friction. They are valid for problems in which vertical dynamics can be neglected compared to horizontal effects. To derive the equations, a Cartesian coordinate system is adopted and we refer to Fig. 2.1 for the case of one (spatial) dimension (1D).

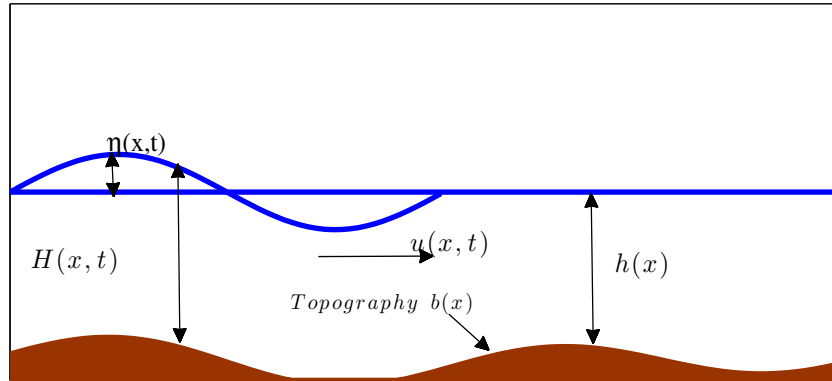


Figure 2.1: Definition sketch. One horizontal dimension.

2.1.1 Derivation of the non-linear shallow water equations

Conservation of mass

Considering that the fluid is ideal and incompressible, and ignoring Coriolis effects, viscous terms and surface stresses, we can define that in the domain $[x_1 \ x_2]$ the rate of exchange of mass equals the mass flux which crosses the domain $[x_1 \ x_2]$ where $x \in \mathbb{R}$

and $t \in \mathbb{R}^+$. The total mass can be defined as:

$$\int_{x_1}^{x_2} \rho H(x, t) dx \quad (2.1)$$

where x, t denote the space-time domain and ρ is the fluid density, $H(x, t) \geq 0$ is the total water depth and the rate of exchange of mass is given as:

$$\frac{\partial}{\partial t} \int_{x_1}^{x_2} \rho H(x, t) dx. \quad (2.2)$$

Integrating vertically the momentum density, we get the total mass flux:

$$\int_b^{H+b} \rho u(x, t) dy = \rho u(x, t) \int_b^{H+b} dy = \rho u(x, t) H(x, t). \quad (2.3)$$

So, the total mass flux which crosses x_1 is $(\rho u H)|_{x_1}$ and $(\rho u H)|_{x_2}$ the one that crosses x_2 .

Consequently, the integral form of the conservation of mass has the form:

$$\frac{\partial}{\partial t} \int_{x_1}^{x_2} H(x, t) = (\rho u)|_{x_1} - (\rho u)|_{x_2}. \quad (2.4)$$

Integrating (2.4) at the interval $[t, t + \Delta t]$ and assuming that both $u(x, t)$ and $H(x, t)$ are differentiable we obtain:

$$\int_t^{t+\Delta t} \int_{x_1}^{x_2} \frac{\partial H}{\partial t} + \frac{\partial(Hu)}{\partial x} = 0, \quad (2.5)$$

and the differential form of the conservation of mass on $\Omega \in \mathbb{R} \times \mathbb{R}^+$ is now given as:

$$\frac{\partial H}{\partial t} + \frac{\partial(Hu)}{\partial x} = 0 \quad (2.6)$$

Conservation of momentum

Conservation of momentum concludes from Newton's second law which states that, the change in velocity (acceleration) with which an object moves is directly proportional to the magnitude of the force applied to the object, and inversely proportional to the mass of the object. In the region $[x_1, x_2]$ it should hold that the momentum fluxes equals to the total forces in x -direction (science we refer to 1D). The mass flux is defined by the material derivative of the velocity:

$$\frac{D}{Dt} \int_{x_1}^{x_2} \int_b^{H+b} \rho u dy dx = \frac{d}{dt} \int_{x_1}^{x_2} \int_b^{H+b} \rho u dy dx + \int_{x_1}^{x_2} \int_b^{H+b} \rho \frac{\partial u^2}{\partial x} dy dx = \quad (2.7)$$

$$= \frac{d}{dt} \int_{x_1}^{x_2} \rho H u dx + (\rho H u^2)|_{x_2} - (\rho H u^2)|_{x_1}. \quad (2.8)$$

The total force applied in the x -direction is the summation of the forces applied, such as the pressure due to the topography $b(x)$ and the pressure due to the wall. All other

forces such as the Coriolis effect and wind stresses are neglected. The pressure applied from the wall is given as:

$$g \left[\int_b^{H+b} \rho(y - H - b) dy \right]_{x_1}^{x_2} = \left[-\frac{1}{2} g \rho H^2 \right]_{x_1}^{x_2}, \quad (2.9)$$

and the pressure applied from the bottom as:

$$-g \int_{x_1}^{x_2} \rho H \frac{db}{dx} dx \quad (2.10)$$

Hence, the total force in the x -direction is

$$\left[-\frac{1}{2} g \rho H^2 \right]_{x_1}^{x_2} - g \int_{x_1}^{x_2} \rho H \frac{db}{dx} dx, \quad (2.11)$$

where g is the gravitational constant. The integral form of mass conservation has the form:

$$\frac{d}{dt} \int_{x_1}^{x_2} H u dx + (H u^2)_{x_2} - (H u^2)_{x_1} = \left[-\frac{1}{2} g H^2 \right]_{x_1}^{x_2} - g \int_{x_1}^{x_2} \frac{db}{dx} dx. \quad (2.12)$$

Assuming, like before, that the functions $H(x, t)$ and $u(x, t)$ are differentiable we obtain the differential form of the mass conservation

$$\frac{\partial(Hu)}{\partial t} + \frac{\partial(Hu^2 + \frac{1}{2}gH^2)}{\partial x} = -gHb_x. \quad (2.13)$$

The resulting set of equations (2.6)-(2.13) can be rewritten in a vector conservative form:

$$\frac{\partial \mathbf{U}}{\partial t} + \frac{\partial \mathbf{F}(\mathbf{U})}{\partial x} = \mathbf{S}(\mathbf{U}) \quad \text{on} \quad \Omega \times [0, t] \subset \mathbb{R} \times \mathbb{R}^+, \quad (2.14)$$

where $\Omega \times [0, t]$ is the space-time Cartesian domain over which solutions are sought, \mathbf{U} is the vector of the conserved variables, \mathbf{F} is the nonlinear flux vector and $\mathbf{S} = \mathbf{S}_b + \mathbf{S}_f$ is the source term which includes the bottom slope and the friction, given as:

$$\begin{aligned} \mathbf{U} &= \begin{bmatrix} H \\ Hu \end{bmatrix}, \quad \mathbf{F}(\mathbf{U}) = \begin{bmatrix} Hu \\ Hu^2 + \frac{1}{2}gH^2 \end{bmatrix}, \\ \mathbf{S}(\mathbf{U}) &= \mathbf{S}_b + \mathbf{S}_f = \begin{bmatrix} 0 \\ -gHb_x \end{bmatrix} + \begin{bmatrix} 0 \\ -gHS_f \end{bmatrix}. \end{aligned} \quad (2.15)$$

For the friction term the Manning empirical form [91] is used in this work, where

$$S_{f_x} = n_m^2 \frac{u|u|}{H^{\frac{4}{3}}}, \quad (2.16)$$

with n_m being the Manning friction coefficient.

The Jacobian matrix of the 1D NSWE (2.14) -(2.15) is

$$\mathbf{F}'(\mathbf{U}) = \frac{\partial \mathbf{F}}{\partial \mathbf{U}} = \mathbf{A} = \begin{bmatrix} 0 & 1 \\ c^2 - u^2 & 2u \end{bmatrix} \quad (2.17)$$

with real eigenvalues

$$\lambda_1 = u - c, \quad \lambda_2 = u + c$$

and the corresponding eigenvectors are

$$\mathbf{r}_1 = [1, u - c]^T, \quad \mathbf{r}_2 = [1, u + c]^T. \quad (2.18)$$

$c = \sqrt{gH}$ is the wave's celerity.

Following the same reasoning as before, we can derive the shallow water equations in two spatial dimensions [170]. Again, ignoring Coriolis effects, viscous terms and surface stresses the system of the 2D non-linear shallow water equations can be written in conservation law form as:

$$\frac{\partial \mathbf{U}}{\partial t} + \nabla \cdot \mathcal{H}(\mathbf{U}) = \mathcal{L}(\mathbf{U}) \quad \text{on} \quad \Omega \times [0, t] \subset \mathbb{R}^2 \times \mathbb{R}^+, \quad (2.19)$$

where the vector of conserved variables and fluxes in x - and y - direction are given by

$$\mathbf{U} = \begin{bmatrix} H \\ Hu \\ Hv \end{bmatrix}, \quad \mathcal{H}(\mathbf{U}) = [\mathbf{F}(\mathbf{U}) \quad \mathbf{G}(\mathbf{U})] = \begin{bmatrix} Hu & Hv \\ Hu^2 + \frac{1}{2}gH^2 & Huv \\ Huv & Hv^2 + \frac{1}{2}gH^2 \end{bmatrix},$$

with $\mathbf{u} = [u, v]^T$ being the vector velocity field, $H(x, y, t) \geq 0$ the flow depth (distance from the bottom to the free surface). We also denote with $\mathbf{q} = [Hu, Hv]^T = [q_x, q_y]$ the unit discharge. The source term $\mathcal{L}(\mathbf{U}) = [\mathbf{S}_b + \mathbf{S}_f]$ models the effects of the shape of the bed topography and friction on the flow. geometrical source term, along the coordinate directions, is given as $\mathbf{S}_b = \mathbf{S}_{b_x} + \mathbf{S}_{b_y}$ where

$$\mathbf{S}_{b_x} = \begin{bmatrix} 0 \\ -gH \frac{\partial b(x, y, t)}{\partial x} \\ 0 \end{bmatrix} \quad \text{and} \quad \mathbf{S}_{b_y} = \begin{bmatrix} 0 \\ 0 \\ -gH \frac{\partial b(x, y, t)}{\partial y} \end{bmatrix}. \quad (2.20)$$

The source term component \mathbf{S}_f includes the bed friction stresses, that represent the energy dissipation influence of the bed roughness on the flow, given as,

$$\mathbf{S}_f = \begin{bmatrix} 0 \\ -gHS_x^f \\ -gHS_y^f \end{bmatrix}, \quad (2.21)$$

where S_{f_x} and S_{f_y} are the friction loss slopes along the coordinate directions given as,

$$S_{f_x} = \frac{n_m^2 u \|\mathbf{u}\|}{H^{\frac{4}{3}}} \quad \text{and} \quad S_{f_y} = \frac{n_m^2 v \|\mathbf{u}\|}{H^{\frac{4}{3}}}, \quad (2.22)$$

The Jacobian matrices of system (2.19) are given as,

$$\frac{\partial \mathbf{F}}{\partial \mathbf{U}} = \mathbf{A} = \begin{bmatrix} 0 & 1 & 0 \\ c^2 - u^2 & 2u & 0 \\ -uv & v & u \end{bmatrix} \quad \text{and} \quad \frac{\partial \mathbf{G}}{\partial \mathbf{U}} = \mathbf{B} = \begin{bmatrix} 0 & 0 & 1 \\ -uv & v & u \\ c^2 - v^2 & 0 & 2v \end{bmatrix} \quad (2.23)$$

with $c = \sqrt{gH}$ being the wave celerity. The eigenvalues of the two matrices are:

$$\lambda_1^A = u - c, \quad \lambda_2^A = u, \quad \lambda_3^A = u + c$$

and

$$\lambda_1^B = v - c, \quad \lambda_2^B = v, \quad \lambda_3^B = v + c$$

respectively, while the corresponding eigenvectors are:

$$\mathbf{r}_1^A = [1, u - c, v]^T, \quad \mathbf{r}_2^A = [0, 0, c]^T, \quad \mathbf{r}_3^A = [1, u + c, v]^T$$

and

$$\mathbf{r}_1^B = [1, u, v - c]^T, \quad \mathbf{r}_2^B = [0, -c, 0]^T, \quad \mathbf{r}_3^B = [1, u, v + c]^T.$$

The eigenvectors and the eigenvalues of the Jacobian matrices are fundamental for constructing the numerical schemes later on.

2.2 Derivation of Madsen and Sørensen's (MS) Boussinesq formulation

According to Madsen et al. [114], the set of the extended Boussinesq-type (BT) equations should meet the following requirements:

- (a) The equations should be expressed in two horizontal dimensions in terms of the surface elevation and the depth-integrated velocity components.
- (b) The resulting linear dispersion characteristics should follow a celerity expression which will be explained below.

As a starting point the standard form of the Boussinesq equations derived by Peregrine [133] has been considered. Formulated in terms of depth-integrated velocities and using $(\cdot)_t = \frac{\partial}{\partial t}$, $(\cdot)_x = \frac{\partial}{\partial x}$ equations read as,

$$\eta_t + P_x + Q_y = 0, \quad (2.24)$$

$$P_t + \left(\frac{P^2}{H}\right)_x + \left(\frac{PQ}{H}\right)_y + gH\eta_x + \tilde{\psi}_1 = 0, \quad (2.25)$$

$$Q_t + \left(\frac{Q^2}{H}\right)_y + \left(\frac{PQ}{H}\right)_x + gH\eta_y + \tilde{\psi}_2 = 0, \quad (2.26)$$

in which

$$\tilde{\psi}_1 = -\frac{1}{2}h^2(P_{xxt} + Q_{xyt}) + \frac{1}{6}h^3\left[\left(\frac{P}{h}\right)_{xxt} + \left(\frac{Q}{h}\right)_{xyt}\right], \quad (2.27)$$

$$\tilde{\psi}_2 = -\frac{1}{2}h^2(Q_{yyt} + P_{xyt}) + \frac{1}{6}h^3\left[\left(\frac{Q}{h}\right)_{yyt} + \left(\frac{P}{h}\right)_{xyt}\right], \quad (2.28)$$

are the dispersive terms. As defined before, H is the total water depth, h is the still-water depth, η is the surface elevation (see Fig. 2.1) and $P = Hu$ and $Q = Hv$ are the depth-integrated velocity components in the x - and y -direction, respectively. We use P and Q instead of Hu and Hv , for a more compact notation. The dispersion terms in the above equations are expressed in terms of h , which means that nonlinear effects arising from the difference between H and h have been neglected. Expanding the derivatives at the second part at the right hand side in (2.27) and (2.28) and assuming that first derivatives of h are small, so that higher derivatives and products of derivatives are consequently neglected we obtain the following simplified form of (2.27) and (2.28).

$$\tilde{\psi}_1 = -\frac{1}{3}h^2(P_{xxt} + Q_{xyt}) - \frac{1}{6}hh_y Q_{xt} - \frac{1}{6}hh_x(2P_{xt} + Q_{yt}), \quad (2.29)$$

$$\tilde{\psi}_2 = -\frac{1}{3}h^2(Q_{yyt} + P_{xyt}) - \frac{1}{6}hh_x P_{yt} - \frac{1}{6}hh_y(2Q_{yt} + P_{xt}). \quad (2.30)$$

A classical procedure to simplify higher order terms is the introduction of the linear long wave approximations [120]:

$$P_t \approx -gh\eta_x, \quad (2.31)$$

$$Q_t \approx -gh\eta_y. \quad (2.32)$$

By spatial differentiation of (2.31)-(2.32) and assuming that the first derivatives of h are small and with higher derivatives and products of derivatives neglected we obtain:

$$P_{xxt} + 2gh_x\eta_{xx} + gh\eta_{xxx} \approx 0, \quad (2.33)$$

$$P_{xyt} + gh_x\eta_{xy} + gh_y\eta_{xx} + gh\eta_{xxy} \approx 0, \quad (2.34)$$

$$Q_{yyt} + 2gh_y\eta_{yy} + gh\eta_{yyy} \approx 0, \quad (2.35)$$

$$Q_{xyt} + gh_y\eta_{xy} + gh_x\eta_{yy} + gh\eta_{yyx} \approx 0. \quad (2.36)$$

For example P_{xxt} type terms can be replaced by η_{xxx} type terms. In shallow water this would make no difference to the solution, but in deeper water the form of the Boussinesq terms is critical for the accuracy of the linear dispersion relation. Madsen et al. [114] add equations (2.34) and (2.36) and multiply the summation with $-Bh^2$ (where B is a free parameter that determines the dispersion properties of the system). They also add (2.35) and (2.36) obtaining the two terms:

$$\begin{aligned} \epsilon_1 &= -Bh^2 \left[(P_{xxt} + Q_{xyt}) + gh(\eta_{xxx} + \eta_{xyy}) + gh_x(2\eta_{xx} + \eta_{yy}) + gh_y\eta_{xy} \right], \\ \epsilon_2 &= -Bh^2 \left[(Q_{yyt} + P_{xyt}) + gh(\eta_{yyy} + \eta_{yxx}) + gh_y(\eta_{xx} + 2\eta_{yy}) + gh_x\eta_{xy} \right], \end{aligned}$$

which are then added to $\tilde{\psi}_1$ and $\tilde{\psi}_2$ respectively. According to the long wave equation, ϵ_1 and ϵ_2 will be insignificant in shallow water and they can be added to the standard Boussinesq equations without affecting their accuracy. By doing so, the dispersion

terms, then read as:

$$\begin{aligned}\tilde{\psi}_1 = & - \left(B + \frac{1}{3} \right) h^2 (P_{xxt} + Q_{xyt}) - Bgh^3 (\eta_{xxx} + \eta_{xyy}) - hh_x \left(\frac{1}{3} P_{xt} + \frac{1}{6} Q_{yt} + 2Bgh\eta_{xx} + Bgh\eta_{yy} \right) \\ & - hh_y \left(\frac{1}{6} Q_{xt} + Bgh\eta_{xy} \right),\end{aligned}\quad (2.37)$$

$$\begin{aligned}\tilde{\psi}_2 = & - \left(B + \frac{1}{3} \right) h^2 (Q_{yyt} + P_{xyt}) - Bgh^3 (\eta_{yyy} + \eta_{xxy}) - hh_y \left(\frac{1}{3} Q_{yt} + \frac{1}{6} P_{xt} + 2Bgh\eta_{yy} + Bgh\eta_{xx} \right) \\ & - hh_x \left(\frac{1}{6} P_{yt} + Bgh\eta_{xy} \right).\end{aligned}\quad (2.38)$$

The value of the coefficient B was determined by matching the resulting linear dispersion relation with a polynomial expansion of Stokes first order theory combined with the use of Padé's approximant. A value of $B = 1/15$ has been defined by [114] as optimal. With a stationary bathymetry $b(x)$, equations (2.24)-(2.26) combined with the dispersive terms (2.37)-(2.38) can be expressed in terms of the conserved variables H , P , Q since $\eta_t = (\eta + h)_t = H_t$, as

$$H_t + P_x + Q_y = 0, \quad (2.39)$$

$$P_t + \left(\frac{P^2}{H} \right)_x + \left(\frac{PQ}{H} \right)_y + gH\eta_x + \tilde{\psi}_1 = 0, \quad (2.40)$$

$$Q_t + \left(\frac{Q^2}{H} \right)_y + \left(\frac{PQ}{H} \right)_x + gH\eta_x + \tilde{\psi}_2 = 0. \quad (2.41)$$

Keeping in mind that topography $b(x)$ is not changing with time we have:

$$gH\nabla\eta = \nabla \left(\frac{gH^2}{2} \right) + gH\nabla b \quad \text{and} \quad \nabla\eta = \nabla H - \nabla b \quad (2.42)$$

thus,

$$\begin{aligned}H_t + P_x + Q_y &= 0, \\ P_t + (Hu^2)_x + (Huv)_y + \left(\frac{gH^2}{2} \right)_x + gHb_x + \tilde{\psi}_1 &= 0, \\ Q_t + (Hv^2)_y + (Huv)_x + \left(\frac{gH^2}{2} \right)_y + gHb_y + \tilde{\psi}_2 &= 0,\end{aligned}$$

which is the same as

$$H_t + P_x + Q_y = 0, \quad (2.43)$$

$$P_t + \left(Hu^2 + \frac{gH^2}{2} \right)_x + (Huv)_y + gHb_x + \tilde{\psi}_1 = 0, \quad (2.44)$$

$$Q_t + (Huv)_x + \left(Hv^2 + \frac{gH^2}{2} \right)_y + gHb_y + \tilde{\psi}_2 = 0. \quad (2.45)$$

In the absence of frequency dispersion, the equation reduce to (2.14), the NSW in their conservative form. Following the works in [62, 163], we re-write the above equations splitting the dispersive terms in those with time derivatives and those who have only spatial derivatives, obtaining:

$$\begin{aligned} \tilde{\psi}_1 &= \left[-\left(B + \frac{1}{3} \right) h^2 (P_{xx} + Q_{xy}) - hh_x \left(\frac{1}{3} P_x + \frac{1}{6} Q_y \right) - hh_y \left(\frac{1}{6} Q_x \right) \right]_t \\ &\quad - Bgh^3 (\eta_{xxx} + \eta_{xyy}) - hh_x (2Bgh\eta_{xx} + Bgh\eta_{yy}) - hh_y (Bgh\eta_{xy}), \end{aligned} \quad (2.46)$$

$$\begin{aligned} \tilde{\psi}_2 &= \left[-\left(B + \frac{1}{3} \right) h^2 (Q_{yy} + P_{xy}) - hh_y \left(\frac{1}{3} Q_y + \frac{1}{6} P_x \right) - hh_x \left(\frac{1}{6} P_y \right) \right]_t \\ &\quad - Bgh^3 (\eta_{yyy} + \eta_{xxy}) - hh_y (2Bgh\eta_{yy} + Bgh\eta_{xx}) - hh_x (Bgh\eta_{xy}). \end{aligned} \quad (2.47)$$

The vector conservative form now reads as:

$$\mathbf{U}_t + \nabla \cdot \mathcal{H}(\mathbf{U}^*) = \mathbf{S}(\mathbf{U}^*) \quad \text{on} \quad \Omega \times [0, t] \subset \mathbb{R}^2 \times \mathbb{R}^+, \quad (2.48)$$

where \mathbf{U} is the vector of the new solution variables, \mathbf{U}^* is the vector of the NSW conserved variables, $\mathcal{H} = [\mathbf{F}, \mathbf{G}]$ are the nonlinear flux vectors and $\mathbf{S} = \mathbf{S}_b + \mathbf{S}_f + \mathbf{S}_d$ is the source term, given as

$$\begin{aligned} \mathbf{U} &= \begin{bmatrix} H \\ \tilde{P}_1^* \\ \tilde{P}_2^* \end{bmatrix}, \quad \mathbf{F}(\mathbf{U}^*) = \begin{bmatrix} Hu \\ Hu^2 + \frac{1}{2}gH^2 \\ Huv \end{bmatrix}, \quad \mathbf{G}(\mathbf{U}^*) = \begin{bmatrix} Hv \\ Hv^2 + \frac{1}{2}gH^2 \\ Huv \end{bmatrix}, \\ \mathbf{S}(\mathbf{U}^*) &= \mathbf{S}_b + \mathbf{S}_f + \mathbf{S}_d = \begin{bmatrix} 0 \\ -gHb_x \\ -gHb_y \end{bmatrix} + \begin{bmatrix} 0 \\ -\tau_1 \\ -\tau_2 \end{bmatrix} + \begin{bmatrix} 0 \\ -\psi_1 \\ -\psi_2 \end{bmatrix} \end{aligned} \quad (2.49)$$

in which:

$$\mathbf{P}^* = \begin{bmatrix} P_1^* \\ P_2^* \end{bmatrix} = \begin{bmatrix} Hu - \left(B + \frac{1}{3}\right)h^2(P_{xx} + Q_{xy}) - hh_x\left(\frac{1}{3}P_x + \frac{1}{6}Q_y\right) - hh_y\left(\frac{1}{6}Q_x\right) \\ Hv - \left(B + \frac{1}{3}\right)h^2(Q_{yy} + P_{xy}) - hh_y\left(\frac{1}{3}Q_y + \frac{1}{6}P_x\right) - hh_x\left(\frac{1}{6}P_y\right) \end{bmatrix}, \quad (2.50)$$

$$\psi = \begin{bmatrix} \psi_1 \\ \psi_2 \end{bmatrix} = \begin{bmatrix} -Bgh^3(\eta_{xxx} + \eta_{xyy}) - hh_x(2Bgh\eta_{xx} + Bgh\eta_{yy}) - hh_y(Bgh\eta_{xy}) \\ -Bgh^3(\eta_{yyy} + \eta_{xxy}) - hh_y(2Bgh\eta_{yy} + Bgh\eta_{xx}) - hh_x(Bgh\eta_{xy}) \end{bmatrix}. \quad (2.51)$$

The source term includes the bottom slope \mathbf{S}_b , friction \mathbf{S}_f (see (2.18)-(2.19)) and part of the dispersive terms is included in \mathbf{S}_d . The term \mathbf{P}^* contains all time derivatives in the momentum equation and the dispersion term ψ contains only spatial derivatives.

2.2.1 Linear dispersion properties and shoaling

Water waves transform, in both phase and energy, due to shoaling, refraction, diffraction and reflection. The degree of refraction, diffraction and reflection depends on the dispersion relation while the degree of shoaling depends on the shoaling coefficient which in turns depends on the topography's steepness. To derive the dispersion relation corresponding to the equations of Madsen and Sørensen [113, 114] the following standard procedure is adopted. We consider the linearized one-dimensional version of equations (2.43)-(2.45) along with (2.46) and (2.47), which yields:

$$\eta_t + P_x = 0, \quad (2.52)$$

$$P_t + gh\eta_x - Bgh^3\eta_{xxx} - \left(B + \frac{1}{3}\right)h^2P_{xt} - h_x\left(2Bgh^2\eta_{xx} + \frac{1}{3}hP_{xt}\right) = 0. \quad (2.53)$$

From the first equation we derive that $\eta_t = -P_x$ and by cross-differentiating

$$\eta_{tt} = -P_{xt} \quad \text{and} \quad \eta_{xxtt} = -P_{xxxt}. \quad (2.54)$$

Differentiating the momentum equation in the x - direction, substituting into (2.54) and dropping the terms with higher derivatives, we obtain the wave equation:

$$\eta_{tt} - gh\eta_{xx} + Bgh^3\eta_{xxx} - \left(B + \frac{1}{3}\right)h^2\eta_{xxt} = h_x\left(g\eta_x + (2B + 1)h\eta_{xt} - 5Bgh^2\eta_{xxx}\right). \quad (2.55)$$

Consider a small amplitude wave with cyclic frequency ω , A the local wave's amplitude and ϕ the phase function, which is related to the local wave number k , by $\phi_x = k(x)$.

$$\eta(x, t) = A(x) \exp i(\omega t - \phi(x)) \quad (2.56)$$

The water depth, the wave number and the wave amplitude are considered as slowly varying functions in space thus, products of derivatives and higher derivatives of these quantities will be neglected. Substituting (2.56) into (2.55) and neglecting all x -derivatives of h, k and A we obtain:

$$-\omega^2 + ghk^2 + Bgh^3k^4 - \left(B + \frac{1}{3}\right)k^2h^2\omega^2 = 0$$

which leads to the linear dispersion relation for the MS equations,

$$C^2 = gh \frac{1 + Bk^2h^2}{1 + \left(B + \frac{1}{3}\right)k^2h^2} \quad (2.57)$$

where $C = \frac{\omega}{k}$ is the wave celerity. The group velocity is given in terms of the celerity as

$$C_g = \frac{1}{2} \left(1 + \frac{2kh}{\sin 2kh}\right) C. \quad (2.58)$$

Shoaling is the effect by which surface waves entering shallower water increase in wave height. It is caused by the fact that group velocity decreases with the reduction of water depth. The linear shoaling equation is derived considering the MS equations and assuming solutions of the form (2.56). Inserting (2.56) into the MS equations and after some algebraic manipulations we get the linear shoaling relation:

$$\frac{A_x}{A} = -S \frac{h_x}{h} \quad (2.59)$$

where S is a slope in a linear relation, called the shoaling coefficient and is defined as:

$$S = \frac{a_3 - a_2a_4}{a_1} \quad (2.60)$$

with

$$a_1 = 2 \left(1 + 2Bk^2h^2 + B\left(B + \frac{1}{3}\right)k^4h^4\right), \quad (2.61)$$

$$a_2 = 1 + 6Bk^2h^2 + 5B\left(B + \frac{1}{3}\right)k^4h^4, \quad (2.62)$$

$$a_3 = 1 + \left(4B - \frac{2}{3}\right)k^2h^2 + B\left(3B + \frac{2}{3}\right)k^4h^4 \quad \text{and} \quad (2.63)$$

$$\alpha_4 = \left[\frac{1 + \left(2B - \frac{1}{3}\right)k^2h^2 + B\left(B + \frac{1}{3}\right)k^4h^4}{1 + 2Bk^2h^2 + B\left(B + \frac{1}{3}\right)k^4h^4} \right]. \quad (2.64)$$

2.3 Derivation of Nwogu's Boussinesq formulation

Nwogu in [127] derived an extended Boussinesq-type (BT) equation system of equations from the Navier-Stokes equations by using the velocity in an arbitrary distance from the still water level as one of the depended variables. The depth of the velocity variable was used as a free parameter to optimize the dispersion characteristics of the equations. The resulting linear dispersion relation of the equations is similar to that presented by Madsen et al. [114]. Assuming that the fluid is inviscid and incompressible and that the flow is irrotational, the governing equations for the fluid motion are the continuity equation and Euler's equations of motion. Two important length scales are the characteristic water depth h_0 for the vertical direction and a typical wavelength l for the horizontal direction. The equations can be expressed in nondimensional form as:

$$\mu^2(u_x + v_y) + w_z = 0, \quad (2.65)$$

$$\mu^2 u_t + \varepsilon \mu^2 u u_x + \varepsilon \mu^2 v u_y + \varepsilon w u_z + \mu^2 p_x = 0, \quad (2.66)$$

$$\mu^2 v_t + \varepsilon \mu^2 u v_x + \varepsilon \mu^2 v v_y + \varepsilon w v_z + \mu^2 p_y = 0, \quad (2.67)$$

$$\varepsilon w_t + \varepsilon^2 u w_x + \varepsilon v w_y + \frac{\varepsilon^2}{\mu^2} w w_z + \varepsilon p_z + 1 = 0. \quad (2.68)$$

The parameters $\varepsilon = \frac{a_0}{h_0}$ and $\mu = \frac{h_0}{l}$ are measures of nonlinearity and frequency dispersion respectively, and are assumed to be small. Equations (2.65)-(2.68) can be expressed in terms of nondimensional, variables, defined as

$$x = \frac{x^*}{l}, \quad y = \frac{y^*}{l}, \quad z = \frac{z^*}{h_0}, \quad t = \frac{\sqrt{g h_0}}{l} t^*$$

where g is again the gravitational acceleration and $*$ is used to denote the dimensional variables. The depended variables are then given as:

$$u = \frac{h_0}{a_0 \sqrt{g h_0}} u^*, \quad v = \frac{h_0}{a_0 \sqrt{g h_0}} v^*, \quad w = \frac{h_0^2}{a_0 l \sqrt{g h_0}} w^*, \quad \eta = \frac{\eta^*}{a_0}, \quad h = \frac{h^*}{h_0}, \quad p = \frac{p^*}{\rho g a_0}$$

where $[u, v, w]$ is the water particle velocity vector, p is the pressure and ρ is the fluid density. In addition, the irrotational assumption leads to the relationships:

$$u_y - v_x = 0, \quad v_z - w_y = 0, \quad w_x - u_z = 0$$

Further and in addition to the equations of motion (2.65)-(2.68), the flow satisfies the kinematic boundary condition at the seabed and the free surface, along with the dynamic boundary condition at the free surface, given as

$$w + \mu^2(uh_x + vh_y) = 0, \quad \text{at } z = -h \quad (2.69)$$

$$w - \mu^2\eta_t - \varepsilon\mu^2u\eta_x - \varepsilon\mu^2v\eta_y = 0, \quad \text{at } z = \varepsilon\eta \quad (2.70)$$

$$p = 0, \quad \text{at } z = \varepsilon\eta. \quad (2.71)$$

Integrating the continuity equation with respect to z , applying the Leibniz rule and the bottom boundary condition we get:

$$w = -\mu^2 \left(\frac{\partial}{\partial x} \int_{-h}^z u dz + \frac{\partial}{\partial y} \int_{-h}^z v dz \right). \quad (2.72)$$

Nwogu in [127] instead of using the bottom velocity or the depth averaged velocity as the velocity variable, he used the velocity $\mathbf{u}_a \equiv \mathbf{u}_{z_a}$ at an arbitrary elevation $z = z_a(x, y)$. Approximating the horizontal velocity \mathbf{u} by a Taylor series expansion about this arbitrary depth one gets:

$$\mathbf{u} = \mathbf{u}|_{z_a} + (z - z_a)\mathbf{u}_z|_{z_a} + \frac{(z - z_a)^2}{2}\mathbf{u}_{zz}|_{z_a} + \dots \quad (2.73)$$

where $\mathbf{u} = [u, v]$. Substitution of (2.72) into the irrotationality conditions and using (2.73) yields to :

$$\mathbf{u} = \mathbf{u}_a + \mu^2 \left(\frac{z_a^2}{2} - \frac{z^2}{2} \right) \nabla(\nabla \cdot \mathbf{u}_a) + \mu^2(z_a - z)\nabla[\nabla \cdot (h\mathbf{u}_a)] + O(\mu^4) \quad (2.74)$$

The velocity w can be expressed, using (2.74) and (2.72), in terms of \mathbf{u}_a :

$$w = -\mu^2 \nabla \cdot (h\mathbf{u}_a) - \mu^2 z \nabla \cdot \mathbf{u}_a + O(\mu^4). \quad (2.75)$$

The pressure field is obtained by integrating the vertical momentum equation (2.68) with respect to z and applying the boundary conditions at the free surface (2.70) and (2.71):

$$p = \eta - \frac{z}{\varepsilon} + \frac{\partial}{\partial t} \int_z^{\varepsilon\eta} w dz + \varepsilon \frac{\partial}{\partial x} \int_z^{\varepsilon\eta} u w dz + \varepsilon \frac{\partial}{\partial y} \int_z^{\varepsilon\eta} v w dz - \frac{\varepsilon}{\mu^2} w^2. \quad (2.76)$$

If we assume that $O(\varepsilon) = O(\mu^2) \ll 1$, the pressure field in terms of \mathbf{u}_a can be obtained by substituting (2.74) and (2.75) in (2.76) then integrate and retain terms up to $O(\varepsilon)$ and $O(\mu^2)$:

$$p = \eta - \frac{z}{\varepsilon} + \mu^2 z \nabla \cdot (h \mathbf{u}_{at}) + \mu^2 \frac{z^2}{2} \nabla \cdot \mathbf{u}_{at} + O(\varepsilon^2, \varepsilon \mu^2, \mu^4) \quad (2.77)$$

Integrating the continuity equation (2.65) and applying the kinematic boundary conditions (2.69)-(2.70) results in:

$$\eta_t + \frac{\partial}{\partial x} \int_{-h}^{\varepsilon \eta} u dz + \frac{\partial}{\partial y} \int_{-h}^{\varepsilon \eta} v dz = 0. \quad (2.78)$$

Following the same procedure for the horizontal momentum equations we get:

$$\frac{\partial}{\partial t} \int_{-h}^{\varepsilon \eta} u dz + \varepsilon \frac{\partial}{\partial x} \int_{-h}^{\varepsilon \eta} u^2 dz + \varepsilon \frac{\partial}{\partial y} \int_{-h}^{\varepsilon \eta} uv dz + \frac{\partial}{\partial x} \int_{-h}^{\varepsilon \eta} p dz - p|_{z=-h} h_x = 0, \quad (2.79)$$

$$\frac{\partial}{\partial t} \int_{-h}^{\varepsilon \eta} v dz + \varepsilon \frac{\partial}{\partial x} \int_{-h}^{\varepsilon \eta} uv dz + \varepsilon \frac{\partial}{\partial y} \int_{-h}^{\varepsilon \eta} v^2 dz + \frac{\partial}{\partial y} \int_{-h}^{\varepsilon \eta} p dz - p|_{z=-h} h_y = 0, \quad (2.80)$$

where (2.65) and (2.69)-(2.71) have been used. Substituting (2.74), (2.75) and (2.77) to (2.78)-(2.80) and integrating, retaining terms up to $O(\varepsilon)$ and $O(\mu^2)$, we obtain the BT equations of Nwogu in non-dimensional form:

$$\begin{aligned} \eta_t + \nabla \cdot [(h + \varepsilon \eta) \mathbf{u}_a] + \mu^2 \nabla \cdot \left\{ \left(\frac{z_a^2}{2} - \frac{h^2}{6} \right) h \nabla (\nabla \cdot \mathbf{u}_a) + \left(z_a + \frac{h}{2} \right) h \nabla [\nabla \cdot (h \mathbf{u}_a)] \right\} &= 0, \\ \mathbf{u}_{at} + \nabla \eta + \varepsilon (\mathbf{u}_a \cdot \nabla) \mathbf{u}_a + \mu^2 \left\{ \frac{z_a^2}{2} \nabla (\nabla \cdot \mathbf{u}_{at}) + z_a \nabla [\nabla \cdot (h \mathbf{u}_{at})] \right\} &= 0. \end{aligned}$$

This set of equations can model the horizontal propagation of irregular, multi-directional waves in water of varying depth, provided $O(\varepsilon) = O(\mu^2) \ll 1$, and $O(\nabla h) = O(1)$. Dropping a from \mathbf{u}_a and * form dimensional variables we can rewrite the equations in dimensional form as:

$$\eta_t + \nabla \cdot (H \mathbf{u}) + \nabla \cdot \left\{ \left(\frac{z_a^2}{2} - \frac{h^2}{6} \right) h \nabla (\nabla \cdot \mathbf{u}) + \left(z_a + \frac{h}{2} \right) h \nabla [\nabla \cdot (h \mathbf{u})] \right\} = 0, \quad (2.81)$$

$$\mathbf{u}_t + g \nabla \eta + (\mathbf{u} \cdot \nabla) \mathbf{u} + \left\{ \frac{z_a^2}{2} \nabla (\nabla \cdot \mathbf{u}) + z_a \nabla [\nabla \cdot (h \mathbf{u})] \right\}_t = 0. \quad (2.82)$$

The extended BT equations of Nwogu can model weakly non-linear and weakly dispersive water waves in variable depth and the applicable range can be defined by the Stokes

(S) (or Ursell number) which relates the nonlinearity and dispersion as

$$S = \frac{\varepsilon}{\mu^2} = O(1).$$

2.3.1 Formulation of Nwogu's BT equation in conservation-like form

The equations above contain the non-conservative variables u , v and η . We rewrite here the equations in terms of the conservative variables H , Hu , Hv , i.e. in conservation law form. Since it holds that $H = h + \eta$ the mass equation (2.81) becomes:

$$H_t + \nabla \cdot (H\mathbf{u}) + \nabla \cdot \left\{ \left(\frac{z_a^2}{2} - \frac{h^2}{6} \right) h \nabla (\nabla \cdot \mathbf{u}) + \left(z_a + \frac{h}{2} \right) h \nabla [\nabla \cdot (h\mathbf{u})] \right\} = 0. \quad (2.83)$$

For the momentum equation we multiply (2.82) with the total water depth H :

$$H\mathbf{u}_t + gH\nabla\eta + H(\mathbf{u} \cdot \nabla)\mathbf{u} + H \left\{ \frac{z_a^2}{2} \nabla (\nabla \cdot \mathbf{u}) + z_a \nabla [\nabla \cdot (h\mathbf{u})] \right\}_t = 0. \quad (2.84)$$

and separating the two equations we write:

$$Hu_t + gH\eta_x + Huu_x + Hvu_y + H \left\{ \frac{z_a^2}{2} (u_{xx} + v_{yy}) + z_a ((hu)_{xx} + (hv)_{yy}) \right\}_t = 0, \quad (2.85)$$

$$Hv_t + gH\eta_y + Huv_x + Hvv_y + H \left\{ \frac{z_a^2}{2} (u_{xy} + v_{yy}) + z_a ((hu)_{xy} + (hv)_{yy}) \right\}_t = 0. \quad (2.86)$$

Using the relation (7.42) and that $(H\mathbf{u})_t = H_t\mathbf{u} + H\mathbf{u}_t$ we have:

$$\begin{aligned} (Hu)_t - H_t u &+ \left(\frac{gH^2}{2} \right)_x + gHb_x + Huu_x + Hvu_y \\ &+ H \left\{ \frac{z_a^2}{2} (u_{xx} + v_{yy}) + z_a ((hu)_{xx} + (hv)_{yy}) \right\}_t = 0, \\ (Hv)_t - H_t v &+ \left(\frac{gH^2}{2} \right)_y + gHb_y + Huv_x + Hvv_y \\ &+ H \left\{ \frac{z_a^2}{2} (u_{xy} + v_{yy}) + z_a ((hu)_{xy} + (hv)_{yy}) \right\}_t = 0. \end{aligned}$$

Substituting now H_t from (2.83) to the above relations and after expanding the derivatives and performing some calculations we obtain:

$$\begin{aligned} (Hu)_t &+ \left(Hu^2 + \frac{1}{2}gH^2 \right)_x + (Hvu)_y + u \left\{ \left(\frac{z_a^2}{2} - \frac{h^2}{6} \right) h(u_x + v_y)_x + \left(z_a + \frac{h}{2} \right) h((hu)_x + (hv)_y)_x \right\}_x \\ &+ u \left\{ \left(\frac{z_a^2}{2} - \frac{h^2}{6} \right) h(u_x + v_y)_y + \left(z_a + \frac{h}{2} \right) h((hu)_x + (hv)_y)_y \right\}_y \\ &+ H \left\{ \frac{z_a^2}{2} (u_{xx} + v_{yx}) + z_a ((hu)_{xx} + (hv)_{yx}) \right\}_t = -gHb_x, \end{aligned}$$

$$\begin{aligned} (Hv)_t &+ \left(Hv^2 + \frac{1}{2}gH^2 \right)_x + (Hvu)_x + v \left\{ \left(\frac{z_a^2}{2} - \frac{h^2}{6} \right) h(u_x + v_y)_x + \left(z_a + \frac{h}{2} \right) h((hu)_x + (hv)_y)_x \right\}_x \\ &+ v \left\{ \left(\frac{z_a^2}{2} - \frac{h^2}{6} \right) h(u_x + v_y)_y + \left(z_a + \frac{h}{2} \right) h((hu)_x + (hv)_y)_y \right\}_y \\ &+ H \left\{ \frac{z_a^2}{2} (u_{xy} + v_{yy}) + z_a ((hu)_{xy} + (hv)_{yy}) \right\}_t = -gHb_y. \end{aligned}$$

The last two equations, along with mass equation (2.83), are now written in terms of the conservative variables $\mathbf{U}^* = [H, Hu, Hv]^T$. The last terms in the left hand side of the equations can be further rearranged, using the chain rule, yielding

$$(Hu + H\mathcal{A})_t + \left(Hu^2 + \frac{1}{2}gH^2 \right)_x + (Huv)_y + u\mathcal{C} + u\mathcal{D} = -gHb_x + H_t\mathcal{A}, \quad (2.87)$$

$$(Hv + H\mathcal{B})_t + (Huv)_x + \left(Hv^2 + \frac{1}{2}gH^2 \right)_y + v\mathcal{C} + v\mathcal{D} = -gHb_y + H_t\mathcal{B} \quad (2.88)$$

where

$$\mathcal{A} = \left(\frac{z_a^2}{2} (u_{xx} + v_{yx}) + z_a ((hu)_{xx} + (hv)_{yx}) \right),$$

$$\mathcal{B} = \left(\frac{z_a^2}{2} (u_{xy} + v_{yy}) + z_a ((hu)_{xy} + (hv)_{yy}) \right),$$

$$\mathcal{C} = \left\{ \left(\frac{z_a^2}{2} - \frac{h^2}{6} \right) h(u_x + v_y)_x + \left(z_a + \frac{h}{2} \right) h((hu)_x + (hv)_y)_x \right\}_x$$

and

$$\mathcal{D} = \left\{ \left(\frac{z_a^2}{2} - \frac{h^2}{6} \right) h(u_x + v_y)_y + \left(z_a + \frac{h}{2} \right) h((hu)_x + (hv)_y)_y \right\}_y.$$

The last terms on the right hand side of equation (2.87) and (2.88) contain the temporal derivative H_t , which is directly given by the continuity equation (2.78) in terms of spatial derivatives only.

Now, the resulting set of equations (2.83), (2.87) and (2.88) can be rewritten in a vector conservative form (2.48) with :

$$\mathbf{U} = \begin{bmatrix} H \\ P_1^* \\ P_2^* \end{bmatrix}, \quad \mathbf{F}(\mathbf{U}^*) = \begin{bmatrix} Hu \\ Hu^2 + \frac{1}{2}gH^2 \\ Huv \end{bmatrix}, \quad \mathbf{G}(\mathbf{U}^*) = \begin{bmatrix} Hv \\ Huv \\ Hv^2 + \frac{1}{2}gH^2 \end{bmatrix}, \quad \mathbf{S}_b = \begin{bmatrix} 0 \\ -gHb_x \\ -gHb_y \end{bmatrix},$$

$$\mathbf{S}_d = \begin{bmatrix} -\psi_c \\ -u\psi_c + \psi_{M_x} \\ -v\psi_c + \psi_{M_y} \end{bmatrix}, \quad (2.89)$$

and \mathbf{S}_f defined in (2.19), where

$$P_1^* = Hu + H\mathcal{A},$$

$$P_2^* = Hv + H\mathcal{B},$$

or in the more compact vector form

$$\mathbf{P}^* = \begin{bmatrix} P_1^* \\ P_2^* \end{bmatrix} = H \left[\frac{z_a^2}{2} \nabla(\nabla \cdot \mathbf{u}) + z_a \nabla(\nabla \cdot h\mathbf{u}) + \mathbf{u} \right], \quad (2.90)$$

$$\psi_c = C + \mathcal{D} = \nabla \cdot \left[\left(\frac{z_a^2}{2} - \frac{h^2}{6} \right) h \nabla(\nabla \cdot \mathbf{u}) + \left(z_a + \frac{h}{2} \right) h \nabla(\nabla \cdot h\mathbf{u}) \right] \quad (2.91)$$

and

$$\psi_M = \begin{bmatrix} \psi_{M_x} \\ \psi_{M_y} \end{bmatrix} = \begin{bmatrix} H_t \mathcal{A} \\ H_t \mathcal{B} \end{bmatrix} = H_t \frac{z_a^2}{2} \nabla(\nabla \cdot \mathbf{u}) + H_t z_a \nabla(\nabla \cdot h\mathbf{u}). \quad (2.92)$$

The governing equations (2.48) along with (2.89) have an identical flux term as the NSW and the new variables in \mathbf{P}^* contain all time derivatives in the momentum equations, including part of the dispersion terms obtained from the chain rule.

2.3.2 Linear dispersion properties and shoaling

As in Section 2.2.1, the dispersion relation for this system of equations is derived from the linearized version of the equations by assuming a steady periodic wave solution. The linearized version of Nwogu's equations, in one horizontal dimension with constant

depth, can be expressed in dimensional form as:

$$\eta_x + hu_x + \left(\frac{z_a^2}{2} - \frac{h^2}{6}\right)hu_{xxx} + \left(z_a + \frac{h}{2}\right)h^2u_{xxx} = 0,$$

$$u_t + g\eta_x + \frac{z_a^2}{2}u_{txx} + z_a hu_{txx} = 0.$$

The dispersion and shoaling properties depend on the depth z_a , where the flow velocity is evaluated. Introducing the parameter $\alpha = \frac{1}{2}\left(\frac{z_a}{h}\right)^2 + \left(\frac{z_a}{h}\right)$ the above equations become:

$$\eta_x + hu_x + \left(\alpha + \frac{1}{3}\right)h^3u_{xxx} = 0, \quad (2.93)$$

$$u_t + g\eta_x + \alpha h^2u_{txx} = 0. \quad (2.94)$$

Assuming a steady periodic profile of the form:

$$\eta(x, t) = \tilde{A} \sin(kx - \omega t), \quad (2.95)$$

$$u(x, t) = \tilde{B} \sin(kx - \omega t) \quad (2.96)$$

where \tilde{A} , \tilde{B} are the respective amplitudes. Substituting (2.95) and (2.96) into (2.93) and (2.94) and performing some calculations we get:

$$-\tilde{A}\omega + h\tilde{B}k - \left(\alpha + \frac{1}{3}\right)h^3\tilde{B}k^3 = 0 \quad (2.97)$$

$$-\tilde{B}\omega + g\tilde{A}k + \alpha h^2\tilde{B}\omega k^2 = 0. \quad (2.98)$$

Solving the above for \tilde{B} leads to:

$$\tilde{B} = \frac{\tilde{A}\omega}{hk\left(1 - \left(\alpha + \frac{1}{3}\right)h^2k^2\right)} = \frac{-\tilde{A}gk}{-\omega + \alpha h^2\omega k^2}$$

which gives the dispersion relation for the equations of Nwogu:

$$C^2 = \frac{\omega^2}{k^2} = gh \frac{1 - \left(\alpha + \frac{1}{3}\right)(kh)^2}{1 - \alpha(kh)^2}. \quad (2.99)$$

It is obvious that depending on the velocity variable used or the value of α , different dispersion relations are obtained. Nwogu [127] chose z_a as to obtain the best fit between the linear dispersion relation of the model and the exact dispersion relation for a wide range of water depths. By matching the celerity (2.99) and the celerity from the Airy

wave theory and minimizing the error:

$$\int_0^\pi \left(\frac{|C - C_{Airy}|}{C_{Airy}} \right)^2 d(kh) + \int_\pi^{2\pi} \left(\frac{|C - C_{Airy}|}{C_{Airy}} \right)^2 d(kh),$$

Nwogu chose $\alpha = -0.39$, which results in $z_a = -0.531h$, over the range of $0 \leq h/L \leq 0.5$ or $kh < \pi$. Roeber et al. in [142, 141] determined an optimal value of $z_a = -0.5208h$ that results in a comparable error of 1% in the celerity for $kh < \pi$ and much smaller error of 4% at $kh = 5$ in comparison to Nwogu [127]. The group velocity for the equations of Nwogu is given in terms of the celerity as [127]

$$C_g = C \left\{ 1 - \frac{\frac{(kh)^2}{3}}{[1 - \alpha(kh)^2] \left[1 - \left(\alpha + \frac{1}{3} \right) (kh)^2 \right]} \right\} \quad (2.100)$$

Using the same approach presented by [114] (see Section 2.3.1) the linearized shoaling equation (2.60) has the coefficients :

$$a_1 = 2 + \frac{(2kh)^2}{1 - \alpha(kh)^2} \left[-\alpha - \frac{2}{3} + \alpha \left(\alpha + \frac{1}{3} \right) (kh)^2 \right], \quad (2.101)$$

$$a_2 = 3 + \frac{(3kh)^2}{(1 - \alpha(kh)^2)^2} \left[-3\alpha - \frac{3}{2} + 3\alpha(2\alpha + 1)(kh)^2 - 3\alpha^2 \left(\alpha + \frac{1}{3} \right) (kh)^4 \right], \quad (2.102)$$

$$a_3 = 2 + \frac{(2kh)^2}{1 - \alpha(kh)^2} \left\{ -\alpha - \frac{3}{2} + \left[\alpha \left(\alpha + \frac{5}{6} \right) - \frac{z_a}{3h} - \frac{2\alpha}{3(1 - \alpha(kh)^2)} \right] (kh)^2 \right\}, \quad (2.103)$$

a_4 is the same as in Section 2.3.1

The linear dispersion relation, the group velocity and the shoaling equation presented for the extended BT equations can be compared against those for the linear Stokes wave. The linear dispersion relation for the Stokes wave is given by

$$C_A^2 = gh \frac{\tanh(kh)}{kh} \quad (2.104)$$

and the group velocity is defined by

$$C_{gA} = C_A \left\{ 1 - \frac{(kh)^2}{3(1 - \alpha(kh)^2) \left[1 - \left(\alpha + \frac{1}{3} \right) (kh)^2 \right]} \right\}. \quad (2.105)$$

Finally the shoaling coefficient is:

$$S = \frac{G \left(1 + \frac{1}{2} G (1 - \cosh(2kh)) \right)}{(1 + G)^2} \quad (2.106)$$

where $G = \frac{2kh}{\sin(2kh)}$. The phase speeds for the two BT equations (using two different values of z_a for Nwogu's equations, the one used by Nwogu [127] and that used by Roeber [142]) are normalized with respect to the linear theory wave speed and plotted in Fig. 2.2 as function of kh . Fig. 2.3 shows the group velocities normalized with C_{gA} . It is observed that the accuracy of both set of equations decreases for large values of kh , i.e. in deeper water. Fig. 2.4 compares the shoaling coefficient produced by each set of extended BT equations, normalized to the one of the Stokes theory. The S value given by MS equations agrees reasonably well in the range of $kh < 0.2\pi$, and starts to deviate as the water depth increases. Nwogu's equations underestimate the S value in the range of $kh > 0.25\pi$, and this underestimation increases with increasing water depth. An extended study and compare of the linear dispersion characteristics and shoaling properties of extended BT equations can be found in [101].

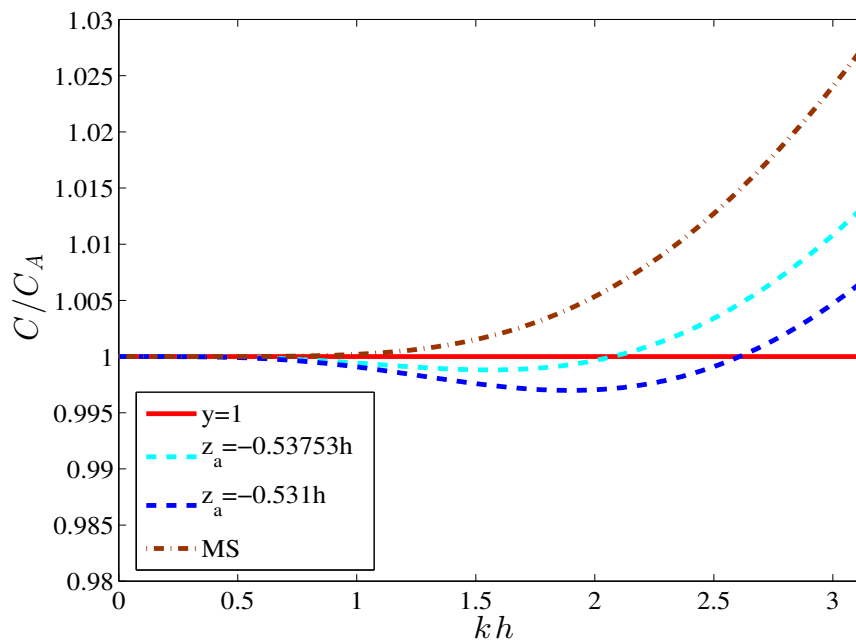


Figure 2.2: Comparison of normalized phase speeds

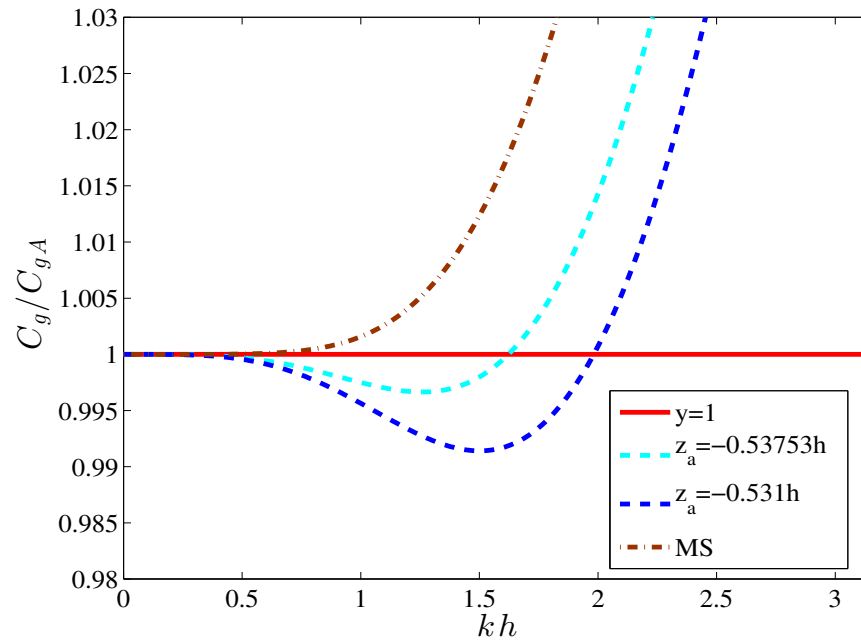


Figure 2.3: Comparison of normalized group velocities

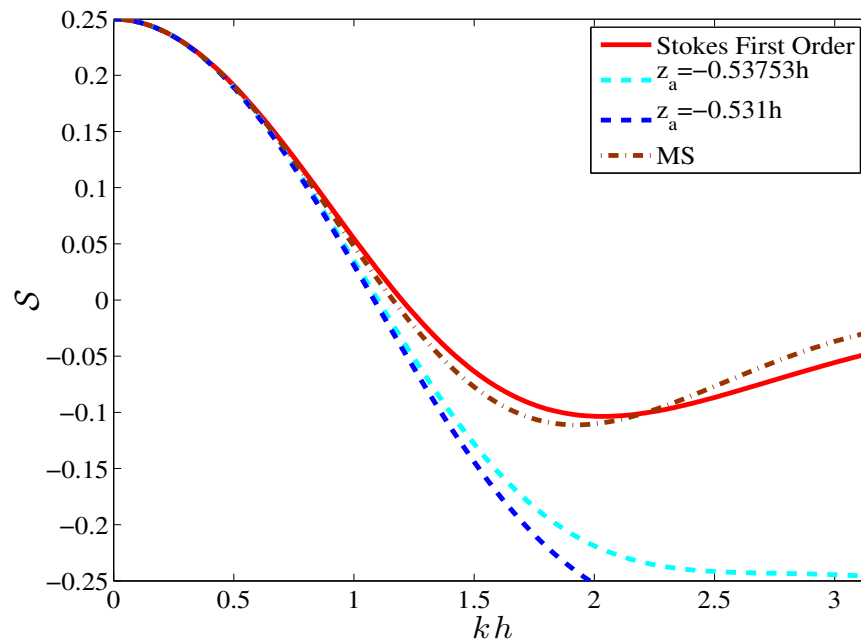


Figure 2.4: Linear shoaling properties

2.4 Steady state solutions

An important property of NSW (2.19), related to the source terms is that the system admits *non-trivial steady-states*. Following from (2.19) these are given by

$$\nabla \cdot (h\mathbf{u}) = 0, \quad (2.107)$$

$$\nabla \left(\frac{\|\mathbf{u}\|^2}{2} + gH \right) + \text{curl}\mathbf{u} \begin{bmatrix} -v \\ u \end{bmatrix} = \begin{bmatrix} -gS_x^f \\ -gS_y^f \end{bmatrix}. \quad (2.108)$$

From the above equilibrium some classes of steady state solutions can be derived, [135, 123], which can help to assess the performance of a numerical scheme. In the numerical applications one often requires the steady state solutions to be preserved exactly, so that small perturbations of these solutions can be resolved without the need of excessive mesh refinement. More details, on that, can be found in the next chapter.

A particular elementary solution, that holds for the NSW and both the BT models, and provides a benchmark for many numerical schemes is the so called flow (or lake) at rest solution that is easily obtained from (2.48) assuming $\mathbf{u} = 0$ and $H+b = D(x, y, 0) = D$ constant in the wet region of the computational domain $\Omega \in \mathbb{R}$. Then, we get the exact solution

$$\mathbf{u} = 0 \quad \forall (x, y) \in \Omega \text{ and } t \geq 0, \quad (2.109)$$

$$H(x, y, t) = \begin{cases} D - b(x, y) & \text{if } b(x, y) < D, \\ 0 & \text{otherwise,} \end{cases} \quad t \geq 0. \quad (2.110)$$

This solution represents flow at rest taking in to account the existence of wet/dry transitions as well and is of importance for the derivation of Finite Volume discretizations presented later on in this study. It is worth saying that, this solution satisfies all the mathematical models described in this chapter.

C-property

A numerical scheme that preserves exactly initial solutions of the lake at rest type (2.109)-(2.110) is said to verify the exact C-property. A numerical scheme that preserves an initial lake at rest solution within an accuracy higher than that of its truncation error is said to verify the approximate C-property.

Chapter 3

Numerical method in One Dimension

A number of numerical schemes has been developed to compute approximate solutions for BT equations. In the past few years, most of them are based on the finite difference (FD) approach. Very recently, hybrid solutions, which combine the Finite Volume (FV) and FD method have been introduced as to incorporate the flexibility and shock-capturing capabilities of the FV method into dispersive wave models. In this chapter a hybrid FV/FD approach is proposed for the BT equations of MS [114] and Nwogu [127] in 1D. In Section 3.1 the two 1D mathematical formulations are presented in a vector conservative-like form and in Section 3.2 a FV discretization for the advective part of the equations and the topography source terms, is presented. Sections 3.3-3.5 describe the discretization of the dispersion terms along with the time integration and in Section 3.6 the boundary conditions used in this work for 1D problems are presented. In the last section a brief review for the wave breaking modeling of the BT models is presented and four selected wave breaking treatments are extensively described.

3.1 One-Dimensional systems

Nwogu's extended Boussinesq equation system, (2.48) along with (2.89), (2.90),(2.91) and (2.92) can be written in one spatial dimension into the following system of equations:

$$\mathbf{U}_t + \mathbf{F}(\mathbf{U}^*)_x = \mathbf{S}(\mathbf{U}^*), \quad (3.1)$$

where again \mathbf{U} is the vector of then new variables, $\mathbf{U}^* = [h, Hu]$ the vector of the NSWE physically conserved variables, \mathbf{F} is the flux vector and \mathbf{S} is the source term, with

$$\begin{aligned} \mathbf{U} &= \begin{bmatrix} H \\ P^* \end{bmatrix}, \quad \mathbf{F}(\mathbf{U}^*) = \begin{bmatrix} Hu \\ Hu^2 + \frac{1}{2}gH^2 \end{bmatrix}, \\ \mathbf{S}(\mathbf{U}^*) &= \mathbf{S}_b + \mathbf{S}_f + \mathbf{S}_d = \begin{bmatrix} 0 \\ -gHb_x \end{bmatrix} + \begin{bmatrix} 0 \\ -\tau \end{bmatrix} + \begin{bmatrix} -\psi_C \\ -u\psi_C + \psi_M \end{bmatrix} \end{aligned} \quad (3.2)$$

in which

$$P^* = Hu + Hz_a \left(\frac{z_a}{2} u_{xx} + (hu)_{xx} \right), \quad (3.3)$$

$$\psi_M = H_t z_a \left(\frac{z_a}{2} u_{xx} + (hu)_{xx} \right), \quad (3.4)$$

$$\psi_C = \left[\left(\frac{z_a^2}{2} - \frac{h^2}{6} \right) hu_{xx} + \left(z_a + \frac{h}{2} \right) h(hu)_{xx} \right]_x. \quad (3.5)$$

P^* is the velocity-like function and contains all time-derivatives in the momentum equation and a part of the dispersion terms, while H_t can be explicitly defined by the continuity equation, so the dispersion terms ψ_C and ψ_M contain only spatial derivatives.

Similarly, the equations derived by Madsen and Sørensen (2.48) along with (2.49), (2.50) and (2.51) can be written in one dimensional form of (3.1) where now:

$$\begin{aligned} \mathbf{U} &= \begin{bmatrix} H \\ P^* \end{bmatrix}, \quad \mathbf{F}(\mathbf{U}^*) = \begin{bmatrix} Hu \\ Hu^2 + \frac{1}{2}gH^2 \end{bmatrix}, \\ \mathbf{S}(\mathbf{U}^*) &= \mathbf{S}_b + \mathbf{S}_f + \mathbf{S}_d = \begin{bmatrix} 0 \\ -gHb_x \end{bmatrix} + \begin{bmatrix} 0 \\ -\tau \end{bmatrix} + \begin{bmatrix} 0 \\ -\psi \end{bmatrix} \end{aligned} \quad (3.6)$$

in which

$$P^* = Hu - \left(B + \frac{1}{3} \right) h^2 (Hu)_{xx} - \frac{1}{3} h h_x (Hu)_x \quad \text{and} \quad (3.7)$$

$$\psi = Bgh^3 \eta_{xxx} + 2h^2 h_x Bg \eta_{xx}. \quad (3.8)$$

As in 2D, the source term $\mathbf{S}(\mathbf{U}^*)$ includes again the bottom slope \mathbf{S}_b , friction \mathbf{S}_f and part of the dispersive terms is included in \mathbf{S}_d . The velocity like function P^* contains all time derivatives in the momentum equation and the dispersion term ψ contains only spatial derivatives.

Remark 1 We should keep in mind that, neglecting the dispersive terms in both the Boussinesq type (BT) equations described above the 1D non-linear shallow water equation system (2.19) is obtained.

3.2 FV spatial discretization

3.2.1 Brief review

In one space dimension, a finite volume method is based on subdividing the spatial domain into intervals, which are called grid cells, and keeping track of an approximation to the integral of \mathbf{U} over each of these volumes. In each time step we update these values using approximations to the flux through the endpoints of the intervals. Denoting $C_i = [x_{i-\frac{1}{2}}, x_{i+\frac{1}{2}}]$ the computational cell and considering a uniform grid spacing, for simplicity, the value \mathbf{U}_i^n will approximate the average value over the i th cell at time t^n as,

$$\mathbf{U}_i^n = \frac{1}{\Delta x} \int_{x_{i-\frac{1}{2}}}^{x_{i+\frac{1}{2}}} \mathbf{U}(x, t^n) \equiv \frac{1}{\Delta x} \int_{C_i} \mathbf{U}(x, t^n) dx, \quad (3.9)$$

where $\Delta x = x_{i+\frac{1}{2}} - x_{i-\frac{1}{2}}$ is the length of the cell. Integrating equation (2.14) along with (2.15) (and without considering the dispersive terms) in C_i we get the semi-discrete form of the conservation law:

$$\begin{aligned} \frac{\partial}{\partial t} \int_{C_i} \mathbf{U} dx + \int_{C_i} \mathbf{F}(\mathbf{U})_x dx &= \int_{C_i} \mathbf{S}(\mathbf{U}) dx \Rightarrow \\ \frac{\partial}{\partial t} \mathbf{U}_i + \frac{1}{\Delta x} [\mathbf{F}(\mathbf{U}_{i+\frac{1}{2}}, t) - \mathbf{F}(\mathbf{U}_{i-\frac{1}{2}}, t)] &= \frac{1}{\Delta x} \int_{C_i} \mathbf{S}(\mathbf{U}) dx. \Rightarrow \\ \frac{\partial}{\partial t} \mathbf{U}_i + \frac{1}{\Delta x} [\mathbf{F}_{i+\frac{1}{2}} - \mathbf{F}_{i-\frac{1}{2}}] &= \frac{1}{\Delta x} \int_{C_i} \mathbf{S}(\mathbf{U}) dx. \end{aligned} \quad (3.10)$$

$\mathbf{F}(\mathbf{U}_{i-\frac{1}{2}}) = \mathbf{F}_{i-\frac{1}{2}}$ is called the numerical flux, corresponding to the intercell boundary at $x = x_{i-\frac{1}{2}}$ between cells C_i and C_{i-1} . In general the numerical flux has the form

$$\mathbf{F}_{i-\frac{1}{2}} = \mathbf{F}_{i-\frac{1}{2}}(\mathbf{U}_{i-k_L}, \dots, \mathbf{U}_{i+k_R}) \quad (3.11)$$

where the non-negative integers k_L and k_R depend on the particular choice of numerical flux. Integrating (3.11) in time from t^n to t^{n+1} and using an appropriate integration rule we can conclude to either explicit or implicit time-stepping schemes. In explicit

methods the arguments are evaluated at the data time level n and in implicit methods arguments are evaluated at the unknown values at the new time level $n + 1$. The last ones can also include data values at time n . In the absence of the source term equation (3.10) takes the form:

$$\frac{\partial}{\partial t} \mathbf{U}_i + \frac{1}{\Delta x} [\mathbf{F}_{i+\frac{1}{2}} - \mathbf{F}_{i-\frac{1}{2}}] = 0. \quad (3.12)$$

The most important thing in deriving a corresponding numerical approximation is to choose a formula for the numerical flux function. The numerical flux can be considered as an approximation to the physical flux and should satisfy the consistency condition [171, 102]. If we sum (3.12) over any set of continuous cells $l \leq j \leq r$, we obtain the overall flux balance:

$$\frac{\partial}{\partial t} \Delta x \sum_{j=l}^r \mathbf{U}_j + [\mathbf{F}_{r+\frac{1}{2}} - \mathbf{F}_{l-\frac{1}{2}}] = 0, \quad (3.13)$$

which means that the total amount of the conserved variable \mathbf{U} changes only because of the fluxes through the end boundaries. The total mass within the computational domain will be preserved or at least will vary correctly provided the boundary conditions are properly imposed. This is called the telescopic property. Conservative methods as the above, can be proved that if they are convergent, then they will converge to a weak solution of the conservation laws [100]. For a convergent FV scheme (i.e. convergence to the true solution of the differential equation as, $\Delta x, \Delta t \rightarrow 0$) two conditions must hold. The first is that the method must be consistent with the differential equation and the second is that it must be stable, meaning that the small errors made in each time step do not grow too fast in later time steps. Conservative numerical methods are used in order to compute properly (velocity, position) shock waves when these are a part of the solution.

As mentioned before, the most crucial step in the construction of a numerical method is the choice of the numerical flux. A very common approach are the Godunov type methods or upwind methods. The first-order upwind method of Godunov [76] is a conservative method of the form (3.12) where the numerical fluxes $\mathbf{F}_{i+\frac{1}{2}}$ are computed using the solutions of the Riemann problem locally. A Riemann problem

centred at $x = 0$ has the form:

$$\begin{aligned} \mathbf{U}_t + \mathbf{F}(\mathbf{U})_x &= 0, \\ \mathbf{U}(x, 0) &= \begin{cases} \mathbf{U}_{left} & \text{if } x < 0, \\ \mathbf{U}_{right} & \text{if } x > 0. \end{cases} \end{aligned} \quad (3.14)$$

The solution to a Riemann problem with piecewise constant initial data consists of waves travelling at constant speeds away from the location of the jump discontinuity in the initial data. It is assumed that at a given time n the initial data have a piece-

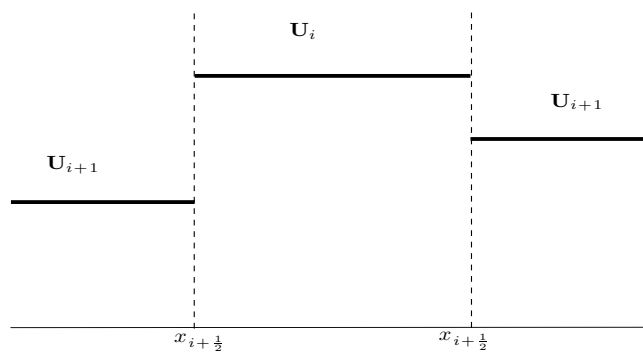


Figure 3.1: Computational cells and piecewise constant distribution for 1D problems.

wise constant distribution of the form (3.9). Figure 3.1 shows a possible distribution of the data at cells $i - 1$, i , $i + 1$. We can see that the data are pairs of constant states separated by discontinuities at intercell boundaries, (e.g. at $x_{i-\frac{1}{2}}$ and $x_{i+\frac{1}{2}}$). Then a local Riemann problem can be defined, e.g. at $x_{i+\frac{1}{2}}$, of the form (3.14) with $\mathbf{U}_{left} = \mathbf{U}_i^n$ and $\mathbf{U}_{right} = \mathbf{U}_{i+1}^n$. In a Godunov-type method [76] the numerical fluxes used are derived evaluating the real flux to the solution of the Riemann problems at $x_{i-\frac{1}{2}}$ and $x_{i+\frac{1}{2}}$. In a practical computation the Riemann problem is solved billions of times making this process the most demanding task in the numerical method. One can use approximate Riemann solvers, which can provide effective computational tools at a competitive cost. According to Toro [170], for the shallow water equations, approximate Riemann solvers may lead to savings of the order of 20% with respect to the exact Riemann solvers. There are two classes of approximate Riemann solvers. In the first class one computes an approximate solution to a state and then the numerical flux is obtained by evaluating the exact physical flux vector at this approximate state. In the second class of solvers one obtains an approximation to the flux directly. Some approximate Riemann solvers which belong to this category are the approximate Riemann solver of Roe [139], the

one of Osher [131], HLL (Harten, Lax and van Leer) [82] and HLLC [168] approximate Riemann solvers. In this study the approximate Riemann solver of Roe [139] is utilized.

One natural approach to define an approximate Riemann solution is to approximate the non-linear system in (3.14) by some linearised problem defined locally at each cell interface (Linearised Riemann Solvers):

$$\mathbf{U}_t + \mathbf{F}(\mathbf{U})_x \approx \mathbf{U}_t + \tilde{\mathbf{A}}_{i-\frac{1}{2}} \mathbf{U}_x = 0, \quad (3.15)$$

where $\tilde{\mathbf{A}}_{i-\frac{1}{2}}$ is a constant coefficient matrix, an approximation to the Jacobian matrix of the system, $\mathbf{F}'(\mathbf{U}) = \frac{\partial \mathbf{F}}{\partial \mathbf{U}}$. Matrix $\tilde{\mathbf{A}}_{i-\frac{1}{2}}$ should satisfy the following conditions:

- $\tilde{\mathbf{A}}_{i-\frac{1}{2}}$ is diagonalizable with real eigenvalues in order (3.15) to be hyperbolic,
- $\tilde{\mathbf{A}}_{i-\frac{1}{2}} \rightarrow \mathbf{F}'(\mathbf{U})$ as $\mathbf{U}_{i-1}, \mathbf{U}_i \rightarrow \mathbf{U}$ so that the method is consistent with the original conservation law,
- $\tilde{\mathbf{A}}_{i-\frac{1}{2}} (\mathbf{U}_i - \mathbf{U}_{i-1}) = \mathbf{F}(\mathbf{U}_i) - \mathbf{F}(\mathbf{U}_{i-1})$.

Following the description of LeVeque [102], the approximate Riemann solution then, consists of m waves proportional to the eigenvectors $\tilde{\mathbf{r}}_{i-\frac{1}{2}}^p$ of $\tilde{\mathbf{A}}_{i-\frac{1}{2}}$, propagating with speeds $s_{i-\frac{1}{2}}^p = \tilde{\lambda}_{i-\frac{1}{2}}^p$ given by the eigenvalues. For this linear Riemann problem, we can write the solution as a linear combination of the eigenvector of the matrix $\tilde{\mathbf{A}}_{i-\frac{1}{2}}$:

$$\Delta \mathbf{U}_{i-\frac{1}{2}} = \mathbf{U}_i - \mathbf{U}_{i-1} = \sum_{p=1}^m \alpha_{i-\frac{1}{2}}^p \tilde{\mathbf{r}}_{i-\frac{1}{2}}^p \quad (3.16)$$

for the coefficients $\alpha_{i-\frac{1}{2}}^p$ and then setting $\mathcal{W}_{i-\frac{1}{2}}^p = \alpha_{i-\frac{1}{2}}^p \tilde{\mathbf{r}}_{i-\frac{1}{2}}^p$ the p wave in the solution. The linearised matrix $\tilde{\mathbf{A}}_{i-\frac{1}{2}}$ should also follow the property that:

- If \mathbf{U}_{i-1} and \mathbf{U}_i are connected to a single wave $\mathcal{W}^p = \mathbf{U}_i - \mathbf{U}_{i-1}$ in the true Riemann solution, then \mathcal{W}^p should also be an eigenvector of $\tilde{\mathbf{A}}_{i-\frac{1}{2}}$

Using the Rankine-Hugoniot condition and applying some calculations [102] the above leads to the condition

$$\tilde{\mathbf{A}}_{i-\frac{1}{2}} (\mathbf{U}_i - \mathbf{U}_{i-1}) = \mathbf{F}(\mathbf{U}_i) - \mathbf{F}(\mathbf{U}_{i-1}).$$

For the Godunov type methods, like the one described so far, converge to discontinuous entropy satisfying weak solutions but they are only first order accurate and

numerically diffusive. Various second order methods such as Lax-Wendroff or Beam-Warming [102] can be derived based on Taylor expansions. It is well known that these schemes produce spurious (unphysical) oscillations in the vicinity of large gradients. One way of resolving this problem is the derivation of non-linear methods which are called Total Variation Diminishing methods (or TVD methods).

Total Variation Diminishing property

For a scalar conservation law of the form

$$\begin{aligned} u_t + f(u)_x &= 0, \\ u(x, 0) &= u_0(x), \end{aligned} \tag{3.17}$$

with $u(x, t) \in \mathbb{R}$, we can use the numerical conservative scheme :

$$u_i^{n+1} = u_i^n - \frac{\Delta t}{\Delta x} \left(f_{i+\frac{1}{2}}^n - f_{i-\frac{1}{2}}^n \right). \tag{3.18}$$

The total variation of the exact solution of a scalar conservation law is

$$TV(u) = \int |u_x| dx.$$

Harten [80] proved that a numerical scheme satisfies the TVD property if it holds that:

$$TV(u^{n+1}) \leq TV(u^n) \text{ where } TV(u^{n+1}) = \sum_i |u_{i+1}^{n+1} - u_i^{n+1}|.$$

The above property can be used in order to minimize the unphysical oscillations produced by the numerical schemes and allows convergence to shocks without spurious oscillations. There are two approaches for constructing TVD methods, the flux limiter approach and the slope limiter approach [50]. The idea in the flux-limiter methods is the combination of a low-order flux formula that works well near discontinuities and a higher order formula that works well in smooth regions [102, 171, 170]. Here will focus on the second approach where the basic idea is to replace the piecewise constant representation of the solution by some more accurate representation, say piecewise linear. Van leer [174, 95, 96] introduced the idea of modifying the piecewise constant data in the first-order Godunov method, as a first step, to achieve higher order of accuracy. This means that instead of using the values U_i and U_{i-1} interpolated values

in either side of the face \mathbf{U}^L and \mathbf{U}^R , are used. This approach is known as the Monotone Upstream-Centred Scheme for Conservation Laws (MUCSL). The MUSCL approach implies high-order accuracy obtained by data reconstruction and the reconstruction is constrained so as to avoid spurious oscillations, and thus the justification of the word monotone in the name of the scheme.

Going back to our scheme again and as mentioned before, we use the approximate Riemann solver of Roe to compute the convective terms. For the approximate Riemann solver the constant coefficient matrix $\tilde{\mathbf{A}}_{i-\frac{1}{2}}$ is an approximation to the Jacobian matrix (see Section 2.2.1) and is found in terms of the data states $\mathbf{U}^R - \mathbf{U}^L = \mathbf{U}_i - \mathbf{U}_{i-1}$ of the Riemann problem [170, 102]. For the NSW in one spatial dimension the matrix $\tilde{\mathbf{A}}_{i-\frac{1}{2}}$ is simply the Jacobian evaluated at mean values:

$$\tilde{H}_{i-\frac{1}{2}} = \frac{H^R + H^L}{2}, \quad \tilde{u}_{i-\frac{1}{2}} = \frac{u^R \sqrt{H^R} + u^L \sqrt{H^L}}{2} \quad (3.19)$$

where $L = i - 1$, $R = i$ and has the form

$$\tilde{\mathbf{A}}_{i-\frac{1}{2}} = \begin{bmatrix} 0 & 1 \\ -\tilde{u}^2 + g\tilde{H} & 2\tilde{u} \end{bmatrix}. \quad (3.20)$$

The eigenvalues of $\tilde{\mathbf{A}}_{i-\frac{1}{2}}$ are $\tilde{\lambda}_{i-\frac{1}{2}}^{1,2} = \tilde{u}_{i-\frac{1}{2}} \pm \tilde{c}_{i-\frac{1}{2}}$, with corresponding eigenvectors

$$\tilde{\mathbf{r}}_{i-\frac{1}{2}}^1 = \begin{bmatrix} 1 \\ \tilde{\lambda}_{i-\frac{1}{2}}^1 \end{bmatrix}, \quad \tilde{\mathbf{r}}_{i-\frac{1}{2}}^2 = \begin{bmatrix} 1 \\ \tilde{\lambda}_{i-\frac{1}{2}}^2 \end{bmatrix}$$

where $\tilde{c}_{i-\frac{1}{2}} = \sqrt{g \frac{H^R + H^L}{2}}$ is the celerity. The numerical fluxes of Roe can be defined as

$$\mathbf{F}_{i-\frac{1}{2}} = \mathbf{F}(\hat{\mathbf{U}}_{i-\frac{1}{2}}) = \tilde{\mathbf{A}}_{i-\frac{1}{2}} \hat{\mathbf{U}}_{i-\frac{1}{2}} \quad (3.21)$$

where $\hat{\mathbf{U}}_{i-\frac{1}{2}}$ is the exact solution of the linear Riemann problem (3.15) at $x_{i-\frac{1}{2}}$. The solution of the Riemann problem is

$$\hat{\mathbf{U}}_{i-\frac{1}{2}} = \mathbf{U}^R - \sum_{p:\lambda_p>0} (\alpha_p \tilde{\mathbf{r}}_p)_{i-\frac{1}{2}} = \mathbf{U}^L + \sum_{p:\lambda_p<0} (\alpha_p \tilde{\mathbf{r}}_p)_{i-\frac{1}{2}}$$

and combining the above we can write that

$$\hat{\mathbf{U}}_{i-\frac{1}{2}} = \frac{\mathbf{U}^L + \mathbf{U}^R}{2} + \frac{1}{2} \left(\sum_{p:\lambda_p < 0} - \sum_{p:\lambda_p > 0} \right) (\alpha_p \tilde{\mathbf{r}}_p)_{i-\frac{1}{2}}$$

and then the Roe flux becomes

$$\mathbf{F}_{i-\frac{1}{2}} = \tilde{\mathbf{A}}_{i-\frac{1}{2}} \hat{\mathbf{U}}_{i-\frac{1}{2}} = \frac{1}{2} \tilde{\mathbf{A}}_{i-\frac{1}{2}} (\mathbf{U}^L + \mathbf{U}^R) - \frac{1}{2} \left[\sum_{p:\lambda_p < 0} - \sum_{p:\lambda_p > 0} \right] (\alpha_p \tilde{\mathbf{A}} \mathbf{r}_p)_{i-\frac{1}{2}} \quad (3.22)$$

and since $\tilde{\mathbf{A}}_{i-\frac{1}{2}} \mathbf{r}_p = \lambda_p \mathbf{r}_p$ this yields:

$$\begin{aligned} \mathbf{F}_{i-\frac{1}{2}} &= \frac{1}{2} \tilde{\mathbf{A}}_{i-\frac{1}{2}} (\mathbf{U}^L + \mathbf{U}^R) - \frac{1}{2} \sum_{p=1}^m (|\lambda_p| \alpha_p \mathbf{r}_p)_{i-\frac{1}{2}} \\ &= \frac{1}{2} (\mathbf{F}(\mathbf{U}^L) + \mathbf{F}(\mathbf{U}^R)) - \frac{1}{2} \sum_{p=1}^m (|\lambda_p| \alpha_p \mathbf{r}_p)_{i-\frac{1}{2}} \end{aligned} \quad (3.23)$$

By denoting with $\Delta_{i-1/2}(\cdot) = (\cdot)_{i-1/2}^R - (\cdot)_{i-1/2}^L$ and $\mathbf{F}_{i-1/2}^{R,L} = \mathbf{F}(\mathbf{U}_{i-1/2}^{R,L})$, the numerical fluxes can be re-written in a matrix form:

$$\mathbf{F}_{i-1/2} = \frac{1}{2} (\mathbf{F}_{i-1/2}^R + \mathbf{F}_{i-1/2}^L) - \frac{1}{2} |\tilde{\mathbf{A}}_{i-\frac{1}{2}}| \Delta_{i-1/2} \mathbf{U} = \frac{1}{2} (\mathbf{F}_{i-1/2}^R + \mathbf{F}_{i-1/2}^L) - \frac{1}{2} \left[\mathbf{X} |\Lambda| \mathbf{X}^{-1} \right]_{i-1/2} \Delta_{i-1/2} \mathbf{U} \quad (3.24)$$

where the Roe average matrix $\tilde{\mathbf{A}}_{i-1/2}$ can be diagonalized, by the right and left eigenvector matrices $\mathbf{X}_{i-1/2}$ and $\mathbf{X}_{i-1/2}^{-1}$, and with $\Lambda_{i-1/2}$ being the diagonal matrix with the approximate eigenvalues in the diagonal.

3.2.2 Topography source term discretization

Up to now we have neglected source terms, such as the one due to the variable topography for the NSWE. In realistic applications the bottom topography variations (bed) add a source term to the equations. A hyperbolic conservation law with source terms, in one dimension, has the form (3.1). When solving the NSWE the numerical balance between discrete numerical fluxes and the topography source discretisation is very important. A scheme that respects this balance is known in the literature as a *well-balanced* scheme. It is currently a very active subject of research, we refer for example to [87, 123, 135, 118, 50, 73]. Well-balanced schemes preserve exactly steady state solutions (see Section 2.5), so that small perturbations of these solutions can be resolved without the need of excessive mesh refinement. The importance of satisfying

well-balanced property is extremely high since we don't introduce "numerical noise" in the equations and we obtain the correct numerical solution. In order to achieve the well balanced property in our schemes, we introduce the (topography source) flux vectors $\Delta \mathbf{S}_i^n$ such that

$$\frac{1}{\Delta x} \int_{C_i} \mathbf{S}(\mathbf{U}) = \frac{1}{\Delta x} \Delta \mathbf{S}_{b_i}^n.$$

Consequently (3.10) takes the form:

$$\frac{\partial}{\partial t} \mathbf{U}_i + \frac{1}{\Delta x} [\mathbf{F}_{i+\frac{1}{2}} - \mathbf{F}_{i-\frac{1}{2}}] = \frac{1}{\Delta x} \Delta \mathbf{S}_{b_i}^n. \quad (3.25)$$

As it has been demonstrated in [18, 87], an upwind discretization scheme should also be used for the topography source term, \mathbf{S}_b , to avoid non-physical oscillations in the solution by satisfying the C^- property (see Section 2.5). To satisfy this, the discrete topography source term should balance the corresponding non-zero flux terms, and as such it must be linearized in the same way and evaluated in the same state (Roe-averaged state) as the flux. The upwind discretization of the source term in (3.25) provides the following two terms (in-going contributions) that are added to the corresponding computational cell giving,

$$\Delta \mathbf{S}_{b_i} = \mathbf{S}_{b_{i+\frac{1}{2}}}^- + \mathbf{S}_{b_{i-\frac{1}{2}}}^+. \quad (3.26)$$

In order to compute $\mathbf{S}_{b_{i+\frac{1}{2}}}^-$ and $\mathbf{S}_{b_{i-\frac{1}{2}}}^+$ we have to project the source term to the eigenvectors of the Roe matrix (3.20):

$$\mathbf{S}_{b_{i-\frac{1}{2}}}^+ = \tilde{\mathbf{A}}^+ \tilde{\mathbf{A}}^{-1} \tilde{\mathbf{S}}_{b_{i-\frac{1}{2}}} = \frac{1}{2} (\tilde{\mathbf{A}} + |\tilde{\mathbf{A}}|) \tilde{\mathbf{A}}^{-1} \tilde{\mathbf{S}}_{b_{i-\frac{1}{2}}} = \frac{1}{2} (\mathbf{I} + |\tilde{\mathbf{A}}| \tilde{\mathbf{A}}^{-1}) \tilde{\mathbf{S}}_{b_{i-\frac{1}{2}}} \Rightarrow$$

$$\mathbf{S}_{b_{i-\frac{1}{2}}}^+ = \frac{1}{2} (\tilde{\mathbf{X}} (\mathbf{I} + \tilde{\mathbf{A}}^{-1} |\tilde{\mathbf{A}}|) \tilde{\mathbf{X}}^{-1}) \tilde{\mathbf{S}}_{b_{i-\frac{1}{2}}} \quad (3.27)$$

and

$$\mathbf{S}_{b_{i+\frac{1}{2}}}^- = \frac{1}{2} (\mathbf{I} - |\tilde{\mathbf{A}}| \tilde{\mathbf{A}}^{-1}) \tilde{\mathbf{S}}_{b_{i+\frac{1}{2}}} = \frac{1}{2} (\tilde{\mathbf{X}} (\mathbf{I} - \tilde{\mathbf{A}}^{-1} |\tilde{\mathbf{A}}|) \tilde{\mathbf{X}}^{-1}) \tilde{\mathbf{S}}_{b_{i+\frac{1}{2}}}. \quad (3.28)$$

Using the weights of the decomposition of the source term onto the eigenvectors of the Roe matrix

$$\tilde{\boldsymbol{\beta}}_{i-\frac{1}{2}} = \tilde{\mathbf{X}}^{-1} \tilde{\mathbf{S}}_{b_{i-\frac{1}{2}}}$$

and using the following discretization of the numerical source term

$$\tilde{\mathbf{S}}_{b_{i-\frac{1}{2}}} = \left[\begin{array}{c} 0 \\ -g \frac{H^R + H^L}{2} (b^R - b^L), \end{array} \right]_{i-\frac{1}{2}} \quad (3.29)$$

where here, $R = i$ and $L = i - 1$, we can re-write (3.27) and (3.28) into the form :

$$\mathbf{S}_{\mathbf{b}i-\frac{1}{2}}^+ = \frac{1}{2} \sum_{p=1}^m \left[\tilde{\beta}_p \tilde{\mathbf{r}}_p \left(1 + \text{sgn}(\tilde{\lambda}_p) \right) \right]_{i-\frac{1}{2}} \quad \text{and} \quad (3.30)$$

$$\mathbf{S}_{\mathbf{b}i+\frac{1}{2}}^- = \frac{1}{2} \sum_{p=1}^m \left[\tilde{\beta}_p \tilde{\mathbf{r}}_p \left(1 - \text{sgn}(\tilde{\lambda}_p) \right) \right]_{i+\frac{1}{2}} \quad (3.31)$$

with

$$(\beta_{1,2})_{i-\frac{1}{2}} = \pm \frac{c_{i-\frac{1}{2}}(b_i - b_{i-1})}{2}. \quad (3.32)$$

The advective numerical flux terms are now equal to the source term for a flow at rest in (3.25), i.e. $\Delta \mathbf{F}_i^n = \Delta \mathbf{S}_{\mathbf{b}i}^n$. After some factorizations we note that for each mesh cell:

$$\begin{aligned} u &= 0 \\ (b^R - b^L) &= -(H^R - H^L). \end{aligned} \quad (3.33)$$

The solution of the non-linear shallow water equations for a flow at rest as described in chapter 2 is:

$$u(x, t) = 0 \quad \text{and} \quad H(x, t) = D - b(x, t)$$

where $D > 0$ a constant number such that $D > \max\{b(x), x \in \Omega\}$. For the above flow condition $\mathbf{U}_t = 0$, which means that the topography source terms balance the corresponding non-zero flux terms $\mathbf{F}(\mathbf{U})_x = \mathbf{S}_{\mathbf{b}}$. Consequently a numerical scheme should keep the balance between the numerical fluxes and the numerical source term: $\mathbf{F}_{i+\frac{1}{2}} - \mathbf{F}_{i-\frac{1}{2}} = \Delta \mathbf{S}_{\mathbf{b}i}$.

3.2.3 Wet/dry front treatment

Most problems of practical interest involve wet and dry zones where the water inundates or recedes and the difficulty in numerical modeling dry areas relates to the obvious fact that the model equations are only defined for wet regions. In the boundary defined by a wet/dry front special considerations and treatments are in need to accurately model transitions between wet and dry areas while at the same time maintain high-order spatial accuracy. As identified also in [136, 51, 91], the following issues have to be addressed:

Dry cell identification

Computational cells with water depth $H \neq 0$ but $H \ll \Delta x$ have to be identified and treated. To identify dry cells, a common treatment is to use a wet/dry tolerance ε_w . If H in a cell is computed lower to ε_w this cell is considered dry, i.e. $H = 0$, $u = 0$. The choice of ε_w is not trivial and its value maybe related to the type of problem simulated and the mesh size.

Conservation of the flow at rest with dry regions

A numerical scheme should correctly compute the flow at rest exact solution (??) regardless of including wet/dry transitions and as such satisfy the extended C-property [38]. If no modifications are made, the numerical schemes presented until now is not well-balanced in this sense for adverse dry slopes (emerging topography). To deal with this problem we have to redefine the bed elevation at the emerging dry cell following [34, 33, 50, 125]. The reason for redefining the bed elevation is to obtain an exact balance at the front between the bed slope and the hydrostatic terms for steady conditions and to avoid the appearance of spurious pressure forces. Considering the case where a wet/dry front exists between computational cells with reconstructed face values L and R . This redefinition (reduction) of the bed elevation is formulated as:

$$\Delta b = \begin{cases} H^L, & \text{if } H^L > \varepsilon_{wd} \text{ and } H^R \leq \varepsilon_{wd} \text{ and } b^R < (b^R - b^L), \\ (b^L - b^R), & \text{otherwise} \end{cases} \quad (3.34)$$

in the calculation of \mathbf{S}_b in equations (3.29). In case that this treatment is not applied the water would climb over adverse bed slopes and the front will be wrongly diffused [34, 33, 38, 50, 125]. We note here that, the above redefinition of the bed elevation is not an actual reduction of the bed elevation value but is only applied in the calculation of \mathbf{S}_b in (3.29). The numerical treatment is similar if R is the wet side and L is identified as dry.

Flow in motion over adverse slopes

With the above redefinition of the discretized topography one can treat situations of emerging topography for a flow at rest. However, further modifications have to be made for a flow in motion. At interfaces between a wet/dry front, we impose, additional to the

above bed redefinition, the following temporary condition for the computation in (5.7), following [38, 50, 125],

$$\text{if } [H^L > \varepsilon_{wd} \text{ and } H^R \leq \varepsilon_{wd} \text{ and } H^L < (b^R - b^L)] \text{ then } u^L = u^R = 0. \quad (3.35)$$

We note that, the actual velocity is not set to zero in the wet cell, but only assumed as such at the face when computing the numerical flux and topography source term contributions. As such, the solution at each wet/dry face is considered to be that corresponding to an emerging bottom situation for a water at rest and then, to compute the time evolved solution, the numerical fluxes and sources corresponding to this approximate situation at the face are used. In this way, the wet/dry front is only allowed to advance when the water gradient in the wet cell is larger than the bottom gradient between cells. In addition, this numerical treatment avoids the appearance of negative values for H as well as un-physical overtopping [38, 39, 50].

Depth positivity and mass conservation

In cases where the bed elevation of a dry cell is less to that of a wet cell (downhill slope) the flow will continue to flood the dry cell and there is no need to modify the bed slope. However, when the bed slope is steep, there is a possibility that more water, than is actually contained in the wet cell, could be computed as flowing into the dry cell, causing the water depth in the wet cell to become negative and the scheme to become unstable.

In the present work and following [33] and [51], if this is the case, the cells with negative depth after one time step are identified and their water depth values and velocity components are set to zero. This adds a very small volume of water to the system. Then, the same volume of water is subtracted from all the wet cells (in the entire computational domain) in order to maintain mass conservation. This volume of subtracted mass is very small and as it is uniformly distributed to all the wet cells in the entire computational domain, an even smaller fraction of that mass volume is actually subtracted from each wet cell. Consequently, the possibility of numerically drying a wet cell during that procedure is almost non existent. The same procedure is adopted for those cells that have been identified as almost dry (by ε_{wd}), and their water depth was set to zero. Mass conservation has been monitored for the test cases considered in this work and the wet-dry treatment presented here is found to ensure absolute mass conservation.

We emphasize here that, while the above treatment steps have been proven successful for the NSW, it is the first time that have been incorporated to the numerical solution of dispersive models.

3.2.4 Higher order reconstruction

For the one-dimensional numerical scheme we have implemented a fourth-order MUSCL-type extrapolation schemes. More precisely, higher order accuracy in the calculation of numerical fluxes is achieved by constructing (left and right) cell interface values using the MUSCL-type extrapolation schemes prior to the evaluation of the numerical flux [62, 163, 148]. The reconstruction schemes are performed to the variables of total water depth H , velocity u , and also to the topography b , for the $(i + \frac{1}{2})$ cell interface.

Remark 2 *In general three choices exist for the presented reconstruction, using physical (primitives), conservative or characteristic variables. The numerical flux function for Roe's approximate solver is basically a function of physical variables. Therefore, when either conservative or characteristic variable reconstruction is performed, an additional step is necessary to transform the state back to physical variables.*

The fourth-order reconstruction scheme is given by Yamamoto et al. [186], and is also given here for completeness:

$$\begin{aligned} H_{i+\frac{1}{2}}^L &= H_i + \frac{1}{6} \left[\varphi(r_1) \Delta^* H_{i-\frac{1}{2}} + 2\varphi\left(\frac{1}{r_1}\right) \Delta^* H_{i+\frac{1}{2}} \right] \text{ and} \\ H_{i+\frac{1}{2}}^R &= H_{i+1} - \frac{1}{6} \left[2\varphi(r_2) \Delta^* H_{i+\frac{1}{2}} + \varphi\left(\frac{1}{r_2}\right) \Delta^* H_{i+\frac{3}{2}} \right] \end{aligned} \quad (3.36)$$

where φ is the van Leer nonlinear slope limiter function [102],

$$\begin{aligned} \varphi(r_1) &= \frac{r_i + |r_i|}{1 + |r_i|} \text{ with } r_1 = \frac{\Delta^* H_{i+\frac{1}{2}}}{\Delta^* H_{i-\frac{1}{2}}}, r_2 = \frac{\Delta^* H_{i+\frac{3}{2}}}{\Delta^* H_{i+\frac{1}{2}}} \text{ and} \\ \Delta^* H_{i+\frac{1}{2}} &= \Delta H_{i+\frac{1}{2}} - \frac{1}{6} \left(\Delta \bar{H}_{i+\frac{3}{2}} - 2\Delta \bar{H}_{i+\frac{1}{2}} + \Delta \bar{H}_{i-\frac{1}{2}} \right) \end{aligned}$$

where

$$\Delta \bar{H}_{i-\frac{1}{2}} = \text{minmod}(\Delta H_{i-\frac{1}{2}}, \Delta H_{i+\frac{1}{2}}, \Delta H_{i+\frac{3}{2}}), \quad (3.37)$$

$$\Delta \bar{H}_{i+\frac{1}{2}} = \text{minmod}(\Delta H_{i+\frac{1}{2}}, \Delta H_{i+\frac{3}{2}}, \Delta H_{i-\frac{1}{2}}), \quad (3.38)$$

$$\Delta \bar{H}_{i+\frac{3}{2}} = \text{minmod}(\Delta H_{i+\frac{3}{2}}, \Delta H_{i-\frac{1}{2}}, \Delta H_{i+\frac{1}{2}}), \quad (3.39)$$

$$\Delta H_{i+1/2} = H_{i+1} - H_i, \quad (3.40)$$

with the minmod limiter function given as:

$$\text{minmod}(a, b, c) = \text{sign}(a) \max(|a|, 2\text{sign}(a)b, 2\text{sign}(a)c).$$

The same hold for the velocity u and the topography b reconstructed values.

Topography source term discretization

As mentioned before, in the presence of topography source terms, and in order to satisfy the exact C -property, the topography source term should balance the corresponding non-zero flux terms. While above holds for the first order scheme, i.e. if the (L) and (R) are not reconstructed ($\mathbf{U}^L = \mathbf{U}_{i-1}$ and $\mathbf{U}^R = \mathbf{U}_i$), this is not the case for higher order schemes. Following the works in [87, 125] a correction term, \mathbf{S}_b^* , should be included in the topography source discretization :

$$\Delta \mathbf{S}_{bi} = \mathbf{S}_{bi+\frac{1}{2}}^- + \mathbf{S}_{bi-\frac{1}{2}}^+ + \mathbf{S}_b^*. \quad (3.41)$$

The first terms on the right hand side is evaluated precisely as before (3.27)-(3.28), except that the interface values are now those of the MUSCL reconstruction of the solution within each cell. The final term is the source term integral approximated over the mesh cell and is evaluated at the Roe average of the left and right states of the linear reconstruction of the solution within the cell. This term reads as,

$$\mathbf{S}_b^* \left(\mathbf{U}_{i+\frac{1}{2}}^L, \mathbf{U}_{i-\frac{1}{2}}^R \right) = \begin{bmatrix} 0 \\ -g \frac{H_{i-\frac{1}{2}}^R + H_{i+\frac{1}{2}}^L}{2} (b_{i-\frac{1}{2}}^R - b_{i+\frac{1}{2}}^L) \end{bmatrix}.$$

The term vanishes for a first order scheme as $b_{i-\frac{1}{2}}^R = b_{i+\frac{1}{2}}^L = b_i$, while for flow at rest we have in addition:

$$\frac{\partial h}{\partial x} = -\frac{\partial b}{\partial x} \Rightarrow b_{i+\frac{1}{2}}^L - b_{i-\frac{1}{2}}^R = -\left(H_{i+\frac{1}{2}}^L - H_{i-\frac{1}{2}}^R \right).$$

3.3 FD discretization of the dispersion terms

Up to now we have described the discretization for the advective part of the BT equations, i.e. the NSW equations flux functions, including the topography terms. Both in Nowgu's and Madsen and Sørensen's BT models the dispersion terms contain spatial derivatives up to third order. According to [179] a fourth-order accurate treatment of the first order derivatives is required so that the truncation errors in the numerical schemes are smaller than the dispersion terms present in the models. As such, we discretize them using fourth-order central finite difference (FD) approximations for first order derivatives, third order central difference approximations for third order derivatives and second order for second order derivatives, resulting to finite-volume/finite-difference schemes for both Boussinesq type-equations in one dimension

3.3.1 Discretization of the dispersion terms for Nwogu's equations

In the conservative form of Nwogu's equations, (2.89) with (2.91) and (2.92), the dispersive terms that contain only spatial derivatives is the term $\mathbf{S}_d = [-\psi_c - u\psi_c + \psi_M]^T$. Integrating the above we conclude to the term $(\psi_c)_i$ (the cell average of the term ψ_c) in the mass and the momentum equation.

$$\begin{aligned}
(\psi_c)_i &= \frac{1}{\Delta x} \int_{C_i} \psi_c \\
&= \frac{1}{\Delta x} \int_{C_i} \left[\left(\frac{z_a^2}{2} - \frac{h^2}{6} \right) hu_{xx} + \left(z_a + \frac{h}{2} \right) h(hu)_{xx} \right]_x \\
&= \frac{1}{\Delta x} \left\{ \left[\left(\frac{z_{ai+1/2}^2}{2} - \frac{h_{i+1/2}^2}{6} \right) h_{i+1/2} (u_{i+1/2})_{xx} + \left(z_{ai+1/2} + \frac{h_{i+1/2}}{2} \right) h_{i+1/2} (h_{i+1/2} u_{i+1/2})_{xx} \right] \right. \\
&\quad \left. - \left[\left(\frac{z_{ai-1/2}^2}{2} - \frac{h_{i-1/2}^2}{6} \right) h_{i-1/2} (u_{i-1/2})_{xx} + \left(z_{ai-1/2} + \frac{h_{i-1/2}}{2} \right) h_{i-1/2} (h_{i-1/2} u_{i-1/2})_{xx} \right] \right\} \quad (3.42)
\end{aligned}$$

Substituting a cell averaged value ϕ_i (let ϕ denote u , hu) in to the Taylor series:

$$\phi = \phi_{i+\frac{1}{2}} + x\phi'_{i+\frac{1}{2}} + \frac{x^2}{2}\phi''_{i+\frac{1}{2}} + \frac{x^3}{6}\phi'''_{i+\frac{1}{2}} + \frac{x^4}{24}\phi''''_{i+\frac{1}{2}} + \dots$$

we can express a cell average value with the values defined at cell interfaces [94, 97]. Through manipulations of Taylor series expansions, the following discretization equa-

tions can be derived and used for the discretization of (3.42):

$$\phi_{i+1/2} = \frac{7(\phi_{i+1} + \phi_i) - (\phi_{i+2} - \phi_{i-1})}{12} + O(\Delta x^4), \quad (3.43)$$

$$(\phi_{i+1/2})_{xx} = \frac{(\phi_{i+2} + \phi_{i-1}) - (\phi_{i+1} - \phi_i)}{2\Delta x^2} + O(\Delta x^2). \quad (3.44)$$

For the momentum equation we have to discretize the term ψ_M that contains a second order derivative u_{xx} and a time derivative H_t . The second order derivative is discretized using:

$$(u_i)_{xx} = \frac{u_{i-1} - 2u_i + u_{i+1}}{\Delta x^2} + O(\Delta x^2), \quad (3.45)$$

thus ψ_M is then given by

$$(\psi_M)_i = (H_i)_t z_{ai} \left(\frac{z_{ai}}{2} \frac{u_{i-1} - 2u_i + u_{i+1}}{\Delta x^2} + \frac{h_{i-1}u_{i-1} - 2h_i u_i + h_{i+1}u_{i+1}}{\Delta x^2} \right). \quad (3.46)$$

with term $(H_i)_t$ explicitly obtained from the mass equation in terms of spatial derivatives only.

3.3.2 Discretization of the dispersion terms for MS equations

For the Madsen and Sørensen's equations, following [62], we discretize the term ψ , using fourth-order central finite difference (FD) approximations for first order derivatives, third order central difference approximations for third order derivatives and second order for second order derivatives, so:

$$(\phi_i)_x = \frac{\phi_{i-2} - 8\phi_{i-1} + 8\phi_{i+1} - \phi_{i+2}}{12\Delta x} + O(\Delta x^4), \quad (3.47)$$

$$(\phi_i)_{xxx} = \frac{\phi_{i+2} - 2\phi_{i+1} + 2\phi_{i-1} - \phi_{i-2}}{2\Delta x^3} + O(\Delta x^3). \quad (3.48)$$

Applying (3.45), (3.47) and (3.48) in equation we get the discrete dispersion term:

$$\begin{aligned} \psi_i &= \frac{Bgh_i^3}{\Delta x^3} \left[\eta_{i+2} + 2\eta_{i+1} + 2\eta_{i-1} - \phi_{i-2} \right] \\ &\quad - \frac{Bgh_i^2}{6\Delta x^3} \left[(h_{i-2} - 8h_{i-1} + 8h_{i+1} - h_{i+2})(\eta_{i-1} - 2\eta_i + \eta_{i+1}) \right]. \end{aligned} \quad (3.49)$$

3.4 Time integration

Time integration scheme should at least match the order of truncation errors from the spatial derivatives in the dispersion terms [179]. With third order spatial derivatives in both equations we use the fourth-order predictor-corrector method proposed in [179]. Time integration for this scheme, is achieved in two stages, namely the third order Adams-Basforth predictor stage and the fourth order Adams-Moulton corrector stage:

1. Predictor stage (Adams-Basforth method)

$$\begin{aligned} \mathbf{U}_i^p &= \mathbf{U}_i^n + \frac{\Delta t^n}{12\Delta x} \left[23 \left(-\Delta \mathbf{F}_i^n + \Delta \mathbf{S}_{b_i}^n + \Delta x \mathbf{S}_{d_i}^n + \Delta x \mathbf{S}_{f_i}^n \right) \right. \\ &\quad - 16 \left(-\Delta \mathbf{F}_i^{n-1} + \Delta \mathbf{S}_{b_i}^{n-1} + \Delta x \mathbf{S}_{d_i}^{n-1} + \Delta x \mathbf{S}_{f_i}^{n-1} \right) \\ &\quad \left. + 5 \left(-\Delta \mathbf{F}_i^{n-2} + \Delta \mathbf{S}_{b_i}^{n-2} + \Delta x \mathbf{S}_{d_i}^{n-2} + \Delta x \mathbf{S}_{f_i}^{n-2} \right) \right] \end{aligned} \quad (3.50)$$

2. Corrector stage (Adams-Moulton method)

$$\begin{aligned} \mathbf{U}_i^{n+1} &= \mathbf{U}_i^n + \frac{\Delta t^n}{24\Delta x} \left[9 \left(-\Delta \mathbf{F}_i^p + \Delta \mathbf{S}_{b_i}^p + \Delta x \mathbf{S}_{d_i}^p + \Delta x \mathbf{S}_{f_i}^p \right) + 19 \left(-\Delta \mathbf{F}_i^n + \Delta \mathbf{S}_{b_i}^n + \Delta x \mathbf{S}_{d_i}^n + \Delta x \mathbf{S}_{f_i}^n \right) \right. \\ &\quad - 5 \left(-\Delta \mathbf{F}_i^{n-1} + \Delta \mathbf{S}_{b_i}^{n-1} + \Delta x \mathbf{S}_{d_i}^{n-1} + \Delta x \mathbf{S}_{f_i}^{n-1} \right) \\ &\quad \left. + \left(-\Delta \mathbf{F}_i^{n-2} + \Delta \mathbf{S}_{b_i}^{n-2} + \Delta x \mathbf{S}_{d_i}^{n-2} + \Delta x \mathbf{S}_{f_i}^{n-2} \right) \right] \end{aligned} \quad (3.51)$$

where $\Delta \mathbf{F}_i$ and $\Delta \mathbf{S}_{b_i}$ are respectively the flux and bed source variations, obtained using (3.24) and (3.27). \mathbf{S}_{d_i} is the discretization of the dispersion terms while \mathbf{S}_{f_i} is the friction term.

The value of the time-step, Δt^n that is used to integrate the governing equations over time, is depended upon the CFL condition. For the one-dimensional solver

$$\Delta t^n = CFL \min_i \left(\frac{\Delta x}{|u_i^n| + \sqrt{gH_i^n}} \right)$$

where CFL is the Courant number between zero and one.

3.5 Evaluation of the velocities

After each time step we obtain the new solution variables for the velocity like function, i.e (3.3) for Nwogu's model and (3.8) for the MS model. From these we have to recover the velocity field. To achieve this we have to discretize (3.3) and (3.8) using the FD method. The procedure is described in [91] but we detail here for completeness. For Nwogu's formulation

$$P_i^* = (Hu)_i + (Hz_a)_i \left(\frac{z_a}{2} u_{xx} + (hu)_{xx} \right)_i$$

using (3.45) to discretize the second order derivatives u_{xx} and $(hu)_{xx}$ we get

$$P_i^* = (Hu)_i + (Hz_a)_i \left[\frac{z_{ai}}{2} \left(\frac{u_{i-1} - 2u_i + u_{i+1}}{\Delta x^2} \right) + \left(\frac{h_{i-1}u_{i-1} - 2hiu_i + h_{i+1}u_{i+1}}{\Delta x^2} \right) \right]. \quad (3.52)$$

Reformulating the equation (3.52) we get:

$$\alpha_i u_{i-1} + \beta_i u_i + \gamma_i u_{i+1} = P_i^*, \quad \forall i = 1, \dots, N \quad (3.53)$$

where

$$\alpha_i = H_i z_{ai} \left(\frac{z_{ai}}{2\Delta x^2} + \frac{d_{i-1}}{\Delta x^2} \right), \quad \beta_i = H_i \left(1 - \frac{z_{ai}^2}{\Delta x^2} - \frac{2z_{ai}d_i}{\Delta x^2} \right) \text{ and } \gamma_i = H_i z_{ai} \left(\frac{z_{ai}}{2\Delta x^2} + \frac{d_{i+1}}{\Delta x^2} \right). \quad (3.54)$$

The central difference scheme only involves left and right neighboring cells and thus forms a tridiagonal linear system $\mathbf{M}\mathbf{V} = \mathbf{C}$ of equations in the form (see also [142]):

$$\begin{bmatrix} \beta_1 & \gamma_1 & & & & \\ \alpha_2 & \beta_2 & \gamma_2 & & & \\ & \ddots & \ddots & \ddots & & \\ & & & \alpha_{N-1} & \beta_{N-1} & \gamma_{N-1} \\ & & & & \alpha_N & \beta_N \end{bmatrix} \begin{bmatrix} u_1 \\ u_2 \\ \vdots \\ u_{n-1} \\ u_N \end{bmatrix} = \begin{bmatrix} P_1^* \\ P_2^* \\ \vdots \\ P_{N-1}^* \\ P_N^* \end{bmatrix} \quad (3.55)$$

with \mathbf{M} a symmetric and positive definite matrix when topography is not introduced, \mathbf{V} the velocity vector, and \mathbf{C} the vector that contains P_i^* , $i = 1, \dots, N$ obtained from the spatial solver. An efficient Thomas algorithm [65] was implemented to solve the system for obtaining the velocity u_i^p in the predictor step and u_i^{n+1} in the corrector one, from the respective variables P_i^* .

For the MS equations the velocity like function has the form:

$$P_i^* = (Hu)_i - \left[\left(B + \frac{1}{3} \right) h^2 (Hu)_{xx} - \frac{1}{3} h h_x (Hu)_x \right]_i \quad (3.56)$$

which requires the approximation of first and second order derivatives. Using again (3.45) for the term $(Hu)_{xx}$, (3.47) for h_x and for $(Hu)_x$ we use the central difference

$$(H_i u_i)_x = \frac{H_{i+1} u_{i+1} - H_{i-1} u_{i-1}}{2\Delta x}.$$

Equation (3.56) results again in a tridiagonal linear system of equations in the form of (3.55) with coefficients, see also [62, 163, 148]:

$$\tilde{\alpha}_i = \left[-k_1 + \frac{k_2}{72} \right], \quad \tilde{\beta}_i = 1 + 2k_1, \quad \tilde{\gamma}_i = - \left[k_1 + \frac{k_2}{72} \right].$$

in which

$$k_1 = \left(B + \frac{1}{3} \right) \left(\frac{h_i^2}{\Delta x^2} \right) \quad \text{and} \quad k_2 = \frac{h_i}{\Delta x^2} (h_{i-2} - 8h_{i-1} + 8h_{i+1} - h_{i+2}).$$

Both matrices can be pre-calculated and used through a numerical simulation.

As suggested by Wei et al. [179], the corrector stage is repeated until the relative error between two successive results reaches a prescribed tolerance. This error is computed for each of the variables H and u and is defined as

$$e = \frac{\sum_i |v_i^{n+1} - \tilde{v}_i^{n+1}|}{|\sum_i v_i^{n+1}|}$$

where v denotes any of the variables and \tilde{v} denotes the previous estimate. In this work the values computed in the corrector step are considered to be the final next time step $(n+1)$ values when $e < 10^{-4}$. The scheme usually converges to the prescribed tolerance in one or two iterations since the predictor step provides very accurate results.

3.6 Boundary conditions and wave generator

To completely define the differential problem, boundary conditions need to be introduced. Two types of boundary conditions are used in this work: outflow an solid (reflective) wall. Since we use a fourth order MUSCL scheme the usage of three ghost cells, in each boundary, are required in order to determine the values of the nodes

closest to the boundary. An outflow boundary condition should allow all energy propagating towards the boundary to pass through so that no waves are reflected back in to the solution domain. For that reason the values of H and u at the ghost cells are extrapolated from the interior cells [148, 91, 102] while sponge layers are placed in front of each boundary. More precisely on this layer the surface elevation was damped by multiplying its value by a coefficient $m(x)$ defined as [185]:

$$m(x) = \sqrt{1 - \left(\frac{x - d(x)}{L_s}\right)^2} \quad (3.57)$$

where L_s is the sponge layer width and $d(x)$ is the normalized distance between the cell center with coordinate x and the absorbing boundary. Our numerical experience and that in [185] show that

$$L \leq L_s \leq 1.5L, \quad (3.58)$$

i.e. the width of the sponge layer is proportional to the wavelength. Solid walls are treated as impermeable and fully reflective, therefore the normal flux at these boundaries must be zero. This concludes that the velocity u_{-g} at the ghost cells must be set as $u_{-g} = -u_g$ from the interior, and an odd and even extrapolation is used for H .

A number of tests require the generation and propagation of monochromatic periodic waves. In order to produce these waves we follow the approach of adding to the mass equation an internal source term of periodic variation in time. In [181] a source function method for the generation of regular and irregular surface waves, using the equations of Nwogu, was derived. In this work, and for the equations of Nwogu [127], this source function wave-making method is adopted in order to let the reflected waves outgo through the wave generator freely. The form of the source function in 1D is:

$$S(x, t) = D^* \exp\left(-\gamma(x - x_s)^2\right) \sin(-\omega t) \quad (3.59)$$

in which

$$\gamma = \frac{80}{\delta^2 L^2}$$

where L is the wave length, ω the wave frequency, x_s is the location of the center of the wave-making area, δ is a parameter that influence the width of the wave generator and

D^* is the source function's amplitude:

$$D^* = \frac{2\sqrt{\gamma}A_0(\omega^2 - \alpha_1 g k^4 h^3)}{\omega k \sqrt{\pi} \exp(k^2/4\gamma) [1 - \alpha(kh)^2]} \quad (3.60)$$

where h is the still water level at the wave generation region, A_0 the wave amplitude, k the wave number, $\alpha = -0.39$ and $\alpha_1 = \alpha + 1/3$.

Remark 3 *To determine the range of values for δ , we performed several tests to verify its effect to the calculating wave height in condition with variance of relative water depth (h/L), input wave height and effective mesh size. It is concluded that, when the water depth is shallow, the value of δ should be large, but when the water depth is deep, its value should be small and that its value has the same variance trend with relative wave height. The typical value of $\delta \in [0.2, 0.8]$ for the model tests.*

Up to now, for the MS equations one way to create regular waves is the use of Dirichlet type boundary conditions see [163]. This way is very inefficient since the produced wave has larger amplitude and highly frequency oscillations can be developed. Additionally this method is only for very small amplitude waves and does not allow for the waves returning to the inflow region and passing out of the domain. Very recently and for the equations of MS, [138] developed an internal wave generator based on the approach of [177]. The limitation of this approach is the complex nature of the generator, since its values must be calibrated, along with the non-physical meaning of the function used. We use and develop the internal source function approach from [138]. The internal wave generator has the form of (3.59) with

$$D^* = \frac{2CA_0\sqrt{\gamma}}{\sqrt{\pi}}, \quad (3.61)$$

with

$$\gamma = \frac{b_w}{L^2}.$$

The width of the generation region results strongly dependent on the value attributed to the parameter γ which also influences the amplitude of the signal obtained. A_0 is the desired wave's amplitude, C is the wave's speed and b_w has been chosen as to give the expression the correct physical. The values of the b_w have to be calibrated in order to obtain the signal sought. The use of the Gaussian function to distribute the generated

wave over several mesh points is similar in principle to the method described by [179]. However further investigation is needed to derive a method for generating waves in a MS model.

Next we apply the two wave generation models to generate monochromatic waves with different periods $T = 1.27, 2.02s$. The domain length is $[-20, 20m]$, grid size $\Delta x = 0.01m$, sponge layer width is $5m$ and the CFL used is 0.5. The source function width (δ) for the equations of Nwogu is kept the same for all the waves presented and equals to 0.3. For the first wave ($T = 1.27s$), the still water level is $h = 0.5m$, amplitude $A = 0.025m$ and wavelength $L = 2.2361m$, while for the second case ($T = 2.02s$) $h = 0.4$ and $A = 0.01$, corresponding to wavelengths $L = 3.63$. The parameter b_w for the equations of MS is 15 for the first wave and 80 for the second wave.

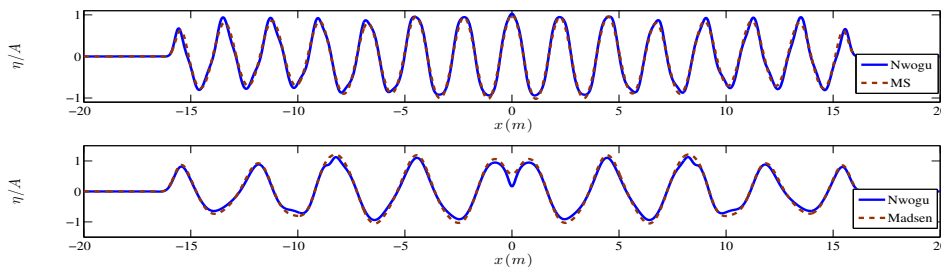


Figure 3.2: Snapshots of surface elevation at $t = 20s$. $T = 1.27s$ (up), $T = 2.02s$ (down).

The generated waves shown in Fig. 3.2, are quite good and the corresponding wave heights are very close to the target one. Moreover, the two equations generate almost the same waves which propagate in a constant form. This indicates that the wave generator for the MS equations can be used despite its arbitrary form.

3.7 Wave breaking modeling

Accurate simulation of wave breaking is an important modeling issue in near-shore environments. It dissipates wave energy through the generation of turbulence, including substantial air entrainment. Since the wave's amplitude increases due to shoaling, the wave's front becomes vertical and the wave's crest overturns. BT equations are unable to describe this phenomenon and an additional mechanism is necessary. A wave breaking model for the BT equations requires two mechanisms to simulate the breaking process numerically. The first one is a "trigger mechanism" related to the initiation and, possibly the termination, of the breaking process. The second mechanism is an energy

dissipation mechanism.

Existing wave breaking trigger models can be classified, in the main, into (a) phase-averaged breaking models and (b) phase resolving breaking models. Phase-averaged trigger models include wave characteristics which are representative of one full phase of the wave. Their limited use to BT models is attributed to the necessity of an algorithm that separates individual waves in order to obtain the wave characteristics such as, wave height and wave length. Extension of these parameterizations to 2D wave cases, and especially for unstructured numerical meshes remains a very difficult task. A review of these wave breaking criteria can be found in Okamoto et al. [129] and references therein.

On the other hand, phase-resolving models use information at certain locations of the wave. There exist mainly two types of phase-resolving wave breaking mechanisms related to the initiation and termination of the breaking process. The first one is controlled by the local slope angle [144] and the second by the vertical speed of the free surface elevation [93]. In the present work, we consider wave breaking criteria of the phase-resolving type and we propose a combination of trigger mechanisms which can be classified as to fall in between of the two aforementioned phase-resolving approaches (namely the local slope and vertical speed variations).

For the energy dissipation a local switch from the BT model to the NSW model can be performed when a wave is characterized as ready to break, by suppressing the dispersion terms. This approach allows for a natural treatment of breaking waves as shocks and we can take advantage of the shock capturing properties of the developed unstructured FV scheme. In addition, by making this decision, i.e. switching locally to NSW equations, we conserve mass and momentum across the wave front of waves characterized as breaking ones. Furthermore, this switching allows a spatial characterization of the computational domain to pre- and post-breaking areas and as such an accurate description of both non-breaking (governed by the BT model) and breaking waves (governed by the NSW model) transformations and treatment of shoreline motion. Such an approach leads to hybrid (one- and two-dimensional) BT-NSW models and has gained attention by several researchers in the past few years, please refer to [25, 163, 164, 91, 147, 141, 130, 160, 165].

In this work two different approaches are implemented and tested here for numerically resolving the wave breaking problem within the FV framework, an eddy viscosity

approach and a hybrid BT-NSW one.

3.7.1 Eddy Viscosity Models

Eddy viscosity models have the longest history in application. These involve extending the momentum equation by the addition of a dissipation term, which implies that a contribution to flow momentum is imposed when breaking occurs, in contrast to the momentum-conserving bore process in the non-dispersive theory. In situations where dissipation is imposed globally and spatial variations in viscosity are small, this effect is minor. However, at the onset of breaking or in models where dissipation is localized and spatial gradients of viscosity are large, this momentum source effect can be quite severe, and should be avoided by correctly specifying the dissipation term. In this work, and for the 1D problem two eddy viscosity models are implemented and tested for comparison purposes and are presented next for completeness.

Kennedy's et al. wave breaking model [93] Kennedy et al. [93] used the eddy viscosity-type formulation to incorporate the equations of Wei et al. [180] with a wave breaking mechanism in order to model the turbulent mixing and dissipation caused by breaking. The mass conservation equation remains unchanged while, an extra eddy viscosity term is added to the momentum equation. So, for the equations of Nwogu (3.1), (3.2) and for MS BT equations (3.1) and (3.6) the source term \mathbf{S}_f can be re-written as

$$\mathbf{S}_f = \begin{bmatrix} 0 \\ -\tau + R_b \end{bmatrix} \quad (3.62)$$

where

$$R_b = (\nu(Hu)_x)_x \quad (3.63)$$

with $\nu = B\delta_b^2 H \eta_t$ the eddy viscosity, which is a function of both space and time and is determined in a similar manner to [189], but with several differences. δ_b is a mixing length coefficient with value $\delta_b = 1.2$ and the quantity B varies smoothly from 0 to 1 so

as to avoid an impulsive start of breaking and the resulting instability. It is given as

$$B = \begin{cases} 1 & \text{if } \eta_t \geq 2\eta_t^* \\ \frac{\eta_t}{\eta_t^*} & \text{if } \eta_t^* < \eta_t \leq 2\eta_t^* \\ 0 & \text{if } \eta_t \leq \eta_t^* \end{cases} \quad (3.64)$$

the parameter η_t^* determines the onset and the cessation of breaking and takes the value:

$$\eta_t^* = \begin{cases} \eta_t^{(F)} & \text{if } t \geq T^* \\ \eta_t^{(I)} + \frac{t - t_0}{T^*}(\eta_t^{(F)} - \eta_t^{(I)}) & \text{if } 0 < t - t_0 \leq T^* \end{cases} \quad (3.65)$$

where T^* is the transition time, t_0 is the time that breaking was initiated, and thus $t - t_0$ is the age of the breaking event. The breaking event begins when η_t exceeds some initial threshold value, but as breaking develops, the wave will continue to break even if H_t drops below this value. The values of $\eta_t^{(I)}$, $\eta_t^{(F)}$ and T^* used here (following [93]) are $c_1 \sqrt{g\eta}$, $c_2 \sqrt{g\eta}$ and $c_3 \sqrt{\eta/g}$ respectively. The values of c_1, c_2, c_3 are problem depended. The largest disadvantage of the above model is that, in some special cases, such as stationary hydraulic jumps, the criterion may not work and wave breaking initiation will not recognized. It is worth to mention that in the present work, no artificial filtering is used in any of the wave breaking models described.

Roeber's et al. wave breaking model [142] Roeber et al. [142] derived a modified version of Kennedy's eddy viscosity wave breaking model (described above), to incorporate the Boussinesq-type equations of Nwogu, written in a conservative form in 1D. The eddy viscosity term added to the momentum equation is (3.63) but in order to determine the eddy viscosity ν a different indicator is used. Kennedy et al. [93] use a velocity indicator derived from η_t in contrast to Rober et al. [142] who used $(Hu)_x$ as the indicator to be consistent with the numerical formulation and to better detect stationary or slow-moving hydraulic jumps that might otherwise not be detected from η_t . Thus

$$\nu = BH|(Hu)_x| \quad (3.66)$$

in which

$$B = 1 - \frac{(Hu)_x}{U_1} \quad \text{for } |(Hu)_x| \geq U_2, \quad (3.67)$$

where U_1 , U_2 denote the flow speeds at the onset and termination of the wave-breaking process and must be calibrated through laboratory experiments. They are expressed in terms of the shallow water celerity as $U_1 = B_1 \sqrt{hH}$ and $U_2 = B_2 \sqrt{hH}$ where B_1 , B_2 are calibration coefficients. Breaking begins when $|(Hu)_x| \geq U_1$ and continues as long as $|(Hu)_x| \geq U_2$. The above criterion may result in breaking on the back of the wave's crest since short period waves may have large values of $|(Hu)_x|$ on both the front and the back of the crest. In order to avoid this, Roeber replaced $(Hu)_x$ in (3.66) and (3.67) by $0.5 [(Hu)_x + (Hu)_x]$ which becomes zero on the back of the crest. The breaking term stays active for a duration equal to $T^* = 5 \sqrt{H/g}$, accounting for the continuing dissipation process behind the broken waves, where the momentum gradient would not exceed the breaking thresholds.

3.7.2 Hybrid wave breaking models

The approach of Hybrid wave breaking models has gained a lot of popularity the last few years, due to their simplicity and efficiency. Following this approach one simply (under certain conditions) turns off the dispersive part of the BT equations in the region where breaking occurs [163, 164, 141, 91, 24]. The hybrid idea is based on the assumption that Boussinesq equations automatically degenerate into NSWE as dispersive terms become negligible compared to nonlinear terms. However, considerations exist in the criteria chosen to characterize wave breaking, the proper switching between the BT equations and to the NSW ones, range of applicability and grid sensitivity. In this approach we first estimate the location of breaking waves using explicit criteria and then the NSW equations are applied on the breaking regions and BT equations elsewhere. In this work we implement and test two Hybrid models, for Nwogu's equations.

Hybrid(ϵ) model

Tonelli and Petti in [163, 164] and for the MS BT model, developed a criterion which is based on the similarity between spilling breakers and moving hydraulic jumps, concluding this criterion to be the ratio of surface elevation to water depth, $\epsilon = \frac{\eta}{d}$. When a

wave moves towards a beach, water depth decreases more rapidly than the wave length due to shoaling, so μ^2 decreases and ϵ increases. The proposed numerical approach of [163] solves NSW in the region where non-linearity prevails and the BT equations elsewhere. The threshold value of the criterion used in order to establish which set of equations should be solved in each computational cell is set to 0.8. Also, in order to make the scheme more stable, once NSW equations have been applied, the value has to drop below 0.35-0.55 for BT equations to be applied again [165]. This approach has been proven successful in many applications, with its main advantage being its simplicity since no calibration parameters are needed, refer to [91, 130, 147] for example. However, the above criterion maybe proven inadequate, especially if waves propagate over a near-shore bar, when numerical wave breaking ceases before all the wave energy is dissipated. This is due to the static application of this breaking approach while a mechanism is needed that tracks propagating breaking fronts. In addition, all the applications of this criterion, thus far, have been restricted to 1D or 2D computations on structured meshes.

Wave breaking criteria and the New Hybrid model

An alternative hybrid model was presented in [24] for the Madsen and Sørensen [114] BT model, where it was assumed that wave breaking occurs when the vertical velocity component at the free surface exceeds a value proportional to the shallow water wave phase celerity, $\eta_t > \gamma$ where $0.35 \leq \gamma \leq 0.65$ such that is a calibration constant which maybe affected by the scale of the wave under consideration. A value of $\gamma = 0.3$ was used for breaking solitary waves on a sloping beach in [24]. In general, this criterion for breaking initiation is similar to one used by Kennedy et al. [93] and can be derived considering the nonlinear advection equation for the free surface [49]. However, like Kennedy et al's eddy viscosity approach, this criterion is inefficient for stably computing stationary (breaking or partially breaking) hydraulic jumps since in these cases $\eta_t \approx 0$.

In the light of the above mentioned works, we propose here the combination of two phase-resolving criteria for triggering wave breaking modeling within our FV scheme. Namely,

- the surface variation criterion: $\eta_t \geq \gamma \sqrt{gh}$ with $\gamma \in [0.35, 0.65]$ and
- the local slope angle criterion: $\eta_x \geq \tan(\phi_c)$ where ϕ_c is the critical front face angle

at the initiation of breaking.

The first criterion flags for breaking when η_t is positive, as breaking starts on the front face of the wave and has the advantage that can be easily calculated during the running of the model. The second criterion acts complementary to the first one and is based on the critical front slope approach in [55, 60]. Depending on the BT model used and the breaker type, e.g. spilling or plunging, the critical slope values are in the range of $\phi_c \in [14^\circ, 33^\circ]$. For certain BT models this has been considered as the least sensitive breaking threshold, with the correct breaking location predicted for $\phi_c \approx 30^\circ$, see for example [106, 160], and is the value adopted in this work. This value for ϕ_c is relatively large for this criterion to trigger by its own the breaking process, for different test cases, in our BT model, but is sufficient to detect breaking hydraulic jumps thus, correcting the limitation of the first criterion.

In the numerical scheme, and for each mesh node in the computational domain at every time step, we first check if at least one of the above criteria is satisfied, and flag the relative computational cell as a breaking or a non-breaking one. Since we refer to 1D formulation, it is relatively easy to distinguish between different breaking waves. Every consecutive group of breaking nodes constitute a breaking wave. With this information in hand, we can treat each wave individually and find certain wave characteristics such as the wave height. The wave front of each breaking wave will be then handled as a bore by the NSW equations and as long as they are governed by these equations the shock will keep dissipating energy.

However, we should take into account that bores stop breaking when their Froude number drops below a critical value. The wave's Froude number (Fr) determines the bore's shape and the transition from one kind of bore to another. If $Fr \gg 1$, a bore is purely breaking and will consist of a steep front and if the Froude number drops below a certain value Fr_c non-breaking undular bores have been observed, see [160] and references therein. Thus, an additional criterion is needed to determine when to switch back to the BT equations for non-breaking bores, allowing for the breaking process to stop. The criterion introduced by [160] is adopted here and is based on the analogy between a broken wave and a bore in the sense of a simple transition between two uniform levels. The wave's Froude number is defined as:

$$Fr = \sqrt{\frac{(2H_2/H_1 + 1)^2 - 1}{8}} \quad (3.68)$$

where H_1 is the water depth at the wave's trough and H_2 the water depth at the wave's crest. Since we have tracked each breaking wave individually (with its own dynamic list), it is relatively straightforward to find H_1 and H_2 for each wave. We simply approximate them by finding the minimum and maximum water depth respectively, from all the breaking nodes corresponding to that wave. If $Fr \leq Fr_c$ all the breaking points of that wave are un-flagged and the wave is considered non-breaking. Following [160] the critical value for Fr_c was set equal to 1.3 in our computations.

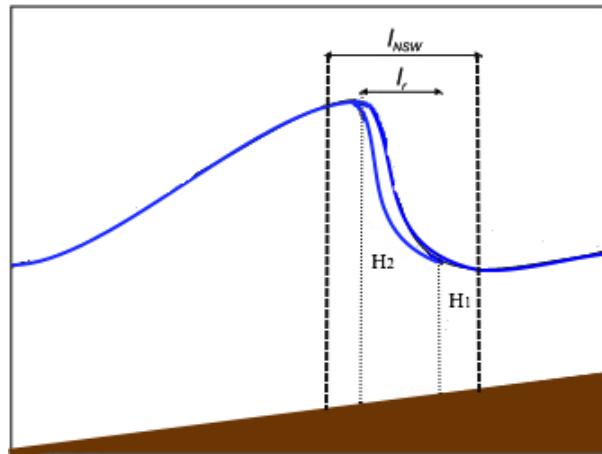


Figure 3.3: Definition sketch for a broken wave and the switching zones from BT to NSW

For each breaking wave, the computational region l_{NSW} (see Fig. 3.3) along the wave direction, over which we switch to NSW, is roughly centered around the wave front. However, non-physical effects may appear at the interface between a region governed by the BT equations and a region that is governed by the NSW model. This is due to the relatively strong variations that may exist in the solution, which affect the estimation of the dispersive terms [147, 160, 130]. In [160] the shallow water region was extended assuming that the l_{NSW} length must be larger than the order of magnitude of the physical length of the wave roller. The length of the roller can be defined as $l_r \approx 2.9(H_2 - H_1)$ and the extend $l_{NSW} \approx 2.5l_r$, which is the value adopted in the present work.

Suppression of the dispersive terms methodology

After the characterization of the breaking regions the NSW model has to be applied computationally in each one of them. This is a very blurred process, since up to now

and to our knowledge, no author, in the existing literature, has been very clear to the definition of that process. In order to solve the NSWE in the computational cells that have been identified as breaking we have to suppress the dispersive terms ψ_c and ψ_M in equation (3.2). We have also to keep in mind that the tridiagonal matrix \mathbf{M} in equation (3.55) have been extracted using P^* from (3.3) which contains the term ψ_M . This means that we must be very careful when switching to the NSWE to keep the balance of the dispersive terms for every computational cell in eq. (3.1). Several researchers, that have followed the hybrid wave breaking modeling in 1D, for example [163, 142], mention that the tridiagonal matrices are constant in time and can be pre-factored, inverted and stored to be used only once at each time iteration. The above approach implies that when a wave breaking mechanism is active, the solution of the tridiagonal system, in each time step, involves the undisturbed matrix \mathbf{M} along with the right hand side that comes from the spatial solver but without considering the dispersive terms in the computational cells characterized as breaking. This leads to numerical instabilities on the wave breaking fronts since equation (2.43) is not satisfied, for the breaking computational cells.

Another way to suppress the dispersive terms is to recalculate the tridiagonal matrix \mathbf{M} at each time iteration. Each line of the matrix that corresponds to a breaking cell is discretized without considering the term $H z_\alpha \left(\frac{z_\alpha}{2} u_{xx} + (hu)_{xx} \right)$ in (3.3), leading to the corresponding line of the Identity matrix. Like before, the right hand side that comes from the spatial solver is calculated without considering the dispersive terms at cells considered as breaking. This treatment is inadequate in regions where dispersion terms are not negligible when compared to the nonlinear terms, since nonphysical oscillations present at the switching points between the BT equations and the NSW ones. An additional concern, following this approach, is the limitation of the recalculation of the matrix in each time step. Matrix \mathbf{M} is symmetric and positive definite (when bottom topography is neglected). Changing its rows may lead to large condition number causing instabilities in the solution of the linear system.

Furthermore in 2D computations where unstructured meshes are used, the matrix of the linear system can not be changed due to its storage (see Section 6.4). Thus any change in that matrix would result in a large increase in the computational cost. For the above reasons concerning both 1D and 2D formulations, we developed a new methodology to handle the switching between the two models (dispersive/non-dispersive) as:

0. Starting with the solution vector $\mathbf{U}_p^n, P^* = 1, \dots, N$, at time t^n ,
1. For all computational cells an $[H_1^{n+1}, H_2^{n+1}, \dots, H_N^{n+1}]^T$ solution is computed from the mass equation using the BT model (named from now on \mathbf{H}_{BT}^{n+1} solution).
 - 1.1 If breaking has been activated (according to our criteria) for a number of computational cells say $N_{br} < N$, an additional solution vector is computed by subtracting the dispersive terms ψ_c from \mathbf{H}_{BT}^{n+1} at these breaking cells, i.e. obtaining a NSW solution for \mathbf{H}^{n+1} at these cells only. This solution is named $\mathbf{H}_{BT/SW}^{n+1}$ from now on.
2. Then, for all computational cells the $\mathbf{P}_{BT}^{*(n+1)} = [P_1^{*(n+1)}, P_2^{*(n+1)}, \dots, P_N^{*(n+1)}]_{BT}^T$ solution from the momentum equation is computed, using the approximation $\partial_t \mathbf{H}^{n+1} \approx \frac{\mathbf{H}_{BT}^{n+1} - \mathbf{H}^n}{\Delta t^{n+1}}$ for the ψ_M computation in (3.4).
 - 2.1 If breaking has been activated for a number of computational cells, an additional solution (named $\mathbf{P}_{BT/SW}^{*(n+1)}$) is computed by subtracting the dispersive terms ψ_c and ψ_M from $\mathbf{P}_{BT}^{*(n+1)}$ at these cells i.e. obtaining a NSW momentum solution $(Hu)^{n+1}$ for the breaking cells, since for the NSW equations $\mathbf{P}^* = Hu$. For these cells only it is easy now to compute $\mathbf{u}_{SW}^{n+1} = [u_1^{n+1}, \dots, u_{N_{br}}^{n+1}]_{SW}^T$ which will be a subset of the actual velocity solution sought.
3. Then, the linear system $\mathbf{M}\mathbf{V} = \mathbf{C}$ from (3.55) is solved with $\mathbf{C} = [\mathbf{P}_1^{*,n+1}, \mathbf{P}_2^{*,n+1}, \dots, \mathbf{P}_N^{*,n+1}]_{BT}^T$ to obtain an approximation of the velocity vector, named $\mathbf{u}_{BT}^{n+1} = [u_1^{n+1}, \dots, u_N^{n+1}]_{BT}^T$.
4. The final solution at $t = t^{n+1}$ will be that of $\mathbf{H}_{BT/SW}^{n+1}$ for the total water depth and $\mathbf{P}_{BT/SW}^{n+1}$ for the momentum equations. For the velocity field vector the solution, denoted as $\mathbf{u}_{BT/SW}^{n+1}$, is derived from the \mathbf{u}_{BT}^{n+1} vector with its values at the breaking nodes replaced by those of \mathbf{u}_{SW}^{n+1} .

Chapter 4

Numerical test and results in one dimension

The numerical schemes for both BT models presented in Chapter 3 have been applied to standard tests cases designed to validate the numerical treatment of the dispersion terms in the governing equations and the wave breaking treatments. Special attention was paid to comparing both BT models to the NSWE for reproducing challenging experimental results. We have classified the numerical tests in two main categories. The non-breaking wave cases in Sections 4.1-4.2 and the breaking wave cases, in Section 4.5-4.8. Numerical tests in Sections 4.2 and 4.3 includes both categories.

4.1 The Carrier and Greenspan (1958) solutions

We first check the validity of the proposed well-balanced discretization and wet/dry front treatment by focusing on moving shoreline problems for waves running up and down uniform sloping beaches. These problems have analytical solutions which were derived by Carrier and Greenspan [37] by making use of the NSWE. These classical tests have been used frequently for assessing the quality of various shoreline boundary condition techniques used in the NSWE, see for example [86, 32, 30, 118]. Thus, for consistency the dispersive (μ^2) terms are usually ignored in the numerical simulations of these problems, see for example [108, 47, 164], or considered to be very small [68]. In the current presentation, and only for these test cases, we chose to ignore the dispersive terms. Details on initial and boundary conditions, as well as the analytical solutions, can be found in the original work of Carrier and Greenspan [37] and in [32, 118].

Non-dimensional variables are defined to compare with the analytical solutions as follows

$$x^* = x/l, \quad \eta^* = \eta/(\alpha l), \quad u^* = u/\sqrt{g\alpha l}, \quad t^* = t/\sqrt{l/(\alpha g)}$$

where l is the characteristic length scale and α the beach slope.

4.1.1 Carrier and Greenspan periodic wave solution

For the first case a monochromatic wave is let runup and rundown on a plane beach with $\alpha = 1/30$. The solution represents the motion of a periodic wave of a dimensionless amplitude $A^* = 0.6$ and frequency $\omega^* = 1$ traveling shoreward and being reflected out to sea generating a standing wave on the beach with $A^*/4$ maximum vertical excursion of the shoreline. The characteristic length scale $l = 20m$. The computational parameters used where $\Delta x = 0.00625m$, $C_r = 0.45$ and $\varepsilon_{wd} = 5 \cdot 10^{-6}m$. The small value of Δx has been chosen as to provide a high resolution at the shoreline, see for example [164]. Fig. 4.1 presents comparisons between the numerical free surface and the analytical one, at different times $t^* \in [2T^*, 2T^* + T^*/2]$ where T^* is the dimensionless period of the oscillations. The qualitative agreement is very good even after a few periods.

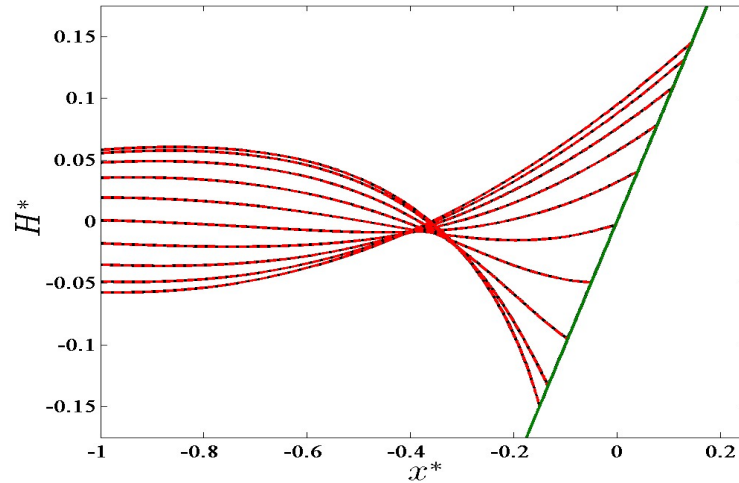


Figure 4.1: The Carrier and Greenspan periodic wave solution: comparison between analytical (solid line) and numerical (red dashed line) results for the free surface elevation at different times $t^* \in [2T^*, 2T^* + T^*/2]$.

The numerical shoreline position x_s was measured as the position of the last wet cell (i.e. where $H \geq \varepsilon_{wd}$) along the beach. Theoretically, the shoreline boundary is defined

by the relations

$$H(x_s, t) = 0 \quad \text{and} \quad u_s \equiv u(x_s, t) = \frac{dx_s}{dt}.$$

Inevitably, the numerical solution produced by the conservative FV scheme is an approximation to the above relations since the zero depth condition is never met [27]. Fig. 4.2 compares the computed and analytical time series of the shoreline position and velocity. Very good accuracy is shown for the vertical sinusoidal motion of the shoreline while for the non-sinusoidal variation of the shoreline velocity small discrepancies are presented when the velocity is close to zero. The velocity results compare well with others in the literature, see for example [68, 164]. It should be pointed here that, the shoreline velocity computation is a difficult task and as such is not correctly captured by some runup models thus, in the literature only variations of the shoreline position are usually presented.

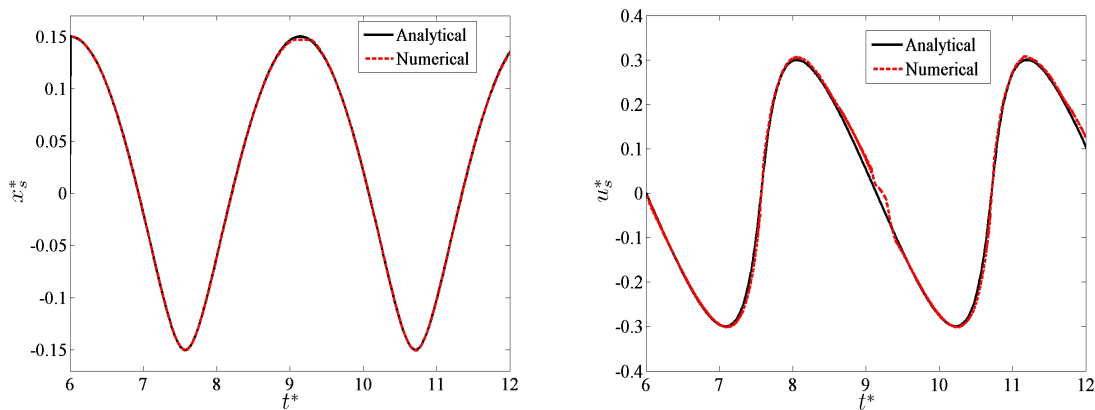


Figure 4.2: The Carrier and Greenspan periodic wave solution: comparison between analytical and numerical results for the shoreline position (left) and shoreline velocity (right) for $t^* \in [T^*, 2T^*]$

4.1.2 The Carrier and Greenspan transient solution

In this case the initial water surface elevation is assumed to be depressed near the shoreline, the fluid is held motionless and then released at $t^* = 0$. For this case $\alpha = 1/50$ and $l = 20m$. In [37] a small parameter e was used to characterize the surface elevation profile. For $e < 0.23$ non-breaking waves are produced and the results presented here are for $e = 0.1$. In the wave's evolution, the shoreline rises above the still water level of value e and then the water surface elevation asymptotically settles back to it. As such,

this test is particularly valuable in testing the ability of the model to compute (nearly) steady states. The computational parameters are the same as in the previous case.

Fig. 4.3 presents the comparisons between the numerical free surface and the analytical one, scaled with parameter e , at different times t^* . The numerical model provides qualitative excellent agreement with the analytic solution. The solution asymptotically reaches an almost steady state which is accurately predicted by the model verifying the extended C -property.

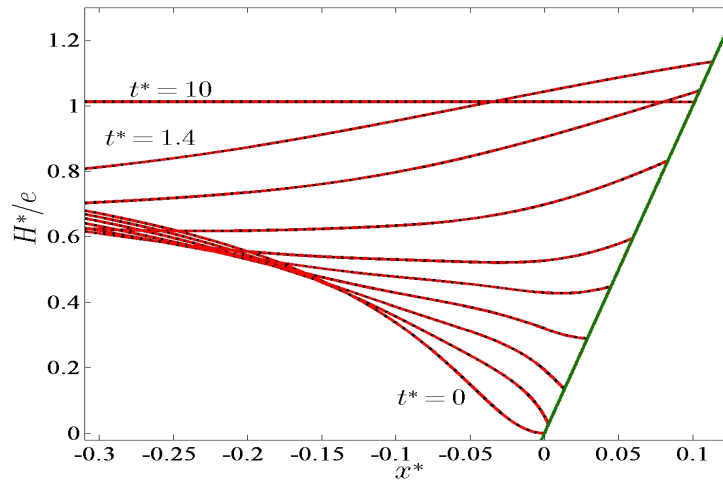


Figure 4.3: The Carrier and Greenspan transient solution: comparison between analytical (solid line) and numerical (red dashed line) results for the free surface elevation at different times t^* .

In Fig. 4.4 the computed and analytical time series of the shoreline position and velocity are presented. It can be observed that the shoreline position asymptotically settles to e and the numerical model remains stable and with good accuracy for this slow convergence. On the other hand, the error on the shoreline velocity slightly increases when the velocity reaches very small values at rundown and exhibits a slightly oscillatory behavior. However, this error remains controlled and diminishing since the numerical solution fully recovers in a short time. This is an expected behavior since the method uses the threshold parameter ε_{wd} to define the last wet cell. Hence, the introduced error is mainly artificial since the velocity is calculated from the conserved variables as $u_s^{n+1} = (Hu)_s^{n+1} / H_s^{n+1}$, with $(Hu)_s^{n+1}$ being a few orders of magnitude less than H_s^{n+1} and practically almost zero. Nevertheless, small spurious errors in the velocity or depth at wet/dry fronts which are below a certain level, e.g. 10^{-4} , are not a concern in practical simulations as long as the solution remains stable for long time. Here, the

numerical solution reaches stably the expected steady state.

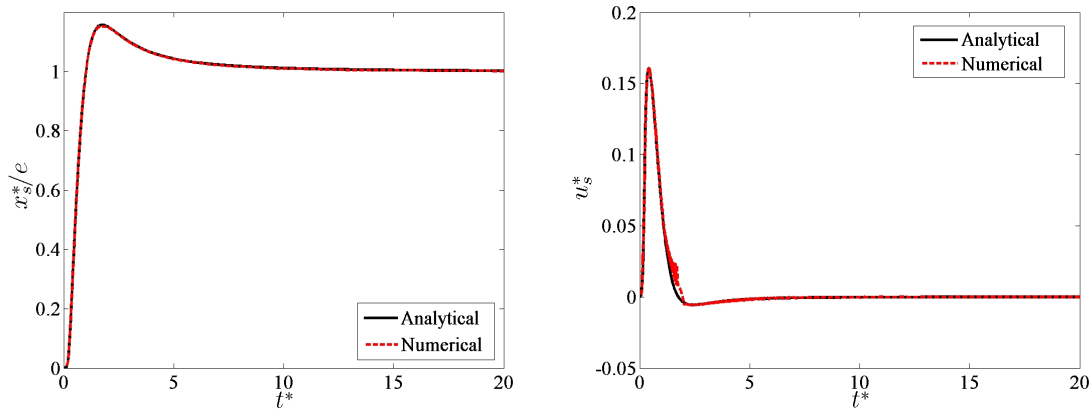


Figure 4.4: The Carrier and Greenspan transient solution: comparison between analytical and numerical results for the shoreline position (left) and shoreline velocity (right) for $t^* \in [0, 20]$

4.2 Solitary wave propagation

One of the most standard tests of the stability and conservative properties of numerical schemes based on BT equations is the propagation of solitary waves over a flat ($b(x) = 0$), long distance frictionless and with constant depth channel. The solitary wave maintains its shape, speed and amplitude as it travels down this channel due to an exact balance between the nonlinear terms that steepen the wave and the dispersion terms that flatten the wave. A numerical model must handle this balance. A combination of numerical errors from poorly balanced schemes and truncation of numerical approximations can lead to serious reductions in the wave height and celerity.

The model is applied to simulate the propagation of solitary waves over a constant depth. The initial wave surface elevation η and velocity of u can be found in [179] for Nwogu's equations and in [163] for MS equations (see Appendix). Three solitary waves of $A = 0.045, 0.9, 0.135m$ propagate in a numerical wave channel of $500m$ ($x \in [-50, 450m]$) and of constant depth $h = 0.45m$. Each wave corresponds to a different parameter $\epsilon = 0.1, 0.2, 0.3$ respectively. The initial position of the solitary wave is at $x = 0m$. We note here that, the given initial conditions (and analytical solutions) are only asymptotically equivalent to the solutions of the models being solved numerically, so the wave being input in the numerical models does not correspond exactly to solitary waveforms predicted by the models. As a result, the initial waves undergo an evolution

at the beginning of the computation to adjust the free surface to a steady profile [163, 179]. Following [179] we reduce all differencing errors to a size that is small relative to all retained terms in the model equations. The scheme used, leads to a truncation error of $O\left(\frac{\Delta x^4}{\mu^2}\right)$ relative to the model dispersive terms at $O(\mu^2)$. In contrast, the leading term, of the dispersive terms themselves are finite-differenced to second order accuracy, leading to errors of $O(\Delta x^2)$ relative to the actual dispersive terms. For that reason we have choose $\Delta x = 0.025$. The CFL number used was 0.3.

Fig. 4.5 shows the surface profiles for the three solitary waves at various times for both formulations. The results indicate that, for both BT models the initial wave undergoes an evolution at the start of the wave channel, with the result that a modified solitary is formed together with a small dispersive tail. The amplitude of the tail and the initial deviation of the wave's height both increase with increasing initial wave height. As depicted in Fig. 4.6, in Nwogu's formulation the solitary wave increases slightly, at the beginning of the propagation and results to a higher wave than the initial one. This results partially from the fact that the analytical solution used as initial condition is only asymptotically equivalent to the model, so that the wave does not correspond exactly to a solitary waveform as predicted by the model [179]. For the MS formulation, and at the first stages of the propagation, the wave changes shape and becomes higher but eventually results to shorter wave heights than the initial ones. The train of small waves, formed are severe but are soon left behind. This transformation is imputed to the low-order approximation of the velocity, given to the model as initial condition. In Fig. 4.7 the solitary wave forms are compared to the analytical solution at two widely separated instances in time. The two waves are translated by a distance predicted through an analytical phase speed C . It can be seen that the numerical predicted phase speed is somewhat smaller than the analytically predicted one and that the difference increases with increasing nonlinearity.

In order to check the conservation of mass we examine the relative mass error, which is defined as:

$$\text{Relative mass error} = \frac{m^n - m^l}{m^l}$$

where m^l is the total mass in the computational domain at time step 0 (t^0) and m^n is the total mass at time step t^n . Fig. 4.8 shows the relative mass error for the two sets of equations examined here and for the solitary wave with $\epsilon = 0.1$. The relative mass error occurred is of order $O(10^{-14})$.

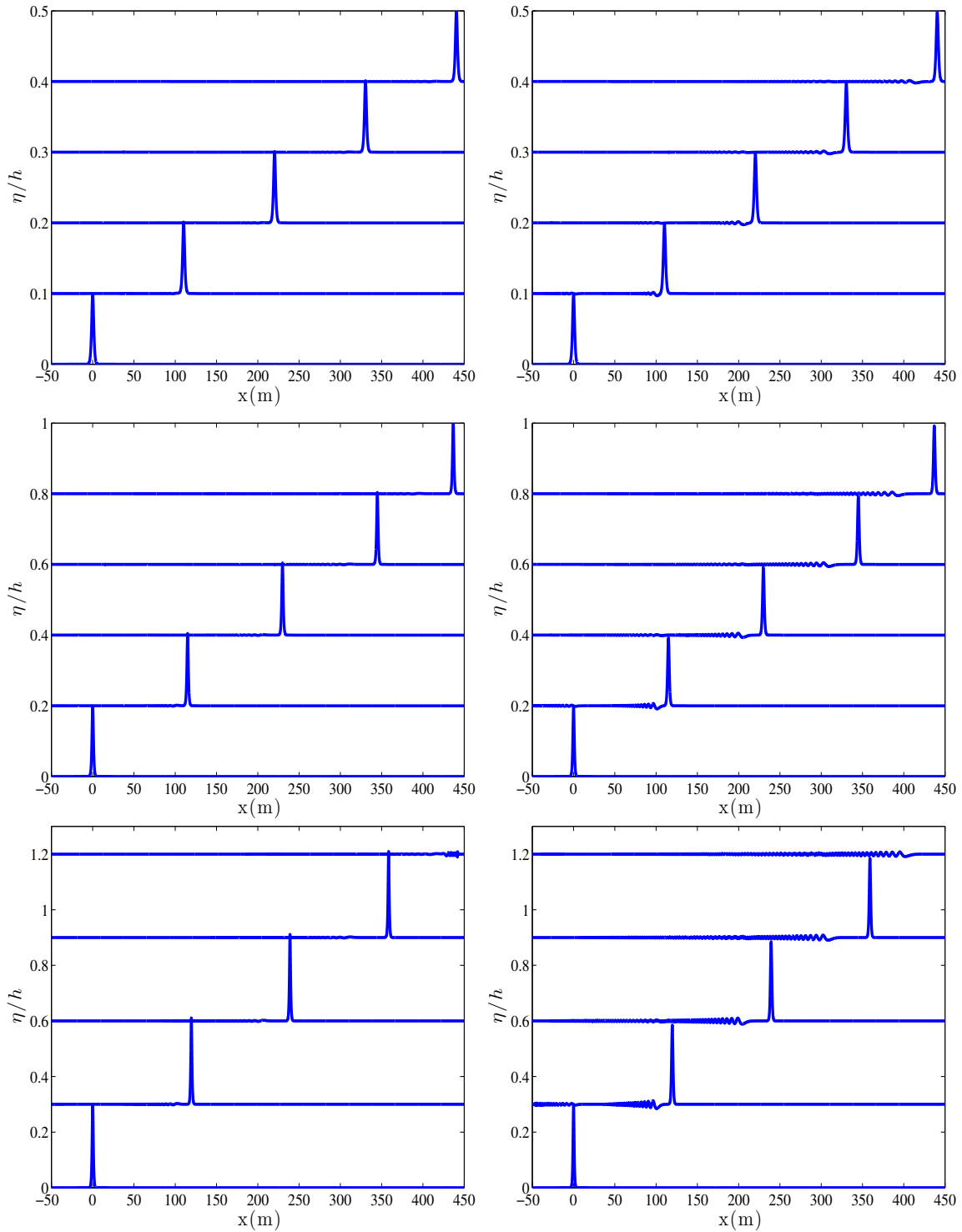


Figure 4.5: Solitary wave propagation ($A/h = 0.1, 0.2, 0.3$ from top to bottom) at times $t = 0, 50, 100, 150, 200$ s for Nwogu's (left) and MS (right) formulations

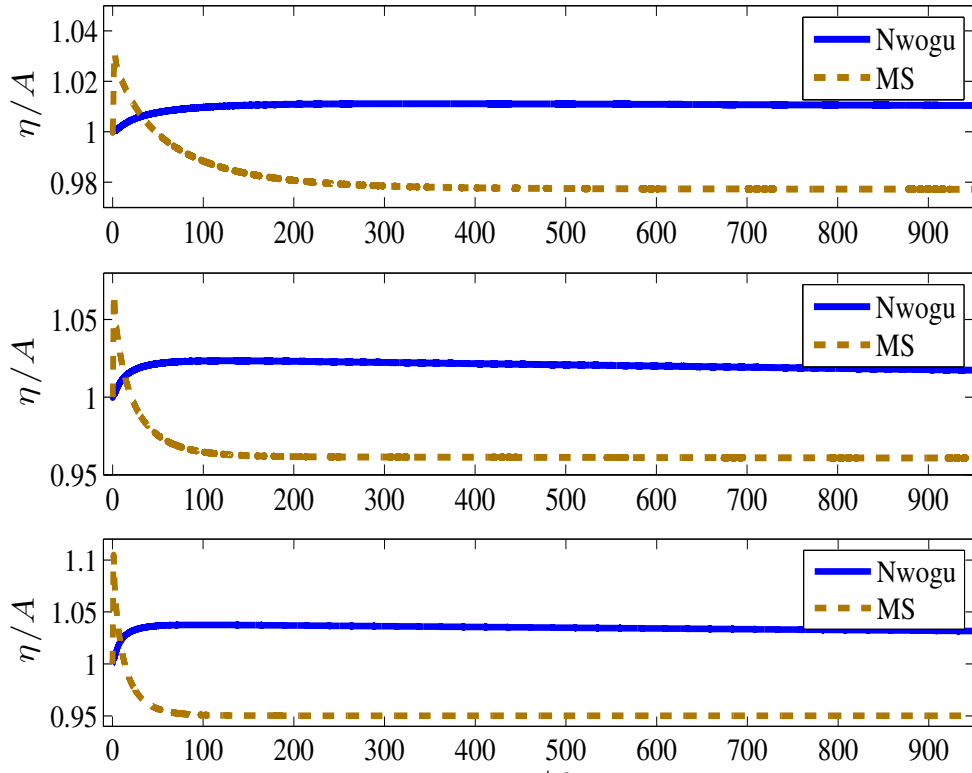


Figure 4.6: Amplitude variations of solitary waves for $\epsilon = 0.1, 0.2, 0.3$ from top to bottom

4.3 Head on collision of two solitary waves

The counter-propagation of two symmetric solitary waves in a flat frictionless channel is tested here. Their collision presents additional challenges to the models by the sudden change of nonlinear and dispersion characteristics. This head-on collision is characterized by the change of shape, along with a small phase-shift of the waves as a consequence of the nonlinearity and dispersion. In a $300m$ long channel with $h = 1m$ two solitary waves with an equal initial height of $A/h = 0.3$ are placed in positions $x = 35m$ and $x = 265m$ and start to propagate in the opposite directions. This higher values of A/h corresponds to stronger nonlinearity in the incident waves, when compared to the previous test case, since both models which are based on equations derived under the assumption that terms of $O(\epsilon^2, \epsilon\mu^2, \mu^4)$ can be neglected. The initial wave surface elevation and velocity can be found in [179] and [163], similar to the previous test case. The computational parameters used were $\Delta x = 0.1m$ and $C_r = 0.4$.

Fig. 4.9 shows the surface profiles at times $t\sqrt{g/d} = 0, 101.2$ and 200 . Similar to the previous test case and due to the incompatibility between the analytical and

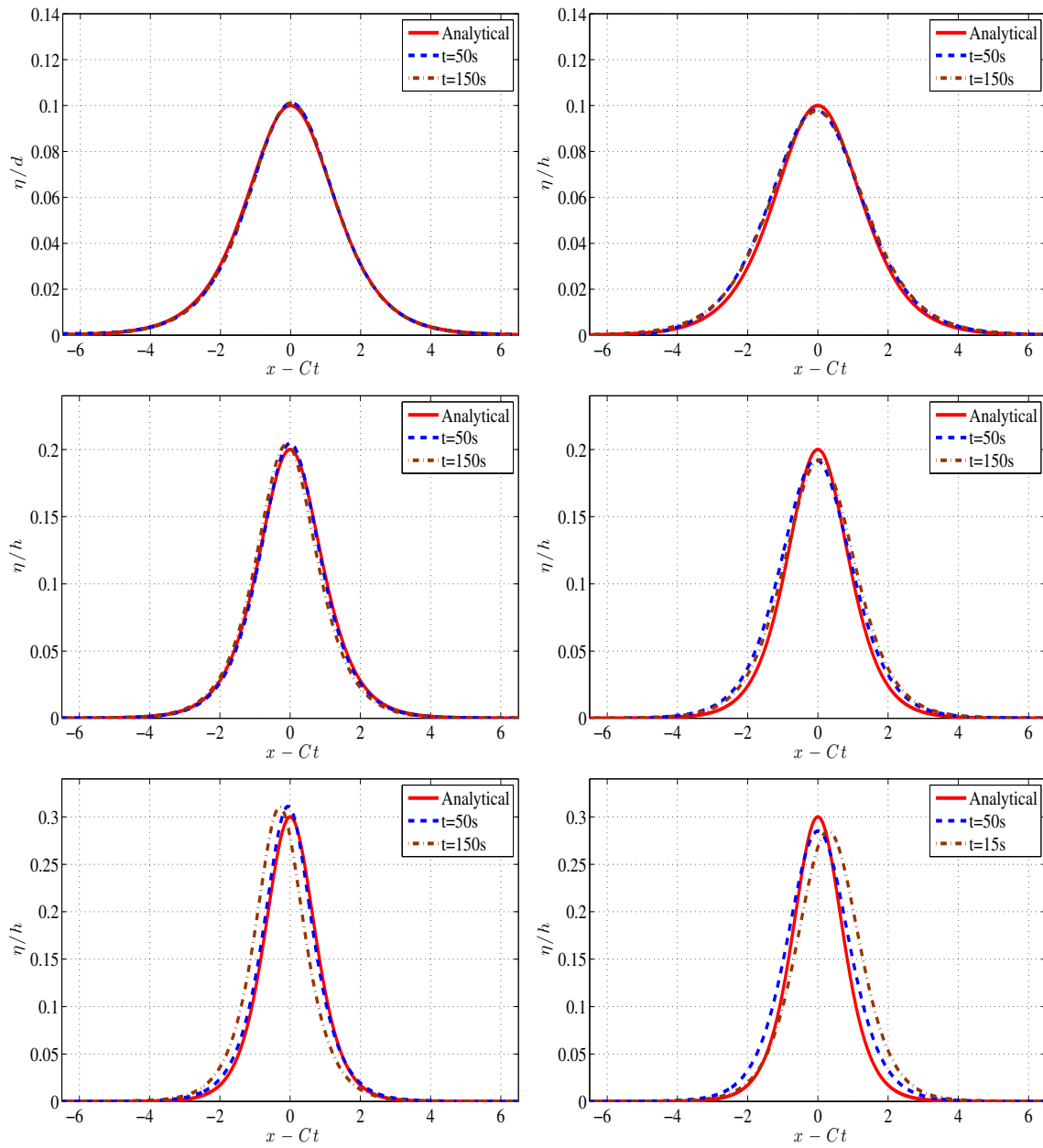


Figure 4.7: The solitary wave's ($A/d = 0.1, 0.2, 0.3$ from top to bottom) shape at $t = 50s$ and $t = 150s$ for Nwogu's (left) and MS (right) formulations

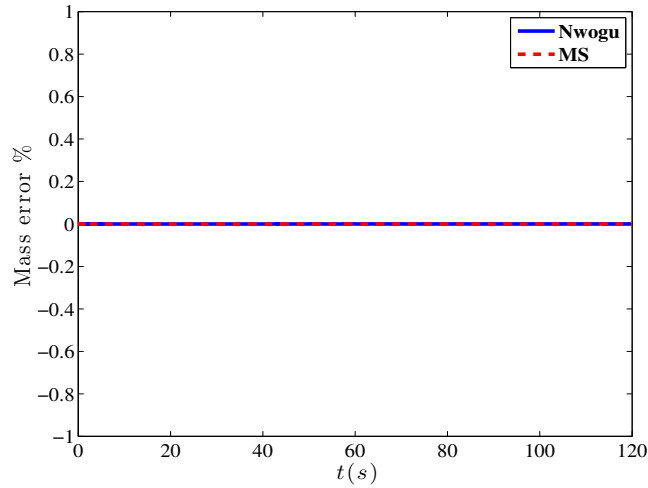


Figure 4.8: Conservation of mass

numerical solutions, the numerical waves initially undergo an evolution and two slightly higher solitary waves are formed which then propagate with a constant amplitude ($A/h = 0.3135$ for Nwogu's equations and $A/h = 0.295$ for the MS ones) until collision, along with small dispersive tails which are left behind. At $t\sqrt{g/h} = 101.2$ the wave gets its highest pick, $A/h = 0.66$ for Nwogu's formulation and $A/h = 0.61$ for the MS formulation. At $t\sqrt{g/h} = 200$ the numerical wave profiles are very close to the initial solitary waveform. After the collision we observe that the numerical solution has a small phase shift compared to the analytic one. The dispersive tails are more intense for the MS model due to the discrepancy between the analytical solution given as input to the model and the solitary wave solution of the numerical model. We remark here that, nonlinear effects for both Nwogu's and the MS model can be reasonably accounted for up to $A/h \approx 0.3$.

4.4 Solitary wave run-up on a plane beach

Solitary wave run-up on a plane beach is one of the most intensively studied problems in long-wave modeling. Synolakis [157] carried out laboratory experiments for incident solitary waves of multiple relative amplitudes, in order to study propagation, breaking and run-up over a planar beach with a slope 1 : 19.85. Many researchers have used this data set to validate numerical models [189, 108, 23, 164, 91, 142, 47, 187, 161]. With this test case we assess the ability of our model to describe shoreline motions and wave

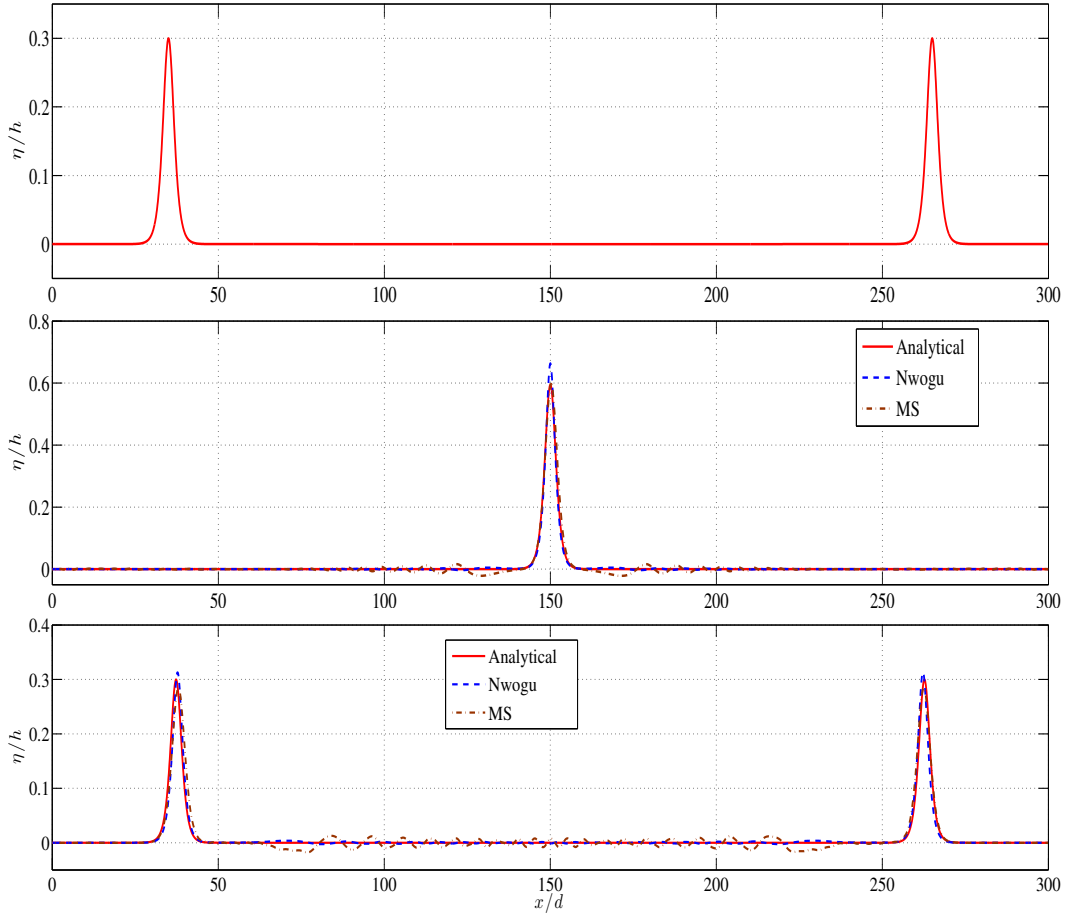


Figure 4.9: Surface profiles of solitary waves at times $t\sqrt{g/d} = 0, 101.2, 200$ (from top to bottom) with $A/d = 0.3$ propagating in opposite directions in a channel of constant depth.

breaking, when it occurs. Experimental data are available from [157] for the surface elevation at different times. Two different cases were considered here. For the first case the incident wave height is $A/h = 0.04$ and for the second one $A/h = 0.28$. According to Synolakis [157] wave breaking occurred during run-down when $A/h > 0.044$ and hence breaking did not occur for the first case (although it very nearly broke on the run-down). The $A/h = 0.28$ wave broke strongly both in the run-up and the run-down phases of the motion. The topography of the problem has the form

$$b(x) = \begin{cases} -x \tan \beta, & x \leq \cot \beta \\ -1, & x > \cot \beta \end{cases} \quad (4.1)$$

and Fig. 4.10 shows a schematic view of the experiments with A indicating the incident wave height, β the beach angle and h the depth of the stagnant water. An initial solitary

wave is placed at point x_1 that is located at half wavelength from the toe of the beach, located at x_0 . The initial surface profile η and velocity \mathbf{u} can be found in [179] for the equations of Nwogu and [157] for the MS equations (see Appendix). Also, a Manning coefficient of $n_m = 0.01$ was used in order to define the glass surface roughness used in the experiments. For both cases the computational domain is $x \in [-2, 100m]$ and the

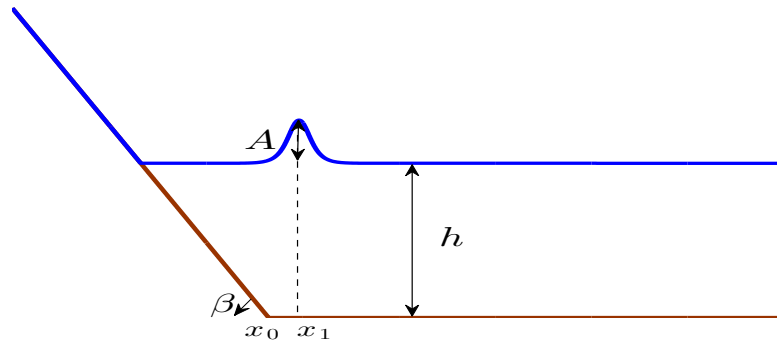


Figure 4.10: Set up for the numerical test of the solitary wave run-up on a plane beach.

numerical parameters used were $\Delta x = 0.05$, $CFL=0.4$, $\epsilon_{wd} = 5 \cdot 10^{-6}$. The still water level is $h = 1m$.

Remark 4 *Solitary waves that propagate in a long friction less channel will reach a permanent form. At that point the dispersive tail lags behind the initial wave. The obtained initial wave is the permanent form solitary wave solution of the desired height which is the correct initial solutions to be used within the BT models.*

4.4.1 Case I

Fig. 4.11 shows a comparison of the surface profiles from the BT models and the NLSWE, along with experimental data, when $A/h = 0.04$ for different non dimensional times. Until time $t\sqrt{g/h} = 32$ the wave approaches the shoreline and we observe that the NSWE slightly over-predict the solution while the numerical results of Nwogu's and MS give identical results for this non-breaking case. Observe that, due to the well-balanced wet/dry treatment applied in the shoreline no unphysical overtopping or water movement appears in the solution at the wet/dry front. By time $t\sqrt{g/h} = 32$ the wave begins to run up the beach and after that the solutions of the three models are almost identical converging to the same solution. The experimental observation that

the wave nearly broke during rundown can be seen at $t\sqrt{g/h} = 62$ where all numerical solutions look similar to that of a hydraulic jump. The measured maximum run up in [157] for this problem was $\mathcal{R} \approx 0.156$ while for all computational models here was almost identical with a value $\mathcal{R} \approx 0.161$.

4.4.2 Case II

The next case involves the run-up and run-down of a solitary wave with $A/h = 0.28$ on the same beach. This is a demanding test case since breaking occurs both in the run-up and the run-down process. We have resided to implement the breaking mechanisms only in BT equations of Nwogu for two reasons.

- Better performance of the BT equations of Nwogu versus the MS equations up have been observed to the non-breaking cases, involving solitary waves, since there is no analytic solution to be used as initial condition, in contrast to the asymptotic solution of [179] for the equations of Nwogu.
- Both the Hybrid(ϵ) and eddy viscosity model have been tested for the equations of MS, see for example [163, 164, 138]
- Kazolea and Delis [91] have also tested the 1D FV/FD model for both the equations of MS and Nwogu including the wave breaking mechanism of [163]. The two BT numerical models provided considerable more accurate results for highly dispaersive waves over increasing water depths, with Nwogu's model having a precedence over the MS one.

The computational parameters used are the same as in case (a). The four different wave breaking mechanisms presented in Section 3.7 are implemented and tested. For the eddy viscosity model of Kennedy the values that determines the onset and the cessation of breaking are $\eta_t^{(I)} = 0.45$ and $\eta_t^{(F)} = 0.15$. The transition time used here is $T^* = 5\sqrt{h/g}$. Numerical results using the eddy viscosity model of Roeber, using $B_1 = 0.5$ and $B_2 = 0.25$ are simultaneously presented. Additionally, the two Hybrid models are presented in the same Figures, using for the surface variation breaking criterion $\eta_t \geq \gamma\sqrt{gh}$ and γ was set to 0.6.

Fig 4.12 and Fig 4.13 show at the left column the two hybrid models compered with experimental data and the same for the two eddy viscosity formulations at the right

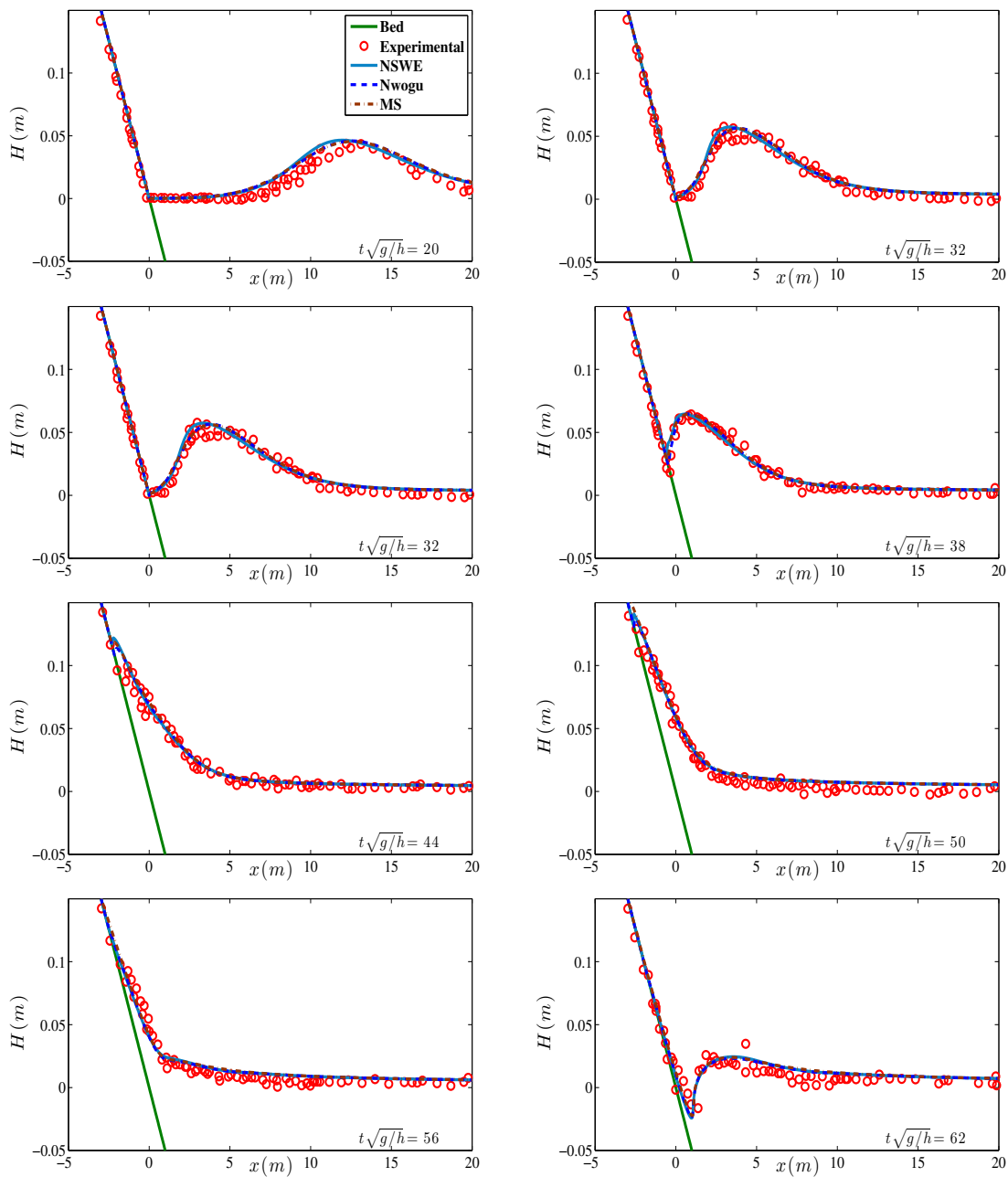


Figure 4.11: Free surface elevation of solitary wave run-up on a plane beach for $A/h = 0.04$.

column. Until time $t\sqrt{g/h} = 10$ the solitary propagates to the shore and the computed results are all the same, as expected, since wave breaking has not initiate yet. The breaking procedure starts around $t\sqrt{g/h} = 15$ where small differences between the models are observed. The two eddy viscosity models have the same behavior up to this time. The solitary wave using the Hybrid(ϵ) is slightly faster and sharper in the bore front compered to the one obtained by the New Hybrid model. As the wave shoals, it is clear that at the initial stages the NSW equations under-predict the wave height and phase. The wave breaking is represented as a bore storing the water spilled from the breaking wave behind the bore.

Wave breaking has fully developed by the time $t\sqrt{g/h} = 20$ where all the models under-predict the wave height. The eddy viscosity model of Roeber suffers from oscillations at the back of the wave and it is also more diffusive at the front of the solitary. Similar observations have been made in [164]. Other researchers in [142, 189, 108] used the same eddy viscosity model up to now have used sparser grids introducing numerical diffusion which act a stabilized mechanism. The Hybrid(ϵ) model is slightly faster that the New Hybrid one and also gives the worst prediction for the wave height. The BT model, when used the Hybrid formulations, reduce to the NSWE during the breaking event so the computed front becomes steeper. This is not the case in the actual wave which is not discontinuous but contains air bubbles and turbulence. Because of the volume conservation in all models, the computed solution fully recovers until the water reaches the maximun run-up point around $t\sqrt{g/h} = 45$.

As the water recedes a breaking wave is created at $t\sqrt{g/h} = 55$ near the still water level. All formulations simulates the process as a hydraulic jump. According to Kennedy et al. [93] the largest disadvantage of the eddy viscosity model is that, in some cases, such as stationary hydraulic jumps, breaking initiation is not recognized. For that reason oscillations at the numerical solution of both the eddy viscosity models where observed after $t\sqrt{g/h} = 55$ and the solution became unstable since no artificial numerical filtering is imposed in any eddy viscosity model. Thus, no results for these models are include in Fig. 4.14 for times $t\sqrt{g/h} = 60$, $t\sqrt{g/h} = 70$ and $t\sqrt{g/h} = 80$. Zelt [189] has also mentioned that it might also be necessary to treat that backwash bore by a completely different breaking algorithm in place of the artificial viscosity model. On the other hand the hybrid breaking models have better agreement with the experimental data.

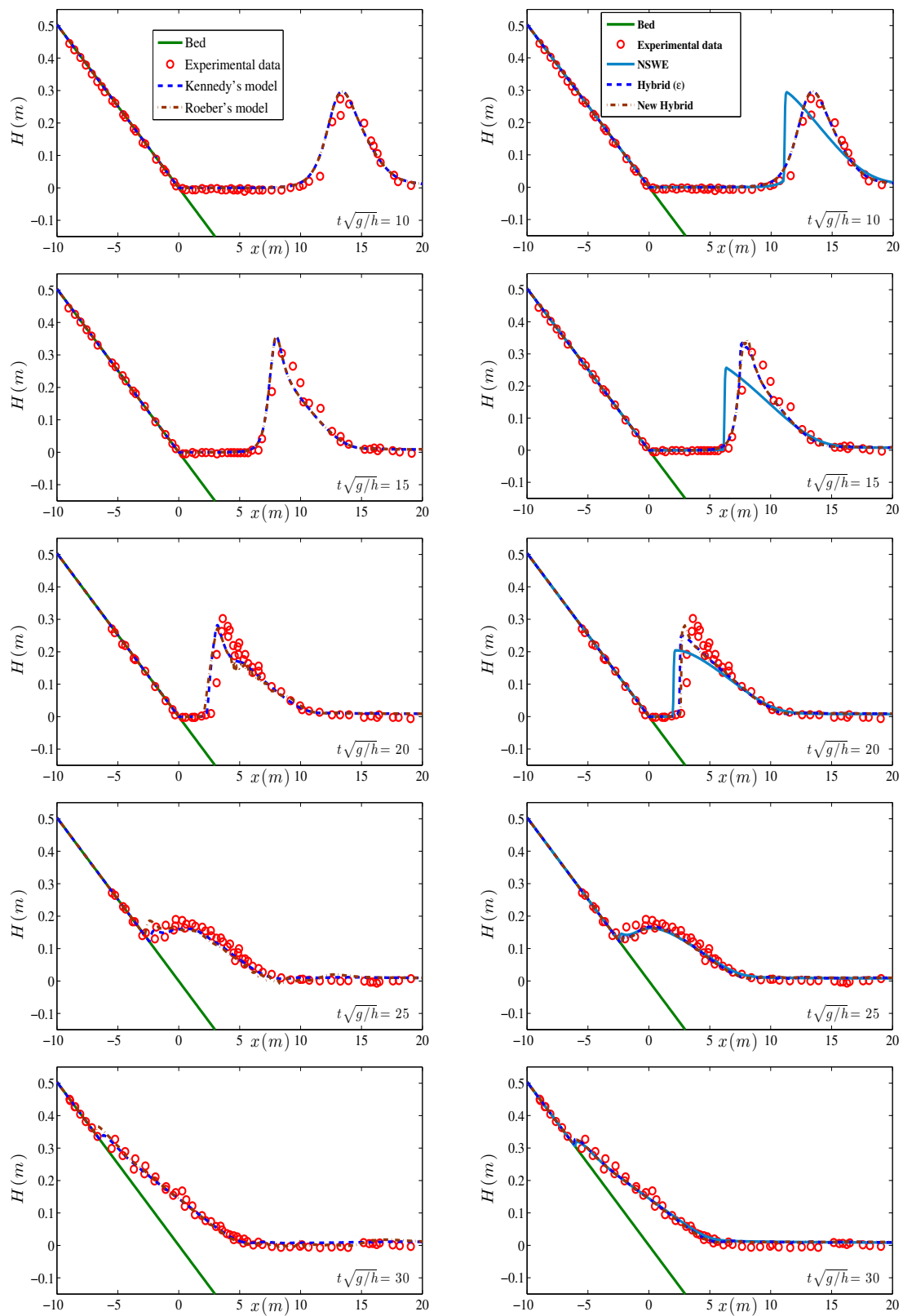


Figure 4.12: Free surface elevation of solitary wave run-up on a plane beach for $A/h = 0.28$. Comparison of eddy viscosity models (left) and Hybrid models (right)

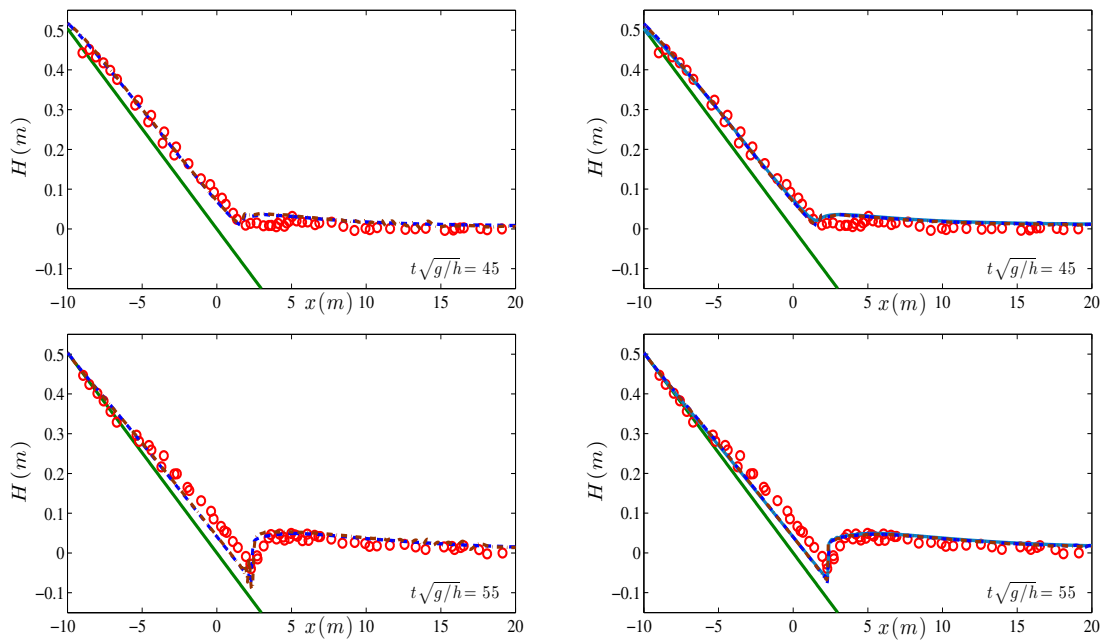


Figure 4.13: Free surface elevation of solitary wave run-up on a plane beach for $A/h = 0.28$. Comparison of eddy viscosity models (left) and Hybrid models (right)

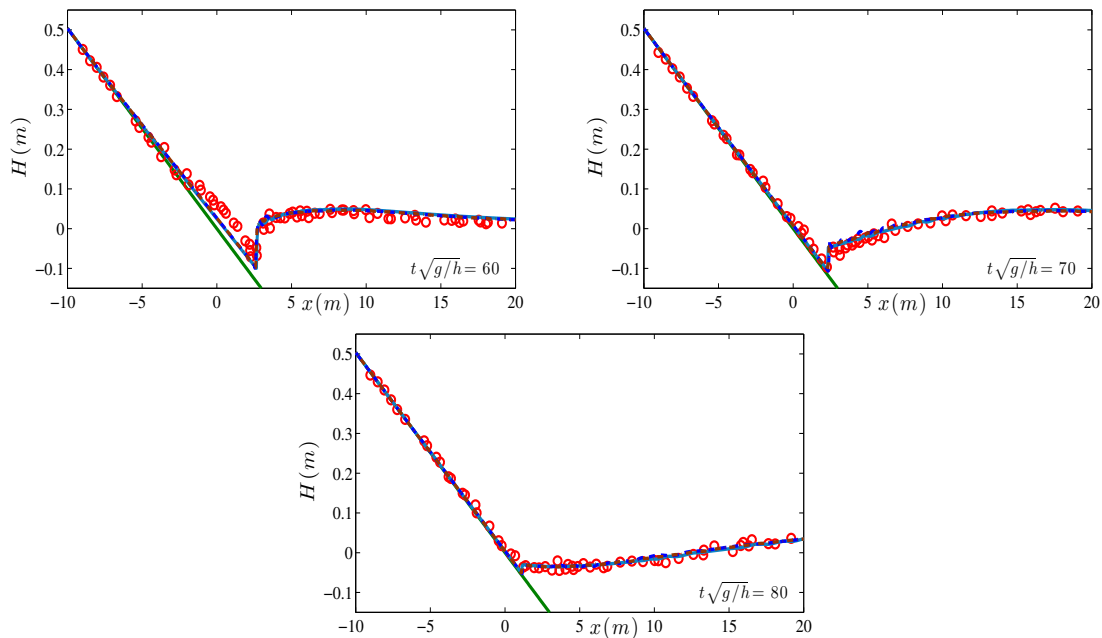


Figure 4.14: Free surface elevation of solitary wave run-up on a plane beach for $A/h = 0.28$. Hybrid models.

4.5 Regular wave propagation over a submerged bar

Beji and Battjes [19] conducted a laboratory experiment to examine sinusoidal wave propagation over a submerged bar. This test was first used by [53] to verify Delft Hydraulics numerical model HISWA, and has been used extensively in the literature for model validation see [187, 148, 142, 164], among others. The experiments were conducted in a $37.7m$ long, $0.8m$ wide, and $0.75m$ high wave flume. A hydraulically driven, piston-type random wave generator was located at the left side of the flume and a $1 : 25$ plane beach with coarse material was placed at the right side to serve as a wave absorber. The submerged trapezoidal bar was $0.3m$ high with front slope of $1 : 20$ and lee slope of $1 : 10$ separated by a level plateau $2m$ in length. We consider here three test cases described in Table 4.1.

Table 4.1: Experimental wave characteristics for Beji and Battjes [19] Tests.

Test	$T(sec)$	$H(m)$	h/L	Breaking type
(a)	2.020	0.020	0.11	non-breaking
(b)	1.010	0.041	0.27	non-breaking
(c)	2.525	0.054	0.0835	plunging breaker

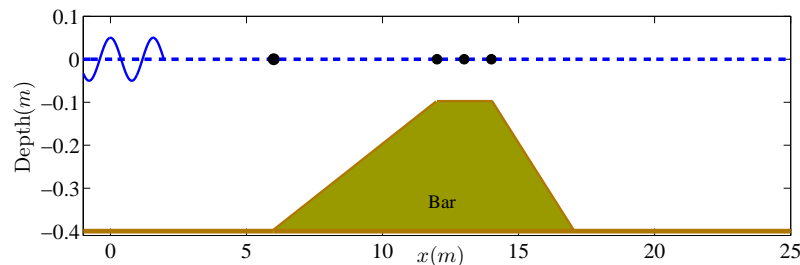


Figure 4.15: Regular wave propagation over a submerged bar: definition of bed topography and wave gauges.

The test configuration consists of a $23m$ channel with a constant depth of $h = 0.4m$. The bathymetry consists of $1 : 20$ front slope and $1 : 10$ back slope separated by a plateau of $2m$ in length. The dimension of the computational domain was set to $x \in [-10, 29]$ with the grid size $\Delta x = 0.04m$. The CFL number used is 0.3 and the sponge layer width $L_s = 4.9, 2.0, 5.2$ for cases (a)-(c) respectively. Sinusoidal waves were generated at $x = 0$. The waves propagated onshore and shoal along the front slope of the bar, forcing development of higher harmonics which are then released from the carrier frequency on the lee side of the bar as the water depth parameter kh

increases rapidly. Depth gauges which measure the free surface elevation are placed along $x = 10.5, 12.5, 13.5, 14.5, 15.5, 17.3, 19$ and $21m$. The numerical data from both formulations are presented and compared with experimental data, for non-breaking cases (a) and (b).

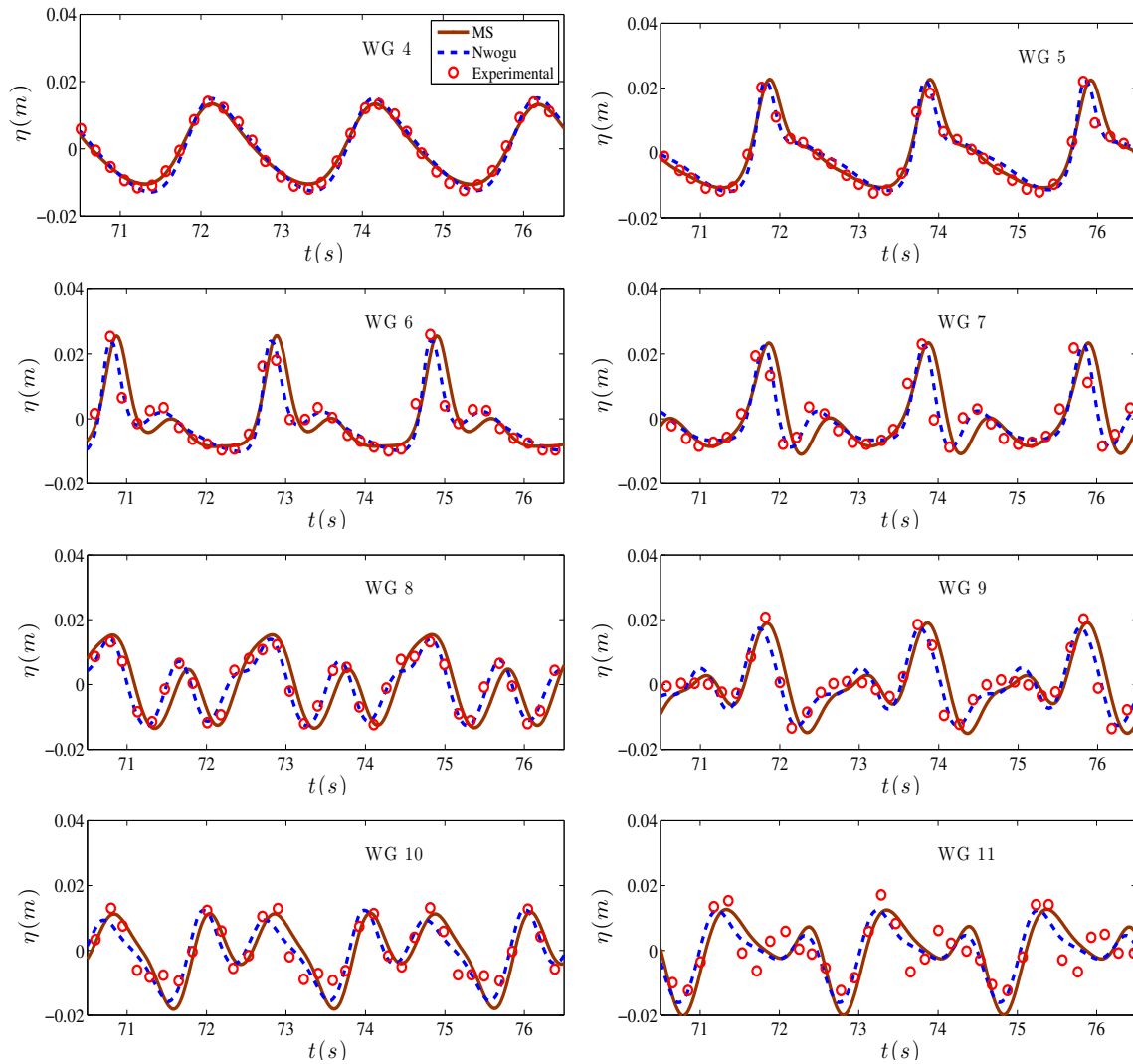


Figure 4.16: Time series of surface elevation at wave gauges for periodic wave propagation over a submerged bar for case (a).

Fig. 4.16 presents the results for case (a). Both formulations present a good agreement with the experimental data. The MS results slightly lag behind the Nwogu's ones. As the waves travel on the front slope lose their symmetry and bound harmonics are generated while on the plateau of the bar energy is transferred to higher harmonics mainly the second one. The schemes perform very well up to WG 8, showing only a phase shift for the MS formulation, despite the fact that the waves propagate down-

slope, and the physical process of wave propagation in to deeper water results in reduction in the potential energy consistent with increase in group velocity. After WG 9 some discrepancies with the data appear. This is due to the release of higher harmonics and the inability of the BT models presented here to fully resolve these harmonics released at the lee side of the bar.

The modeling of wave configuration for case (b) , is shown in Fig. 4.17. Since the incoming wave is characterized as short wave [19], it does not develop any tail waves as it grows in amplitude, keeps the vertical symmetry and appears as higher order Stokes wave. Excellent agreement is observed between numerical and experimental data, at WGs 4-6. The wave decomposition as it enters deeper region is not as drastic as in case (a) but second order harmonics are released with $kh > 6$ (see WG 9) which the models are unable to resolve. We should keep in mind that, for Nwogu's equation, and by using the z_a value proposed by Roeber [142] the model produces larger wavelengths and smaller amplitudes for short period waves in deeper waters. At the next gauges the models recover since the main energy is contained in waves with $kh \leq 3$ [142]. It should be noted that part of the discrepancies between the laboratory data and the models result might be due to the experimental setup [138, 142].

The next case presented is case (c), where wave breaking occurs on the top of the bar. In this test case the wave's period is $T = 2.525s$ and the wave's height is $0.054m$. The sponge layer width used was $L_s = 7.18m$. Every other computational parameter remains the same. The wave breaking that occurs is of the plunging type. Since the eddy viscosity models presented have been proved inadequate in some cases (see Section 4.5) we have decided to compare and discuss only Hybrid breaking models. Since we are interested only on the breaking behavior of the model and due to the inability of the BT equations to fully resolve higher harmonics released at the lee side of the bar [92], as it was demonstrated for the cases (a) and (b), only four wave gauges where placed at $x = 6, 12, 13, 14m$ respectively.

The numerical time series of surface elevation, for the two hybrid breaking models, at the four wave gauges are plotted against the test data in Fig. 4.18, where the different behavior between the two models is depicted. At $x = 6m$ the two models coincide as expected, since the wave breaking starts around $x = 12m$. At that gauge, and in all gauges that follow, the wave shape is well-reproduced by the new hybrid model but is over-predicted by the hybrid(ϵ) model, resulting in a different wave shape in the last

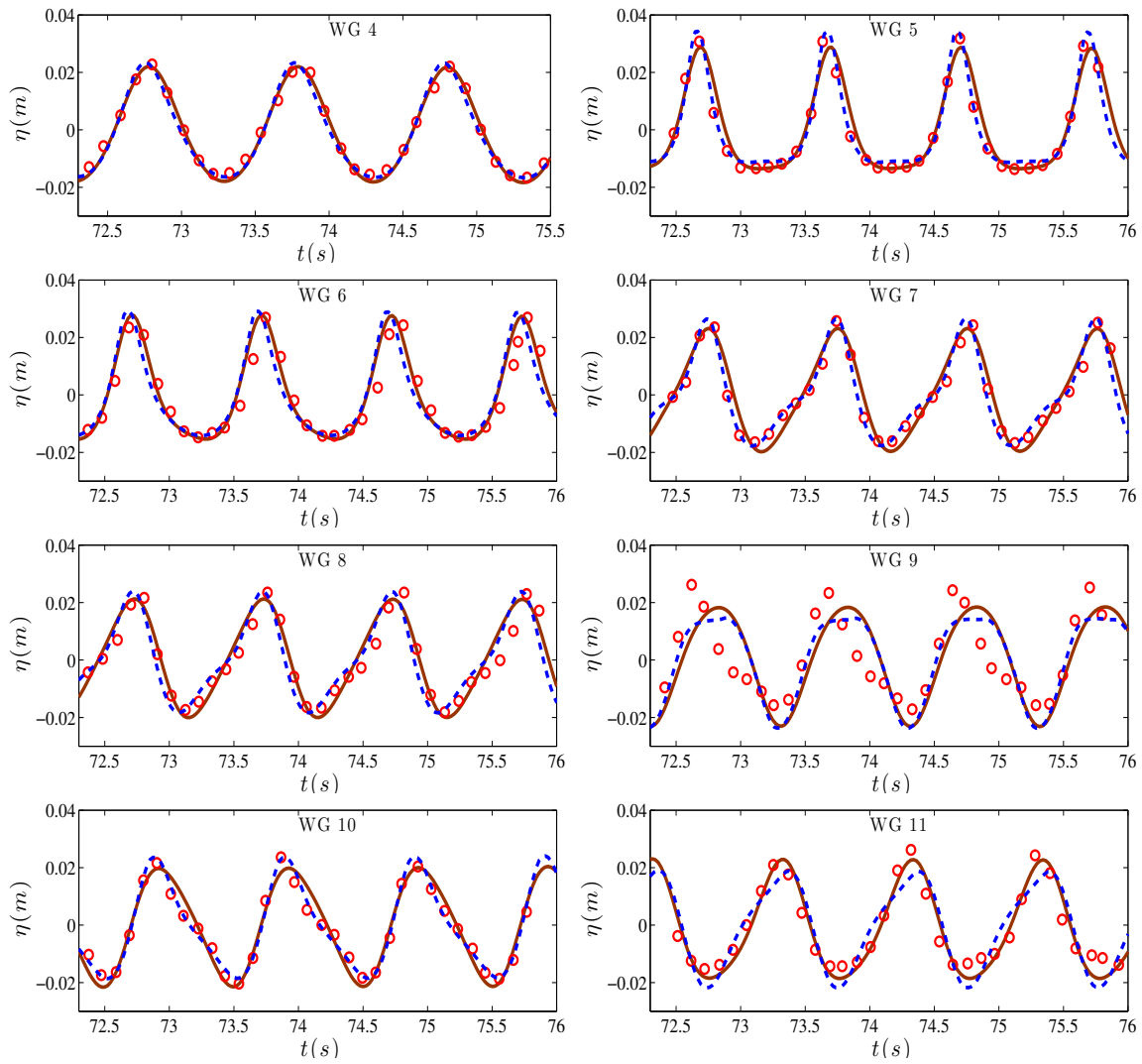


Figure 4.17: Time series of surface elevation at wave gauges for periodic wave propagation over a submerged bar for case (b).

gauge. These results are due to inability of this model to dissipate correctly the wave energy of the broken waves on the top of the bar, since wave breaking ceases before all the wave energy is dissipated, as discussed in Section 3.7.2. This is clearly shown in Fig. 4.19 where the wave-by-wave treatment and the l_{NSW} area for the two BT models is illustrated. For the new hybrid model the onset of breaking is correctly predicted and the wave breaking mechanism follows the wave front leading to a wave height decay. For the hybrid(ϵ) model the criterion used seems to be poor, since the initiation of breaking delays and remains active for less time than necessary. Fig. 4.19 covers approximately one period.

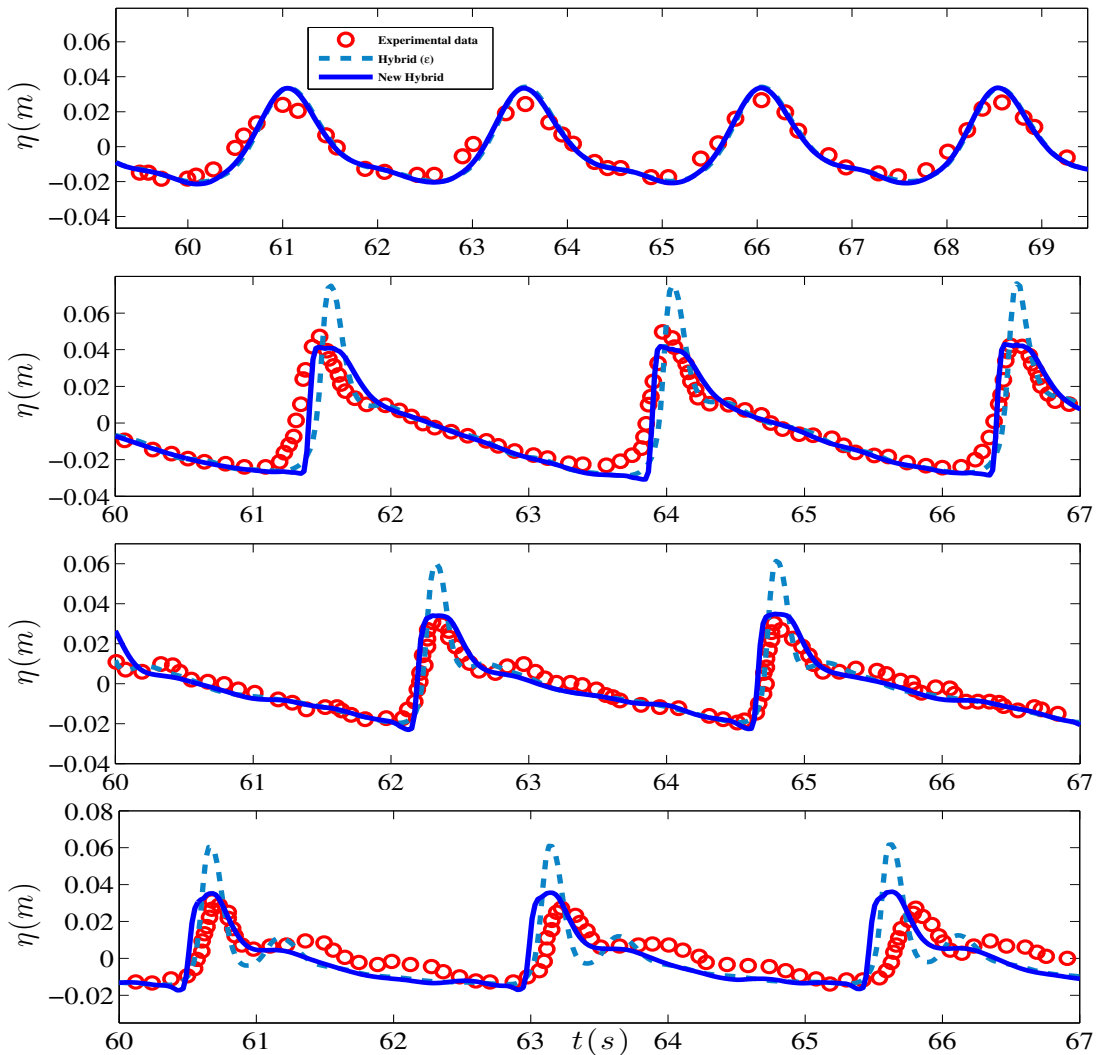


Figure 4.18: Time series of surface elevation at wave gauges for periodic wave breaking over a submerged bar for case (c)

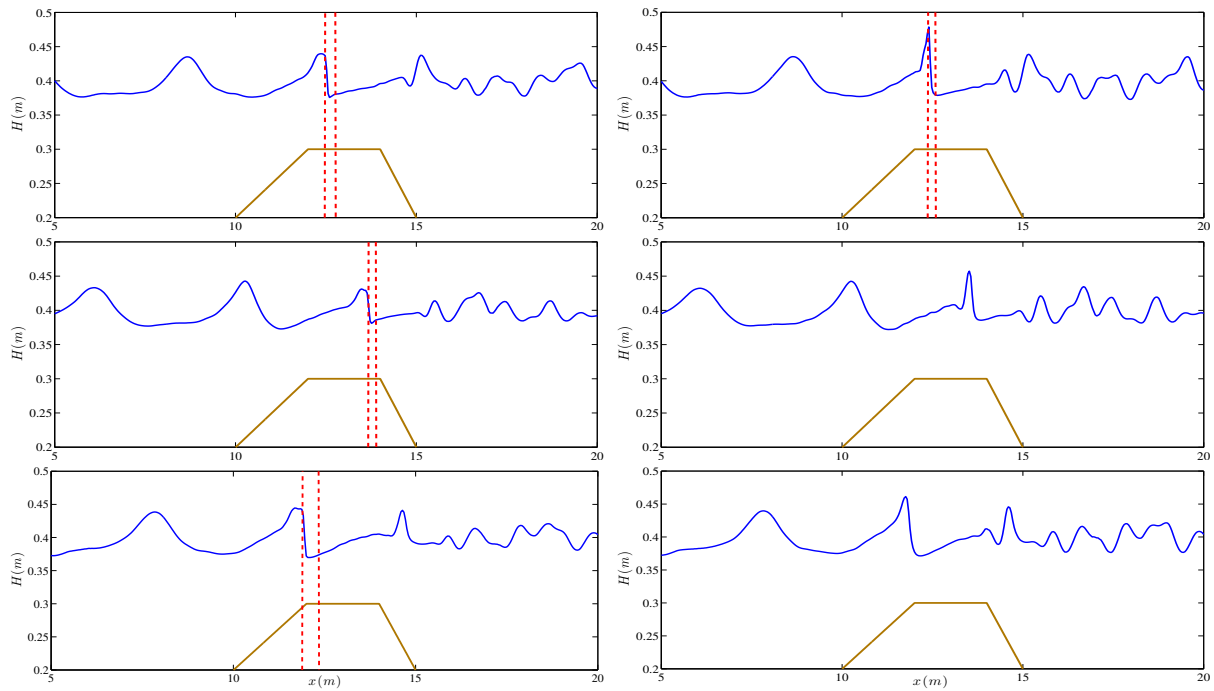


Figure 4.19: Spatial snapshot of breaking wave propagation over a bar for the New Hybrid model (left) and the Hybrid(ϵ) model (right). Between two consecutive vertical lines, the flow is governed by NSW equations

4.6 Solitary wave propagation over fringing reefs

Two relatively new challenging test cases that examine the ability of the model in handling simultaneously nonlinear dispersive waves together with wave breaking and bore propagation are presented in this section. The experiments were carried out at the O.H. Hinsdale Wave Research Laboratory at Oregon State University from 2007-2009. Two flumes were used. The first one is 48.8m long, 2.16m wide and 2.1m high and the second has length of 104m, a width of 3.66m and a height of 4.57m with a reef crest. Multiple wave gauges that measure the free surface elevation and the velocity profile have placed appropriate, for each case, along the flume's center line. Fig. 4.20 shows a schematic view of the flumes along with the position of the wave gauges, for the two test cases.

4.6.1 Dry reef

The first test case involves a bathymetry which consists of a 1/5 sloping fore reef and a 1m high reef flat. A steep solitary wave is generated at the left boundary and

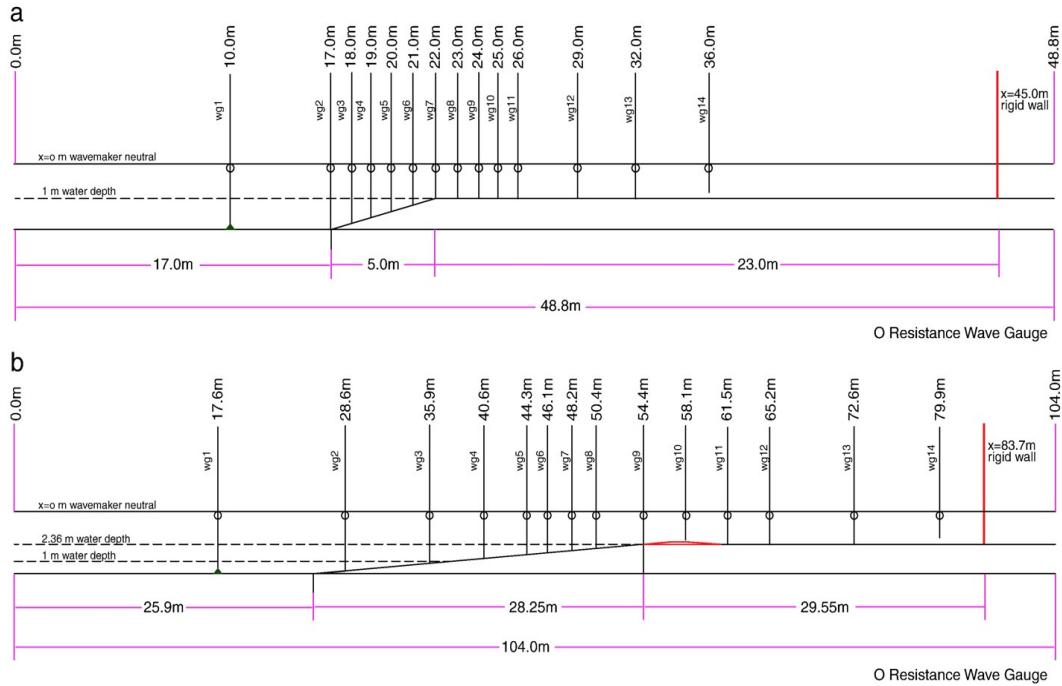


Figure 4.20: Schematics of flume experiments over fringing reefs. (a) 48.8-m flume. (b) 104-m flume. Figure is obtained from [142]

propagated downstream. The computational domain used in this test is $[0, 45m]$ with a grid step $\Delta x = 0.05$. $CFL=0.3$ and $\epsilon_{vd} = 1 \cdot 10^{-6}$. Wall boundary conditions were placed at both ends of the computational domain. As suggested in [142], $n_m = 0.012$ was used to define the roughness of the concrete surface. 14 wave gauges were placed at $x = 10, 17, 18, 19, 20, 21, 22, 23, 24, 25, 26, 29, 32$ and $36m$ to record the free surface waves. This is a very demanding test case since the strong nonlinearity of the solitary wave is over the weak nonlinear properties of the governing equations.

Fig. 4.22 shows the evolution of the water surface profile for various times. The solitary waves propagates undisturbed downstream until it reaches the toe of the slope where shoaling begins due to the topography. The wave steepens at the front but it does not form a plunging breaker over the step $1/5$ slope. As the wave surges over the reef, it undergoes a gradual transition from sub to supercritical flow, in the laboratory experiment. The numerical model simulates the process at time $t = 17.97s$ as a collapsing bore. The water inundates the reef flat, propagates over the dry reef and then is reflected by the wall. the wave propagation is well simulated as the celerity of the wave front is accurately predicted. Around time $t = 20.52s$ a momentarily stationary hydraulic jump is deformed at the apex of the reef, which is recognized and treated by

the wave breaking mechanism used.

Fig. 4.23 compares the computed and recorded surface elevation time series at the specific wave gauges. Like [166] only the uprush phase is considered here because the actual reflection at the end wall could not reproduced numerically due to the presence of lateral openings in the flume. WGs 1-6 show the propagation and shoaling of the solitary wave over the incline bottom topography. The numerical solution agrees reasonably well with the experimental data. The wave's arrival along with the solitary wave's amplitude are very well captured. An under prediction is observed at WG 6 at the run-down process, which result in a slightly over prediction of the wave's amplitude, at the WGs 7-10, which are located on the reef.

4.6.2 Submerged reef

In a computational domain for $x \in [0, 83.7m]$ the topography includes a fore reef slope of $1/12$, a $0.2m$ reef crest and a water depth $h = 2.5m$. The reef crest is then exposed by $6cm$ and submerges the flat with $h = 14cm$. This test case involves a $0.75m$ high solitary wave i.e. $A/h = 0.3$. The computational parameters used were the same as the dry reef case. Experimental results for the free surface waves were recorded at 14 resistance wave gauges. We refer to [142] for the experimental set up and gauge locations.

Fig. 4.24 compares the measured and computed wave profiles, for BT model and the NSW equations, as the numerical solitary wave propagates. Until time $t = 32.5$ the solitary wave propagates onshore and shoals due to the inclined bathymetry. As a result of shoaling the wave breaks around $t = 34.5s$ forming a plunging breaker. Both models are mimicking the breaker as a collapsing bore that slightly underestimates the wave height but conserved the total mass. Then the broken wave propagates on the back slope of the reef generating a super-critical flow that displays the stagnant water on the reef flat. While the bore propagates downstream a hydraulic jump develops at the back of the reef which becomes stationary momentarily around $t = 40s$. The use of the new hybrid model is crucial, since it handles simultaneously with the hydraulic jump and the propagating bore, recognizing correctly different bore fronts. The propagating bore is reflected by the wall around time $t = 41s$ and by time $t = 54s$ has overtoped the reef crest generating a hydraulic jump on the fore reef and a reflected bore at the back of the reef that travels downstream. At this point and as the water rushes down the fore reef, the flow transitions from flux to dispersion-dominated through the hydraulic

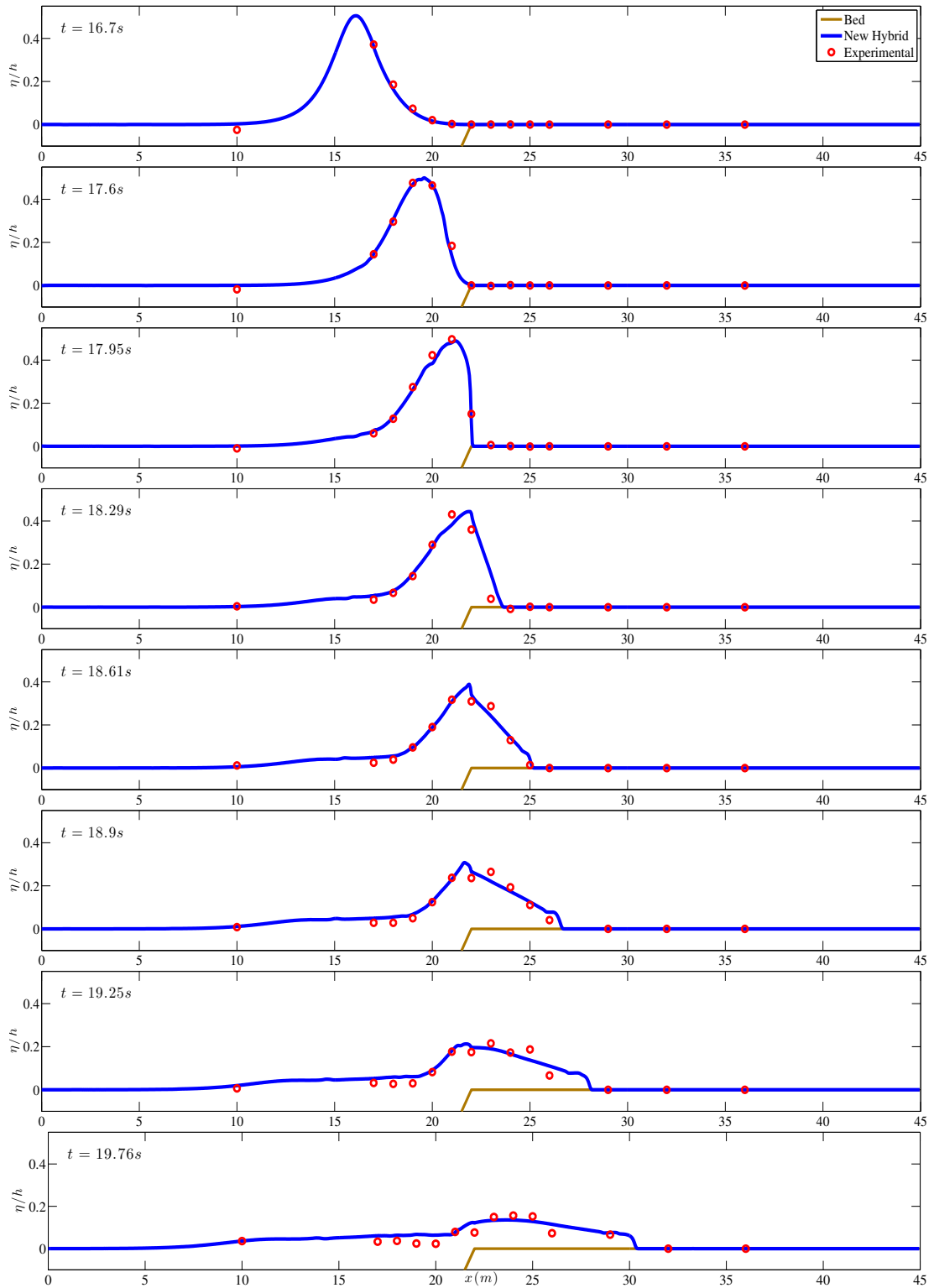


Figure 4.21: Evolution of the water surface profile for the test case of solitary wave propagation over a dry reef (cont. in Fig. 4.19)

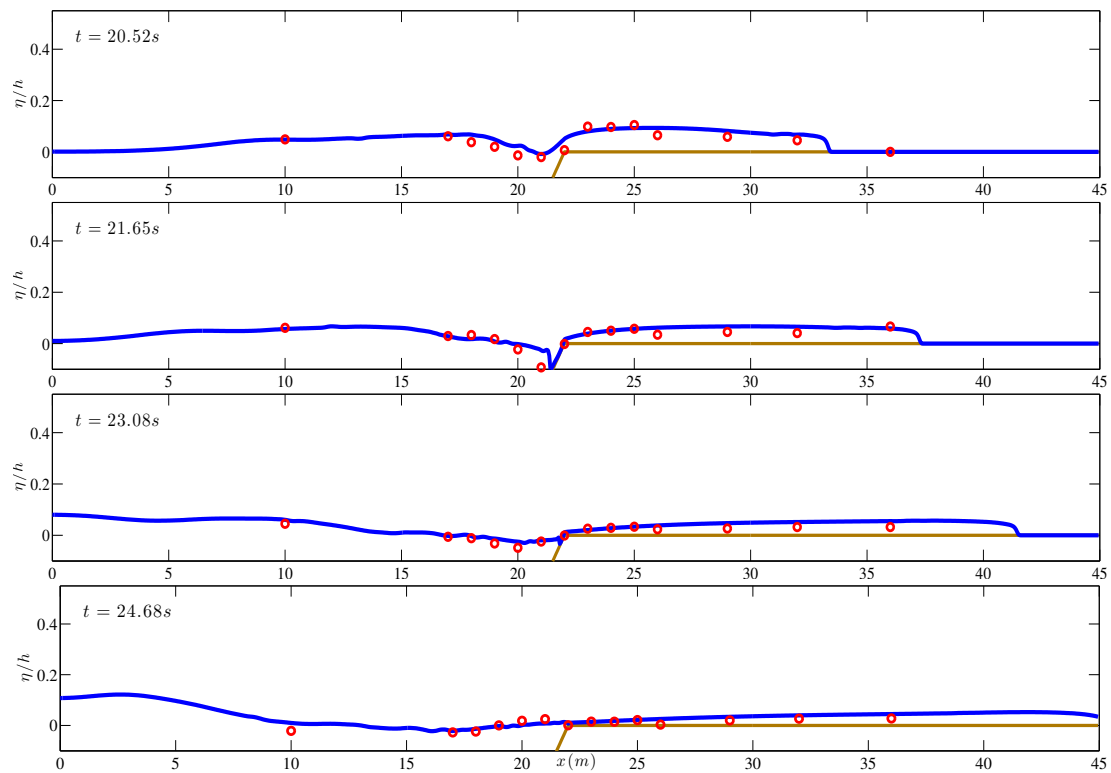


Figure 4.22: Evolution of the water surface profile for the test case of solitary wave propagation over a dry reef.

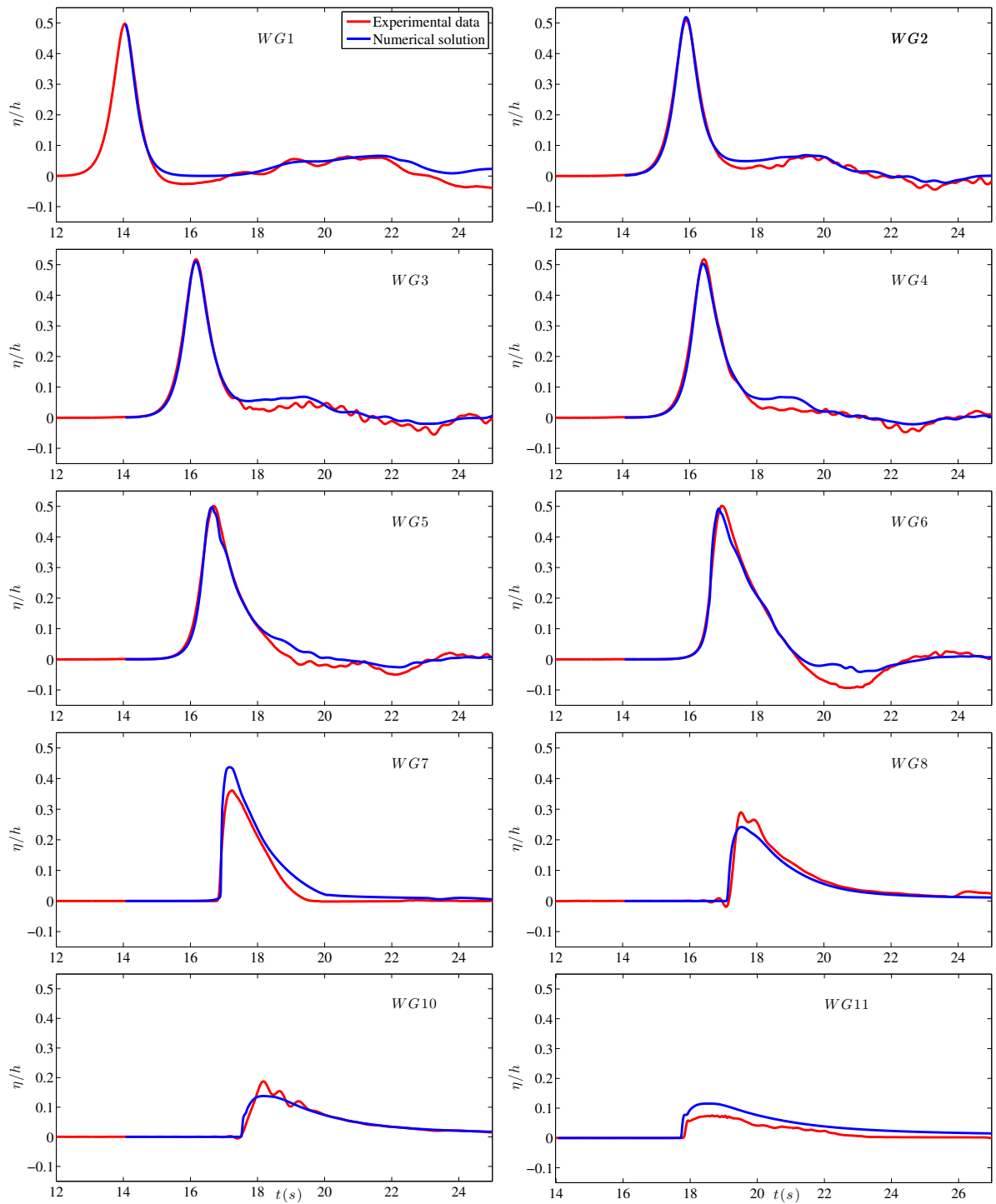


Figure 4.23: Time series of free surface elevation at wave gauges for the submerged reef case.

jump. NSW treat this jump as a propagating shock while the BT equations reproduces correctly the decaying undular bore produced by the hydraulic jump.

Fig. 4.26 compares the computed and recorded surface elevation time series at specific wave gauges. The recorded data from the wave gauges at $x \leq 50.4m$ shows the effect of the Airy type waves on the free surface. The hydraulic jump developed at the fore reef produced a train of waves over the increasing water depth and the resulting undulations were intensified as higher harmonics were released. As a matter of fact, wave gauges near the toe of the slope recorded highly dispersive waves of $kd > 30$ [142]. The BT model used managed to reproduce these highly dispersive waves with the correct phase and height strengths for this difficult problem and seems to compare in favor with the results presented in [142] and [166]. The results in [166] appear to be slower and smoother, compared to the experimental data and this is due to the nonphysical usage of the NSW equations in the region where the undular bore is formed and propagate. The time series at $x = 58.1m$ present the initial and subsequently overtoppings at the reef crest and confirm the efficiency of the proposed wet/dry front treatment. The numerical model reproduced these overtoppings at the correct phase but slightly overestimated the height of the arrival waves. At the gauges located at $x = 65.2m$ and $72.6m$ the arrival of the initial wave, the first reflected bore from the end wall, its subsequent reflection from the back reef as well as any subsequent reflections are almost correctly reproduced by the numerical model, verifying also the correct numerical boundary treatment.

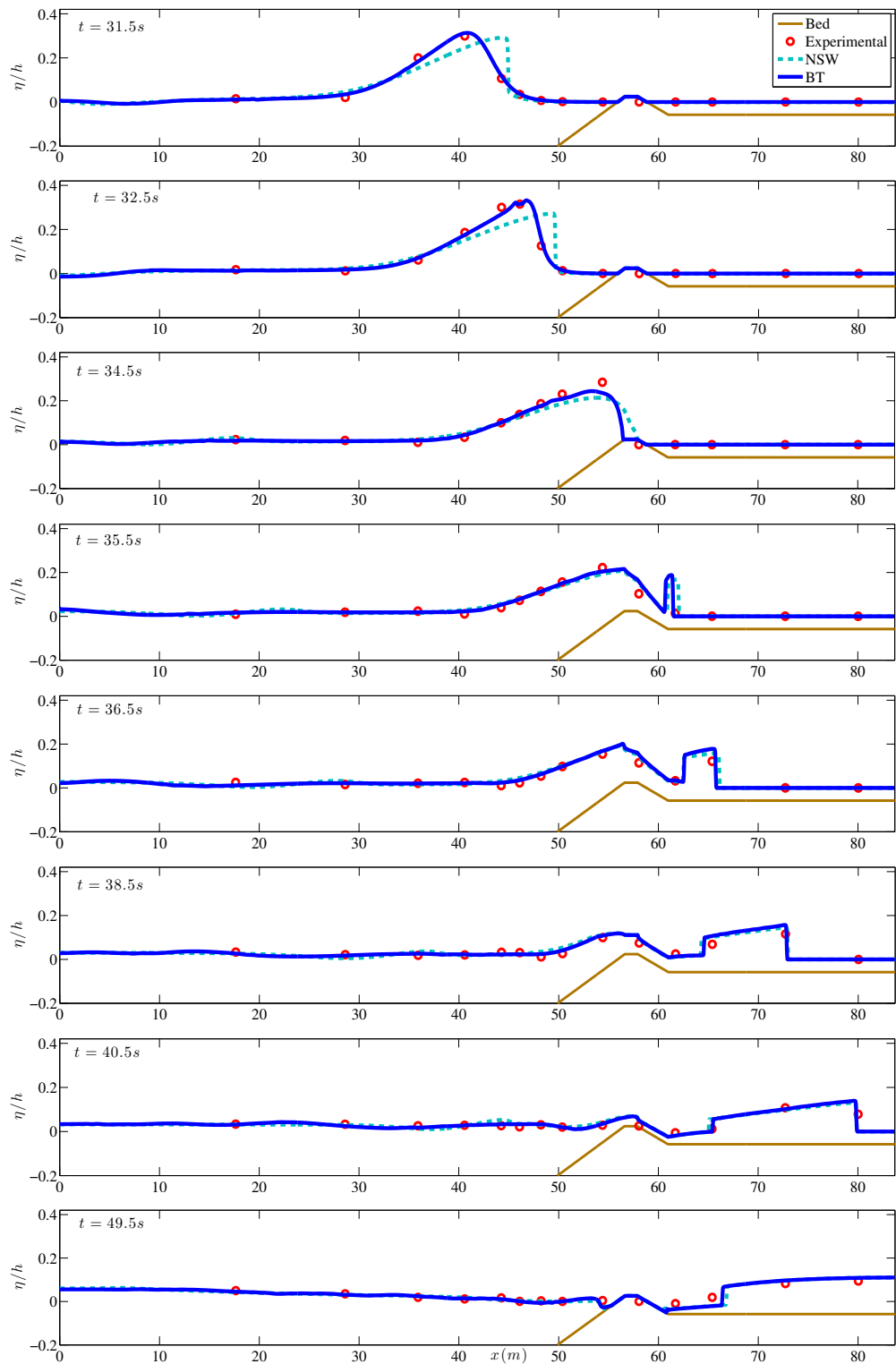


Figure 4.24: Evolution of normalized surface profile and wave transformation over an exposed reef for $A/h = 0.3$ and $1/12$ slope (continued in Fig 4.25).

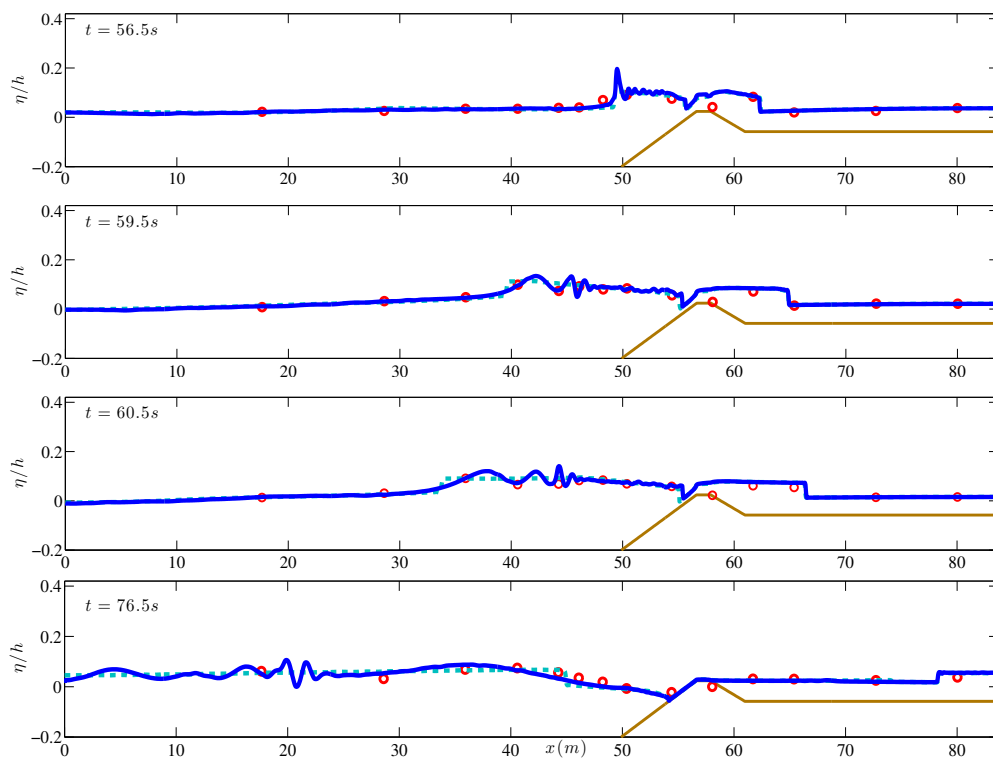


Figure 4.25: Evolution of normalized surface profile and wave transformation over an exposed reef for $A/h = 0.3$ and $1/12$ slope.

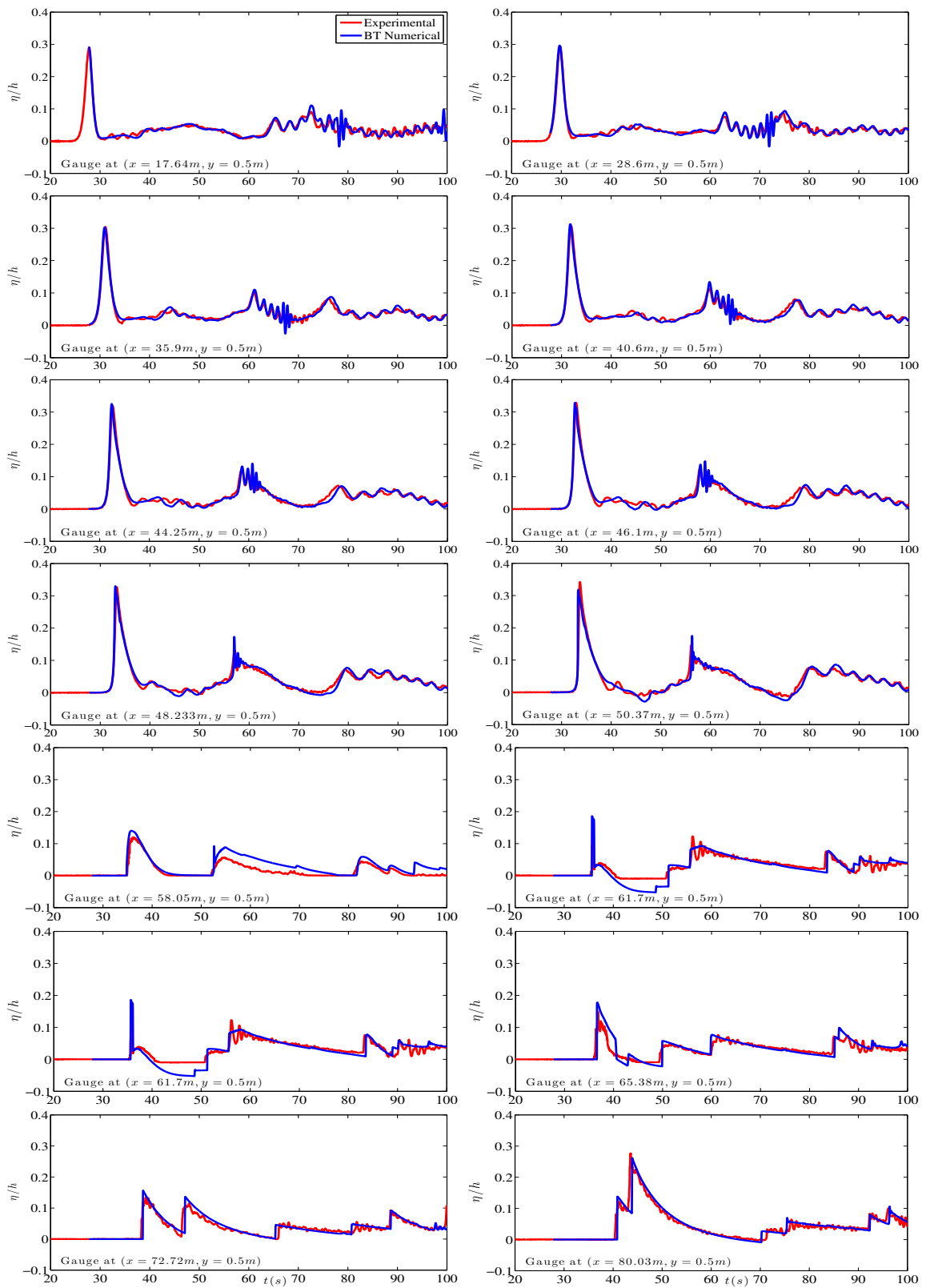


Figure 4.26: Time series of free surface elevation at wave gauges for the submerged reef case.

Chapter 5

Finite Volume methods on unstructured meshes

The general 2D FV approach requires partitioning a computational domain $\Omega \subset \mathbb{R}^2$ into a set of non overlapping control volumes and numerical implementation of an integral conservation law over each control volume. In this Chapter two types of finite volume schemes are considered for the NSWE. A Node Centered Finite Volume (NCFV) and a Cell Centered Finite Volume (CCFV) approach. In the NCFV scheme solution values are defined at the mesh nodes while for the CCFV schemes solutions are defined at the centroid of the control volumes. A brief review of the grid terminology used here is presented in Section 5.1. The two FV approaches for the 2D NSWE are described in Section 5.2 along with the topography source term discretization in Section 5.3. Sections 5.4-5.6 present the wet/dry treatment used in this work along with the friction discretization and the time integration. Finally, a comparison of the two FV schemes is presented using numerical tests with known analytical solutions.

5.1 Grid terminology

In this work, an initial conforming triangulation of Ω composes the so-called primal mesh. The *median-dual* partition is used to generate non-overlapping control volumes for the node-centered discretization. These control volumes cover the entire computational domain and compose a mesh that is dual to the primal mesh. For CCFV schemes the primary triangular cells serve as control volumes. The locations of discrete solutions are called *data points* while the cell boundaries are called *faces* and the term *edge*

refers to a line connecting the neighboring data points. Each face is characterized by two vectors, the edge vector, which connects the data points of the cells sharing the face and the direct-area vector, which is normal to the face and has amplitude equal to the face length.

The grids used in this work can be classified as *regular* or *irregular* ones. Regular grids are derived by a smooth mapping from grids with a periodic node connectivity and periodic cell distribution and include, but not limited to, grids derived from Cartesian ones. Four types of grids are considered in the present work: (I) Equilateral triangular grids; (II) Regular triangular grids derived from regular quadrilateral grids where squared cell are divided by the diagonals in four cells; (III) Regular triangular grids derived from quadrilateral grids by the same diagonal splitting of each quadrangle; and (IV) Randomly perturbed (distorted) grids. For the randomly perturbed grids generated in the present work, grid irregularities are introduced by perturbing the grid nodes of a type-I equilateral triangular grid, from their original positions by random shifts. For the production of such perturbed grids, we define the random perturbation in each dimension defined as $0.4r\Delta x$, where $r \in [-1/2, 1/2]$ is a random number and Δx is the local mesh size along the given dimension. These representative grid types, constructed and used in this work, are shown in Fig. 5.1 and can be considered as typical of those usually applied for the numerical solution of the NSWE. Our main interest is the accuracy and stability properties of FV schemes on general irregular (mostly unstructured) grids with a minimum set of constraints. In particular, we do not require any grid smoothness, neither on individual grids nor in the limit of grid refinement. The major requirement, in order to perform convergence studies and fair comparison between the two types of schemes, for a sequence of refined grids is to satisfy the *consistency refinement property* [159, 54, 55]. This property requires the maximum distance across the grid cells to decrease consistently with increase of the total number of grid data points, N . In particular the maximum distance should tend to zero as $N^{-1/2}$. As such this property enables meaningful assessment of the asymptotic order of convergence. For a given computational domain, and with out loss of generality, with dimensions $L_x \times L_y$ in the x - and y -direction respectively, we define a subdivision of L_x by N_x line segments, namely $\Delta x = L_x/N_x$ and depending on the grid type the corresponding subdivision Δy of L_y can be easily determined. As such, we define the characteristic length (effective mesh size) for each grid as $h_N = \sqrt{\frac{L_x \times L_y}{N}}$. For a consistently refined grid we half Δx

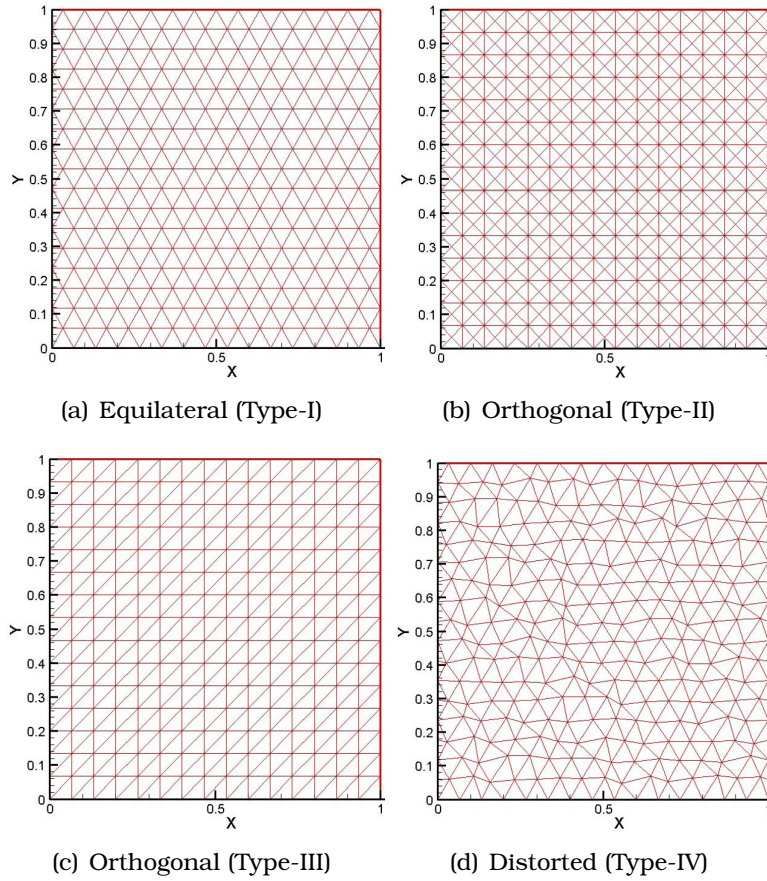


Figure 5.1: Representative grid types

hence defining $\Delta x' = \Delta x/2$ and it follows that, for the new refined grid $h'_N \simeq h_N/2$ and $N' \simeq 4N$. If a continued inconsistent refinement is applied instead, the discretization error convergence eventually degrades.

For a fair comparison between NCFV and CCFV schemes we need to derive *equivalent meshes* based on the degrees of freedom i.e. grid data points N . As such, and following from the above, equivalent grids can be easily defined as those having the same h_N and by keeping in mind that for a CCFV scheme N corresponds to the number of triangular cells in a computational mesh while for a NCFV scheme to the mesh nodes (denoted as N^*). In Table 1 typical grid values are presented for a computational domain with $L_x = L_y = 1$.

In order to measure the irregularity introduced on a grid, i.e the deviation from a type-I grid, we use the ratio between the circum-radius (R) and in-radius (r) of each triangle that is $A = \frac{R}{r}$. For a type-(I) grid $A = 2$ for the internal triangles, for type-II and type-III grids $A = 1 + \sqrt{2}$ while for a type-IV distorted grid $A \geq 2$. In Fig. 2 a metrics

Table 5.1: Typical grid values for characteristic length and degrees of freedom

N_x	Grid Type											
	Type-I & -IV				Type-II				Type-III			
	N	N^*	h_N	h_N^*	N	N^*	h_N	h_N^*	N	N^*	h_N	h_N^*
15	527	297	0.0436	0.0580	900	481	0.033	0.0455	450	256	0.0471	0.0625
30	2074	1102	0.0220	0.0301	3600	1861	0.0166	0.0231	1800	961	0.0235	0.0322
60	8349	4305	0.0109	0.0152	14400	7321	0.0083	0.0116	7200	3721	0.0117	0.0163
120	33258	16888	0.0055	0.0077	57600	29041	0.0041	0.0058	28800	14641	0.0058	0.0082
240	133237	67137	0.0027	0.0039	230400	115681	0.0020	0.0029	115200	58081	0.0029	0.0041

comparison for a consistently refined type-(IV) distorted grid with its equilateral and orthogonal counterparts is presented, in order to demonstrate the consistent production of all distorted grids. The metrics of the equilateral type-I grid are not equal to 2 for the 100% of the triangles due to the existence of orthogonal triangles at the left and right boundaries of the domain (see Fig. 5.1). From Fig. 5.2 it is evident that the distorted (type-IV) grid is closer to the equilateral (type-I) grid than the orthogonal ones. However, as it will become clearer later on, this metric is not adequate for the orthogonal types of grids since other geometrical characteristics are also involved, which eventually affect the performance of a numerical scheme on these types of grids.

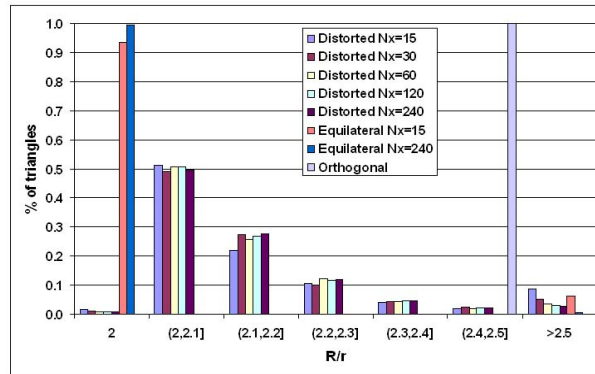


Figure 5.2: Distribution of Grids Metrics

5.2 Finite Volume (FV) approaches to conservation laws

A FV scheme can be categorized, in the main, as of the cell-centered (CCFV) or the node-centered (NCFV) (also referred as vertex-centered) type [9, 84, 75, 22, 119, 121]. A third approach also exists, the so called FV of the edge type introduced in [17]. First we have to define the general formalism of the finite volume methods. Following the notation of

[121, 125, 51] we consider a conforming triangulation \mathcal{T}^{hN} of the computational domain Ω to be a set of finitely many triangular subsets $T_p \subset \Omega$, $i = 1, 2, \dots, N$, such that the following conditions are satisfied:

- $\Omega = \bigcup_{p \in \{1, 2, \dots, N\}} T_p$,
- every T_p is closed,
- for two $T_p, T_q \in \mathcal{T}^{hN}$ with $p \neq q$ their interiors satisfy $T_p^\circ \cap T_q^\circ = \emptyset$,
- every one-dimensional face of any $T_p \in \mathcal{T}^{hN}$ is either a subset of $\partial\Omega$ or a face of another $T_q, q \neq p$.

This triangulation \mathcal{T}^{hN} constitutes our *primal grid*. For the CCFV approach, the finite control volumes used to satisfy the integral form of the equation are the mesh elements themselves (the *primal grid*). For the NCFV approach, the control volumes are elements of the mesh *dual* to the primal one. In a NCFV layout three possible definitions of the control volumes exists: the centroid dual, created by connecting the centroids of the triangular elements which are joined to the concerned node, the Dirichlet tessellation which is formed by connecting the centers of the circume-circles of the same element and finally the median dual obtained by linking the centroids of the elements and midpoints of the edges around the node [9]. In the edge type control volumes the nodes are placed on the edges of an original triangulation see [17, 41, 42] for details. In this work, from the NCFV approaches the median dual approach will be implemented and tested.

Integrating a system of conservation laws

$$\mathbf{U}_t + \nabla \cdot \mathcal{H}(\mathbf{U}) = \mathcal{L} \quad \text{on} \quad \Omega \times [0, t] \subset \mathbb{R}^2 \times \mathbb{R}^+, \quad (5.1)$$

over a computational domain Ω we obtain the integral form of (5.1):

$$\frac{\partial}{\partial t} \iint_{\Omega} \mathbf{U} d\Omega + \iint_{\Omega} (\nabla \cdot \mathcal{H}) d\Omega = \iint_{\Omega} \mathcal{L} d\Omega. \quad (5.2)$$

Application of the Gauss divergence theorem to the flux integral leads to

$$\frac{\partial}{\partial t} \iint_{\Omega} \mathbf{U} d\Omega + \oint_{\Gamma} (\mathcal{H} \cdot \tilde{\mathbf{n}}) d\Gamma = \iint_{\Omega} \mathcal{L} d\Omega, \quad (5.3)$$

where Γ is the boundary of the volume Ω and $\tilde{\mathbf{n}} = [\tilde{n}_x, \tilde{n}_y]^T$ is the unit outward normal vector. By denoting:

$$\mathbf{U}_P = \frac{1}{|\Omega_P|} \iint_{\Omega} \mathbf{U} d\Omega$$

the average value of the conserved quantities over a volume $\Omega_P \subset \Omega$ at a given time, equation (5.3) can be written for every cell as,

$$\frac{\partial \mathbf{U}_P}{\partial t} = -\frac{1}{|\Omega_P|} \oint_{\partial \Gamma_P} (\mathbf{F} \tilde{n}_x + \mathbf{G} \tilde{n}_y) d\Gamma + \frac{1}{|\Omega_P|} \iint_{\Omega_P} \mathcal{L} d\Omega. \quad (5.4)$$

5.2.1 Node-centered FV scheme on triangles

We first present NCFV approximations, following [125], where the control volumes are elements of the mesh dual to the primal grid \mathcal{T}^{hN} . The boundary ∂C_P of the control volume C_P around each internal node P is defined by connecting the barycenters of the surrounding triangles (having P as a common vertex) with the mid-points of the corresponding edges that meet at node P (see Fig. 5.3).

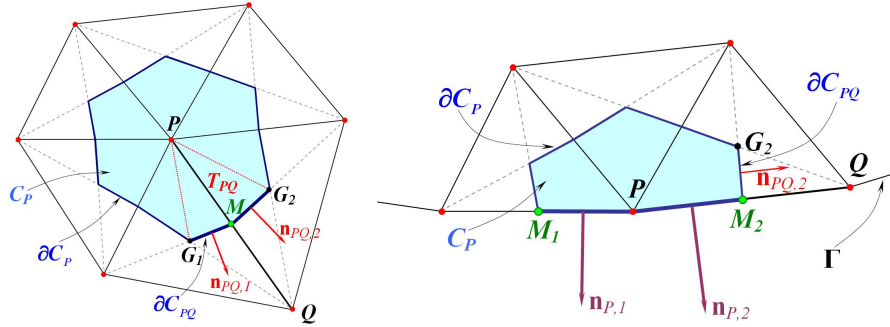


Figure 5.3: Control cell definitions, for an internal mesh node (left) and a boundary node (right), for the NCFV scheme

We define $\partial C_{PQ} = \partial C_P \cap \partial C_Q$ and M as the midpoint of edge PQ . The outward normal vector to ∂C_{PQ} is $\mathbf{n}_{PQ} = [n_{PQx}, n_{PQy}]^T$, while $\tilde{\mathbf{n}}_{PQ} = [\tilde{n}_{PQx}, \tilde{n}_{PQy}]^T$ is the corresponding unit vector. If $\mathbf{n}_{PQ,1}$ is normal to $\overline{G_1M}$ (with a norm equal to the length of $\overline{G_1M}$), and $\mathbf{n}_{PQ,2}$ is normal to $\overline{MG_2}$, then:

$$\mathbf{n}_{PQ} = \int_{\partial C_{PQ}} \tilde{\mathbf{n}} dl = \mathbf{n}_{PQ,1} + \mathbf{n}_{PQ,2},$$

where dl is measured along ∂C_{PQ} . The subcell T_{PQ} is the union of triangles G_1MP and MG_2P .

For a boundary mesh node P the definition of the control cell is described also in Fig. 5.3. The outward normal vector to $\overline{M_1PM_2}$ is $\mathbf{n}_P = [n_{Px}, n_{Py}]^T$, while $\tilde{\mathbf{n}}_P = [\tilde{n}_{Px}, \tilde{n}_{Py}]^T$ is the corresponding unit vector. If $\mathbf{n}_{P,1}$ is normal to $\overline{M_1P}$ (with a norm equal to the length of $\overline{M_1P}$), while $\mathbf{n}_{P,2}$ is normal to $\overline{PM_2}$ then:

$$\mathbf{n}_P = \int_{\overline{M_1PM_2}} \tilde{\mathbf{n}} dl = \mathbf{n}_{P,1} + \mathbf{n}_{P,2},$$

where dl is measured along $\overline{M_1PM_2}$. Further in the case of a boundary node P , $\partial C_{PQ} = \overline{M_2G_2}$ and if $\mathbf{n}_{PQ,2}$ is normal to $\overline{MG_2}$ then:

$$\mathbf{n}_{PQ} = \int_{\partial C_{PQ}} \tilde{\mathbf{n}} dl = \mathbf{n}_{PQ,2},$$

where dl is measured along ∂C_{PQ} .

If Γ is the domain's boundary and $K_P := \{Q \in \mathcal{N} \mid \partial C_P \cap \partial C_Q \neq \emptyset\}$, the set of neighboring nodes to P then, ∂C_P for a boundary node is described as:

$$\partial C_P = \bigcup_{Q \in K_P} \partial C_{PQ} + (\partial C_P \cap \Gamma).$$

Following from equation (5.4), and splitting the integral of the source term in a sum of integrals over the subcells T_{PQ} , $Q \in K_P$, the integral form of the equation on the constructed volume gives

$$\begin{aligned} \frac{\partial \mathbf{U}_P}{\partial t} = & - \frac{1}{|C_P|} \sum_{Q \in K_P} \left\{ \int_{\partial C_{PQ}} (\mathbf{F}\tilde{n}_x + \mathbf{G}\tilde{n}_y) dl \right\} - \frac{1}{|C_P|} \int_{\partial C_P \cap \Gamma} (\mathbf{F}\tilde{n}_x + \mathbf{G}\tilde{n}_y) dl \\ & + \frac{1}{|C_P|} \sum_{Q \in K_P} \left\{ \iint_{T_{PQ}} \mathcal{L} dx dy \right\}. \end{aligned} \quad (5.5)$$

We then introduce the flux vectors

$$\Phi_{PQ} = \int_{\partial C_{PQ}} (\mathbf{F}\tilde{n}_x + \mathbf{G}\tilde{n}_y) dl$$

and

$$\Phi_{P,out} = \int_{\partial C_P \cap \Gamma} (\mathbf{F}\tilde{n}_x + \mathbf{G}\tilde{n}_y) dl.$$

Hence, equation (5.5) becomes

$$\frac{\partial \mathbf{U}_P}{\partial t} = - \frac{1}{|C_P|} \sum_{Q \in K_P} \Phi_{PQ} - \frac{1}{|C_P|} \Phi_{P,out} + \frac{1}{|C_P|} \sum_{Q \in K_P} \left\{ \iint_{T_{PQ}} \mathcal{L} dx dy \right\}. \quad (5.6)$$

For all edges of the unstructured mesh the flux vector Φ_{PQ} should be computed and added (with the proper sign) to the flux sum of the two adjacent cells C_P and C_Q respectively. This flux vector is approximated assuming a uniform distribution of \mathcal{H} over ∂C_{PQ} , equal to its value at the midpoint M of edge PQ , thus

$$\Phi_{PQ} = \int_{\partial C_{PQ}} (\mathbf{F}\tilde{n}_x + \mathbf{G}\tilde{n}_y) dl \approx (\mathbf{F}\tilde{n}_x + \mathbf{G}\tilde{n}_y)_M \|\mathbf{n}_{PQ}\| = (\mathbf{F}n_{PQ,x} + \mathbf{G}n_{PQ,y})_M.$$

A fundamental aspect of FV methods is the idea of substituting the true flux at the control volume faces by a numerical flux function, a Lipschitz continuous function of

two face values, \mathbf{U}_{PQ}^L and \mathbf{U}_{PQ}^R . The key ingredient is the choice of this numerical flux function. In general this function is calculated as an exact or even better approximate local solution of the Riemann problem posed at the face. As such, and in order to evaluate the scalar product $\mathbf{Z} = \mathcal{H} \cdot \tilde{\mathbf{n}} = \mathbf{F}n_{PQx} + \mathbf{G}n_{PQy}$ at M and the corresponding flux vector, a one dimensional Riemann problem is assumed between the left (L) and right (R) states existing at the two sides of point M , defined by the vectors \mathbf{U}_{PQ}^L and \mathbf{U}_{PQ}^R respectively. In the present work, this Riemann problem is solved using the well known approximate Riemann solver of Roe [139]. Considering a simplified Riemann problem solved in an exact way, Roe's solver is widely used. The solver is based on the assumption that the Jacobian matrix (7) is constant and calculated using consistency and conservation conditions. Thus,

$$\Phi_{PQ} = \frac{1}{2} \left\{ \mathbf{Z}(\mathbf{U}_{PQ}^L, \mathbf{n}_{PQ}) + \mathbf{Z}(\mathbf{U}_{PQ}^R, \mathbf{n}_{PQ}) \right\} - \frac{1}{2} \left| \tilde{\mathbf{J}}_{PQ} \right| (\mathbf{U}_{PQ}^R - \mathbf{U}_{PQ}^L), \quad (5.7)$$

where $\tilde{\mathbf{J}}_{PQ}$ is the Jacobian matrix, computed using the Roe-averaged values of the primitive variables, $\mathbf{W} = [H, u, v]^T$, and $\left| \tilde{\mathbf{J}}_{PQ} \right|$ is defined as

$$\left| \tilde{\mathbf{J}}_{PQ} \right| = \left(\tilde{\mathbf{P}} \left| \tilde{\mathbf{\Lambda}} \right| \tilde{\mathbf{P}}^{-1} \right)_{PQ},$$

with $|\mathbf{\Lambda}|$ being the diagonal matrix containing the absolute values of the eigenvalues of \mathbf{J} . The $\tilde{}$ denotes that the matrices are computed using the Roe-averaged values of the primitive variables as,

$$\tilde{H} = \sqrt{\tilde{H}^L \cdot \tilde{H}^R}, \quad \tilde{c} = \sqrt{g \frac{\tilde{H}^L + \tilde{H}^R}{2}}, \quad \tilde{u} = \frac{\sqrt{\tilde{H}^L} u^L + \sqrt{\tilde{H}^R} u^R}{\sqrt{\tilde{H}^L} + \sqrt{\tilde{H}^R}}, \quad \tilde{v} = \frac{\sqrt{\tilde{H}^L} v^L + \sqrt{\tilde{H}^R} v^R}{\sqrt{\tilde{H}^L} + \sqrt{\tilde{H}^R}}.$$

Equation (5.7) can be alternatively written in the following form, which was used during our implementation

$$\Phi_{PQ} = \mathbf{Z}(\mathbf{U}_{PQ}^L, \mathbf{n}_{PQ}) + \tilde{\mathbf{J}}_{PQ}^-(\mathbf{U}_{PQ}^R - \mathbf{U}_{PQ}^L), \quad (5.8)$$

where $\tilde{\mathbf{J}}_{PQ}^- = \left(\tilde{\mathbf{P}} \tilde{\mathbf{\Lambda}}^- \tilde{\mathbf{P}}^{-1} \right)_{PQ}$, $\tilde{\mathbf{\Lambda}}^- = \text{diag} \{ \tilde{\lambda}_i^- \}$, with $\tilde{\lambda}_i^- = \min(\tilde{\lambda}_i, 0)$, $i = 1, 2, 3$ and

$$\mathbf{Z}(\mathbf{U}_{PQ}^L, \mathbf{n}_{PQ}) = \mathbf{F}^L n_{PQx} + \mathbf{G}^L n_{PQy} = \begin{bmatrix} H(u n_{PQx} + v n_{PQy}) \\ Hu(u n_{PQx} + v n_{PQy}) + \frac{1}{2} g H^2 n_{PQx} \\ Hv(u n_{PQx} + v n_{PQy}) + \frac{1}{2} g H^2 n_{PQy} \end{bmatrix}^L.$$

For a first order in space scheme the left and right states are approximated with their corresponding values at data points P and Q respectively i.e. $\mathbf{U}_{PQ}^L = \mathbf{U}_P$ and $\mathbf{U}_{PQ}^R = \mathbf{U}_Q$. The initial Roe scheme may allow nonphysical numerical solutions (expansion shocks), [102]. As such, and in order to ensure that the entropy condition is respected in the numerical solution, an entropy correction may be added [81, 140, 52, 102, 171].

We remark here that, modified versions of Roe's solver as well as other approximate Riemann solvers, e.g. of the HLL-type, can be applied for the construction of the numerical flux, with some of them being very successful in dealing with the solution of the NSWE, we refer for example to [171, 44, 170, 39, 78, 71, 169, 167, 73] among others. The choice of Roe's solver in this work is justified by its wide popularity and applicability and more importantly by the well established numerical treatment of the topography source terms in order to satisfy the C -property, which can be easily incorporated in this solver.

Second-order scheme for the node-centered numerical flux

In order to improve the spatial accuracy of the scheme more mesh cells should be considered when computing the numerical flux on the cell faces. Most FV implementations on unstructured triangular grids calculate the left and right states at a cell face assuming that the solution varies linearly in each cell, starting from the given initial constant or average solution values of adjacent cells. As such, the second order scheme implemented in the numerical solver is based on a MUSCL [173] reconstruction of the primitive variables, $\mathbf{W} = [H, u, v]^T$, which is exact for linear initial data, using a slope limiter to control the total variation of the reconstructed field.

For the NCFV approach the MUSCL scheme is applied for each edge; the left and right states of the primitive variables, \mathbf{W} , at the midpoint M of edge PQ are then approximated as

$$w_{i,PQ}^L = w_{i,P} + \frac{1}{2} \mathbf{r}_{PQ} \cdot (\nabla w_i)_P, \quad (5.9)$$

$$w_{i,PQ}^R = w_{i,Q} - \frac{1}{2} \mathbf{r}_{PQ} \cdot (\nabla w_i)_Q, \quad (5.10)$$

with w_i the component of \mathbf{W} and \mathbf{r}_{PQ} the vector connecting nodes P and Q . In order to prevent oscillations from developing in the numerical solution strict monotonicity in the reconstruction is enforced by using van Albada-van Leer edge-based nonlinear

slope limiter [172, 75, 176, 5] resulting in reconstructed values

$$\begin{aligned} w_{i,PQ}^L &= w_{i,P} + \frac{1}{2} \text{LIM} \left((\nabla w_i)_P^{\text{upw}} \cdot \mathbf{r}_{PQ}, (\nabla w_i)^{\text{cent}} \cdot \mathbf{r}_{PQ} \right); \\ w_{i,PQ}^R &= w_{i,Q} - \frac{1}{2} \text{LIM} \left((\nabla w_i)_Q^{\text{upw}} \cdot \mathbf{r}_{PQ}, (\nabla w_i)^{\text{cent}} \cdot \mathbf{r}_{PQ} \right), \end{aligned}$$

where

$$\begin{aligned} (\nabla w_i)^{\text{cent}} \cdot \mathbf{r}_{PQ} &= w_{i,Q} - w_{i,P}, \\ (\nabla w_i)_P^{\text{upw}} &= 2(\nabla w_i)_P - (\nabla w_i)^{\text{cent}}, \\ (\nabla w_i)_Q^{\text{upw}} &= 2(\nabla w_i)_Q - (\nabla w_i)^{\text{cent}}, \end{aligned}$$

and

$$\text{LIM}(a, b) = \begin{cases} \frac{(a^2 + e)b + (b^2 + e)a}{a^2 + b^2 + 2e} & \text{if } ab > 0, \\ 0 & \text{if } ab \leq 0, \end{cases} \quad (5.11)$$

where $0 < e \ll 1$, used to prevent division by zero ($e = 10^{-16}$ in our implementation) and prevents the activation of the limiter in smooth flow regions [176]. Slope limiters suppress the numerical oscillations in a non-linear manner by prohibiting the generation of any new local extrema at the cell interface. As it was pointed out in [2, 3], edge-based limiters may not preserve mean values in the cell, however, can greatly reduce the number of times the limiter is invoked. Edge-based limiters chatter far less than the volume-cell limiters and thus achieve better iterative convergence to steady-state. In addition, the above limiter is differentiable for linearly varying flow variables. Other limiters can be also applied [75, 155, 85, 22], however, and for consistency, all the results presented later in this work were produced with the above described limiter.

The gradient $(\nabla \mathbf{W})_P$ has to be computed in each mesh node P by applying the Green-Gauss theorem in the region Ω_P , see Fig. 4, described by the union of all triangles which share the vertex P , following [9, 8, 10]. $(\nabla \mathbf{W})_P$ is computed as integral averaged by taking into account that the discrete solution of \mathbf{W} varies linearly, which means that the gradient is constant on Ω_P (Green-Gauss linear reconstruction). As such,

$$\iint_{\Omega_P} \nabla w_i dA = \oint_{\partial\Omega_P} w_i \tilde{\mathbf{n}} dl,$$

which can be proven to result in

$$(\nabla w_i)_P = \frac{1}{|C_P|} \sum_{Q \in K_P} \frac{1}{2} (w_{i,P} + w_{i,Q}) \mathbf{n}_{PQ}. \quad (5.12)$$

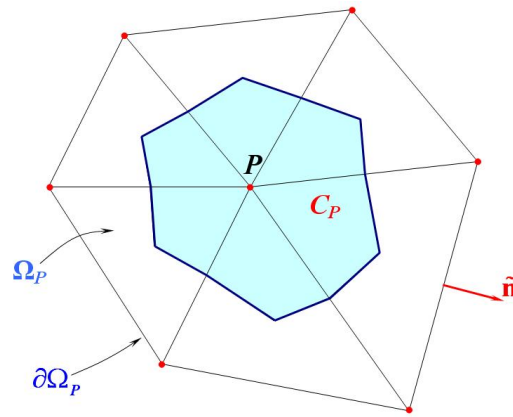


Figure 5.4: Definition of the region where the gradient for the NCFV scheme is computed

The choice of the Green-Gauss (G-G) linear reconstruction in this work is motivated mainly by the fact that the G-G reconstruction represents a linear function exactly for NCFV discretizations on triangles [8]. Even though the gradient calculation is exact whenever the numerical solution varies linearly over the support of the reconstruction, the mesh nodes on the NCFV approach usually are not located at the gravity centers of median dual control volumes and as such the cell averaging property for $w_{i,PQ}^L$ in (5.9), i.e.

$$\frac{1}{|C_P|} \iint_{C_P} w_{i,PQ}^L dx dy = w_{i,P},$$

and the local maximum principle are only approximately satisfied using the G-G technique [10]. Nevertheless, the above condition is not strictly necessary for the numerical scheme to be conservative and the application of the limiter function yields a FV scheme possessing a global extremum diminishing property [13]. Other reconstruction techniques such as of least squares (both un-weighted and weighted) can be used but their accuracy (especially for CCFV discretizations) may fail to provide suitable gradient estimates, and not only, for stretched curved meshes, [? ?] and as such provide a reduced order of accuracy.

In case that node P is a boundary one (see Fig. 5.3) the previous formula is modified as follows:

$$(\nabla w_i)_P = \frac{1}{|C_P|} \left\{ \sum_{Q \in K_P} \frac{1}{2} (w_{i,P} + w_{i,Q}) \mathbf{n}_{PQ} + w_{i,P} (\mathbf{n}_{P,1} + \mathbf{n}_{P,2}) \right\}.$$

We note here that, the same reconstruction procedure is used to compute the gradi-

ent for the bed elevation $B(x, y)$, which is needed for the discretization of the bed slope source term, as it will become clear in later sections.

Treatment of the Boundary Conditions for the NCFV scheme

In the NCFV approach the degrees of freedom (i.e. data points) are located directly on the boundary; consequently this approach is well suited for Dirichlet boundary conditions. However, a fundamental problem arises in the node-based discretization when two adjacent faces (with a boundary node at their intersection) have different type of boundary conditions [119]. Boundary conditions based on mesh faces rather than mesh vertices should be better adopted and a weak formulation is used, where the boundary condition is introduced into the residual through a modified boundary flux, as shown in Fig. 5.3. In this way the boundary conditions are formulated here in a similar way for both the node-centered and cell-centered discretizations (with the advantage of not using ghost cells in the node-centered approach).

In order to obtain a correct numerical model for shallow flow problems an adequate discretization procedure for the different types of boundary conditions is in need. The idea of using the weak formulation to calculate the flux at the boundary face can be used in the description of inflow, outflow, and wall boundary conditions. The sufficient conditions imposed at the boundaries combined with equations obtained from characteristic theory give the information needed for the calculation of the boundary flux. According to the theory of characteristics [84, 171], the Riemann invariants of the 1D NSWE are,

$$R^{\pm} = u \pm 2c$$

which are conserved along $dx/dt = u \pm c$, respectively, when the contribution of the source terms are neglected. R^+ and R^- represent the state to the left and right of a boundary face, respectively. Assuming that the right side of the boundary is outside the computational domain the inward R^- condition can be replaced by the boundary condition itself. For the 2D equations the conservation of the outward Riemann invariant for the NCFV approach, and referring for example at the face PM_1 in Fig. 5.3, is given as

$$\mathbf{u}_P \cdot \tilde{\mathbf{n}}_{P,1} + 2\sqrt{gh_P} = \mathbf{u}^* \cdot \tilde{\mathbf{n}}_{P,1} + 2\sqrt{gh^*}, \quad (5.13)$$

where P and \star denote the variables at the boundary node P and interface (boundary) variables respectively. Equation (5.13) is combined with the boundary conditions for a given flow regime to compute the normal flux at the boundary in a weak form. In general, the normal flux using the interface variables is given as

$$\Phi_{P,out} = \mathbf{Z}(\mathbf{U}^\star, \mathbf{n}_{P,1}) = \begin{bmatrix} H^\star (u^\star n_{P,1x} + v^\star n_{P,1y}) \\ H^\star u^\star (u^\star n_{P,1x} + v^\star n_{P,1y}) + \frac{1}{2}g(H^\star)^2 n_{P,1x} \\ H^\star v^\star (u^\star n_{P,1x} + v^\star n_{P,1y}) + \frac{1}{2}g(H^\star)^2 n_{P,1y} \end{bmatrix} \quad (5.14)$$

and according to equation (5.6) this flux is added to the control volume of node P .

According to the theory of characteristics, [84, 29, 36], and according to the flow regime the following situations have to be considered:

- (1) *Subcritical inflow*. In this case two characteristics "enter" the computational domain, so two conditions must be imposed. When the $\mathbf{u}^\star \cdot \tilde{\mathbf{n}}$ is imposed the water depth H^\star is calculated from equation (5.13) as

$$H^\star = \left((\mathbf{u}_P \cdot \tilde{\mathbf{n}}_{P,1} - \mathbf{u}^\star \cdot \tilde{\mathbf{n}}_{P,1}) / (2\sqrt{g}) + \sqrt{h_P} \right)^2.$$

When the discharge $\mathbf{q}^\star = H^\star \mathbf{u}^\star$ is imposed, H^\star can be obtained by solving iteratively for $c^\star = \sqrt{gH^\star}$

$$2(c^\star)^3 - (\mathbf{u}_P \cdot \tilde{\mathbf{n}}_{P,1} + 2c_P)(c^\star)^2 + g\mathbf{q}^\star \cdot \tilde{\mathbf{n}}_{P,1} = 0.$$

- (2) *Subcritical outflow*. In this case only one characteristic "enters" the domain, so only one condition is required at the boundary. In the case the water depth h^\star is imposed, and keeping in mind that the normal and tangential velocities to the boundary face are respectively

$$\mathbf{u}_P \cdot \tilde{\mathbf{n}}_{P,1} = u_P \tilde{n}_{P,1x} + v_P \tilde{n}_{P,1y}$$

and

$$\mathbf{u}_P \cdot \tilde{\mathbf{t}}_{P,1} = -u_P \tilde{n}_{P,1y} + v_P \tilde{n}_{P,1x},$$

equation (5.13) gives for the boundary normal velocity

$$\mathbf{u}^\star \cdot \tilde{\mathbf{n}} = \mathbf{u}_P \cdot \tilde{\mathbf{n}} + 2\sqrt{g}(\sqrt{H_P} - \sqrt{H^\star}).$$

Then the transverse velocity is passively advected [171], so $\mathbf{u}^* \cdot \widetilde{\mathbf{t}}_{P,1} = \mathbf{u}_P \cdot \widetilde{\mathbf{t}}_{P,1}$. Transforming back to the Cartesian system using

$$u^* = (\mathbf{u}^* \cdot \widetilde{\mathbf{n}}_{P,1x})\widetilde{n}_{P,1x} - (\mathbf{u}^* \cdot \widetilde{\mathbf{t}}_{P,1})\widetilde{n}_{P,1y}$$

and

$$v^* = (\mathbf{u}^* \cdot \widetilde{\mathbf{n}}_{P,1})\widetilde{n}_{P,1y} + (\mathbf{u}^* \cdot \widetilde{\mathbf{t}}_{P,1})\widetilde{n}_{P,1x},$$

the normal flux (5.14) can be calculated.

(3) *Supercritical inflow.* All characteristics "enter" the domain, so all the variables H^*, u^*, v^* must be imposed and no numerical boundary conditions are needed.

(4) *Supercritical outflow.* All characteristics "exit" the domain, so none of the variables must be imposed and

$$H^* = H_P, \quad \mathbf{u}^* = \mathbf{u}_P.$$

(5) *Wall boundary.* For solid boundary walls $\mathbf{u}^* \cdot \widetilde{\mathbf{n}}_{P,1} = 0$ in (5.14) is imposed for slip wall and $\mathbf{u}^* \cdot \widetilde{\mathbf{n}}_{P,1} = \mathbf{u}^* \cdot \widetilde{\mathbf{t}}_{P,1} = 0$ for no-slip wall, with h^* computed by using (5.13).

Remark 5 We point out that we always have to verify that the flow regime is subcritical or not by checking if

$$(\mathbf{u}_P \cdot \widetilde{\mathbf{n}}_{P,1} - c_P)(\mathbf{u}_P \cdot \widetilde{\mathbf{n}}_{P,1} + c_P) \leq 0$$

is satisfied or not by the numerical values obtained and modify the boundary treatment accordingly.

Remark 6 For periodic boundary conditions we assure that there is a one-to-one correspondence between the nodes and edges of the two periodic boundaries. Then, the values of the conserved variables at the "inlet" periodic boundary are set equal to the corresponding ones at the "outlet" periodic boundary.

The above boundary treatment preserves the second order accuracy of the scheme for smooth flows as the boundary node values, used for the computation of the boundary fluxes, have been calculated with second order accuracy. The location of the degrees of freedom directly on the boundary in the node-centered discretization scheme simplifies the implementation of the various types of boundary conditions. Additionally, boundary conditions based on mesh faces are compatible with the edge-based formulation of the computational procedure.

5.2.2 Cell-centered schemes on triangles

We now construct CCFV approximations on the primal \mathcal{T}^{h_N} grid. In this approach, the control volumes are identical with the grid cells $T_p, p = 1, \dots, N$, and the flow variables are located at the centroids of the triangular cells, see Fig. 5.5. The set of indices of the neighboring triangles of T_p is denoted by

$$K(p) := \{q \in \mathbb{N} \mid T_p \cap T_q \text{ is a face of } T_p\}.$$

Following from (6) the integration of the equations over the control volume formed by the triangle T_p is given by

$$\frac{\partial \mathbf{U}_p}{\partial t} = -\frac{1}{|T_p|} \sum_{q \in K(p)} \left\{ \int_{\partial T_q \cap \partial T_p} (\mathbf{F} \tilde{\mathbf{n}}_{q_x} + \mathbf{G} \tilde{\mathbf{n}}_{q_y}) dl \right\} + \frac{1}{|T_p|} \iint_{T_p} \mathcal{L} d\Omega, \quad (5.15)$$

with $|T_p|$ being the area of the triangle and $\tilde{\mathbf{n}}_q = [\tilde{n}_{q_x}, \tilde{n}_{q_y}]^T$ the outer (with respect to T_p) unit normal vector at the face $\partial T_q \cap \partial T_p$.

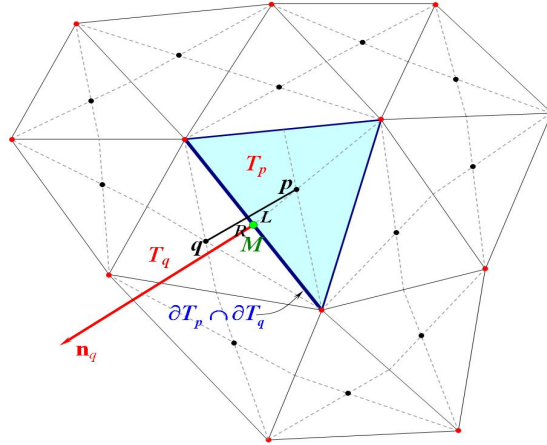


Figure 5.5: Control cell definition, for an internal mesh node, for the CCFV scheme

We then again introduce the flux vectors at each cell face

$$\Phi_q = \int_{\partial T_q \cap \partial T_p} (\mathbf{F} \tilde{\mathbf{n}}_{q_x} + \mathbf{G} \tilde{\mathbf{n}}_{q_y}) dl.$$

Hence, equation (5.15) becomes

$$\frac{\partial \mathbf{U}_p}{\partial t} = -\frac{1}{|T_p|} \sum_{q \in K(p)} \Phi_q + \frac{1}{|T_p|} \iint_{T_p} \mathcal{L} d\Omega. \quad (5.16)$$

With the usual choice of a one-point quadrature rule and assuming a uniform distribution of \mathcal{H} over each face, equal to its value at the midpoint M we have

$$\Phi_q \approx (\mathbf{F} \tilde{\mathbf{n}}_{q_x} + \mathbf{G} \tilde{\mathbf{n}}_{q_y})_M |\partial T_q \cap \partial T_p| = (\mathbf{F} \tilde{\mathbf{n}}_{q_x} + \mathbf{G} \tilde{\mathbf{n}}_{q_y})_M \|\mathbf{n}_q\| = (\mathbf{F} n_{q_x} + \mathbf{G} n_{q_y})_M.$$

Again following from the NCFV approach the approximate Riemann solver of Roe is utilized and as such

$$\Phi_q = \mathbf{Z}(\mathbf{U}_p^L, \mathbf{n}_q) + \tilde{\mathbf{J}}_{LR}^-(\mathbf{U}_q^R - \mathbf{U}_p^L). \quad (5.17)$$

A first order in space scheme again results if the left and right states are approximated with their corresponding values at points p and q respectively i.e. $\mathbf{U}_p^L = \mathbf{U}_p$ and $\mathbf{U}_q^R = \mathbf{U}_q$.

Second-order scheme for the cell-centered numerical flux

For the CCFV approach the MUSCL reconstruction scheme is also applied. It is important to note here that we wish to use the same edge-type slope limiter as for the NCFV scheme in order to calculate the left and right states at a cell face. In order to do so two different approaches were compared for calculating the extrapolated values, w^L and w^R .

Naive calculation of reconstructed values. Since we wish to apply the edge-based modified van Albada limiter (in order to have the advantages stated earlier) we are forced to compute reconstructed values at the intersection point D of face $\partial T_q \cap \partial T_p$ and \overline{pq} , see Fig. 5.6, as we have to compare with the reference value $w_{i,q} - w_{i,p}$. Thus,

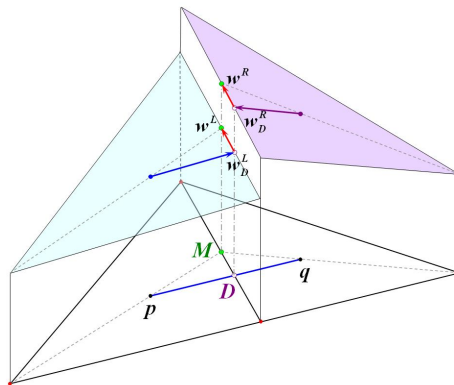


Figure 5.6: Linear representation for the CCFV schemes

we start by computing

$$(w_{i,p})_D^L = w_{i,p} + \mathbf{r}_{pD} \cdot \nabla w_{i,p}, \quad (5.18)$$

$$(w_{i,q})_D^R = w_{i,q} - \mathbf{r}_{Dq} \cdot \nabla w_{i,q}, \quad (5.19)$$

where D in general does not coincide with M , \mathbf{r} is the position vectors relative to the centroid of the cells and ∇w the gradient operator, yet to be defined. It is easy to show that such reconstruction is now conservative in the sense that

$$\frac{1}{|T_p|} \iint_{T_p} (w_{i,p})_D^L dx dy = w_{i,p}. \quad (5.20)$$

As it was pointed out in [85], when (5.20) holds the resulting numerical scheme will satisfy a local maximum principle for an appropriate restriction on the time-step as long as the reconstructed values within each cell do not lead to any new extrema at the midpoints of the faces of that cell.

Then for the limited version, using (5.11), and since point D does not in general coincide with the midpoint of \overline{pq} the ratio of the corresponding lengths has to be used resulting in,

$$(w_{i,p})_D^L = w_{i,p} + \frac{\|\mathbf{r}_{pD}\|}{\|\mathbf{r}_{pq}\|} \text{LIM} \left((\nabla w_i)_p^{\text{upw}} \cdot \mathbf{r}_{pq}, (\nabla w_i)^{\text{cent}} \cdot \mathbf{r}_{pq} \right); \quad (5.21)$$

$$(w_{i,q})_D^R = w_{i,q} - \frac{\|\mathbf{r}_{Dq}\|}{\|\mathbf{r}_{pq}\|} \text{LIM} \left((\nabla w_i)_q^{\text{upw}} \cdot \mathbf{r}_{pq}, (\nabla w_i)^{\text{cent}} \cdot \mathbf{r}_{pq} \right), \quad (5.22)$$

where now the limiter arguments are given as

$$\begin{aligned} (\nabla w_i)^{\text{cent}} \cdot \mathbf{r}_{pq} &= w_{i,q} - w_{i,p}, \\ (\nabla w_i)_p^{\text{upw}} &= 2(\nabla w_i)_p - (\nabla w_i)^{\text{cent}}, \\ (\nabla w_i)_q^{\text{upw}} &= 2(\nabla w_i)_q - (\nabla w_i)^{\text{cent}}. \end{aligned}$$

In an ideal unstructured grid, the variables are extrapolated to the center M of the cell face and as such a one-point interpolation of the surface integral will be second order accurate. If the variables are extrapolated to a different location, then the one-point interpolation is expected to be only first-order accurate, especially for types of grids where the distance between M and D is large [85].

To see this and refereing to Fig. 5.6, let us consider the case where the centroidal values at p and q are equal. Then, the gradient is normal to \overline{pq} . As a result the value at M is different from the value at p and q , as well as to that at D , being an extremum when compared to cell averages. If a limiting procedure is applied in the computation of the reconstructed values at M (by comparing with the difference between the values at p and q as in (29) and (30)) the limiter will clip the gradients at both p and q , regardless of the limiter used [15]. This will result in a first order flux computation since now the

values at M are equal to the cell average ones. With the correction proposed next the problem described above is avoided.

Corrected calculation of reconstructed values. The above inconsistency, i.e. the non-coincidence between M , where the numerical fluxes are enforced, and D , where the reconstructed values are computed, should be corrected. The first order error term introduced with the above reconstruction is a function of the distance between the optimal location M and the extrapolated location D . Hence, a novel way of applying an edge-based limiter to a CCFV scheme is presented in this work. First we compute the limited reconstructed values (5.21) and (5.22) at point D and then a simple directional correction is applied in order to calculate the reconstructed values at M (which will then be used on the Riemann solver). As such, and refereing to Fig. 5.6, this correction reads as

$$w_{i,p}^L = (w_{i,p})_D^L + \mathbf{r}_{DM} \cdot (\nabla w_i)_p, \quad (5.23)$$

$$w_{i,q}^R = (w_{i,q})_D^R + \mathbf{r}_{DM} \cdot (\nabla w_i)_q. \quad (5.24)$$

As the gradient used in this correction term is unlimited we expect that accurate gradient computations would result in an accurate correction, in the sense of retaining second order accuracy. In addition, and as it would be clear from the numerical tests, the effect of this correction would be more pronounced in cases where the distance between D and M is large.

Keeping in mind that we want to keep a common framework for both the NCFV and the CCFV approach it remains to define appropriate gradient operators with which to create a linear reconstruction of the solution within each cell.

Three element (compact stencil) gradient. Our first choice for calculating the gradient operator is the one that makes use of the three neighboring triangles of T_p , i.e. those in $K(p)$, which is often called the von Neumann neighboring of T_p [9]. For this choice, the gradient is computed in the region, C_p^c , defined by the centroids of the three triangles, by taking into account that the gradient is constant (G-G linear reconstruction), see Fig. 5.7. As such,

$$\iint_{C_p^c} \nabla w_i dA = \oint_{\partial C_p^c} w_i \tilde{\mathbf{n}} dl,$$

which results in

$$\nabla w_{i,p} = \frac{1}{|C_p^c|} \sum_{\substack{q,r \in K(p) \\ r \neq q}} \frac{1}{2} (w_{i,q} + w_{i,r}) \mathbf{n}_{qr}.$$

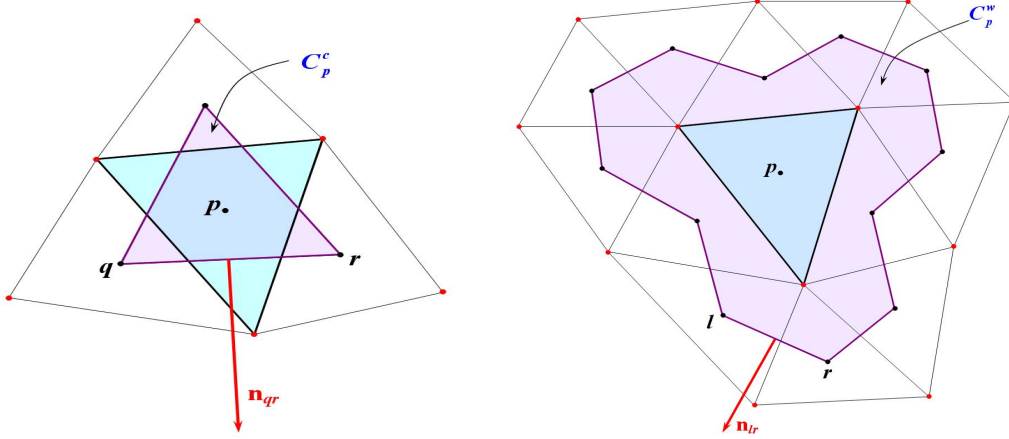


Figure 5.7: CCFV compact (top) and wide (bottom) stencils used for gradient reconstruction

Extended element (wide stencil) gradient. In this case, and in order to increase the support of the computational stencil, the gradient is computed in the region, C_p^w , which is defined for every T_p by connecting the barycenters of the triangles $T_l, l = 1, \dots, m$, having a common vertex with T_p [9]. This set of indices is denoted by

$$K'(p) := \{l \in \mathbb{N} \mid T_p \cap T_l \text{ is a vertex of } T_p\}.$$

The G-G linear reconstruction in this case results in

$$\nabla w_{i,p} = \frac{1}{|C_p^w|} \sum_{\substack{l,r \in K'(p) \\ r \neq l}} \frac{1}{2} (w_{i,l} + w_{i,r}) \mathbf{n}_{lr},$$

where \mathbf{n}_{lr} is the outward unit normal vector to the edge connecting the barycenters of triangles T_l and T_r .

It can be instructive to compare the number of points involved in gradient computations with the two different stencils for a grid consisting of equilateral triangles (type-I). In this case the two methods use 3 and 12 points in their stencils respectively. Having identified the support stencil and the number of points involved in computing the gradient, it would be interesting to determine whether these gradients are centered at

the centroid of the cell with $O((\Delta x)^2, (\Delta y)^2)$. It should be stated that a gradient estimate of $O(\Delta x, \Delta y)$ is sufficient for second-order accuracy of the overall scheme. However, a gradient which is properly centered at the centroid for a regular triangular grid turns out to be advantageous in mimicking a Fromm-type [173] of construction with favorable dispersion characteristics, at least for one-dimensional flows. It can be inferred that, even for this limiting case of equilateral triangles, the x - and y - gradients computed using three-point stencils are not properly centered. On the contrary, the 12-point stencil yields a perfectly centered gradient. Although perfect centering of the x - and y - components of the gradient, in the limiting case of equilateral triangles, is an attribute for any multidimensional reconstruction procedure it is equally important to ensure that the implementation of limiters can be readily carried out in the prescribed framework.

Treatment of the Boundary Conditions for the CCFV scheme

To treat boundary conditions in CCFV approach we adopt the very popular approach of ghost cells. The ghost cells are additional layers of grid cells outside the physical domain (see Fig. 8). The cells are only virtual, although geometrical quantities are associated with them. The geometrical quantities are usually taken from the corresponding cell at the boundary. Here, in most cases, the barycenter of the ghost cell is the mirror of the barycenter of the boundary cell relative to the boundary, see Fig. 5.8. Every other quantity is computed as mentioned in the above sections. The purpose of the ghost cells is to simplify the computation of the fluxes, gradients etc. along the boundaries. The primitive variables in the ghost cells $(H^\star, u^\star, v^\star)$ are obtained from the boundary conditions.

Following from Section 4.1.2 the conservation of the outward Riemann invariant is now given as

$$\mathbf{u}^L \cdot \tilde{\mathbf{n}} + 2\sqrt{gH^L} = \mathbf{u}^\star \cdot \tilde{\mathbf{n}} + 2\sqrt{gH^\star}, \quad (5.25)$$

where L and \star denote the (reconstructed) variables at the left (inside) and interface (boundary) variables respectively. Equation (5.25) is again combined with the boundary conditions for a given flow regime to compute the normal flux at the boundary in a weak

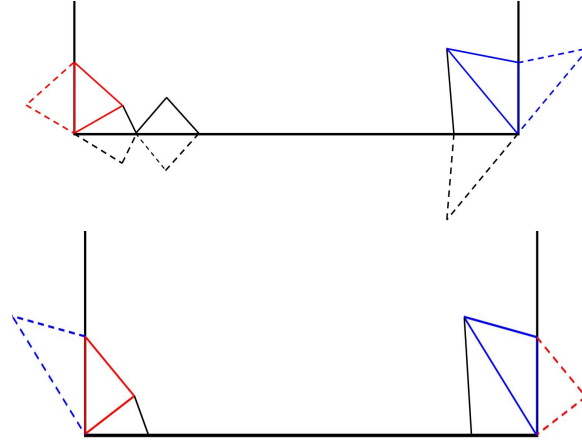


Figure 5.8: Ghost cells for CCFV schemes, general formulation (top) and for periodic boundary conditions (bottom)

form. Following from that the normal flux using the interface variables is now given as

$$\Phi^* = \mathbf{Z}(\mathbf{U}^*, \mathbf{n}) = \begin{bmatrix} H^*(u^* n_x + v^* n_y) \\ H^* u^* (u^* n_x + v^* n_y) + \frac{1}{2} g(H^*)^2 n_x \\ H^* v^* (u^* n_x + v^* n_y) + \frac{1}{2} g(H^*)^2 n_y \end{bmatrix}. \quad (5.26)$$

Remark 7 For periodic boundary conditions we assure that there is a one-to-one correspondence between the nodes and faces of the two periodic boundaries; ghost cells are produced for periodic boundary conditions by duplicating and shifting the internal boundary cells of the corresponding periodic boundary (Fig. 5.8). The conserved variables and the gradients (since we cannot compute the gradients at the ghost cells) at each ghost cell are set equal to the ones of the duplicated internal cell of the corresponding periodic boundary.

At this point it is important to demonstrate the different characteristics of the grids used, with respect to the distance between points D (intersection point of face $\partial T_q \cap \partial T_p$ and \overline{pq}) and M (the middle of a cell's face, where the numerical fluxes are enforced) for internal faces, as well as boundary ones, for the CCFV formulation. Typical behaviors for the four types of grids used in this work are exhibited in Fig. 5.9. For the Equilateral (type-I) grids and at the face between two equilateral cells, points D and M coincide. On the contrary, when the face belongs to cells incorporating at least one non-equilateral cell, then D and M do not coincide, with the maximum deviation

observed on the corresponding boundaries. For the Orthogonal (type-II) grids on a face being the hypotenuse of the orthogonal triangle D and M coincide, while in any other case a large distance between the two points exists. On the boundary faces, D and M coincide. For the Orthogonal (type-III) grids, and for all the internal faces. D and M coincide, while a large difference is present on the boundary faces (when periodic boundary conditions are not used). For the Distorted (type-IV) grids there is always a difference between the locations of points D and M .

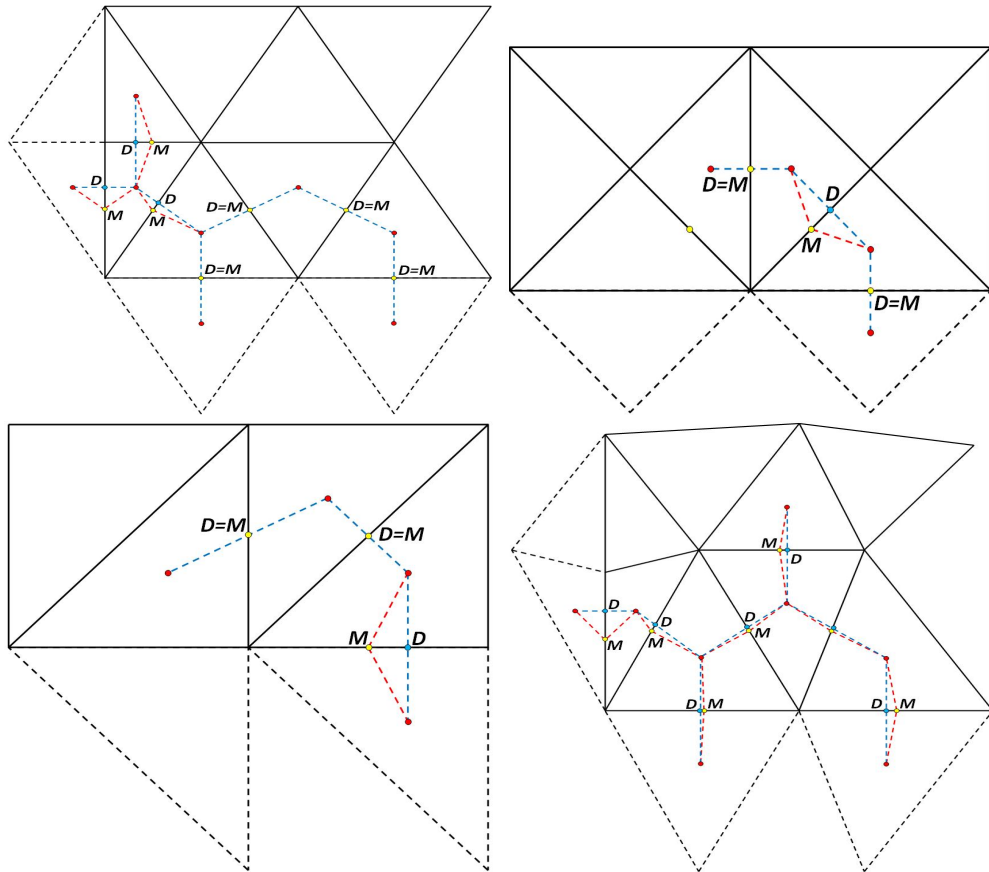


Figure 5.9: Schematic representation for the location of D and M on the different grid types

Moreover, in orthogonal (type-II) grids, the midpoint M of the common face between two adjacent triangles may lie outside the control volume used to compute the gradient with the compact stencil, see Fig. 5.10. This is not the case when the wide stencil gradient is used. In addition, as can be seen in Fig. 5.10, there is a relatively large distance between the barycenter of the control volume and that of the gradient volume. These can constitute reasons for a reduced effectiveness of the proposed correction in the reconstruction (equations (31) and (32)), when the compact gradient stencil is used,

with the type-II orthogonal grids as it will be clear from the numerical tests later on.

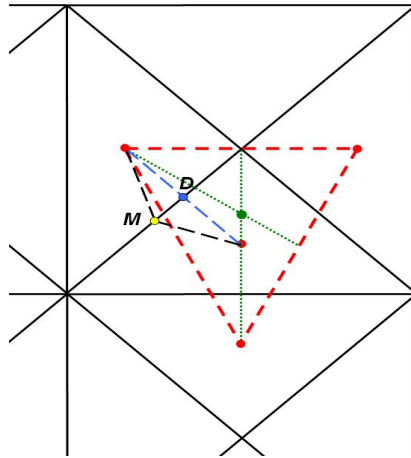


Figure 5.10: Relative positions between M and the gradient volume for the compact stencil

All the above geometric characteristics should be taken into account when a CCFV scheme is applied in a particular grid type, as well as in the interpretation of the results. The above geometric characteristics also justify the proposed correction to the reconstruction of the extrapolated values, following from (31) and (32).

5.3 Topography source term discretizations

In order to satisfy the numerical balance between the topography source and the numerical fluxes and as such to achieve the well-balanced property in our 2D unstructured schemes, we introduce the (topography source) flux vectors Ψ such that, for the CCFV and NCFV scheme respectively as

$$\iint_{T_p} \mathbf{R}(\mathbf{U}) dx dy = \sum_{q \in K(p)} \Psi_q \quad \text{and} \quad \iint_{C_p} \mathbf{R}(\mathbf{U}) dx dy = \sum_{Q \in K_p} \Psi_{PQ}.$$

This discrete flux vector of the source term depends on the values of the variables on the boundary of the computational cell for each approach, and on the corresponding normal vector. As it has been shown in [18] and [17], an upwind discretization scheme should be also used for the bed topography elevation source term to avoid non-physical oscillations in the solution by satisfying the C -property in hydrostatic flow conditions (flow at rest). In order to achieve this the source term integral is projected onto the

eigenvectors of the flux Jacobian $\widetilde{\mathbf{J}}$ and in its linearized form can be written in the following way:

$$\boldsymbol{\Psi} = \widetilde{\mathbf{P}}\widetilde{\mathbf{P}}^{-1}\widetilde{\mathbf{R}}.$$

In order to obtain the exact hydrostatic solution (and as such satisfy the exact C -property) the topography source term should balance the corresponding non-zero flux terms, so it must be linearized in the same way and evaluated in the same state (Roe-averaged state) as the flux terms. The upwind discretization of the face source term provides the following two terms (in-going and out-going contributions) that are added to the corresponding computational cells respectively:

$$\boldsymbol{\Psi}^- = \widetilde{\mathbf{P}}\mathbf{I}^-\widetilde{\mathbf{P}}^{-1}\widetilde{\mathbf{R}}, \quad \boldsymbol{\Psi}^+ = \widetilde{\mathbf{P}}\mathbf{I}^+\widetilde{\mathbf{P}}^{-1}\widetilde{\mathbf{R}},$$

where $\mathbf{I}^\pm = \widetilde{\boldsymbol{\Lambda}}^\pm\widetilde{\boldsymbol{\Lambda}}^{-1}$ and $\widetilde{\mathbf{R}}$ is a proper discrete representation of the topography source. With some algebraic manipulation we obtain:

$$\boldsymbol{\Psi}^- = \frac{1}{2}\widetilde{\mathbf{P}}\left(\mathbf{I} - \left|\widetilde{\boldsymbol{\Lambda}}\right|\widetilde{\boldsymbol{\Lambda}}^{-1}\right)\widetilde{\mathbf{P}}^{-1}\widetilde{\mathbf{R}} \quad (5.27)$$

and similarly:

$$\boldsymbol{\Psi}^+ = \frac{1}{2}\widetilde{\mathbf{P}}\left(\mathbf{I} + \left|\widetilde{\boldsymbol{\Lambda}}\right|\widetilde{\boldsymbol{\Lambda}}^{-1}\widetilde{\mathbf{P}}^{-1}\widetilde{\mathbf{R}}\right). \quad (5.28)$$

The face normal source term $\widetilde{\mathbf{R}}$ in the above equations is approximated in the following manner, in order to balance the corresponding flux terms in hydrostatic conditions, for the CCFV and NCVF scheme respectively

$$\widetilde{\mathbf{R}}|_q = \begin{bmatrix} 0 \\ -g\frac{H^L + H^R}{2}(B^R - B^L)n_{qx} \\ -g\frac{H^L + H^R}{2}(B^R - B^L)n_{qy} \end{bmatrix}_q \quad \text{and} \quad \widetilde{\mathbf{R}}|_{PQ} = \begin{bmatrix} 0 \\ -g\frac{H^L + H^R}{2}(B^R - B^L)n_{PQx} \\ -g\frac{H^L + H^R}{2}(B^R - B^L)n_{PQy} \end{bmatrix}_{PQ}.$$

For both FV approaches the numerical flux terms should now equal the source term for hydrostatic conditions (flow at rest), i.e.,

$$\mathbf{Z}(\mathbf{U}^L, \mathbf{n}) + (\widetilde{\mathbf{P}}\widetilde{\boldsymbol{\Lambda}}\widetilde{\mathbf{P}}^{-1})(\mathbf{U}^R - \mathbf{U}^L) = \frac{1}{2}\widetilde{\mathbf{P}}\left(\mathbf{I} - \left|\widetilde{\boldsymbol{\Lambda}}\right|\widetilde{\boldsymbol{\Lambda}}^{-1}\right)\widetilde{\mathbf{P}}^{-1}\widetilde{\mathbf{R}}, \quad (5.29)$$

which should give at a cell face: $u = v = 0$, $B^R - B^L = -(H^R - H^L)$. While equation (5.29) holds for first order scheme, i.e. if the (L) and (R) values are not reconstructed, this is not the case for the second order MUSCL discretization. As such, and following [87] for the CCFV approach and [125] (where an analytical proof can also be found)

for the NCFV approach, a term, $\tilde{\Psi}$, should be added to the source term discretization (righthand side of (5.29)) for maintaining the correct balance. For the CCVF and NCFV schemes the terms to be added respectively read

$$\tilde{\Psi}|_q = \begin{bmatrix} 0 \\ -g \frac{H^L + H_p}{2} (B^L - B_p) n_{qx} \\ -g \frac{H^L + H_p}{2} (B^L - B_p) n_{qy} \end{bmatrix} \quad \text{and} \quad \tilde{\Psi}|_{PQ} = \begin{bmatrix} 0 \\ -g \frac{H^L + H_P}{2} (B^L - B_P) n_{PQx} \\ -g \frac{H^L + H_P}{2} (B^L - B_P) n_{PQy} \end{bmatrix}.$$

The above terms vanish for the first order schemes as $B^L = B_p$ (and $B^L = B_P$) and for hydrostatic conditions we have: $B^L - B_p = -(H^L - H_p)$ (and $B^L - B_P = -(H^L - H_P)$).

The above added high-order corrections of the topography source terms gives an exact balance between the numerical flux and slope source terms for the flow at rest problem resulting in a fully second-order scheme. We note here that, the above treatment correctly enforces the well-balance property for the steady solution in (13) when $B(x, y) < H_0 \forall (x, y) \in \Omega$, i.e. totally wetted computational domain.

5.4 Wet-dry front treatment and mass conservation

As it was described in one dimension (see section 3.2.3) , further modifications are needed in the boundary defined by a wet dry front in order to accurately model the transitions between wet and dry areas while at the same time maintain higher order spatial accuracy. As in one dimension we have to deal with the following issues:

Dry cell identification As described before, in order to identify dry cells we have to define a tolerance parameter ε_{wd} . If the water depth in a computational cell is below that value the cell is considered dry and we set $\mathbf{W} = [0, 0, 0]^T$. The value of ε_{wd} is computed according to the dual grid geometrical characteristics. This value must be small compared to the mesh size and has the desirable property of approaching zero as h_N approaches zero in order to converge to an exact solution. Following [136] a robust definition of ε_{wd} is

$$\varepsilon_{wd} = \left(\frac{h_N}{L^{ref}} \right)^2 \tag{5.30}$$

where h_N is the characteristic mesh length and L^{ref} is a reference geometrical dimension of the spatial domain calculated as:

$$L^{ref} = \max_{P,Q} \|\mathbf{x}_P - \mathbf{x}_Q\|_{\inf},$$

where P and Q are the mesh nodes with coordinates \mathbf{x}_P and \mathbf{x}_Q respectively.

Consistent depth reconstruction in dry regions In the presence of wet/dry fronts over topography there should be a consistent computation between ∇H and ∇b for achieving proper second order accuracy. It is obvious that, for a wet/wet steady case in each computational cell $\nabla H = -\nabla b$. Following from that, in the MUSCL reconstruction for hydrostatic conditions we must have inside (at faces) of each computational P -cell that

$$b^L - b_P = -(H^L - H_P) \Rightarrow (\nabla b)_P = -(\nabla H)_P \quad (5.31)$$

and similar for an adjacent Q -cell $(\nabla b)_Q = -(\nabla H)_Q$. In cells with wet/dry interfaces it is obvious that this is not the case anymore when dry cells are involved in the ∇H calculation since more cells (the dry ones) actually contribute to the reconstruction of ∇b but not in that of ∇H . As such, a simple improvement was proposed in [51] to maintain formally full second order accuracy in the case of wet/dry bed. If in the gradient calculation of a wet cell a dry cell is involved we correct the H^L and/or H^R reconstructed face values by forcing

$$H^L = H_P - (b^L - b_P) \quad \text{and/or} \quad H^R = H_Q - (b^R - b_Q)$$

By doing so, compatible reconstructed vales for H are computed and the balance in equation (5.31) is achieved.

Conservation of the flow at rest with dry regions The redefinition of bed elevation (in the calculation of $\widetilde{\mathbf{S}}_{b,PQ}$) in order to obtain an exact balance at the front between the bed slope and the hydrostatic terms for steady conditions is (see section 3.2.3) :

$$\Delta b = \begin{cases} -(H^R - H^L), & \text{if } H^L > \varepsilon_{wd} \text{ and } H^R \leq \varepsilon_{wd} \text{ and } H^R < (b^R - b^L), \\ (b^L - b^R), & \text{otherwise.} \end{cases}$$

Flow in motion over adverse slopes In two dimensions, at the faces having a wet/dry front we impose, additional to the above bed redefinition, the following temporary condition for the computation of the corresponding numerical fluxes and source terms, following [38, 50, 125],

$$\text{if } [H^L > \varepsilon_{wd} \text{ and } H^R \leq \varepsilon_{wd} \text{ and } H^L < (b^R - b^L)] \text{ then } u^L = u^R = v^L = v^R = 0.$$

The numerical treatment is similar if R is the wet side and L is identified as dry.

Depth positivity and mass conservation See section 3.2.3.

5.5 Friction term discretization

According to [33, 123, 122, 145] a pointwise explicit treatment of the friction term produces numerical oscillations when the roughness coefficient is high. To handle properly the friction term we follow the proposed technique by [33, 145, 122]. Starting from a separate implicit formulation for the friction terms one can have for the momentum variables at the i th cell

$$(Hu)_i^{n+1} = (Hu)_i^* - (gH_i S_x^f)_i^{n+1} \Delta t^n \quad (5.32)$$

$$(Hv)_i^{n+1} = (Hv)_i^* - (gH_i S_y^f)_i^{n+1} \Delta t^n \quad (5.33)$$

where the values signalled with $*$ are computed, without taking into account the friction forces, using any FV scheme that has been described to the previous sections. Setting

$$R_f = \frac{n_m^2 \|\mathbf{u}\|}{H^{\frac{4}{3}}}$$

we can write for the first equation (5.32) (and similar for equation (5.33)):

$$\begin{aligned} (Hu)_i^{n+1} &= (Hu)_i^* - (gH_i u_i R_f)_i^{n+1} \Delta t^n \\ &= (Hu)_i^* - (gH_i u_i)_i^{n+1} \left[(1 - \theta)(R_f)_i^{n+1} + \theta(R_f)_i^n \right] \Delta t^n \end{aligned}$$

By separating implicit and explicit parts we get

$$\begin{aligned} &(Hu)_i^{n+1} \left[1 + (1 - \theta)g(R_f)_i^{n+1} \Delta t^n \right] \\ &= (Hu)_i^* - g(Hu)_i^n \theta (R_f)_i^n \Delta t^n \end{aligned} \quad (5.34)$$

and considering $(R_f)^{n+1} \simeq (R_f)^*$ we can write equation (5.34) as

$$(Hu)_i^{n+1} = \frac{(Hu)_i^* - \theta g(Hu)_i^n (R_f)_i^n \Delta t^n}{1 + (1 - \theta) g(R_f)_i^* \Delta t^n}.$$

In a similar way we can obtain

$$(Hv)_i^{n+1} = \frac{(Hv)_i^* - \theta g(Hv)_i^n (R_f)_i^n \Delta t^n}{1 + (1 - \theta) g(R_f)_i^* \Delta t^n}.$$

The parameter θ is the implicitness parameter. When $\theta = 0$ the friction source term is computed totally implicit and when $\theta = 1$ is computed in totally explicit manner. The above treatment can be incorporated in the Runge-Kutta time-stepping procedure in a straight forward manner. According to [123] and [122] the explicit discretization of the friction terms interferes with the CFL stability condition and an additional limit on the time step size for both first- and second- order approaches is required using a grid of a given mesh size otherwise stability can only be ensured by refining the grid. Both possibilities offer stability at a high computational cost especially near wet/dry fronts which are characterized by small values of water depth and friction term domination over the bed slope terms. On the other hand, the implicit discretization of the friction terms is not time dependent and as such it does not require further time step restrictions other than the CFL condition. However an implicit treatment has an effect on the order of convergence [51].

5.6 Time integration

In the previous sections we considered the spatial discretization procedures within the FV framework. In order to obtain a fully discrete scheme, we must discretize the time evolution operator. In the present work an explicit modified four stage Runge-Kutta (RK) scheme, due to its enhanced stability region, [98, 99], was implemented for integration over time for both the NCFV and CCVF approach. By denoting $\mathcal{L}(\mathbf{U})$ the discrete spatial operator the discretized form of equations (14) and (23) can be written as:

$$\frac{\partial \mathbf{U}_i}{\partial t} = \mathcal{L}(\mathbf{U}). \tag{5.35}$$

The RK scheme is described as follows:

$$\begin{aligned} \mathbf{U}_i^{(0)} &= \mathbf{U}_i^n; \\ \mathbf{U}_i^{(k)} &= \mathbf{U}_i^{(0)} + a_k \Delta t^n \mathcal{L}(\mathbf{U}_i^{(k-1)}), \text{ for } k = 1, \dots, 4; \\ \mathbf{U}_i^{n+1} &= \mathbf{U}_i^{(4)}, \end{aligned}$$

where $\Delta t^n = t^{n+1} - t^n$ is the time step. The optimal values (in the sense of the CFL condition) for a_k are the following, [98, 99]:

$$a_1 = 0.11, \quad a_2 = 0.26, \quad a_3 = 0.5 \quad \text{and} \quad a_4 = 1.0.$$

As it is stated in [98, 99], when we use the parameter $a_3 = 0.5$, it can be shown that the corresponding RK method is second-order accurate in time in both linear and non-linear cases. Also in the same references it was noted that, although the standard four stage RK scheme (which is fourth order accurate in time in the linear case) is well adapted to centered approximations, the best four stage RK scheme for upwind approximations, which allows large time steps, is only second order accurate in time. The above scheme reduces to Euler integration for $k = 1$ and $a_1 = 1$.

If R_P is the minimum distance from vertex P to ∂C_P , then the global time step Δt^n is estimated for the NCFV scheme by the CFL stability condition as

$$\Delta t^n = CFL \cdot \min_P \left(\frac{R_P}{\left(\sqrt{u^2 + v^2} + c \right)_P^n} \right). \quad (5.36)$$

Similar for the CCFV approach, if R_p is the minimum distance from the barycenter to the faces of the triangle T_p then Δt^n is estimated by the CFL stability condition as

$$\Delta t^n = CFL \cdot \min_P \left(\frac{R_p}{\left(\sqrt{u^2 + v^2} + c \right)_P^n} \right). \quad (5.37)$$

5.7 Comparison of CCFV and NCFV discretization for the NSW equations

In the work of Delis et al.[51] an extended comparison of a cell centered and a node centered unstructured finite volume discretization for the NSW equations is presented and discussed. In this section we will talk about it briefly in order to provide justification for our choice of approach, namely the NCFV one for the construction of the numerical

scheme for the extended 2D BT equations. Table ?? presents a summary of the schemes presented previously for the NSCFV and the different CCFV formulations for the NSWE. Three numerical tests are presented here in order to explore the performance of the

Table 5.2: Summary and description of the Finite Volume schemes

Scheme	Description
NCFV	Node-Centered FV Scheme
CCFVc1	Cell-Centered FV compact (naive) reconstruction stencil
CCFVc2	Cell-Centered FV compact reconstruction stencil (corrected)
CCFVw1	Cell-Centered FV wide (naive) reconstruction stencil
CCFVw2	Cell-Centered FV wide reconstruction stencil (corrected)

schemes. Additional numerical results can be found in [51]. Convergence studies for the numerical convergence rates, computed for problems with known analytical solution, for both formulations, are presented. For unstructured meshes, and in order to measure solution error, the volume weighted norm L_K of the error has to be used [?], defined as

$$\|U_i - U_i^{ex}\|_{L_K(\Omega)} = \left(\frac{\sum_{i=1}^N |\Omega_i| (U_i - U_i^{ex})^K}{\sum_{i=1}^N |\Omega_i|} \right)^{\frac{1}{K}},$$

where U_i^{ex} is the exact solution and U_i the numerical one, defined at node i for the NCFV scheme and at cell center of T_i for the CCFV scheme, of the conserved variables (H , Hu and Hv), while Ω_i is the corresponding volume and N is the number of the corresponding data points.

For steady state solutions (as well as for time dependent solutions converging to steady states) we consider the solution as being convergent when the norm of the water height (as well as for the u and v) drops to machine accuracy ($\approx 10^{-15}$), i.e.

$$\|\tau(h)\|_{L_1} \leq 10^{-15}. \quad (5.38)$$

The CFL value used in all the test cases that follow was set to 0.9 unless otherwise stated.

5.7.1 The traveling vortex solution

To verify the numerical order of accuracy (in terms of the flux discretization and limiting procedures) for both FV formulations and suppress the influence of other modifications introduced here for the topography, wet/dry front and boundary treatment, we present

a test case of a traveling vortex. Following from [137, 136] on a computational domain $\Omega = [0, 1] \times [0, 1]$ we simulate a vortex with center starting at $(x_c, y_c) = (0.5, 0.5)$ and moving from left to right with velocity $\mathbf{u} = [6, 0]^T$. Periodic boundary conditions are applied to the left and right and weak far field conditions at the top and bottom. The initial solution is given by

$$H(r_c, 0) = 10 + \begin{cases} \frac{1}{g} \left(\frac{1}{5}\omega\right)^2 (\phi(\omega r_c) - \phi(\pi)) & \text{if } \omega r_c \leq \pi \\ 0 & \text{else} \end{cases}$$

with

$$\phi(z) = 2 \cos(z) + 2z \sin(z) + \frac{1}{8} \cos(2z) + \frac{z}{4} \sin(2z) + \frac{3}{4} z^2$$

and velocity

$$\mathbf{u}_0 = \mathbf{u} + \begin{cases} 15(1 + \cos(\omega r_c))(y_c - y, x - x_c)^T & \text{if } \omega r_c \leq \pi \\ 0 & \text{else} \end{cases},$$

where r_c denotes the distance from the vortex core, $\omega = 4\pi$ the angular wave frequency and $g = 1$ the gravitational constant for this case.

In Fig. 5.11 the results of the NCFV scheme using the type-IV distorted grid (with $H_N^* = 0.0039\text{m}$) are presented, in terms of contour plots of the solution for depth H up to time $t = 1/6$, when the vortex is back to its initial position. Next we report grid convergence studies on all different grids, having been consistently refined, and for the five schemes considered in this work (see Table 3). In Fig. 5.12 convergence results in the L_2 norm for the NCFV scheme are presented. As it can be seen also in Table 4 in the Appendix, convergence results for H exhibit a higher than two asymptotic rate. The results show that we achieve the expected second order of accuracy in both the L_1 and L_2 norm, and more importantly an almost identical behavior for all grid types is exhibited for all conserved variables.

In Fig. 5.13 the corresponding convergence results for the CCFVc1 scheme are presented. A completely different behavior (compared to that of the NCFV scheme) is exhibited since second order accuracy was only achieved for equilateral (type-I) and orthogonal (type-III) grids. For the other two types of grids the asymptotic rate of convergence was reduced to one for the orthogonal (type-II) grid and slightly higher than one for the distorted (type-IV) grid. This behavior was expected as in type-I and type-III grids point D coincides with point M (see Fig. 5.9), and as such there is a consistency

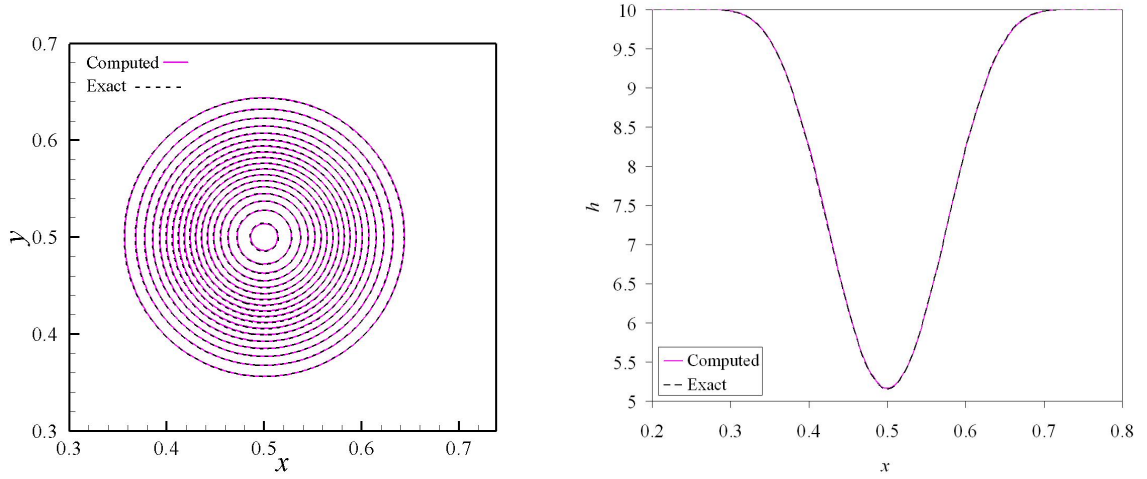


Figure 5.11: Traveling vortex: Contour plots for h (left) and at $y = 0$ (right), $t = 1/6$

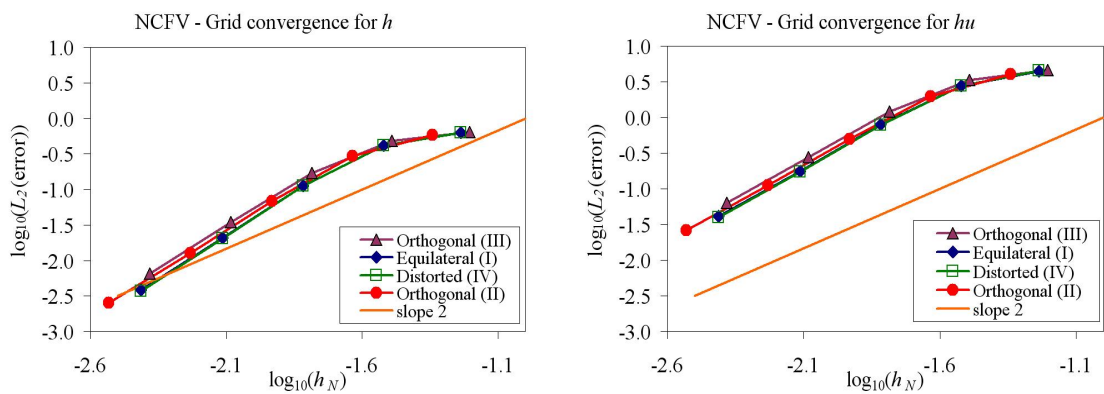


Figure 5.12: Traveling vortex: Convergence results for the NCFV scheme at $t = 1/6$

between the evaluation of the reconstructed values and the flux computation in each face of the triangular volumes. Contrary to this, for type-II and type-IV grids, there is a difference between points D and M , larger and constant for most faces in type-II grids, smaller and variable between different cells in type-IV, resulting in the different convergence behaviors obtained.

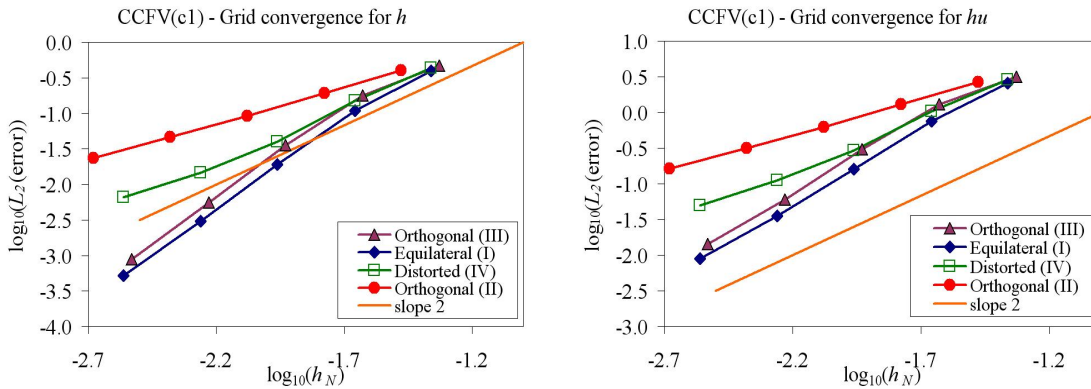


Figure 5.13: Traveling vortex: Convergence results for the CCFVc1 scheme at $t = 1/6$

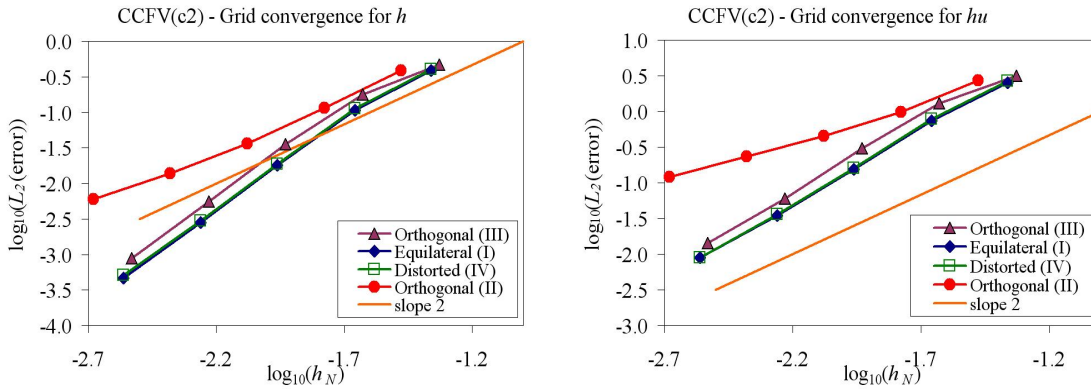


Figure 5.14: Traveling vortex: Convergence results for the CCFVc2 scheme at $t = 1/6$

Next and in Fig. 5.14, the corresponding convergence results for the CCFVc2 scheme are presented. The application of the proposed correction term for the compact gradient computation scheme managed to considerably improve the convergence results for the distorted (type-IV) grids, while only slight improvements are evident for orthogonal (type-II) grids. The reason for that lies in the larger distance between D and M for the type-II grids (see Fig. 5.9) and is also attributed to the fact that point M lies outside the gradient volume (Fig. 5.10).

In Fig. 5.15 the corresponding convergence results for the CCFVw1 scheme are presented which are shown to exhibit an almost identical behavior with the results of the

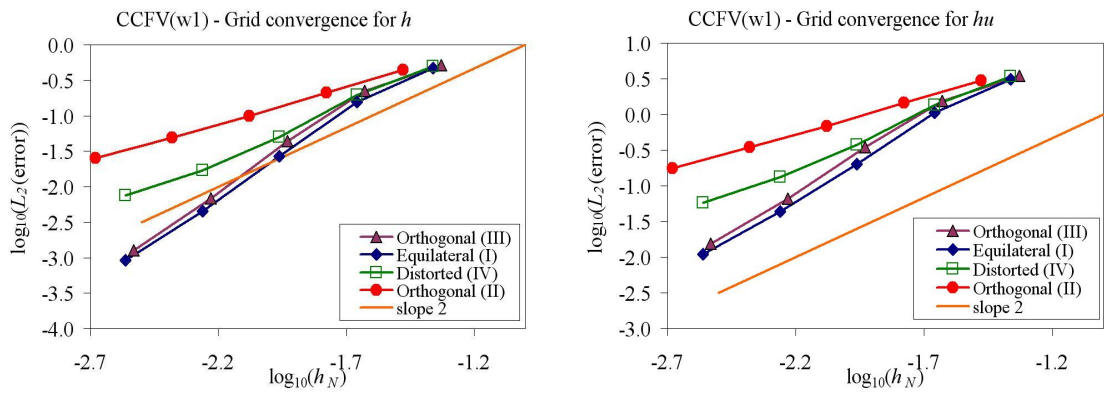


Figure 5.15: Traveling vortex: Convergence results for the CCFVw1 scheme at $t = 1/6$

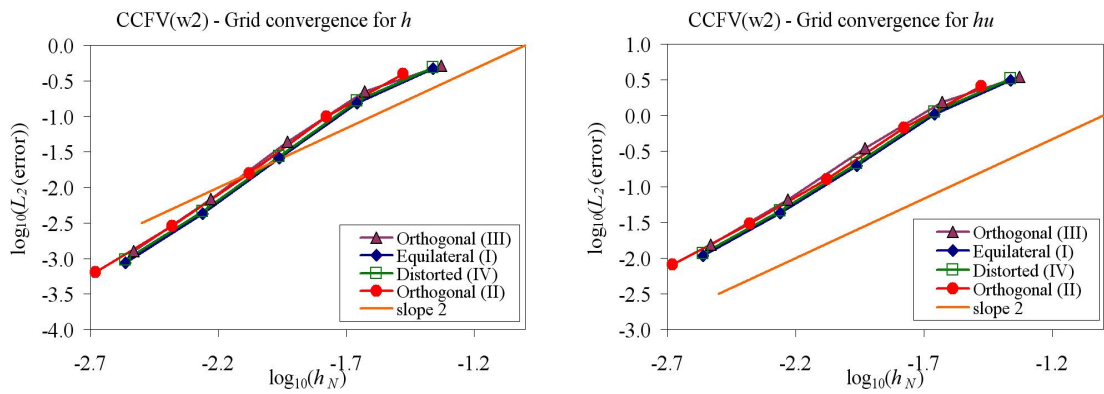


Figure 5.16: Traveling vortex: Convergence results for the CCFVw2 scheme at $t = 1/6$

CCFVc1 scheme (Fig. 5.13). The application of the proposed correction for this scheme (with the wide stencil gradient computation) resulted in a dramatic improvement of the results, as it can be observed in Fig. 5.16 for the CCFVw2 scheme results. Now we achieve the expected second order of accuracy in both norms, and more importantly almost identical behavior for all grid types, similar to the results obtained from the NCFV scheme. In addition the accuracy of the numerical solution has been greatly improved in all types of grids compared to that for the CCFVw1 scheme. This shows that the proposed correction for the calculation of the reconstructed values is more effectively combined with the wide stencil of gradient calculation, since this term (in Eq. (5.23) and (5.24)) is unlimited.

Finally, comparative convergence results for h (in the L_1 norm) are presented in Fig. 5.17, for all schemes, and for each grid used. For type-I and type-III grids, the convergence rates are almost identical, as expected, regardless of the scheme used, since for the CCFV schemes locations D and M now coincide. It is worth noting that the CCFV schemes provide better numerical accuracy than the NCFV one on equivalent grids for this test case. For the other two grid types the results summarize the observations made above, concerning the effects of the proposed correction for the face reconstructed values for the CCFV formulation.

5.7.2 Thacker's planar solution

Few analytical solutions are available for the 2D NSW with free moving boundary, involving run-up and run-down phenomena (wetting-drying-wetting). The 2D analytical solution of the NSW compared here is due to Thacker [158]. Thacker's solutions have been used by a number of researchers in order to evaluate their numerical models, we refer for example in [86, 108, 70, 40, 118, 35, 136, 6, 31, 117, 137, 125]. The test cases chosen here are considered in some of the above mentioned references as being perhaps the most difficult for a numerical model. One major difficulty is the correct determination of the wet region with acceptable accuracy. The motion is oscillatory with a small enough amplitude limit, imposed by the long wave assumption, and since bottom frictions are not included in the model there is no energy dissipation. The flow takes place inside a parabola of revolution, defining as such the bottom topography, on

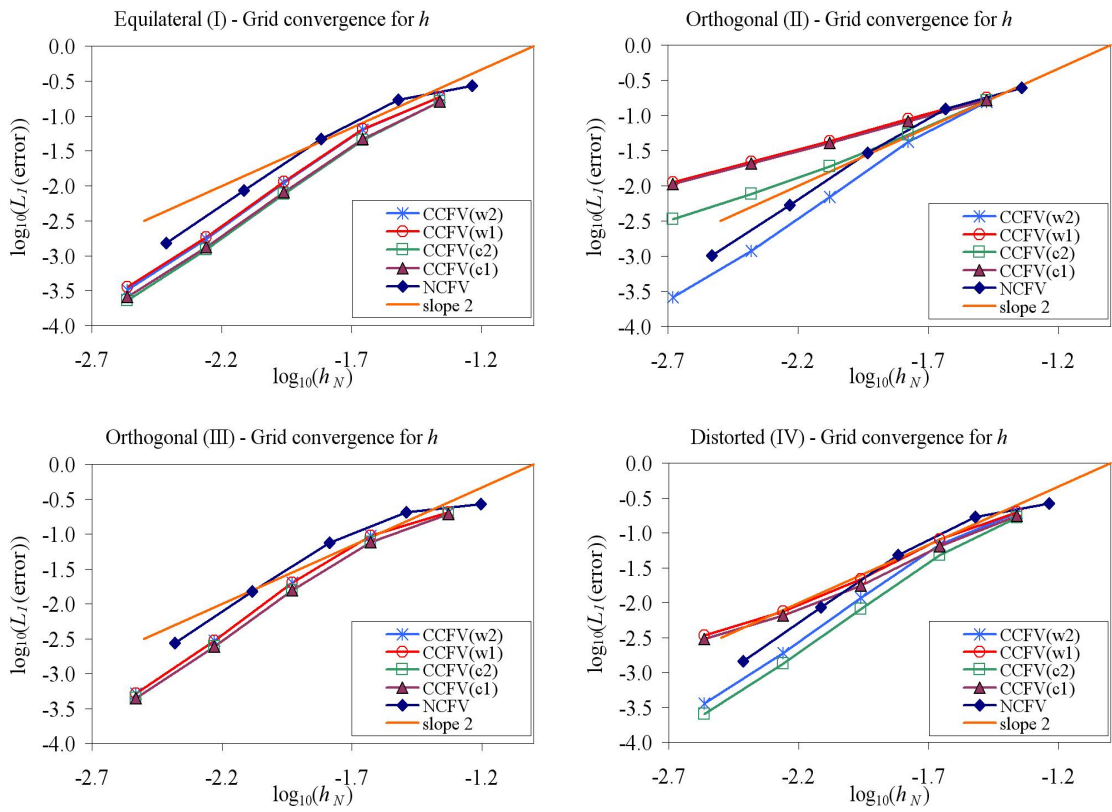


Figure 5.17: Traveling vortex: Convergence comparisons for h in all grids for all schemes

a computational $\Omega = [-2, 2] \times [-2, 2]$ domain as

$$B(x, y) = B(r_c) = 1 - h_0 \left(1 - \frac{r^2}{a^2}\right),$$

where $r = \sqrt{x^2 + y^2}$, h_0 is the water depth at the center point for a zero elevation and a is the distance from the center point to the zero elevation of the shoreline.

In this case elevation profile leads to an exact solution of the form

$$\begin{aligned} h(x, y, t) &= 1 + \frac{\eta h_0}{a^2} (2x \cos(\omega t) + 2y \sin(\omega t) - \eta), \\ \mathbf{u} &= [-\eta \omega \sin(\omega t), \eta \omega \cos(\omega t)]^T \end{aligned}$$

where $\omega = \sqrt{2gh_0}/a$. The free parameters chosen here are $a = 1$, $\eta = 0.5m$ and $h_0 = 0.1m$, while the exact solution evaluated at $t = 0$ is used as initial condition for the free surface elevation and velocity field. The solution is periodic with a period $T = 2\pi/\omega$. The exact solution, though relatively simple, represents a severe test case for most 2D methods [86, 40, 117] and it is not driven by external boundary conditions.

First and in Fig. 5.18, a 3D view of the numerical solution along with a contour comparison with the exact solution for h at $t = 4T$ is presented. These results have been obtained using the CCFVw2 scheme on a distorted type-IV grid with $h_N = 0.0219m$. Qualitative very similar results were obtained for the other two schemes and grids used. No visible distortions can be observed in the numerical solution which remains almost perfectly circular during the complete 4 periods and almost indistinguishable from the exact solution.

Next, in Fig. 5.19 we compare the numerical results and the analytical solutions at $t = 4T$ for the shoreline, the velocity field and the velocities along $y = 0$, for the three schemes on the same distorted grid. The moving shoreline is accurately computed with no signs of spurious oscillations and the planar form of the free surface maintained throughout the computation. As it is mentioned in several works, see for example [86, 70, 40, 117], to obtain accurate approximations of the velocity field is a much more difficult issue. As it can be observed, for the u velocity, only small discrepancies are present, close to the wet/dry front interface and where the water depth is vanishing. Despite this difficulty, the position of the wet/dry fronts have been accurately captured and more importantly this perturbation is not amplified for long time simulations and doesn't seem to disturb the accuracy of the moving shoreline predictions. The results

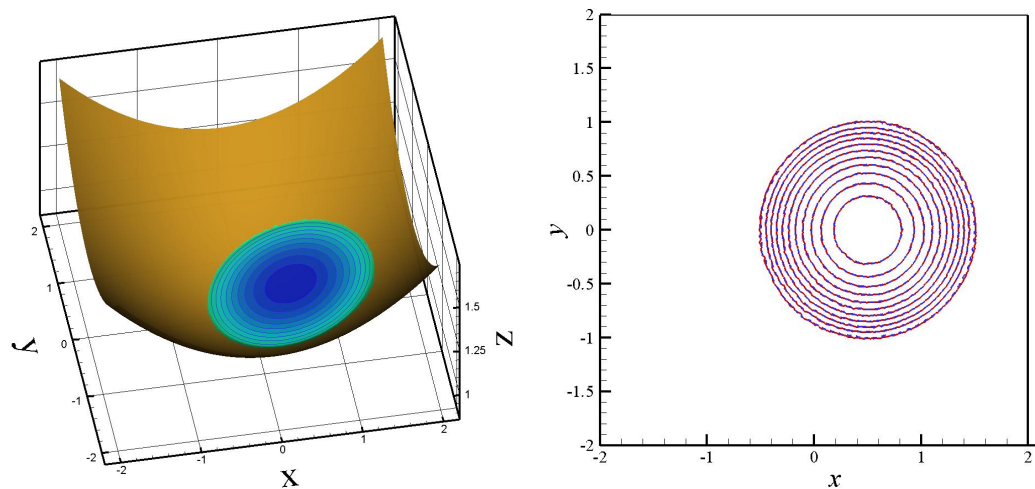


Figure 5.18: Thacker's Planar: Numerical results for the CCFVw2 scheme using the distorted type-IV grid for time $t = 4T$, 3D view (left) and contour plots for h between the analytical (dashed line) and numerical solution

presented appear more accurate than those in [86, 117] and compare in favor with those presented in [70?] where a similar grid resolution was applied.

To study the effect of the grid resolution on the scheme's performance we present the same results obtained with the finer distorted grid in Fig. 5.20. The improvement in accuracy for the shoreline and velocities is evident. More importantly, this improvement is more pronounced for the NCFV scheme compared to the CCFV ones, where the discrepancies are of the same magnitude to the coarse mesh. We note here that, the results for the NCFV scheme were obtained with half the degrees of freedom compared to the CCFV ones, for both grid resolutions.

In Fig. 5.21 comparative convergence results for h (in the L_1 norm) for all schemes and for grid type-IV, are presented. All three schemes exhibit very similar asymptotic behavior for this test problem with the two CCFV schemes show almost identical behavior and achieve a slightly better accuracy compared to the NCFV one. For a more extensive comparison, including convergence results, between all schemes and for each grid used, please refer to [51].

5.7.3 A 2D potential solution with topography

To test convergence in the presence of the topography source term and as such the well-balanced discretization as well as the proposed boundary treatment, we consider here a

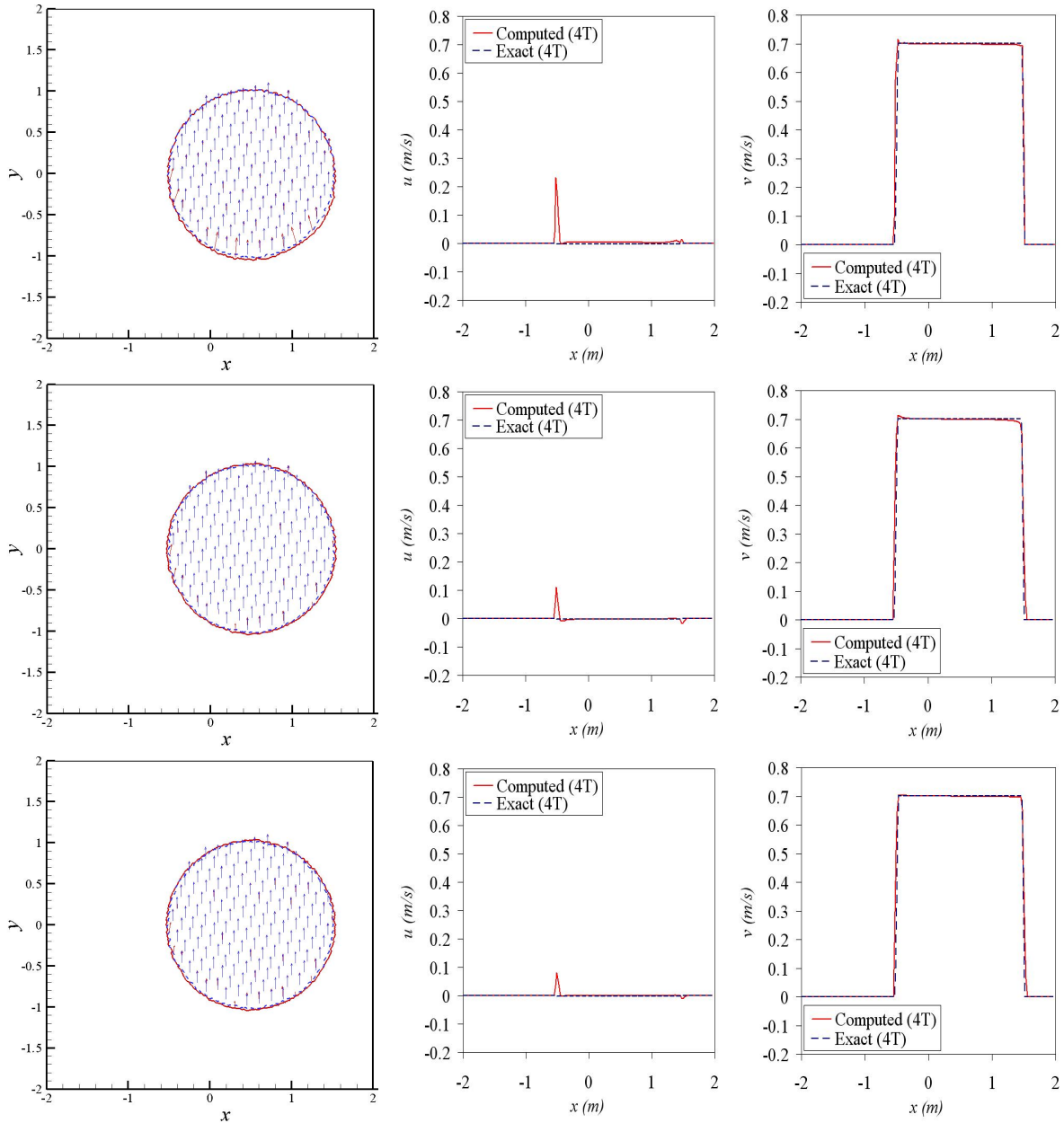


Figure 5.19: Thacker’s Planar: Shoreline and velocities at $t = 4T$ on the type-IV grid ($h_N^* = 0.0308$) for the NCFV scheme (top), the CCFVc2 (middle) and the CCFVw2 scheme (bottom) with $h_N = 0.0219$

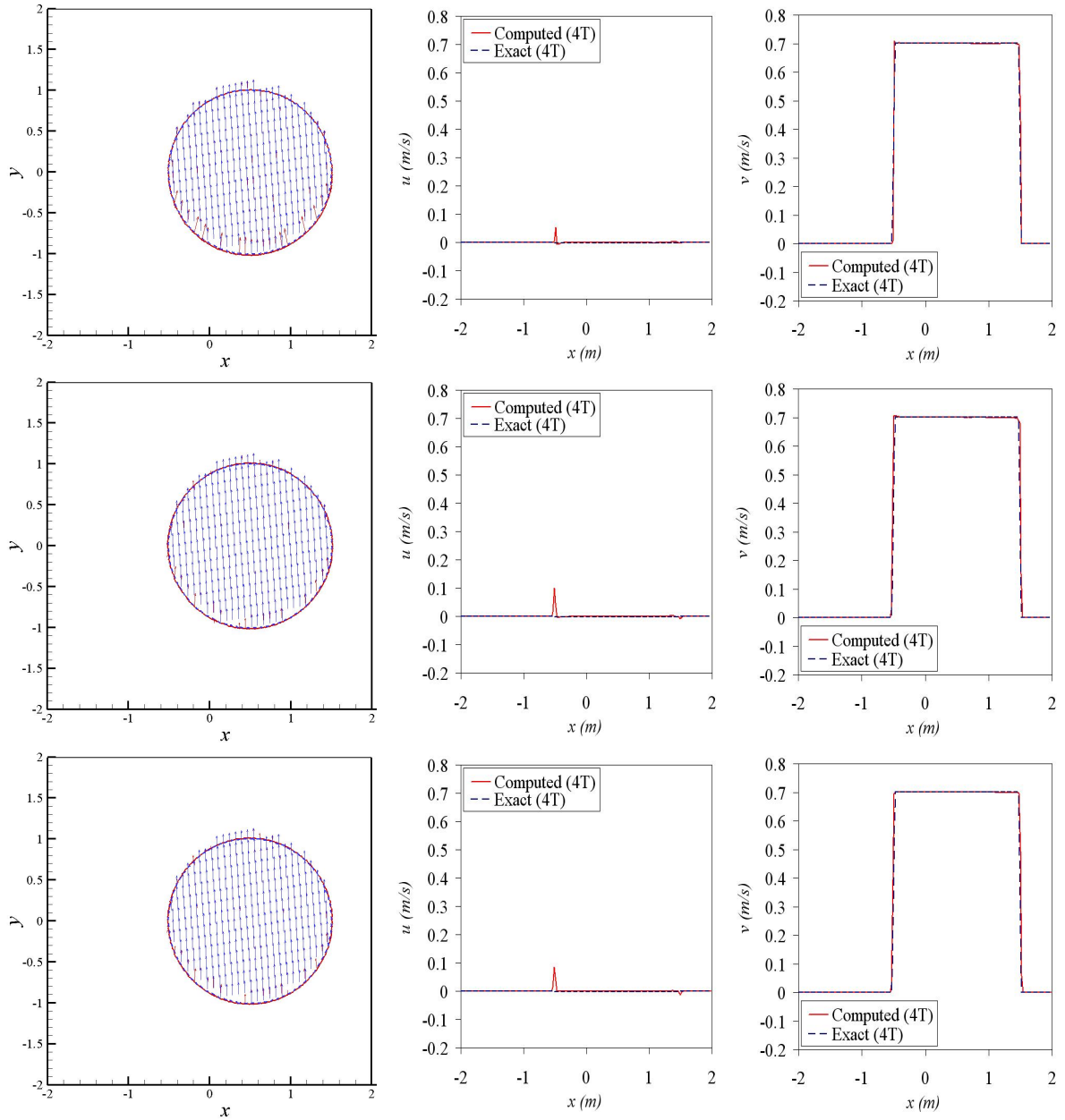


Figure 5.20: Thacker's Planar: Shoreline and velocities at $t = 4T$ on the type-IV grid ($h_N^* = 0.0154$) for the NCVF scheme (top), the CCFVc2 (middle) and the CCFVw2 scheme (bottom) with $h_N = 0.0110$

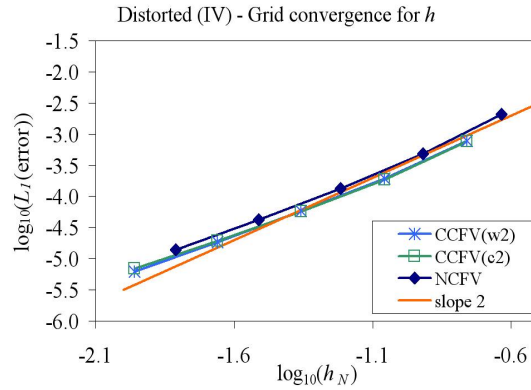


Figure 5.21: Thacker's Planar: Convergence comparisons for h in grid type-IV.

particular member of the family of 2D exact solutions presented in [135] which satisfies the frictionless steady state equations (10) and (11). On a domain $\Omega = [-1, 1] \times [-1, 1]$ we consider a solution for the water depth in which the velocity field is divergence-free, and obtained from the harmonic function $\psi = xy$ as

$$\mathbf{u} = \left[\frac{\partial \psi}{\partial y}, -\frac{\partial \psi}{\partial x} \right]^T.$$

The water depth is taken as $H = \psi + \alpha$, while the bed height is computed as

$$B(x, y) = g^{-1} \left(30 - \frac{\|\nabla \psi\|^2}{2} \right) - \psi - \alpha.$$

We take $\alpha = 1.5$ and the gravity acceleration $g = 10$ for this case. In addition, the bottom and top boundaries are sub-critical inlets, while the left and right boundaries are sub-critical outlets since the Froude number never exceeds one in the domain. Starting the computations from the exact solution we march towards steady-state.

Fig. 5.22 presents the iterative convergence histories for the water height residual obtained with the NCFV and the CCFVw2 schemes and on the Distorted grid. Similar results were obtained for u and v . The solution converged to machine accuracy for all different refinements. The NCFV shows a fastest convergence (less iterations) in each refinement, compared to the CCFVw2 scheme. Additionally, looking on the convergence behavior, the largest differences between the different type of grids in the CCFVw2 scheme, is due to the geometrical properties of the boundary cells and the application of the compact gradient stencil on them. For the NCFV formulation the results verify the second order accuracy of the scheme including the topography source term discretization and boundary conditions implementation.

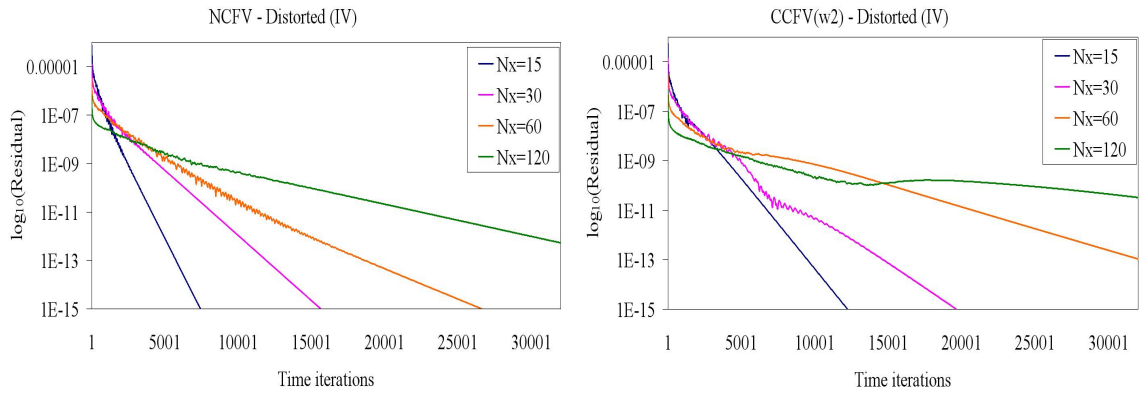


Figure 5.22: 2D potential solution: h residual convergence for the NCFV and the CCFVw2 schemes

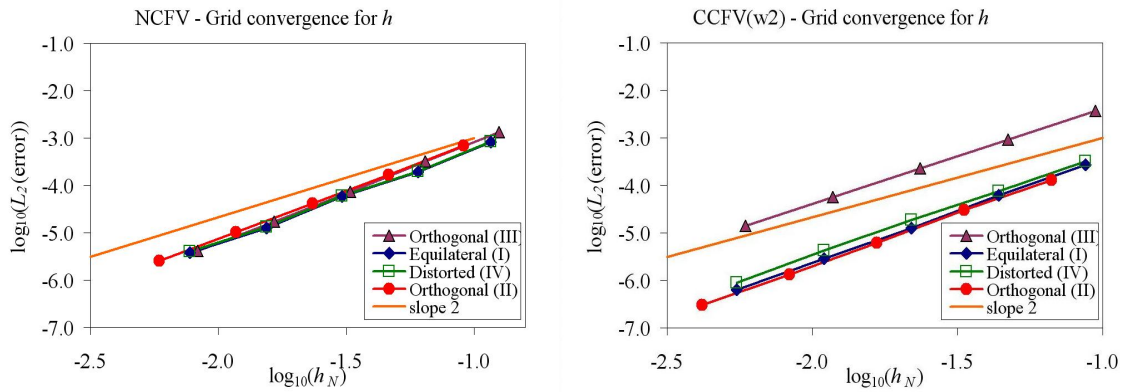


Figure 5.23: 2D potential solution: Convergence results for the NCFV and the CCFVw2 schemes

5.7.4 Discussion

In Section 5.7 an extended comparison of the CCFV and NCFV discretizations for the NSW was presented. More precisely, a NCFV of the median dual type and two CCFV formulations have been considered in order to compare them and study their relative performance, robustness and effectiveness, within a controlled environment for a fair and extensive comparison. Both FV schemes used the same approaches for the well-balancing and the accurate treatment of wet/dry fronts, customized in each formulation. From the above comparison some major conclusions can be drawn.

1. In terms of the convergence behavior to second order, the NCFV scheme exhibited consistently identical behavior on all grid types, for all conserved variables and in different norms used, for all the test problems considered. This is probably due to the way that the control volume (in the dual mesh) is constructed, which is more uniform for the different types of grids than those in the CCFV approach (where the control volumes are the primal mesh triangles themselves). To this end, the NCFV scheme is not affected by the grid geometry and as such any grid type can be adequate for implementing and studying such a scheme.
2. The edge based limiting procedure which was implemented in the MUSCL reconstruction was proved inadequate for the CCFV schemes since the center of the face where numerical fluxes are evaluated does not coincide in general with the location to which reconstructed values are computed, leading to an order reduction. On the other side it was proved very effective for the NCFV formulation.
3. The proposed correction when applied to CCFV schemes greatly improves the convergence behavior and the order reduction. When applied to the wider stencil (CCFVw2) an almost identical behavior with the NCFV scheme is achieved, but we must always keep in mind the extra computational cost introduced.
4. NCFV has the advantage of not using ghost cells for the boundary treatment in addition to CCFV formulations where the effect of the grid's geometrical characteristics at the boundaries can lead to an order reduction.
5. Wet/dry treatment is accurate for both FV approaches, accurately predicted moving shorelines and remained stable and non-oscillatory for long simulation times on all grid types.

For the above reasons the NCFV scheme for the NSW equations has been chosen in order to be extended as to include dispersion characteristics for deeper water simulations.

Chapter 6

An unstructured FV scheme for BT equations

Until now and in 2D we have assumed that the dispersion terms of the equations of Nwogu (2.48), (2.89) and MS (2.48), (2.49) were zero. In this case both equations degenerate to the NSWE which described and discretized in the previous sections of this chapter. After the discretization and the comparison of the two one dimensional Boussinesq-type equations and the NSWE in Chapter 3, it was revealed that although the NSWE can be sufficient in some cases to predict maximum runup values and the general characteristics of propagating waves, the two BT numerical models provided considerable more accurate results for highly dispersive waves over increasing water depths, with Nwogu's model having a precedence over the MS one. For that reason Nwogu's model has been chosen in order to be discretized in two dimensions under an unstructured FV framework and a novel approach is presented in Sections 6.1-6.6. A new methodology is presented in Section 6.7 to handle wave breaking over complex bathymetries using the proposed model of Nwogu.

Following the same procedure as in Section 5.2, we integrate the BT equations of Nwogu (2.89), written in a conservation like form, over the computational domain. After integration of the equations over each computational cell, C_P , and application of Gauss

divergence theorem to the flux integral the equations reads as:

$$\begin{aligned} \frac{\partial \mathbf{U}_P}{\partial t} &= -\frac{1}{|C_P|} \oint_{\partial \Gamma_P} (\mathbf{F}\tilde{n}_x + \mathbf{G}\tilde{n}_y) d\Gamma + \frac{1}{|C_P|} \iint_{C_P} \mathcal{L} d\Omega \Rightarrow \\ \frac{\partial \mathbf{U}_P}{\partial t} &= -\frac{1}{|C_P|} \oint_{\partial \Gamma_P} (\mathbf{F}\tilde{n}_x + \mathbf{G}\tilde{n}_y) d\Gamma + \frac{1}{|C_P|} \iint_{C_P} \mathbf{S}_b dx dy + \frac{1}{|C_P|} \iint_{C_P} \mathbf{S}_f dx dy \\ &+ \frac{1}{|C_P|} \iint_{C_P} \mathbf{S}_d dx dy. \end{aligned} \quad (6.1)$$

In the above equation, the advection terms (the first integral at the right handside) and the source terms due to the topography \mathbf{S}_b are discretized in the same way as the one described in Chapter 5. The approximate Riemann solver of Roe [139] is used for the advective fluxes (see Section 5.2.1) along with a well balanced topography source term upwinding (see Section 5.3) and accurate numerical treatment of wet/dry fronts. Higher-order spatial accuracy is achieved through a MUSCL-type reconstruction technique.

6.1 Higher-order reconstruction

In Section 5.2 a second-order scheme for the NCFV formulation was described. The MUSCL methodology of van Leer [173] can be extended to node-centered unstructured formulations in order to reach higher order spatial accuracy. As described in Section 5.2, this extension relies on the evaluation of the fluxes with extrapolated U_{PQ}^{*R} and U_{PQ}^{*L} at the midpoint M of the edge PQ . So for each component w_i of the primitive variables $\mathbf{W} = [H, u, v]$ (5.10) and (5.9) hold where the extrapolation gradients $(\nabla w)^{L,R}$ are obtained using a combination of centered and upwind gradients in order to increase the accuracy of the basic MUSCL reconstruction. Following [7, 51, 149] and using (5.11) we define

$$(\nabla w_i)_P^u = 2(\nabla w_i)_P - (\nabla w_i)^{cent}, \quad (6.2)$$

$$(\nabla w_i)_Q^u = 2(\nabla w_i)_Q - (\nabla w_i)^{cent}, \quad (6.3)$$

as the upwind gradients at nodes P and Q respectively, with $(\nabla w_i)_P$ and $(\nabla w_i)_Q$ the average of the gradients on the computational cell C_P and C_Q . Then the extrapolation

gradients $(\nabla w)^{L,R}$ can be obtained [7] as

$$(\nabla w_i)^L = (1 - \beta)(\nabla w_i)^{cent} \cdot \mathbf{r}_{PQ} + \beta(\nabla w_i)_P^u \cdot \mathbf{r}_{PQ}, \quad (6.4)$$

$$(\nabla w_i)^R = (1 - \beta)(\nabla w_i)^{cent} \cdot \mathbf{r}_{PQ} + \beta(\nabla w_i)_Q^u \cdot \mathbf{r}_{PQ}, \quad (6.5)$$

which for $\beta = 1/3$ leads to a third-order accurate reconstruction for linear problems. Nevertheless, this reconstruction reduces the numerical dissipation introduced in the nonlinear flux computations and, as it would become clear from the numerical results, produces accurate solutions for smooth flow conditions. However, in cases where the contribution of the dispersive terms is negligible e.g. when only NSW part of the model has to be solved, the reconstruction presented above can create extrema particularly in the presence of shocks in the solution since monotonicity is not preserved. In this situations and to reduce the oscillations in the solution, a slope limiting procedure has to be used. To prevent such oscillations from developing in the numerical solution strict monotonicity in the reconstruction is enforced by using Van Albada-Van Leer edge-based nonlinear slope limiter [7, 51, 172, 176, 75] resulting in reconstructed values:

$$w_{i,PQ}^L = w_{i,P} + \frac{1}{2} \Phi((\nabla w_i)_P^u \cdot \mathbf{r}_{PQ}, (\nabla w_i)^{cent} \cdot \mathbf{r}_{PQ}) (\nabla w_i)^L \cdot \mathbf{r}_{PQ}, \quad (6.6)$$

$$w_{i,PQ}^R = w_{i,Q} + \frac{1}{2} \Phi((\nabla w_i)_Q^u \cdot \mathbf{r}_{PQ}, (\nabla w_i)^{cent} \cdot \mathbf{r}_{PQ}) (\nabla w_i)^R \cdot \mathbf{r}_{PQ}, \quad (6.7)$$

where the Φ is the nonlinear limiter function defined as

$$\Phi(a, b) = \frac{ab + |ab| + e}{a^2 + b^2 + e} \quad (6.8)$$

where $0 < e \ll 1$, used to prevent division by zero ($e = 10^{-16}$ in our implementation) and prevents the activation of the limiter in smooth flow regions [176]. Limiter (6.6) has been constructed as to restore higher order accuracy in all norms. In addition, the above limiter is differentiable for linearly varying flow variables. Continuous differentiability helps in achieving smooth transitions between discontinuous jumps with first-order representation and sharp but continuous gradients, which require higher-order consistency.

Again, the same reconstruction procedures are used to compute the bed elevation $b(\mathbf{x})$, at either side of a cell's face, which are needed for the discretization of the bed slope source term, as it will become clear in later sections.

Remark 8 Using physical variables, i.e. $\mathbf{W} = [H, u, v]$, for the presented reconstruction, is cheapest since fewer transformations are necessary and the gradients that have to be computed for the reconstruction can be re-used to compute dispersive terms later on. Furthermore in [14] an extensive study was presented comparing conservative and physical variable reconstructions, for 2D unstructured FV schemes solving the NSW equations. concluding that physical variable reconstructions is advantageous in some cases.

6.2 Divergence edge-based formula

For the the discretization of the dispersive terms \mathbf{S}_d in 2.89, the gradient $(\nabla w)_P$ and the divergence of the velocity vector $(\nabla \cdot \mathbf{u})_P$, have to be computed in each mesh node. For the gradient computation the edge formula, described in Section 5.2.1 is used. In this section we present an edge formula for the integral average divergence of the velocity vector, over the region Ω_P , (see Fig. 5.4) . Again, following from the divergence theorem, approximating the line integrals by trapezoidal quadrature and rearranging we get,

$$\int_{\Omega_P} \nabla \cdot \mathbf{u} d\Omega = \oint_{\partial\Omega_P} \mathbf{u} \cdot \tilde{\mathbf{n}} dl = \sum_{Q \in K_P} \frac{3}{2} (\mathbf{u}_P + \mathbf{u}_Q) \cdot \mathbf{n}_{PQ}.$$

Thus, the integral average of the divergence at a cell node is given by

$$(\nabla \cdot \mathbf{u})_P = \frac{3}{|\Omega_P|} \sum_{Q \in K_P} \frac{1}{2} (\mathbf{u}_P + \mathbf{u}_Q) \cdot \mathbf{n}_{PQ} = \frac{1}{|C_P|} \sum_{Q \in K_P} \frac{1}{2} (\mathbf{u}_P + \mathbf{u}_Q) \cdot \mathbf{n}_{PQ}, \quad (6.9)$$

since of $|C_P| = \frac{1}{3}|\Omega_P|$ in the median-dual formulation. In the case that P is a boundary node, and referring again on Fig. 5.4, the integral average of the divergence is computed as

$$(\nabla \cdot \mathbf{u})_P = \frac{1}{|C_P|} \left\{ \sum_{Q \in K_P} \frac{1}{2} (\mathbf{u}_P + \mathbf{u}_Q) \cdot \mathbf{n}_{PQ} + \mathbf{u}_P \cdot (\mathbf{n}_{P,1} + \mathbf{n}_{P,2}) \right\}. \quad (6.10)$$

6.3 Discretization of the dispersion terms

The mass equation in (6.1) contains the integral average of the dispersive term ψ_C in the source term \mathbf{S}_d . To produce the discrete average, that approximates this term, we

use the divergence theorem, which leads to

$$\begin{aligned}
(\psi_c)_P &= \frac{1}{|C_P|} \iint_{C_P} \psi_c d\Omega = \frac{1}{|C_P|} \iint_{C_P} \nabla \cdot \left[\left(\frac{z_a^2}{2} - \frac{h^2}{6} \right) h \nabla(\nabla \cdot \mathbf{u}) + \left(z_a + \frac{h}{2} \right) h \nabla(\nabla \cdot h\mathbf{u}) \right] \\
&= \frac{1}{|C_P|} \oint_{\partial C_P} \left[\left(\frac{z_a^2}{2} - \frac{h^2}{6} \right) h \nabla(\nabla \cdot \mathbf{u}) + \left(z_a + \frac{h}{2} \right) h \nabla(\nabla \cdot h\mathbf{u}) \right] \cdot \tilde{\mathbf{n}} dl \\
&= \frac{1}{|C_P|} \sum_{Q \in K_P} \left\{ \int_{\partial C_{PQ}} \left[\left(\frac{z_a^2}{2} - \frac{h^2}{6} \right) h \nabla(\nabla \cdot \mathbf{u}) \right] \cdot \tilde{\mathbf{n}} dl + \int_{\partial C_{PQ}} \left[\left(z_a + \frac{h}{2} \right) h \nabla(\nabla \cdot h\mathbf{u}) \right] \cdot \tilde{\mathbf{n}} dl \right\}
\end{aligned}$$

As for the nonlinear flux vector Φ_{PQ} , and for all edges, the above integrals should be computed and added to the computational cells C_P . Like before, we assume a uniform distribution of the integrated quantities over ∂C_{PQ} equal to their values at the midpoint M of the edge PQ thus,

$$\int_{\partial C_{PQ}} \left(\frac{z_a^2}{2} - \frac{h^2}{6} \right) h \nabla(\nabla \cdot \mathbf{u}) \cdot \tilde{\mathbf{n}} dl \approx \left[\left(\frac{z_a^2}{2} - \frac{h^2}{6} \right) h \right]_M [\nabla(\nabla \cdot \mathbf{u}) \cdot \mathbf{n}_{PQ}]_M, \quad (6.11)$$

$$\int_{\partial C_{PQ}} \left(z_a + \frac{h}{2} \right) h \nabla(\nabla \cdot h\mathbf{u}) \cdot \tilde{\mathbf{n}} dl \approx \left[\left(z_a + \frac{h}{2} \right) h \right]_M [\nabla(\nabla \cdot h\mathbf{u}) \cdot \mathbf{n}_{PQ}]_M. \quad (6.12)$$

The right hand side terms in (6.11) and (6.12) require the evaluation of the gradient of the divergence of the velocity vector and $h\mathbf{u}$ along the edge midpoints M . Hence, the evaluation of the gradient of a quantity w at M requires the definition of a new computational cell constructed by the union of the two triangles which share edge PQ (see Fig. 6.1). By denoting with

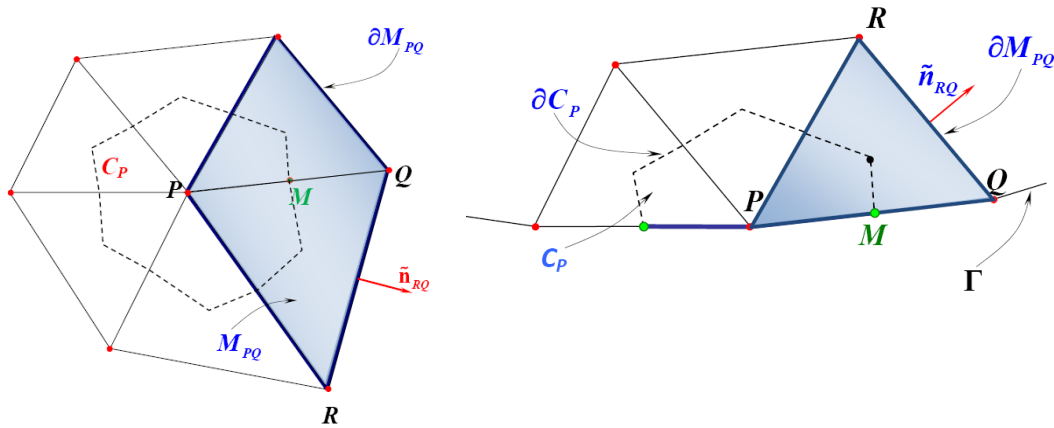


Figure 6.1: Computational cells for the gradient of the divergence: internal cell (left) and boundary cell (right)

$$K_{PQ} := \{R \in \mathbb{N} \mid R \text{ is a vertex of } M_{PQ} \text{ and } RQ \in \partial M_{PQ}\},$$

the Green-Gauss reconstruction gives

$$\iint_{M_{PQ}} \nabla w d\Omega = \oint_{\partial M_{PQ}} w \tilde{\mathbf{n}}_{RQ} dl = \sum_{\substack{R, Q \in K_{PQ} \\ R \neq Q}} \frac{1}{2} (w_R + w_Q) \mathbf{n}_{RQ}$$

that leads to

$$(\nabla w)_M = \frac{1}{|M_{PQ}|} \sum_{\substack{R, Q \in K_{PQ} \\ R \neq Q}} \frac{1}{2} (w_R + w_Q) \mathbf{n}_{RQ}, \quad (6.13)$$

with \mathbf{n}_{RQ} the vector normal to the edge RQ . In case of a boundary node cell M_{PQ} is reduced to the triangle PQR (see Fig. 6.1) and the computed value from (6.13) is assigned to M . Next, it is obvious that, to calculate $[\nabla(\nabla \cdot \mathbf{u})]_M$ and $[\nabla(\nabla \cdot h\mathbf{u})]_M$ in (6.11) and (6.12), formula (6.13) can be applied with the integral averages of the divergence $(\nabla \cdot \mathbf{u})_R$ and $(\nabla \cdot h\mathbf{u})_R$ at nodes $R \in K_{PQ}$ computed using (6.9).

Next, for the the dispersive source terms in the momentum equations we have

$$\frac{1}{|C_P|} \iint_{C_P} -\mathbf{u}\psi_c + \psi_M d\Omega = -\mathbf{u}_P \iint_{C_P} \psi_c d\Omega + \frac{1}{|C_P|} \iint_{C_P} \psi_M d\Omega.$$

The first term of the right hand side of the equation is discretized as before and the second term takes the discrete form:

$$\begin{aligned} (\psi_M)_P &= \frac{1}{|C_P|} \iint_{C_P} \psi_M d\Omega = \frac{1}{|C_P|} \iint_{C_P} H_t \frac{z_a^2}{2} \nabla(\nabla \cdot \mathbf{u}) + H_t z_a \nabla(\nabla \cdot h\mathbf{u}) d\Omega \\ &= \frac{1}{|C_P|} \iint_{C_P} H_t \frac{z_a^2}{2} \nabla(\nabla \cdot \mathbf{u}) d\Omega + \frac{1}{|C_P|} \iint_{C_P} H_t z_a \nabla(\nabla \cdot h\mathbf{u}) d\Omega \\ &\approx \left[H_t \frac{z_a^2}{2} \right]_P |C_P| [\nabla(\nabla \cdot \mathbf{u})]_P + [H_t z_a]_P |C_P| [\nabla(\nabla \cdot h\mathbf{u})]_P, \end{aligned}$$

where the divergence $(\nabla \cdot \mathbf{u})_P$ and $(\nabla \cdot h\mathbf{u})_P$ are computed again using formula (6.9).

6.4 Time integration and velocity field recovery

Since a higher-order spatial scheme is used, the necessity of at least a third-order scheme in time is crucial in order to be compatible with the third-order spatial scheme. For that reason we use the third order explicit Strong Stability-Preserving Runge-Kutta (SSP-RK) method was adopted [77, 153]. This SSP-RK method is commonly called the third order TVD Runge-Kutta scheme. Having defined $\mathcal{L}(\mathbf{U})$ the discrete spatial

operator (see Section 5.4) the third-order SSP-RK method is described as follows:

$$\begin{aligned}\mathbf{U}_P^{(1)} &= \mathbf{U}_P^{(n)} + \Delta t^n \mathcal{L}(\mathbf{U}^{(n)}); \\ \mathbf{U}_P^{(2)} &= \frac{3}{4}\mathbf{U}_P^{(n)} + \frac{3}{4}\mathbf{U}_P^{(1)} + \Delta t^n \frac{1}{4}\mathcal{L}(\mathbf{U}^{(1)}); \\ \mathbf{U}_P^{(n+1)} &= \frac{1}{3}\mathbf{U}_P^{(n)} + \frac{2}{3}\mathbf{U}_P^{(2)} + \Delta t^n \frac{2}{3}\mathcal{L}(\mathbf{U}^{(2)}); \end{aligned}$$

where $\Delta t^n = t^{n+1} - t^n$ is the time step and it is estimated using the CFL stability condition (5.36).

After each RK step a linear system $\mathbf{M}\mathbf{V} = \mathbf{C}$, with $\mathbf{M} \in \mathbb{R}^{2N \times 2N}$, $\mathbf{V} = [\mathbf{u}_1, \mathbf{u}_2, \dots, \mathbf{u}_N]$ and $\mathbf{C} = [\mathbf{P}_1^*, \mathbf{P}_2^*, \dots, \mathbf{P}_N^*]$, has to be solved to obtain the velocities u, v from $\mathbf{P}^* = [P_1^* \ P_2^*]^T$, the vector of variables from the momentum equation obtained from the FV solver. Matrix \mathbf{M} is constructed from the discretization of \mathbf{P}^* and is a grid depended sparse matrix without a standard structure. Keeping in mind that \mathbf{u} is our unknown vector, each two lines of the matrix correspond to a node P on the grid and for each such node we have,

$$H_P^{(i)} \left[\frac{z_a^2}{2} \nabla(\nabla \cdot \mathbf{u}) + z_a \nabla(\nabla \cdot h\mathbf{u}) + \mathbf{u} \right]_P^{(i)} = \mathbf{P}_P^{*(i)}, \quad i = 1, 2, n+1. \quad (6.14)$$

Now, the gradients $\nabla(\nabla \cdot \mathbf{u})_P$ and $\nabla(\nabla \cdot h\mathbf{u})_P$ need to be computed again by applying the formulas used in the previous sections for the gradient and divergence discretizations. However, it is important here to keep the unknown information used in (6.14) at the minimum possible level and exploit already computed geometrical information. To this end, for the gradient computations in (6.14), and refereing also to formula (5.12), the arithmetic average in (5.12) can be replaced by the values at the midpoints M of the edges. Hence, and dropping the superscript index, (6.14) now reads as

$$H_P \left[\frac{(z_a)_P^2}{2} \frac{1}{|C_P|} \sum_{Q \in K_P} (\nabla \cdot \mathbf{u})_M \mathbf{n}_{PQ} + \frac{(z_a)_P}{|C_P|} \sum_{Q \in K_P} (\nabla \cdot h\mathbf{u})_M \mathbf{n}_{PQ} + \mathbf{u}_P \right] = \mathbf{P}_P^*, \quad (6.15)$$

and is now obvious that we have to compute $\nabla \cdot \mathbf{u}$ and $\nabla \cdot h\mathbf{u}$ at M . Refereeing again to Fig. 6.1, the computational cell M_{PQ} , used previously for the computation of the gradients at M , can be utilized using the idea behind formula (6.9) for these divergence computations. Hence, the discrete averages of the divergence can be computed as follows for $(\nabla \cdot \mathbf{u})_M$,

$$(\nabla \cdot \mathbf{u})_M = \frac{1}{|M_{PQ}|} \iint_{M_{PQ}} \nabla \cdot \mathbf{u} d\Omega = \frac{1}{|M_{PQ}|} \oint_{\partial T_{PQ}} \mathbf{u} \cdot \tilde{\mathbf{n}} dl \approx \frac{1}{|M_{PQ}|} \sum_{\substack{R, Q \in K_{PQ} \\ R \neq Q}} \frac{1}{2} (\mathbf{u}_R + \mathbf{u}_Q) \cdot \mathbf{n}_{RQ}. \quad (6.16)$$

A similar computation is used for the calculation of $(\nabla \cdot h\mathbf{u})$. By performing the above approximation we restrict the unknown information used in (6.15), i.e. values of \mathbf{u} , only to that coming from the nodes that are neighbors of node P , i.e. nodes $Q \in K_P$.

Substituting the above relationship to the first addend of the left hand side of equation (6.15) gives

$$\begin{aligned} & \frac{(z_a^2)_P}{2} \frac{1}{|C_P|} \sum_{Q \in K_P} \left[\frac{1}{|M_{PQ}|} \sum_{\substack{R, Q \in K_{PQ} \\ R \neq Q}} \frac{1}{2} (\mathbf{u}_R + \mathbf{u}_Q) \cdot \mathbf{n}_{RQ} \right] \mathbf{n}_{PQ} = \\ & \frac{(z_a^2)_P}{2|C_P|} \sum_{Q \in K_P} \left[\frac{1}{2|M_{PQ}|} \sum_{\substack{R, Q \in K_{PQ} \\ R \neq Q}} \mathbf{u}_R \cdot (\mathbf{n}_{PR} + \mathbf{n}_{RQ}) \right] \mathbf{n}_{PQ}, \end{aligned}$$

which can be further rewritten as

$$\frac{(z_a^2)_P}{2|C_P|} \sum_{Q \in K_P} \left[\frac{1}{2|M_{PQ}|} \left(\sum_{\substack{R, Q \in K_P \cap K_{PQ} \\ R \neq Q}} \mathbf{u}_R \cdot (\mathbf{n}_{PR} + \mathbf{n}_{RQ}) + \mathbf{u}_P \cdot (\mathbf{n}_{SP} + \mathbf{n}_{PR}) \right) \right] \mathbf{n}_{PQ},$$

leading to the more compact presentation

$$\frac{(z_a^2)_P}{2} \frac{1}{|C_P|} \sum_{Q \in K_P} (\nabla \cdot \mathbf{u})_M \mathbf{n}_{PQ} = \frac{(z_a^2)_P}{2|C_P|} \sum_{Q \in K_P} (\mathbf{A}_{Q_x} u_Q + \mathbf{A}_{Q_y} v_Q + \mathbf{A}_{P_x} u_P + \mathbf{A}_{P_y} v_P) \quad (6.17)$$

where $\mathbf{A}_{Q_x}, \mathbf{A}_{Q_y}, \mathbf{A}_{P_x}, \mathbf{A}_{P_y} \in \mathbb{R}^2$ and depend only on the geometric characteristics quantities \mathbf{n}_{PQ} , the vectors normal to the edges of ∂M_{PQ} and the area $|M_{PQ}|$. The same is valid for the second add end on the left hand side of (6.15) with the difference that the velocity coefficients are now also depended from the steel water level h . Thus, the sparse $2N \times 2N$ linear system to be solved can be presented as

$$\begin{aligned} & \frac{(z_a^2)_P}{2|C_P|} \sum_{Q \in K_P} ([\mathbf{A}_{Q_x} \mathbf{A}_{Q_y}] \mathbf{u}_Q + [\mathbf{A}_{P_x} \mathbf{A}_{P_y}] \mathbf{u}_P) + \frac{(z_a)_P}{|C_P|} \sum_{Q \in K_P} ([\mathbf{B}_{Q_x} \mathbf{B}_{Q_y}] \mathbf{u}_Q + [\mathbf{B}_{P_x} \mathbf{B}_{P_y}] \mathbf{u}_P) \\ & + \mathbf{I} \mathbf{u}_P = \frac{1}{H_P} \mathbf{P}_P^*, \quad (6.18) \end{aligned}$$

with $P = 1, \dots, N$. Any two consecutive rows of the system's matrix \mathbf{M} , corresponding to each node P , have nonzero entries that correspond to the coefficients of the unknown velocities at node P and its neighbors $Q \in K_P$. More specifically, the columns of the 2×2 matrices in (6.18) are given by

$$\mathbf{A}_{Q_x} = \frac{1}{2|M_{PQ}|} \sum_{R, Q \in K_P \cap K_{PQ}} (n_{PR_x} + n_{RQ_x}) \mathbf{n}_{PQ}, \quad \mathbf{A}_{Q_y} = \frac{1}{2|M_{PQ}|} \sum_{R, Q \in K_P \cap K_{PQ}} (n_{PR_y} + n_{RQ_y}) \mathbf{n}_{PQ},$$

$$\mathbf{B}_{Q_x} = \frac{1}{2|M_{PQ}|} \sum_{R, Q \in K_P \cap K_{PQ}} h_R(n_{PRx} + n_{RQx})\mathbf{n}_{PQ}, \quad \mathbf{B}_{Q_y} = \frac{1}{2|M_{PQ}|} \sum_{R, Q \in K_P \cap K_{PQ}} h_R(n_{PRy} + n_{RQy})\mathbf{n}_{PQ},$$

$$\mathbf{A}_{P_x} = \frac{1}{2|M_{PQ}|} (n_{SPx} + n_{PRx})\mathbf{n}_{PQ}, \quad \mathbf{A}_{P_y} = \frac{1}{2|M_{PQ}|} (n_{SPy} + n_{PRy})\mathbf{n}_{PQ},$$

$$\mathbf{B}_{P_x} = \frac{1}{2|M_{PQ}|} h_P(n_{SPx} + n_{PRx})\mathbf{n}_{PQ}, \quad \mathbf{B}_{P_y} = \frac{1}{2|M_{PQ}|} h_P(n_{SPy} + n_{PRy})\mathbf{n}_{PQ}.$$

The number of geometrical entries in each summation is always two, while the number of entries in the summation $\sum_{Q \in K_P}$ is equal to the number of the neighbors of P . This means that the maximum non-zero elements of the matrix \mathbf{M} in each row P in (6.18) are two times the number of the neighbors of P plus one.

Remark 9 *In the case where the dispersion terms are zero in the model equations, i.e. only the nonlinear part of the shallow water equations is to be solved, matrix $\mathbf{M} \equiv \mathbf{I}$, the identity matrix, as expected.*

Remark 10 *The division by the total water depth H_P in the right hand side of system (40) can cause numerical difficulties if $H_P \leq \epsilon_{wd}$ or if $H_P = 0$, i.e. for dry cells. In these cases the components of the right hand side that correspond to dry cell have to be set equal to zero.*

6.4.1 Solution of the linear system

The $2N \times 2N$ matrix \mathbf{M} of the linear system is sparse and structurally symmetric but is also mesh dependent. The properties of the sparse matrix vary depending on the physical situation of each problem solved, the type of the grid used and the number of the nodes on the grid. The most popular format, for storing general sparse matrices with N_z non-zero entries, like the one that is produced here, is the compressed sparse row (CSR) format [143]. The linear system was solved, at every time step, using Bi-Conjugate Gradient Stabilized method (BiCGStab) [143] which is an iterative method for the numerical solution of non-symmetric linear systems. This is a Krylov subspace method and was used here with a residual error tolerance of $5 \cdot 10^{-6}$ with the numerical solution for the velocities at the previous time step given as initial guess. The choice of this method was justified after a check on the eigenspectrum of different matrices was performed. To this end, we produced different matrices using different triangular

meshes and different physical conditions e.g. spatial dimensions and values of constant depth h , in order to check the spectrum of eigenvalues for each such produced matrix. For sparse and relatively sparse meshes all the eigenvalues were close to unity but if grids were refined the resulting matrices had much larger spread of complex eigenvalues.

An extended study for the behavior of the linear systems, produced by different kind of grids and different initial conditions has been performed in [69]. We present here, for completeness, the behavior of the solution of the linear systems using different iterative methods and three preconditioners. The sparse matrix \mathbf{M} , has been produced by the distorted grid (type IV) (see Chapter 5). In table 6.1 the number of the non-zero elements (N_z) of the matrices produced from two different still water levels ($h = 1m$ and $h = 100m$) using a consisted refinement (see Section 5.1). The dimension of the numerical domain is $(x, y) \in [0, 1] \times [0, 1]$.

N_x	$h = 1m$	$h = 100m$
15	7715	7713
30	29746	29741
60	118293	7714

Table 6.1: Non-zero elements for two different still water levels (type IV).

N_x is the node number along the x axis. In this study [69] the right hand side of the system $\mathbf{M}x = \mathbf{b}$ is the sum of the columns of the matrix \mathbf{M} . The number of iterations required by four different iterative methods to converge, is presented in Table 6.2. More precisely, Generalized Minimum RESidual method (GMRES), BIConjugate Gradient Stabilized method (BICGSTAB), Conjugate Gradient method (CG), Transpose-Free Quasi-Minimal Residual method (TFQMR)

N_x	GMRES	BICGTAB	CG	TFQMR
15	1999	581	-	649
30	-	-	-	-
60	-	3365	-	-

Table 6.2: Number of iterations for the linear systems produced using $h = 1m$.

Since the iterations for solving the linear system were increased as the mesh was refined the use of an effective preconditioner was necessary. Three well known preconditioners, based on Incomplete LU factorization (ILU0, ILUT and ILUK), are implemented

and tested using the SPARSKIT package [143]. A general ILU factorization process computes a sparse lower triangular matrix L and a sparse upper triangular matrix U so that the residual matrix $LU - M$ satisfies certain constraints such as having zero entries in some locations and it can be derived by performing Gaussian elimination and dropping some elements in predetermined non-diagonal positions. Two threshold values were used, for the element dropping, the fill-in value ($lfil$) and the drop tolerance value (dpt). Tables 6.3-6.5 present the number of iterations for each iterative method, using the ILUT preconditioner with $lfil = 300$ and $dpt = 10^{-5}$, the ILU0 and the ILUK preconditioner with $lfil = 300$ respectively.

N_x	GMRES	BICGTAB	CG	TFQMR
15	4	5	5	5
30	6	7	7	7
60	8	9	-	9

Table 6.3: Number of iterations for the linear systems produced using $h = 1m$, the ILUT preconditioner with $lfil = 300$ and $dpt = 10^{-5}$

N_x	GMRES	BICGTAB	CG	TFQMR
15	206	181	-	187
30	499	363	-	361
60	1326	729	-	777

Table 6.4: Number of iterations for the linear systems produced using $h = 1m$, the ILU0 preconditioner

The ILU0 factorization technique is appropriate for small sparse matrices but is inefficient as matrices become larger. ILUK results as the best preconditioner for these matrices, since ILUK preconditioner is closer to the inverse of the matrix \mathbf{M} due to the maintenance of all elements. One should keep in mind that the computational time cost using ILUK is greater than using ILUT.

N_x	GMRES	BICGTAB	CG	TFQMR
15	2	3	2	3
30	2	3	2	3
60	3	3	3	3

Table 6.5: Number of iterations for the linear systems produced using $h = 1m$, the ILUK preconditioner with $lfil = 300$.

Further the reverse Cuthill{McKee (RCM) algorithm [72] was incorporated in our solver in order to reorder the matrix elements as to minimize its bandwidth. Table 6.7

displays iterations and computational time needed for the top two performing iterative methods up to now (GMRES and BICGSTAB) using ILUT and ILUk preconditioners. T is the total computational time, T_p is the time needed for the preconditioner computation and T_r is the time needed for the reordering process.

	GMRES					BICGSTAB			
	N_x	it	T	T_p	T_r	it	T	T_p	T_r
$lfil = 300$	15	9	0.019	0.015	5.11E-4	11	0.017	0.012	3.1E-4
$dpt = 10^{-5}$	30	24	0.21	0.015	1.92E-3	23	0.21	0.015	1.93E-3
ILUT+RCM	60	781	15.3	2.22	7.5E-3	225	6.14	2.48	7.36E-3

	GMRES					BICGSTAB			
	N_x	it	T	T_p	T_r	it	T	T_p	T_r
$lfil = 300$	15	4	0.01	0.015	5.32E-4	5	0.01	0.013	5.25E-4
$dpt = 10^{-10}$	30	5	0.17	0.15	1.89E-3	5	0.174	0.15	1.83E-3
ILUT+RCM	60	6	2.33	2.22	4.55E-3	7	2.38	2.25	7.326E-3

Table 6.6: Number of iterations for the linear systems produced using $h = 1m$ (up) $h = 100m$ (down) and the ILUT preconditioner.

	GMRES					BICGSTAB			
	N_x	it	T	T_p	T_r	it	T	T_p	T_r
$lfil = 300$	15	3	0.019	0.017	5.4E-4	3	0.021	0.019	5.099E-4
	30	4	0.22	0.21	1.88E-3	5	0.22	0.21	1.86E-3
ILUk+RCM	60	4	3.45	3.38	5.35E-3	5	3.16	3.06	7.56E-3

Table 6.7: Number of iterations for the linear systems produced using $h = 100m$ and the ILUk preconditioner.

Conclusively the best combination (examining iterations and the convergence time) for the numerical solution of the sparse linear system under study is:

- For the systems result using shallow and intermediate still water level, GMRES or BICGSATB solvers using ILUT and RCM is the best combination.
- For deeper water the results using iterative methods combined with ILUT ($dpt = 10^{-10}$) are similar to those obtained using ILUk.

Finally, in the present work, we implemented the ILUT preconditioner from SPARSKIT package [143]. A drop-tolerance of $1 \cdot 10^{-5}$ was used, combined with a maximum fill-in of 50-200 elements per row, depending on the problem testing. One should keep in mind that mesh independence is rarely achieved with ILUT preconditioner [67]. Convergence

to the solution was obtained in one or two steps for the test problems presented in Chapter 7.

Remark 11 *The way this linear system is constructed and solved is important for the proposed wave breaking treatment presented later on. The system's matrix is constructed at the beginning of each simulation and as such its structure is stored in CSR format at a preprocessing stage and subsequently utilized to solve the linear system at each time step. So its data structure can not be changed during the time marching process in a numerical simulation.*

6.5 Boundary conditions and the internal source function

Two types of boundary conditions have been considered here. Wall and outflow boundary conditions. Since we follow the node-centered type FV approach, the degrees of freedom are located directly on the boundary and boundary conditions based on mesh faces have been adopted. to this end the weak formulation is used which is extensively described in Section 5.3.1. The idea of using the weak formulation to calculate the flux (and dispersion terms) at the boundary has been used in the description of wall (solid) and outflow boundary conditions. In the present work, no analytical investigation of the numerical treatment of boundary conditions is performed because of the complexity of the model. Instead, this important property is studied using a somehow heuristic approach based on several benchmark tests. Our objective is to ensure that the discretized counterparts of boundary conditions do not introduce any numerical instability in the system and at the same time preserves the spatial accuracy of the numerical scheme used in the inner region.

In a computational domain Ω and for a solid, impermeable and fully reflective wall the kinematic boundary condition can be stated as

$$\mathbf{u} \cdot \tilde{\mathbf{n}} = 0 \text{ for } \mathbf{x} \in \partial\Omega, \quad (6.19)$$

where $\tilde{\mathbf{n}}$ the unit outward normal vector. In the continuous case, a free surface boundary condition can be derived form the mass equation in (6.1) over Ω written as

$$\frac{\partial}{\partial t} \iint_{\Omega} H d\Omega + \int_{\partial\Omega} \left[H\mathbf{u} + \left(\frac{z_a^2}{2} - \frac{h^2}{6} \right) h\nabla(\nabla \cdot \mathbf{u}) + \left(z_a + \frac{h}{2} \right) h\nabla(\nabla \cdot h\mathbf{u}) \right] \cdot \tilde{\mathbf{n}} dl = 0. \quad (6.20)$$

By conservation of mass, we require that the rate of change of the excess volume to be zero since there is no loss or gain of mass through the wall. Hence, (6.19) implies that along the wall

$$\left[\left(\frac{z_a^2}{2} - \frac{h^2}{6} \right) h \nabla (\nabla \cdot \mathbf{u}) + \left(z_a + \frac{h}{2} \right) h \nabla (\nabla \cdot h \mathbf{u}) \right] \cdot \tilde{\mathbf{n}} = 0, \quad (6.21)$$

that will completely satisfy (6.20). Thus, and refereing for example in Fig. 1 for faces M_1P and PM_1 , it follows form (6.19) and (6.21) that, for system (2.46) integrated at a boundary cell, the line integrals in (6.11) and (6.12) along faces M_1P and PM_1 should be zero. Then the normal advective flux, $\Phi_{P\Gamma}$, at the boundary, in a weak form, is the one given by (5.14).

Absorbing boundaries should dissipate the energy of incoming waves perfectly, in order to eliminate unphysical reflections. In front of this kind of boundaries a sponge layer is defined. On this layer, the surface elevation was damped by multiplying its value by a coefficient $m(\mathbf{x})$ defined as [185]

$$m(\mathbf{x}) = \sqrt{1 - \left(\frac{\mathbf{x} - d(\mathbf{x})}{L_s} \right)^2} \quad (6.22)$$

where L_s is the sponge layer width (where $L \leq L_s \leq 1.5L$) and $d(\mathbf{x})$ is the normal distance between the cell center with coordinates \mathbf{x} and the absorbing boundary. This coefficient was applied in the cells of the sponge layer inside the Runge-Kutta time stepping. Since longer wave lengths require longer sponge layers, we have to increase the numerical domain when using a sponge layer and dealing with long waves, such as solitary waves, in order to fully damp the wave motion resulting in an increased computational coast. A combination of an open (outflow) boundary condition and sponge layer can handle both short and long waves and thus reduce the computational cost.

For the wave generation in the 2D model presented in this section we use the internal wave generation of Wei et al. [181]. This source function was obtained using Fourier transform and Green's functions to solve the linearized and non-homogeneous equations of Peregrine and Nwogu models. In the present model, this source function wave-making method is adopted in order to let the reflected waves outgo through the wave generator freely. The internal wave generation along with the sponge layer we consider to be more attractive than a wave absorbing-generating boundary condition since the source function inside the numerical domain does not interact with the reflected waves, and the sponge layer is able to absorb both long and short waves. Like 1D

described in section 3.6 a source function $S(\mathbf{x}, \mathbf{t})$ is added in to the mass conservation equation at each time step. The form of the source function in 2D is now:

$$S(\mathbf{x}, \mathbf{t}) = \mathbf{D}^* \exp\left(-\gamma(\mathbf{x} - \mathbf{x}_s)^2\right) \sin(\lambda y - \omega t) \quad (6.23)$$

in which $\lambda = \kappa \sin \theta$ is the wave number in the y -direction and θ is the wave's incident angle. All the other parameters can be found in Section 3.6.

6.6 Wave breaking treatment

As presented in Chapter 3 four main categories of wave breaking treatment have been developed for Boussinesq-type equations the past few years. The *surface roller model*, *the vorticity model*, *the eddy viscosity model* and *hybrid models*. In this work, and for the 2D formulation, two wave breaking models are implemented and tested within the FV frame. The first one is the eddy viscosity wave breaking treatment of Kennedy [93] and the second one is the hybrid model introduced by [163]. The first three categories involve addition of a dissipative term to the momentum (or/and the mass) equation with prescribed criteria for onset and termination of wave breaking and energy dissipation rates.

6.6.1 Eddy viscosity wave breaking treatment of Kennedy et al.[93]

As described for the 1D FV model for the equations of Nwogu [127] (see Chapter 3), the mass conservation equation remains unchanged while an eddy viscosity term is added to the momentum conservation equation. So the conservative-like form of the equations of Nwogu is (2.48) with (2.89) where now the source terms vector is $\mathbf{S} = \mathbf{S}_b + \mathbf{S}_d + \mathbf{S}_f$ with

$$\mathbf{S}_f = \begin{bmatrix} 0 \\ -\tau_1 + R_{b_x} \\ -\tau_2 + R_{b_y} \end{bmatrix}. \quad (6.24)$$

The eddy viscosity terms have the form

$$\mathbf{R}_b = \begin{bmatrix} R_{b_x} \\ R_{b_y} \end{bmatrix} = \begin{bmatrix} \nabla \cdot \widetilde{\mathbf{R}}_{b_x} \\ \nabla \cdot \widetilde{\mathbf{R}}_{b_y} \end{bmatrix} \quad (6.25)$$

with

$$\widetilde{\mathbf{R}}_{b_x} = \begin{bmatrix} \nu(Hu)_x \\ \frac{\nu}{2}((Hu)_y + (Hv)_x) \end{bmatrix} \quad \text{and} \quad \widetilde{\mathbf{R}}_{b_y} = \begin{bmatrix} \frac{\nu}{2}((Hu)_y + (Hv)_x) \\ \nu(Hv)_y \end{bmatrix}.$$

The above terms can be shown that they conserve the overall momentum [93]. The eddy viscosity is given by

$$\nu = B\delta_b^2 H\eta_t \tag{6.26}$$

with δ_b is a mixing length coefficient. According to [93] values between 0.5 and 1.5 give very similar results with the one of 1.2 giving the best ones. The quantity B as in one dimension varies smoothly from 0 to 1 so as to account for the initiation and termination of wave breaking and to avoid an impulsive start of breaking.

$$B = \begin{cases} 1, & \eta_t \geq 2\eta_t^* \\ \frac{\eta_t}{\eta_t^*} - 1, & \eta_t^* \leq \eta_t \leq 2\eta_t^* \\ 0, & \eta_t \leq \eta_t^* \end{cases} \quad \text{with} \quad \eta_t^* = \begin{cases} \eta_t^{(F)}, & t \geq T^* \\ \eta_t^{(I)} + \frac{t-t_0}{T^*}(\eta_t^{(F)} - \eta_t^{(I)}), & 0 \leq t - t_0 \end{cases}$$

which accounts for the initiation and termination of the breaking procedure. The magnitude of η_t^* decreases in time from some initial value $\eta_t^{(I)}$ to a final value $\eta_t^{(F)}$. T^* is the transition time and t_0 the time that breaking begins. The values of $\eta_t^{(I)}$ and $\eta_t^{(F)}$ are case depended. For the test cases used here good agreement with the laboratory data is obtained with $0.3\sqrt{gh} \leq \eta_t^I \leq 0.7\sqrt{gh}$ and $0.15\sqrt{gh} \leq \eta_t^F \leq 0.4\sqrt{gh}$. The transition time used here is $T^* = 7\sqrt{h/g}$.

In order to discretize the breaking terms we follow the FV framework introduced up to now. Integrating the eddy viscosity terms over a computational cell and applying the divergence theorem we obtain:

$$(\mathbf{R}_b)_P = \frac{1}{|C_P|} \iint_{C_P} \mathbf{R}_b d\Omega = \frac{1}{|C_P|} \iint_{C_P} \begin{bmatrix} \nabla \cdot \widetilde{\mathbf{R}}_{b_y} \\ \nabla \cdot \widetilde{\mathbf{R}}_{b_x} \end{bmatrix} d\Omega = \frac{1}{|C_P|} \sum_{Q \in K_P} \int_{\partial C_{PQ}} \begin{bmatrix} \widetilde{\mathbf{R}}_{b_x} \cdot \widetilde{\mathbf{n}} \\ \widetilde{\mathbf{R}}_{b_y} \cdot \widetilde{\mathbf{n}} \end{bmatrix} dl.$$

The above vector is approximated assuming a uniform distribution of $\mathbf{R}_b \cdot \widetilde{\mathbf{n}}$ over ∂C_{PQ} and equal to its value at the midpoint M of edge PQ , thus

$$(\mathbf{R}_b)_P \approx \frac{1}{|C_P|} \sum_{Q \in K_P} \begin{bmatrix} \widetilde{\mathbf{R}}_{b_x} \cdot \mathbf{n}_{PQ} \\ \widetilde{\mathbf{R}}_{b_y} \cdot \mathbf{n}_{PQ} \end{bmatrix}_M \tag{6.27}$$

The right hand side terms in equation (6.27) require the evaluation of $\widetilde{\mathbf{R}}_{b_x}$ and $\widetilde{\mathbf{R}}_{b_y}$ along the edge midpoints M . Hence we use the computational cell M_{PQ} (see Fig.) constructed by the union of the two triangles that share edge PQ . The Green-Gauss reconstruction that concludes to the equation (6.13) is used for the computation of the vectors $\nabla(Hu), \nabla(Hv)$ and consequently for the terms $\widetilde{\mathbf{R}}_{b_x}$ and $\widetilde{\mathbf{R}}_{b_y}$. The value of the eddy viscosity term at M , ν_M is computed as the arithmetic average of the eddy viscosity values at nodes P and Q (ν_P and ν_Q respectively). Furthermore η_t which is necessary for the computation of ν_P and B is explicitly obtained from the mass equation.

6.6.2 Hybrid wave breaking treatment

The hybrid BT-NSW approach has been widely used for 2D BT models, the last few years, due to its simplicity and efficiency [163, 141, 147]. Like 1D formulation, considerations still exist in the criteria chosen to characterize wave breaking, the proper switching between the BT equations and to the NSW ones, range of applicability and grid sensitivity. In addition, this approach has never been applied to unstructured meshes before the present work, to the best of our knowledge. Tonelli and Petti in [163, 164] for the MS BT model and Shi et. al. [147] for the equations of Chen [43] developed a 2D wave breaking treatment but only for structured meshes. In this approach, and like 1D formulation described in Section 3.7.2, we first estimate the location of breaking waves using explicit criteria and then the NSW equations are applied on the breaking regions and BT equations elsewhere. The criterion used is the ratio of surface elevation to water depth, $\epsilon = \frac{\eta}{d}$ and is set to 0.8. So, the proposed numerical approach of [163] solves NSWE in the region where $\epsilon > 0.8$ and BT elsewhere. Also, in order to make the scheme more stable, once NSW equations have been applied, the value has to drop below 0.35-0.55 for BT equations to be applied again [165]. The limitation of this treatment remains the static application of this breaking approach (see Section 3.7.2). This approach is also applied in this work and we name the model that utilizes this approach Hybrid(ϵ).

It should be stress here that, application of any hybrid approach to the unstructured FV scheme presented here is not straightforward and a special treatment is in need to perform a stable switch between the BT and NSW model which minimizes mesh dependence and stability issues on finer meshes.

Wave breaking criteria and the New Hybrid model

Following the idea introduced in Section .3.7.2 for the 1D model we extend the the combination of two phase-resolving criteria for triggering wave breaking modeling within our FV scheme for the 2D approach. Namely, the two criteria used are:

- the surface variation criterion: $\eta_t \geq \gamma \sqrt{gh}$ with $\gamma \in [0.35, 0.65]$ and
- the local slope angle criterion: $\|\nabla\eta\|_2 \geq \tan(\phi_c)$ where ϕ_c is the critical front face angle at the initiation of breaking.

As in 1D, the first criterion flags for breaking when η_t is positive, as breaking starts on the front face of the wave and has the advantage that can be easily calculated during the running of the model. The second criterion acts complementary to the first one and is based on the critical front slope approach in [55, 60]. The value used in this work is $\phi_c \approx 30^\circ$ and even though it is relatively large for this criterion to trigger by its own the breaking process, it is sufficient to detect breaking hydraulic jumps thus, correcting the limitation of the first criterion.

In the numerical scheme and for each mesh node in the computational domain at every time step, we check if at least one of the above criteria is satisfied, and flag the relative node as a breaking or a non-breaking one. Then, each breaking wave, with its corresponding breaking mesh nodes, has to be identified. Thus, for each breaking wave we have to create a distinct dynamic list that contains all of its nodes characterized as breaking ones. To achieve this, and as such distinguish between different breaking waves, the following procedure is performed: a flagged breaking node is randomly chosen and its neighbors in the mesh data structure are identified. From these neighboring nodes we check which ones have been flagged as breaking ones and we add them to the list. We continue by following the same procedure for the next element in the list until we reach the last element on the list (for which its breaking neighboring nodes are already in the list).

The next step to the proposed New Hybrid model, is to characterize the non-breaking bores and switch back to the BT equations, allowing for the breaking process to stop. We are keeping in mind that bores stop breaking when their Froude (Fr) number drops below a critical value. Since we have distinguished the different breaking waves (with its own dynamic list) we can treat each wave individually. It is easy to find the water depth at the wave's trough and the water depth at the wave's crest and then use eq.

(3.68) in order to find the wave's Fr number. If $Fr \leq Fr_c$ all the breaking points of that wave are un-flagged and the wave is considered non-breaking. Following [160] the critical value for Fr_c was set equal to 1.3 in our computations.

Finally an extension of each wave breaking region is performed, according to the corresponding wave's height. Knowing all the breaking nodes in each dynamic list, we find the nodes that possess the maximum and minimum values of x-coordinate (x_{max}, x_{min}), and those that possess the maximum and minimum value of y-coordinate. Further and for the x-direction, if $\Delta x_b = x_{max} - x_{min} < l_{NSW}$ (see Section 3.7) we extend the wave breaking region, including to the dynamical list the nodes that lay in the interval $[x_{min} - 0.5 * (\Delta x_b - l_{NSW}), x_{max} + 0.5 * (\Delta x_b - l_{NSW})] \times [y_{min}, y_{max}]$.

Suppression of the dispersive terms methodology

After the characterization of the breaking regions the NSW model has to be applied computationally in each one of them. This means that all dispersive terms, ψ_c and ψ_M in (1) have to be suppressed at mesh nodes triggered as breaking ones. Several researchers have followed similar approach in their hybrid models, we refer to [163, 164, 165, 141, 147] for 2D applications. In the aforementioned works, a FV/FD approach has been adopted on structured meshes. The corresponding two linear systems produced (along the x- and y-direction respectively) for the velocity field recovery (see Section 5.9) are tridiagonal ones which can be more easily adapted in time since the equations corresponding to breaking nodes theoretically must be as those in the identity matrix, since the dispersive terms are suppressed. However, in [163] and [141] it was stated that the matrices were precalculated and used throughout the computations.

As we stated in Remark 11, also for our unstructured solver the matrix of the linear system can not be changed due to its storage in the compressed sparse row (CSR) format. Any change in the matrix structure through time marching would result in a large increase in the computational cost. Furthermore, it is not clear how the switching between the two models is implemented, with an additional concern for issues of sensitivity to grid spacing. According to [147] there is a discontinuity at the switching point between the BT equations and NSW ones. This has been observed in our tests as well. This discontinuity is introduced to the dispersive terms of the BT equations causing spurious oscillations at the switching points. The frequency of these oscillations

increases with grid refinement, producing instabilities.

For the above reasons there is the need of a robust and efficient implementation of the switching procedure. A methodology to stably handle the switching between the two models is developed within the unstructured FV framework of the present work and is detailed below:

0. Starting with the solution vector $\mathbf{U}_p^n, P = 1, \dots, N$, at time t^n ,
1. For all computational cells an $[H_1^{n+1}, H_2^{n+1}, \dots, H_N^{n+1}]^T$ solution is computed from the mass equation using the BT model (named from now on \mathbf{H}_{BT}^{n+1} solution).
 - 1.1 If breaking has been activated (according to our criteria) for a number of computational cells say $N_{br} < N$, an additional solution vector is computed by subtracting the dispersive terms ψ_c from \mathbf{H}_{BT}^{n+1} at these breaking cells, i.e. obtaining a NSW solution for \mathbf{H}^{n+1} at these cells only. This solution is named $\mathbf{H}_{BT/SW}^{n+1}$ from now on.
2. Then, for all computational cells the $\mathbf{P}_{BT}^{n+1} = [\mathbf{P}_1^{n+1}, \mathbf{P}_2^{n+1}, \dots, \mathbf{P}_N^{n+1}]_{BT}^T$ solution from the momentum equation is computed, using the approximation $\partial_t \mathbf{H}^{n+1} \approx \frac{\mathbf{H}_{BT}^{n+1} - \mathbf{H}^n}{\Delta t^{n+1}}$ for the ψ_M computation in (4).
 - 2.1 If breaking has been activated for a number of computational cells, an additional solution (named $\mathbf{P}_{BT/SW}^{n+1}$) is computed by subtracting the dispersive terms ψ_c and ψ_M from \mathbf{P}_{BT}^{n+1} at these cells i.e. obtaining a NSW momentum solution $[(Hu)^{n+1}, (Hv)^{n+1}]^T$ for the breaking cells, since for the NSW equations $\mathbf{P} = [P_1, P_2]^T = [Hu, Hv]^T$. For these cells only it is easy now to compute $\mathbf{u}_{SW}^{n+1} = [\mathbf{u}_1^{n+1}, \dots, \mathbf{u}_{N_{br}}^{n+1}]_{SW}^T$ which will be a subset of the actual velocity solution sought.
3. Then, the linear system $\mathbf{M}\mathbf{V} = \mathbf{C}$ from (18) is solved with $\mathbf{C} = [\mathbf{P}_1^{n+1}, \mathbf{P}_2^{n+1}, \dots, \mathbf{P}_N^{n+1}]_{BT}^T$ to obtain an approximation of the velocity vector, named $\mathbf{u}_{BT}^{n+1} = [\mathbf{u}_1^{n+1}, \dots, \mathbf{u}_N^{n+1}]_{BT}^T$.
4. The final solution at $t = t^{n+1}$ will be that of $\mathbf{H}_{BT/SW}^{n+1}$ for the total water depth and $\mathbf{P}_{BT/SW}^{n+1}$ for the momentum equations. For the velocity field vector the solution, denoted as $\mathbf{u}_{BT/SW}^{n+1}$, is derived from the \mathbf{u}_{BT}^{n+1} vector with its values at the breaking nodes replaced by those of \mathbf{u}_{SW}^{n+1} .

Chapter 7

Numerical test and results in two dimensions

In this Chapter numerical tests and results in two horizontal dimensions are presented in order to validate the numerical model described in Chapters 5-6. Section 7.1 presents one of the most common test cases for BT models while Section 7.2 examines the spatial accuracy and efficiency of the proposed numerical approach. Sections 7.3-7.6 examine non-breaking test cases while Sections 7.7-7.11 examine wave breaking test cases comparing the wave breaking mechanisms presented in Section 6.6. All the numerical results are compared with experimental data.

7.1 2D Solitary wave propagation in a channel

This test case is the 2D extension of the test case in Section 4.2. As described in Section 4.2 a solitary wave should maintain its shape and speed as it travels down a flat frictionless channel. The purpose of this test case is to show that our numerical model keep the balance between the nonlinear terms that steepen the wave and the dispersive terms that flatten the wave. In this numerical experiment, we consider a $2500m$ long and $h = 10m$ deep channel. The overall dimension of the numerical channel are for $(x, y) \in [-100m, 2400m] \times [-5, 5m]$. The initial condition used corresponds to a $A = 2m$ high solitary wave, i.e. $A/h = 0.2$, initially positioned at $x = 200m$. The initial wave surface elevation η and velocity \mathbf{u} can be found in [179]. As shown also in the test case described in Section 4.2 the initial waves undergo an evolution at the beginning of the computation to adjust the free surface to a steady profile [179, 163, 187] since the given

initial conditions (and analytical solution) are only asymptotically equivalent to the solution of the model being solved numerically. For that reason, the wave being input in the numerical model does not correspond exactly to solitary waveforms predicted by the model. For the computation a triangular grid consisting of equilateral triangles, with side length of 0.75m, was used, leading to a mesh of $N = 53,304$ nodes. The CFL number used was set equal to 0.65.

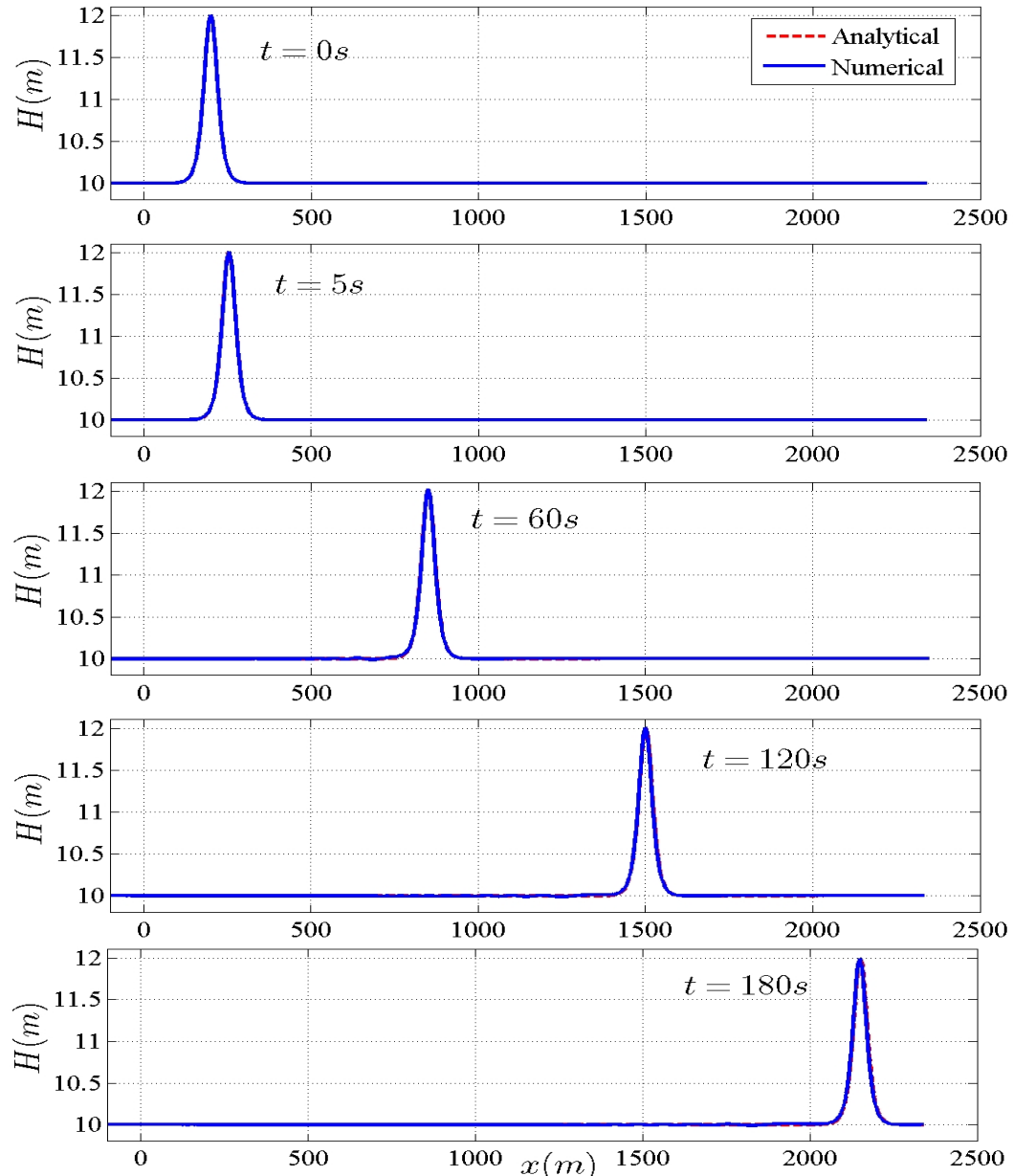


Figure 7.1: Solitary wave profiles along a channel of constant depth

Fig. 7.1 shows the initial solitary wave and the computed waveforms along the

channel for $y = 0$ at 5,60, 120, and 180s using the third order FV scheme. The wave height increases slightly ($A = 12.01m$) at the very beginning producing also a very small dispersive tail, due to the the specific initial condition used. Then the computed waveform stabilizes with $A \approx 1.99m$ and the wave height remains steady for the remainder of the simulation. The computed permanent waveform maintains its symmetry and phase speed which are very close to the (asymptotic) analytical solution.

7.2 Spatial accuracy and efficiency

As an indication of the accuracy and efficiency of the proposed numerical approach, we consider the propagation of a solitary wave of amplitude $A = 0.1m$ over an undisturbed depth $h = 1m$. The wave is initially centered at $x = 50m$ and the spatial domain $(x, y) \in [0, 300m] \times [0, 5m]$. Again, the approximate solution from [179] is used as initial condition. As there does not exist any closed form solitary wave solution for the Nwogu equations, the error $E(\eta)$ is computed by comparing with a numerical reference solution at $t = 30s$, given by a fine (uniform) unstructured mesh (Type-II) of $N = 232, 849$ nodes and the CFL number used was set equal to 0.4 (as to decrease the temporal errors). This type of mesh is chosen as to be able to obtain such a comparison with the reference solution. The major requirement, in order to perform convergence studies, for a sequence of refined grids, is to satisfy a consistency refinement property [51] (see also Section 5.1).

In Table 7.1 and Fig. 7.2 the L_2 and L_∞ errors and asymptotic orders of convergence are presented. The asymptotic order obtained is close to the optimal one for the presented third order scheme.

N	h_N	$\ E(\eta)\ _2$	\mathcal{R}	$\ E(\eta)\ _\infty$	\mathcal{R}
1504	1.0940	3.90E-03	-	2.74E-02	-
3907	0.6788	9.05E-04	2.10	7.01E-03	1.97
15013	0.3463	1.40E-004	2.70	1.20E-03	2.55
58825	0.1749	1.85E-005	2.92	1.72E-04	2.80

Table 7.1: Propagation of a solitary wave: L_2 and L_∞ error norms and convergence rates (\mathcal{R}) for η

Next, computational times measured in seconds (CPU times) versus accuracy are presented in Fig. 7.3 for the same grids used above. In addition, the total and per time-

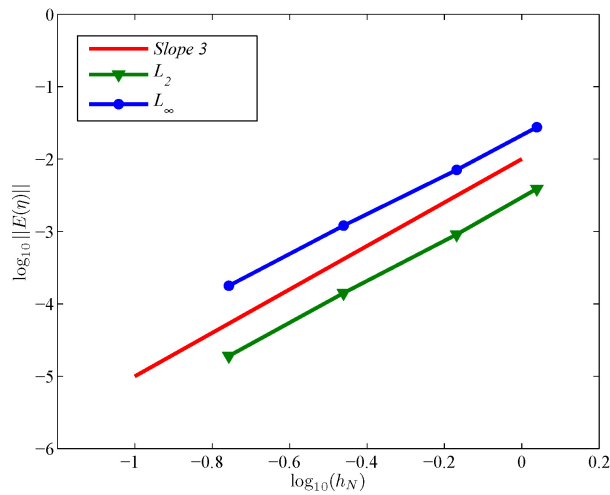
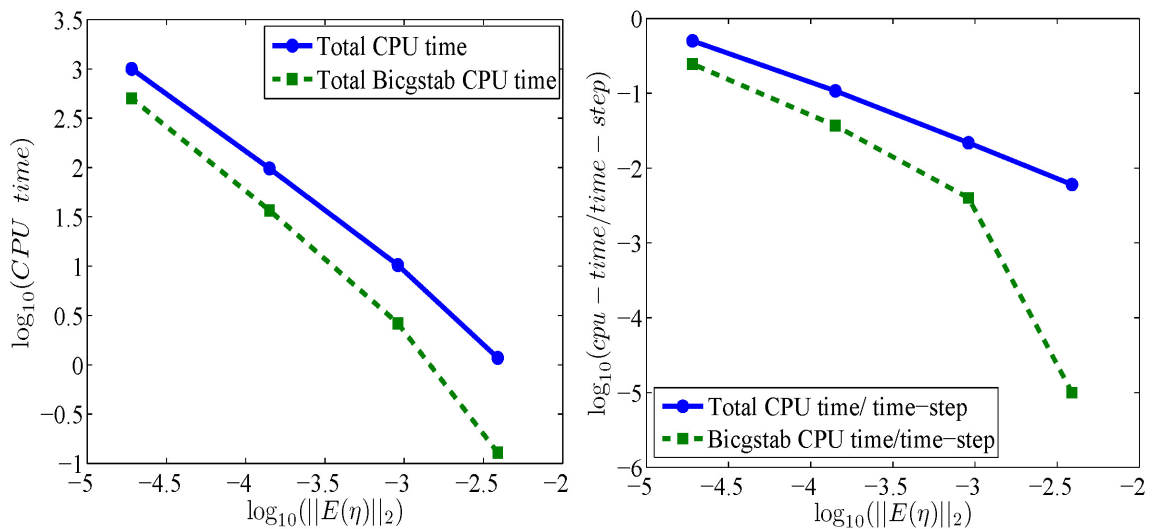


Figure 7.2: Convergence rates for the propagation of a solitary wave

step CPU times for the solutions of the $2N \times 2N$ sparse linear system, using the BiCGStab method, are also given. The CPU time to advance the model one time-step grows like $O(\|E(\eta)\|^{-1})$ (linearly) while the time needed by the BiCGStab like $O(\|E(\eta)\|^{-0.85})$, for the finer grids. However, and due to the increase of the number of time steps needed on finer grids, the total CPU time grows approximately like $O(\|E(\eta)\|^{-1.25})$ while the total time needed by the BiCGStab like $O(\|E(\eta)\|^{-1.5})$ and starts to dominate the overall time, as grids get refined.

Figure 7.3: CPU times as a function of accuracy in the L_2 norm

To assess the effect the increase of the number of grid points N has to the storage requirements of the non-zero elements (N_z) of the $2N \times 2N$ sparse linear system and to

the computational efficiency, we present relevant comparison in Fig. 7.4. As expected, the N_z entries grow linearly with respect to N . The BiCGStab CPU time per time step scales like $O(N^{3/2})$ however, the total CPU time per time step is growing like $O(N^{5/4})$, close to linear. We would like to point here that, reasonable work has been done to optimize the implementation of the numerical model.

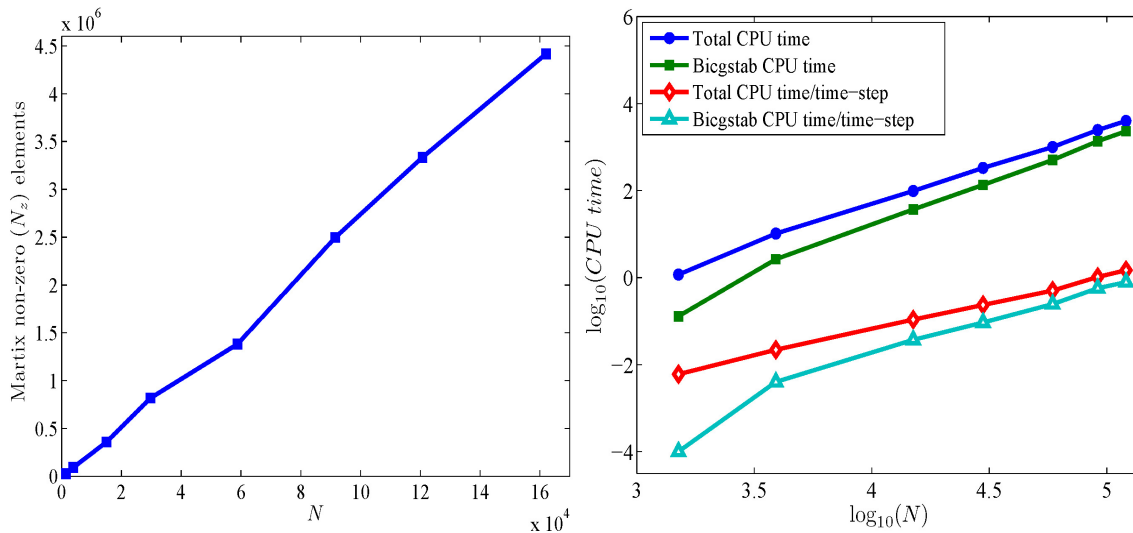


Figure 7.4: Non-zero elements as a function of N (left) and CPU times as a function of N (right)

7.3 Solitary interaction with a vertical circular cylinder

In this test case, the propagation and scattering of a solitary wave by a vertical circular cylinder is numerically investigated. In [4], laboratory experiments to investigate the interaction of a solitary wave with a vertical cylinder were conducted and the relevant data has been used to validate numerical models, e.g. in [4, 59, 185]. In a wave flume with dimensions $(x, y) \in [-4, 10m] \times [0, 0.55m]$ and an undisturbed water depth $h = 0.15m$, a $0.16m$ -diameter circular cylinder was placed $(x, y) = (4.5, 0.275)$. The solitary wave with wave amplitude $A = 0.0375m$ was initially centered at $x = 0m$, with its shape given again by the *sech*-profile solution from [179], leading to a wave with nonlinearity $\epsilon = A/h = 0.25$.

Six wave gauges were used to measure the water surface elevation at the following locations: WG1= (4.4, 0.275), WG2= (4.5, 0.170), WG3= (4.5, 0.045), WG4= (4.6, 0.275), WG5= (4.975, 0.275), and WG6= (5.375, 0.275). Absorbing boundary conditions with a

sponge layer width $L_s = 3m$ where placed from the upstream and downstream boundaries, while wall boundary conditions were imposed at side walls. The cylinder is represented as a discrete topography function in the numerical model. A triangular grid was used, which was refined around the cylinder edge using the h -enrichment technique from [125] leading to a mesh of $N = 10,609$ nodes with maximum edge length equal to $0.03m$ and minimum $0.01m$. A detail of the mesh and the gauge locations are shown in Fig. 7.5. The CFL number used was set equal to 0.45.

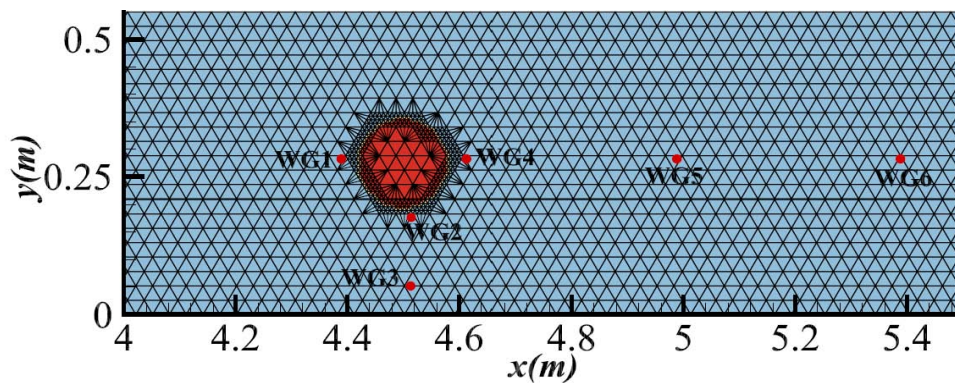


Figure 7.5: Mesh and wave gauge locations for the solitary wave-cylinder interaction

Fig. 7.6 presents a sequence of snapshots of the evolution of the solitary wave and the wave-cylinder interaction. We emphasize here the absence of motion around the cylinder before its interaction with the wave, verifying the well-balanced property of the scheme in the presence of wet/dry fronts. After the solitary wave has impinged on the cylinder short scattered waves are generated. These short waves propagate upstream, and the main wave recovers to solitary shape.

Numerical and measured surface water elevation time histories at the six wave gauges are compared in Fig. 7.7. In addition, we compare the numerical solution of the Boussinesq model and that of the NSWE. The numerical solution of the Boussinesq model provided very accurate results in terms of the wave elevation and phase speed, for almost all gauges, that are comparable to those obtained in [185] by a Navier-Stokes solver. It should be noted that, even though the circular form of the cylinder can not be perfectly represented by the grid, the obtained results were stable and very satisfactory. On the other hand, the predicted solution using the NSWE is highly inaccurate since, as expected, the solitary wave can not maintained its shape and phase speed using this model. This leads to wave steepening and subsequent transformations creating a

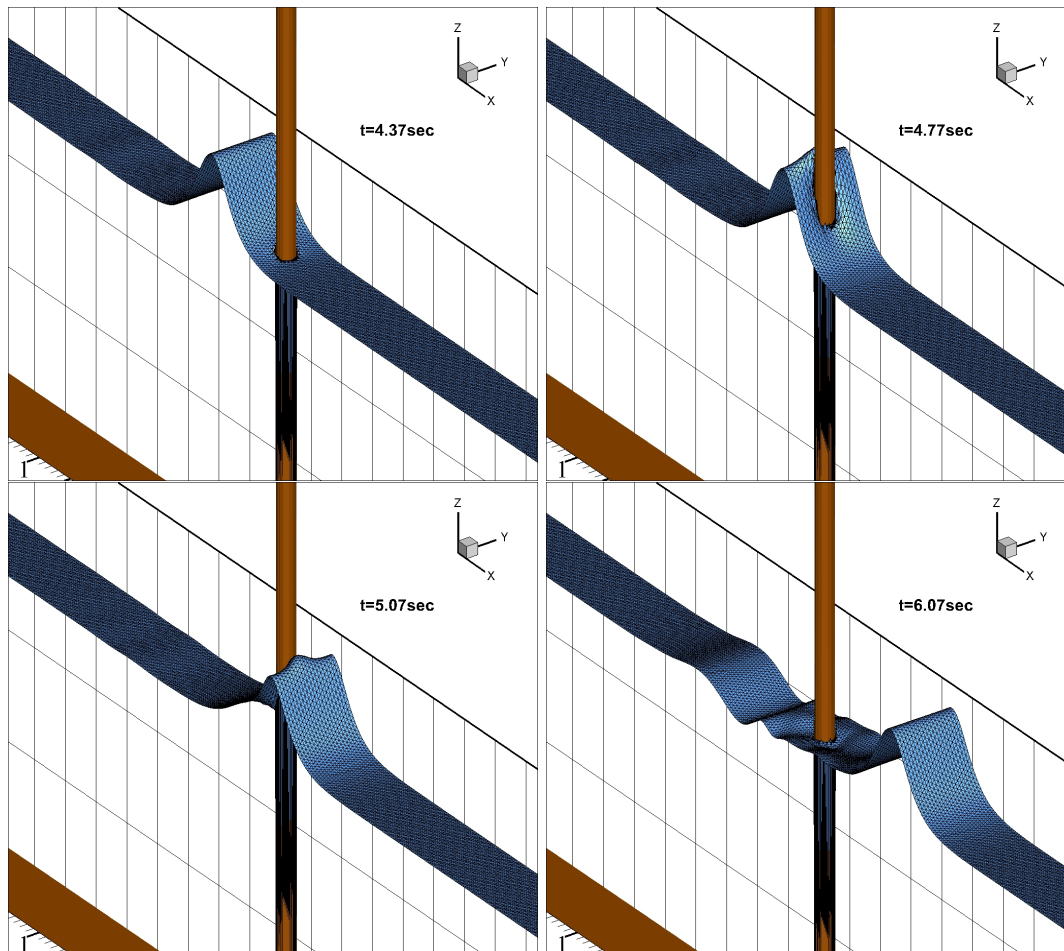


Figure 7.6: Solitary wave-cylinder interaction: 3D view of the free surface at different time instances

faster wave with the wrong shape and phase speed.

7.4 2D run-up of a solitary wave on a conical island

To investigate solitary wave runup on a conical island, large-scale laboratory experiments were performed and presented in [28] motivated largely by the fact that during several events in the 1990s, involving large tsunami waves, unexpectedly large run-up heights were observed on the lee side of small islands. The produced data sets have been frequently used to validate runup models, we refer for example to [104, 161, 162, 108, 26, 86, 67, 125, 187, 45, 164] among others. The laboratory experiments were performed in a large-scale basin at the US Army Engineer Waterways Experimental Station, for the study of three dimensional tsunami run-up on an

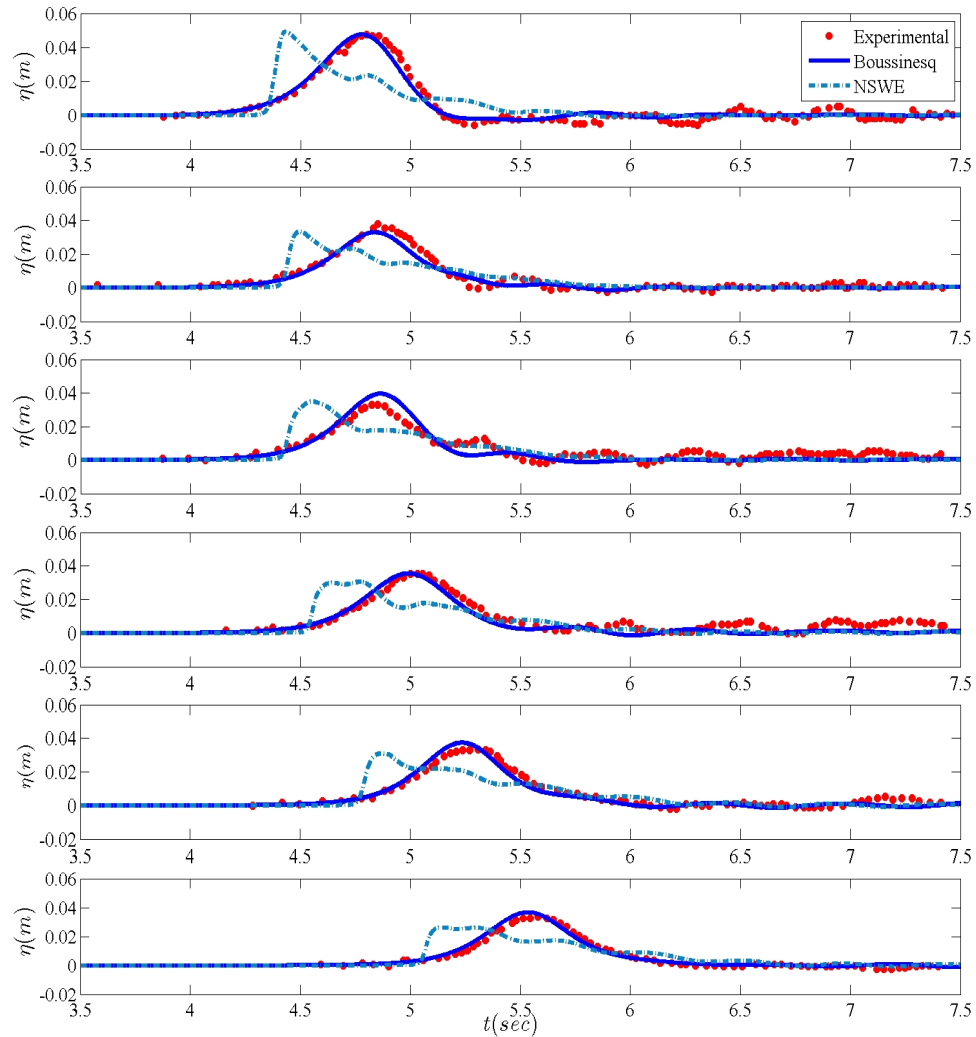


Figure 7.7: Solitary wave-cylinder interaction: numerical and experimental results for η at WG1-WG6 (from top to bottom)

idealized conical island, see [28, 188] for a detailed description and data. These experiments were also studied by analytical means in [88].

In a $25 \times 30m$ basin with a conical island situated near the center, a directional wave-maker was used to produce planar solitary waves of specified crest lengths and heights. The island had a base diameter of $7.2m$, a top diameter of $2.2m$, and it was $0.625m$ high with a side slope 1 : 4. A series of gauges were distributed around the island within the experimental setup in order to measure the free surface elevation. Here we compare the present model with measured data, for both free surface elevation at five wave gauges specified and maximum run-up around the island. It should be mentioned that, the waves generated in the laboratory are dispersive hence this constitutes an almost ideal

test for the accuracy of the present model.

In our numerical model the computational domain was for $(x, y) \in [-5, 28m] \times [0, 30m]$. At the beginning of each simulation the propagating solitary wave was initially centered at $x = 0m$, with its shape given again by the fourth-order *sech*-profile solution from [179]. Sponge layers with width $L_s = 3m$ were imposed at the upstream and downstream boundaries of the computational domain while wall boundary conditions were imposed at side walls. Two cases were reproduced by generating two different incoming waves in a constant depth $h = 0.32m$. The first (case B) is with $A/h = 0.09m$ and the second (case C) with $A = 0.18m$. These values are slightly lower than the target experimental ones because they have been chosen to better represent the recorded data at WG2 downstream of the wavemaker and thus the incident wave conditions to the conical island [108, 67, 187, 164]. Bed friction is neglected following [26, 86], based on the findings in [104], where it was noted that, the computed results are not sensitive to the surface roughness coefficient due to the steep 1:4 slope of the conical island.

When the length of an incoming wave in the long-shore direction is much larger than the base diameter of the island, as in our simulations, a serious run-up is expected at the lee side of the island due to wave refraction around the island that generates two trapped waves. For the experiments with $A/h = 0.09$ it was reported in [161] that wave breaking occurred locally on the lee side of the island where the waves collide, whereas with $A/h = 0.18$ it was reported that wave breaking occurred every where around the island. However, the wave breaking was not too energetic and was characterized as a gentle spilling in [28] and as it will be demonstrated next it does not seem to have a large effect on the numerical results.

For both cases, and after an initial refinement (enrichment), to represent the conical island, the mesh produced $N = 40,855$ nodes with maximum edge length equal to 0.2 and minimum 0.07. The grid used is an Orthogonal (Type II) one. Part of the final mesh can be seen in Figure 7.8 and wave gauge locations. Wave Gauges (WG) 6 and 9 are located near the front face of the island, with WG 9 situated very near the initial shoreline. WG 16 and 22 are also located at the initial shoreline, where WG 16 is on the side of the island and WG 22 on the lee side. The actual gauges position in the physical domain where (6.82, 13.05), (9.36, 13.80), (10.36, 13.80), (12.96, 11.22) and (15.56, 13.80) respectively. The CFL value used in this case was set equal to 0.6. The calculated $\varepsilon_{wd} \approx 5 \cdot 10^{-6}$ for this case.

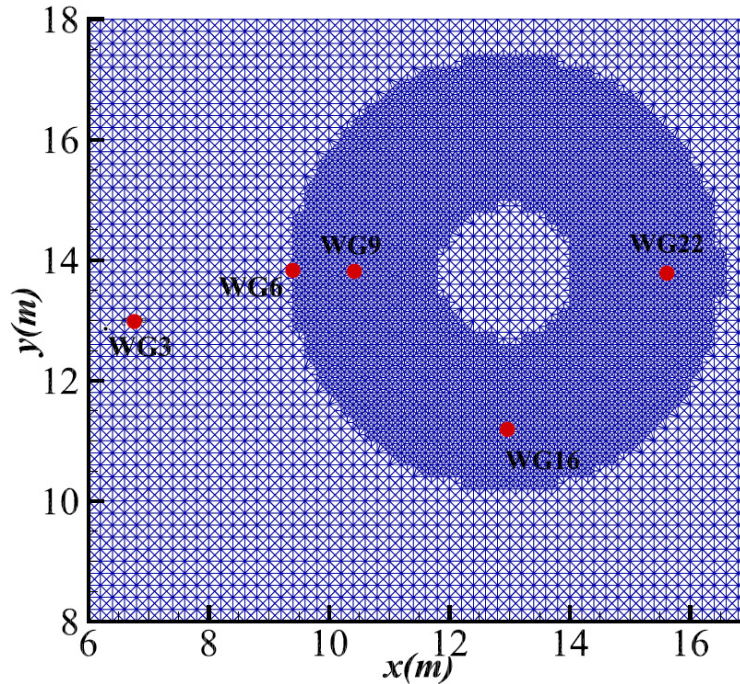


Figure 7.8: Runup of solitary waves on a conical island: mesh and wave gauge locations

Figs 7.9 and 7.10 present a sequence of screenshots, for case B and C respectively, depicting the evolution of the solitary waves as they hit the circular island and show the refraction and trapping of the solitary waves over the island slope. It can be observed that the incident solitary waves generate an initial high run-up in the front side of the island and we emphasize here the absence of motion around the island up to this time. Without utilizing the well-balance wet/dry front treatment presented in Section 5.3 the model would have artificially initiated unphysical motion over the wet/dry interface corrupting the numerical solution. After the maximum magnitude has been reached, the wave runs down the inundated area back to the initial waterline while a portion of the refracted waves propagates around the island towards the lee side, generating two trapped waves at each side of the island. After a short time, these two waves collide at the lee side generating the second high runup. Then, these waves pass through each other and go further propagating around the island. The free surface is rather smooth with indistinguishable frequency dispersion before the wave wraps around the island. As the solitary wave travels down the basin, high-frequency dispersive waves become evident around the island especially on the lee side. Test case C with $A/h = 0.18$ provides a vivid depiction of the generation and propagation of the dispersive waves. Fig. 7.10 shows the generation of the first group of dispersive waves as the trapped waves wrap

around the island and collide on the lee side. After the collision, the second group of dispersive waves is generated due to energy leakage from the two trapped waves that continue to wrap around to the front. The interaction of the first and second groups of dispersive waves generates a mesh-like wave pattern behind the island. Similar observations and results were presented in [187]. It should be noted here that these high-frequency dispersive waves can not be reproduced with a NSWE model see for example [125].

The wave gauges were used to record the transformations of the solitary wave around the island in terms of the free surface elevation and phase speed. With reference to Fig. 7.11 the computed and measured time series at WGs 6, 9, 16 and 22 are presented. These gauges provide sufficient coverage of the representative wave conditions in the experiment. The measured data at WG 2 provided a reference for adjustment of the timing of the computed waveforms [187]. For both cases, the numerical results show a very good agreement with the measured time series including the depression (at the rundown) following the leading wave. Deviations between the numerical and experimental results are becoming more apparent at later times and qualitatively these deviations are similar to those found in the literature. As it was noted in [67], the likely reason for the observed discrepancies after the initial runup is that the front waveforms of the experimental solitary wave were generated more accurately than the rear, which also included a spurious tail, as has been discussed previously in [28, 88]. The model accurately describes the phase of the peak, but slightly overestimates the leading wave amplitude at WG 9 for both cases and WG 22 for case B. These small discrepancies are very likely due to dissipative breaking effects (especially for case C), which are not accounted for in the present model. However, it does not seem that the effects of breaking affected the stability of our model and the inundation around the island, as it can be observed in Fig. 7.11(b) from the results obtained for WG 22.

The maximum run-up is compared with the measured values in Fig. 7.12. For both test cases the match between the computed and measured run-up around the island is very accurate, and is similar or even better to that achieved in previous cited references. The runup on the lee side of the island, caused by the collision of the edge waves circling the island, is well captured for both cases. For case B, as emphasized in [104], the maximum run-up measured at the lee side is actually of the same order of magnitude to that at the front side, but focused on a small area. Our numerical results

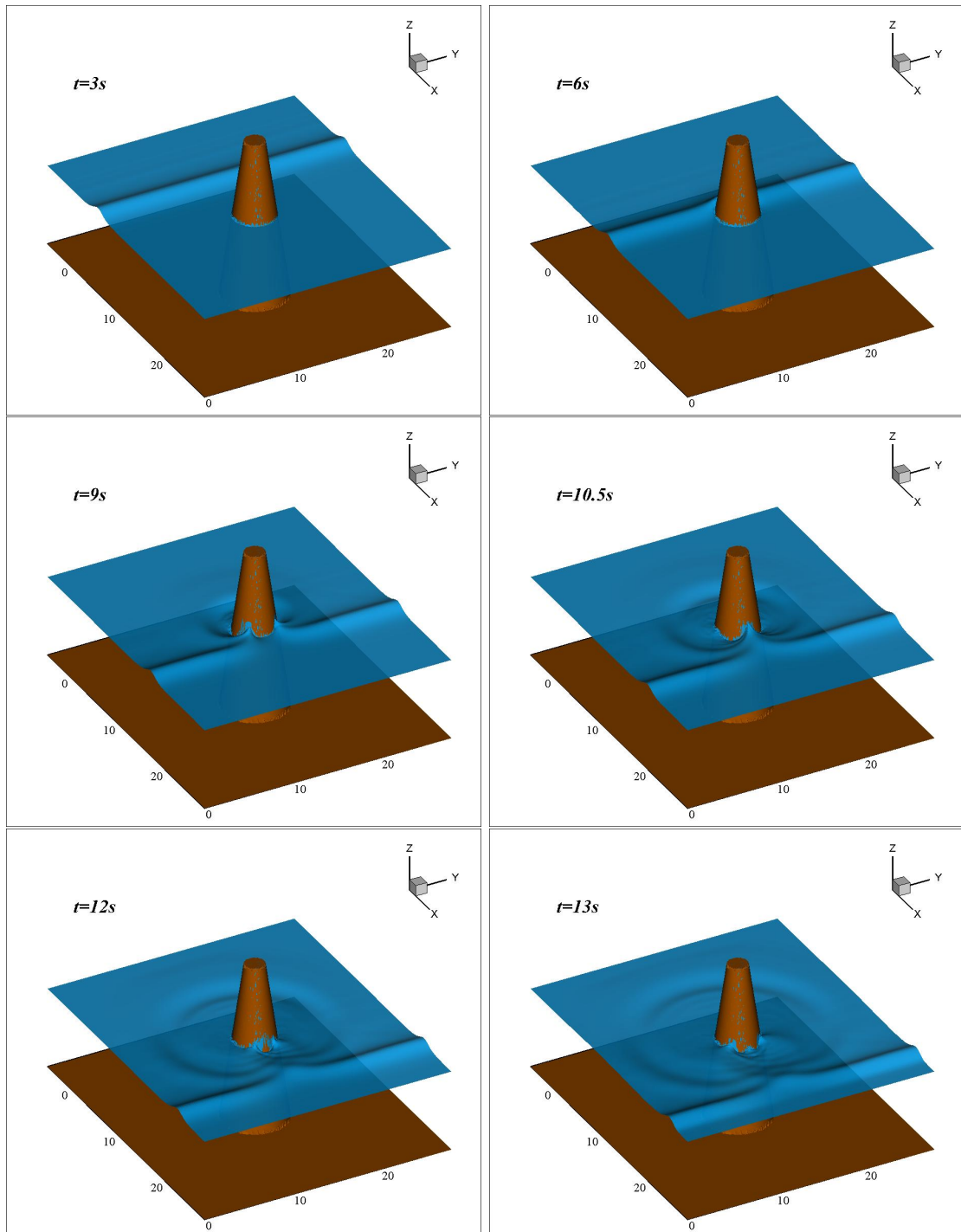


Figure 7.9: Evolution of the solitary wave around the conical island for $A/h = 0.09$ (case B)

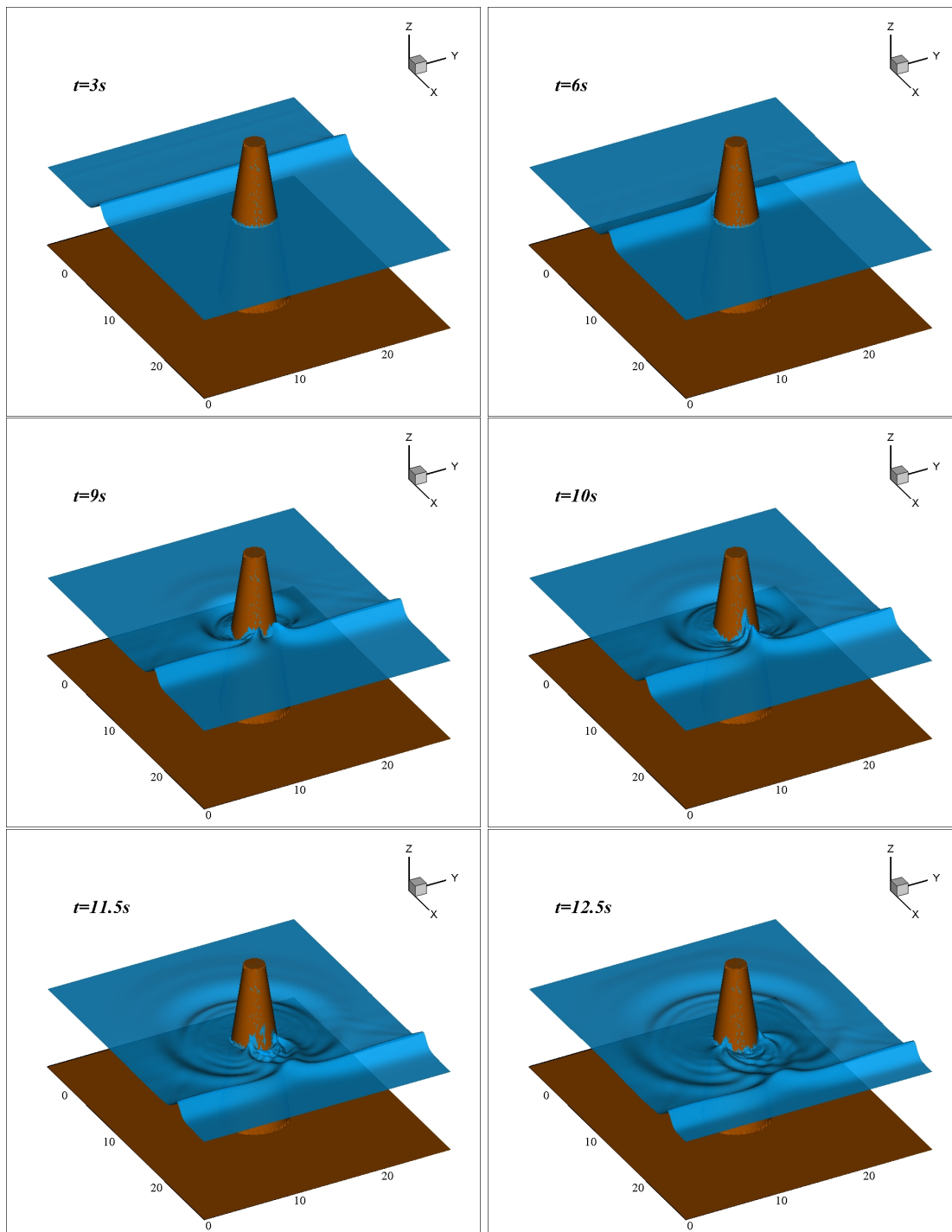


Figure 7.10: Evolution of the solitary wave around the conical island for $A/h = 0.18$ (case C)

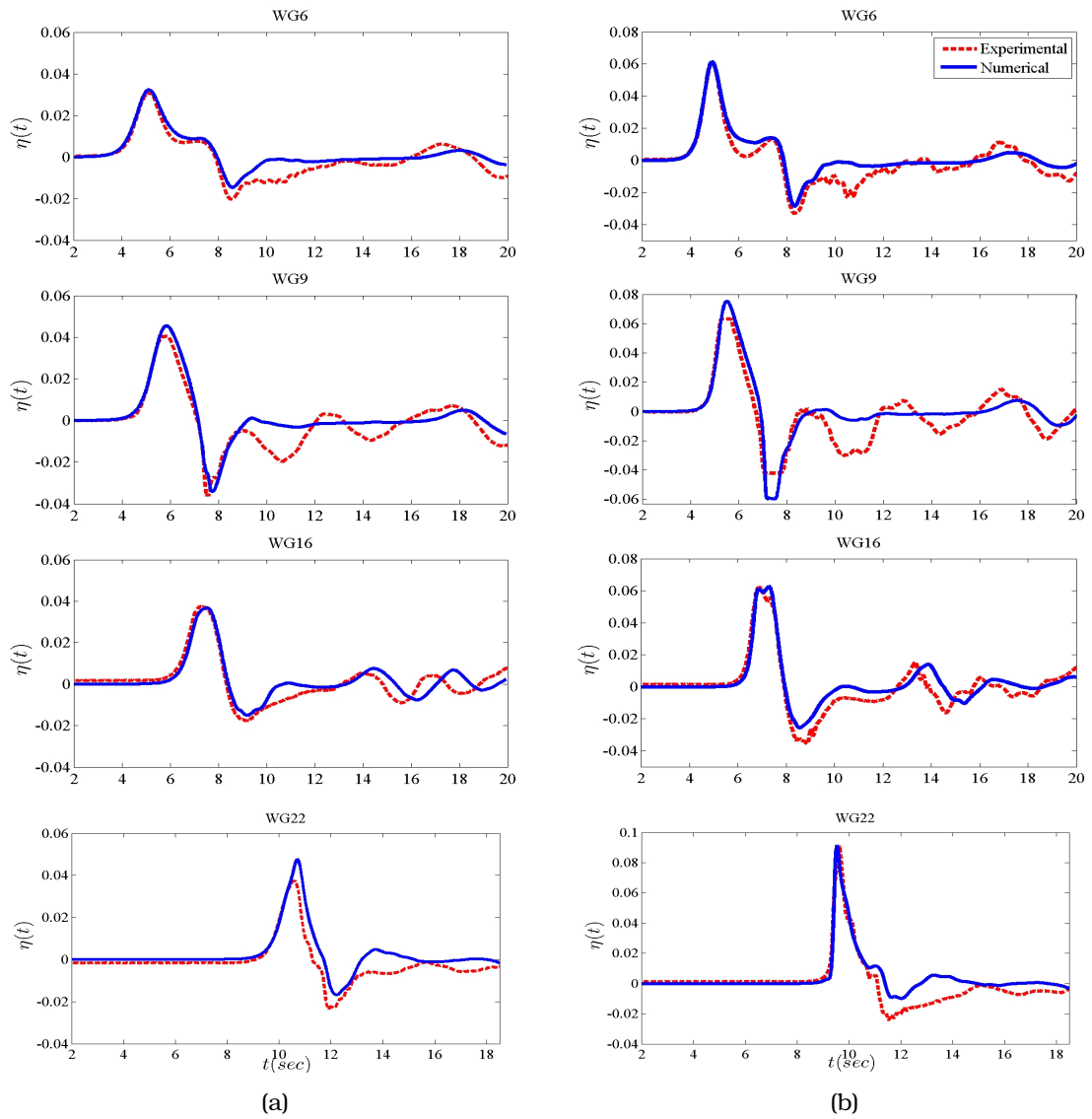


Figure 7.11: Time series of surface elevation at wave gauges around the conical island: (a) $A/h = 0.09$; (b) $A/h = 0.18$

agree with this observation. The inundated area during the run-up is much wider at the front of the island, where almost the entire front is effected, than the lee side but the maximum amplitudes are almost similar.

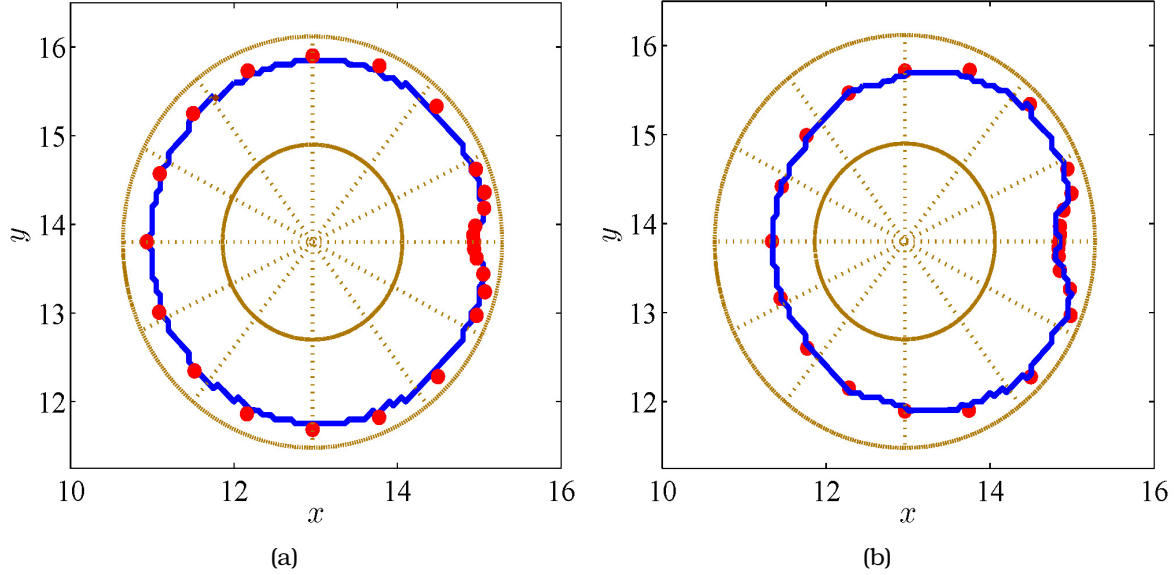


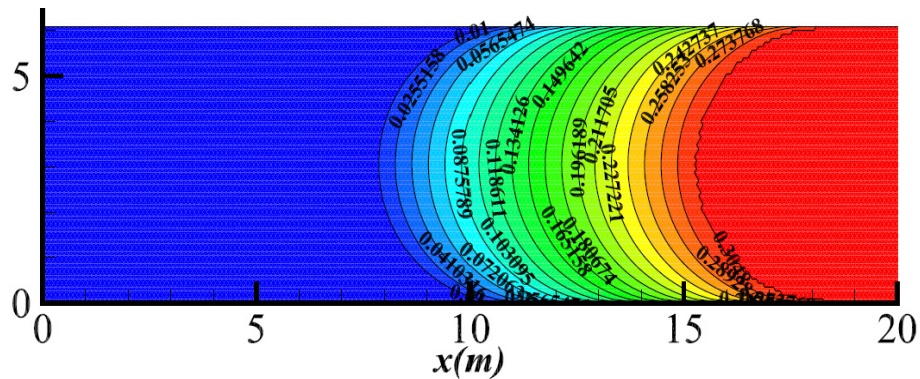
Figure 7.12: Experimental measurements and numerical runup around the conical island with (a) $A/h = 0.09$ and (b) $A/h = 0.181$

7.5 Wave propagation over a semicircular shoal

In this test case we compare the numerical model against the experimental measurements of Whalin [182] for regular waves propagating over a semi-circular shoal. This has become a standard test case for 2D dispersive numerical models to test nonlinear refraction and diffraction, we refer for example [114, 103, 178, 152, 63, 64, 60, 163]. Whalin carried out a set of experiments on wave trains propagating over a semicircular shoal to study the focusing effect induced by the bottom topography. The wave tank was of size $25.6m \times 6.096$ and its middle portion consisted in a semi-circular shoal leading the water depth to decrease from 0.4572 m (at the wavemaker) to 0.1524 m (at the end of the tank). The water depth is described by

$$h(x, y) = \begin{cases} 0.4572 & x \leq 10.67 - \Lambda(y), \\ 0.4572 + 0.04(10.67 - \Lambda(y) - x) & 10.67 - \Lambda(y) < x < 18.29 - \Lambda(y), \\ 0.1524 & x \geq 18.29 - \Lambda(y), \end{cases}$$

where $\Lambda(y) = \sqrt{6.096y - y^2}$. A detail of the resulting bottom topography is shown in Fig. 7.13.



diffraction. Fig. 7.15 compares the spatial evolution of the first and second harmonics with the experimental data, based on a Fourier analysis of the time series of the surface elevation. The water surface elevation was measured along the centreline of the tank, with distance $0.5m$ apart, and harmonic analysis was performed to obtain the amplitude of frequency components. It can be observed that both the first and second harmonics increase in magnitude in the focal zone and the numerical harmonics are consistent with the laboratory data but slightly underestimate it.

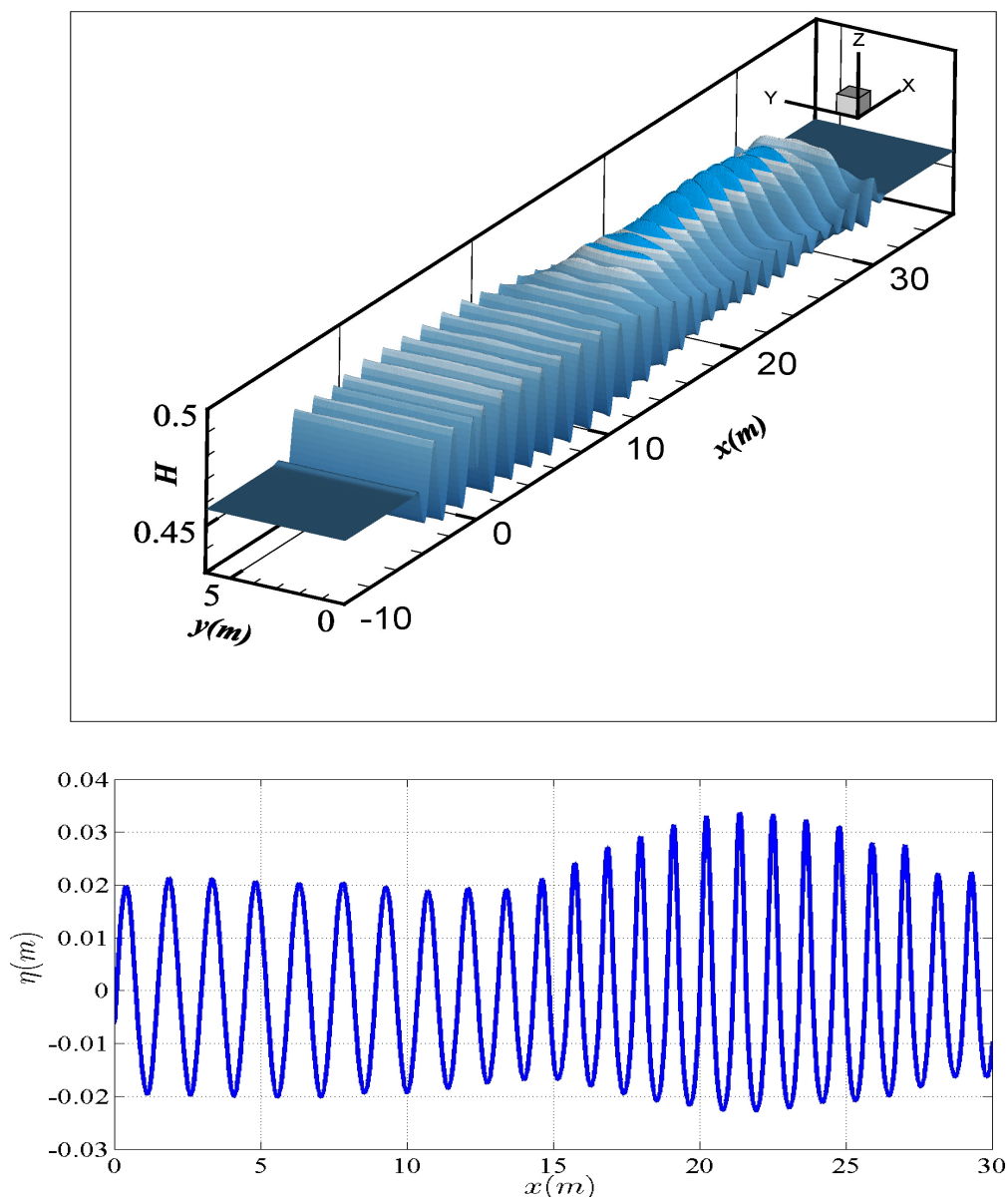


Figure 7.14: Shoaling of regular waves: perspective view of the free surface (top) and surface elevation along the centerline at $t = 40s$ for $T = 1s$

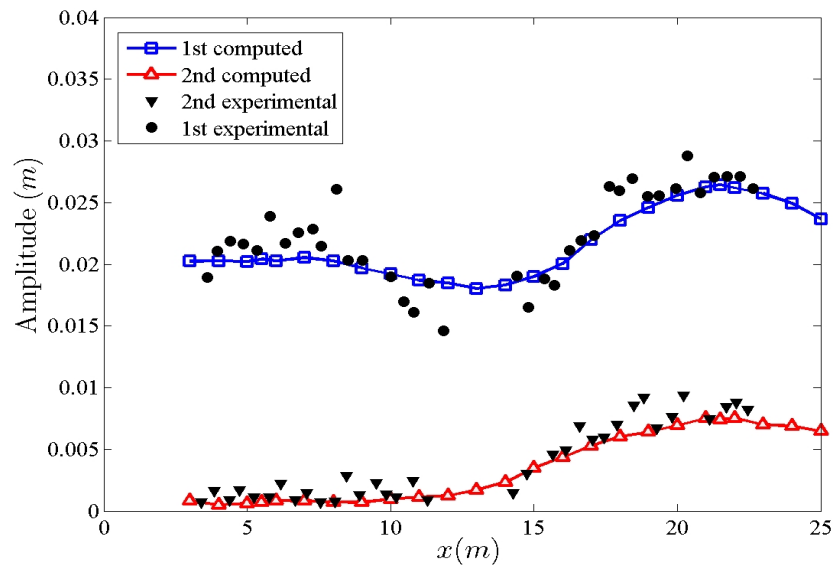


Figure 7.15: Shoaling of regular waves: comparison of the computed and experimental results for the wave amplitudes for the first and second harmonics along the centerline for $T = 1s$

The other two cases have weaker dispersive degree but a higher relative nonlinearity. Fig. 7.16 gives an illustration of the 3D wave patterns after $t = 48.5s$ and the surface elevation along the centerline for the case of $T = 2s$. For this relative longer wave, in addition to the obvious shoaling, the semicircular shoal focus the waves at $x \approx 19.2m$ along the centerline, earlier than in the previous case. The incoming waves are linear, but after the focusing on the shoal, higher harmonics become significant due to nonlinear effects. The energy transfer to higher harmonics is presented in Fig. 7.17 where the spatial evolution of the first, second and third harmonics is compared with the experimental data. As the waves propagate over the shoal, nonlinear effects from wave-wave and wave-bed interactions become more evident, leading to the rapid growth of the second and third harmonics. The results are consistent and in very good agreement with the experimental data, where the modulation of the harmonic amplitude can be seen in all cases. The results are similar or compare in favor to previous studies using weakly nonlinear and dispersive BT models.

Fig. 7.18 gives an illustration of the fully developed wave patterns after $t = 48s$ and the surface elevation along the centerline for the case of $T = 3s$. For this test case with nearly shallow water conditions, the combined refraction-diffraction over the semicircular shoal becomes more complicated due to significant relative nonlinearity.

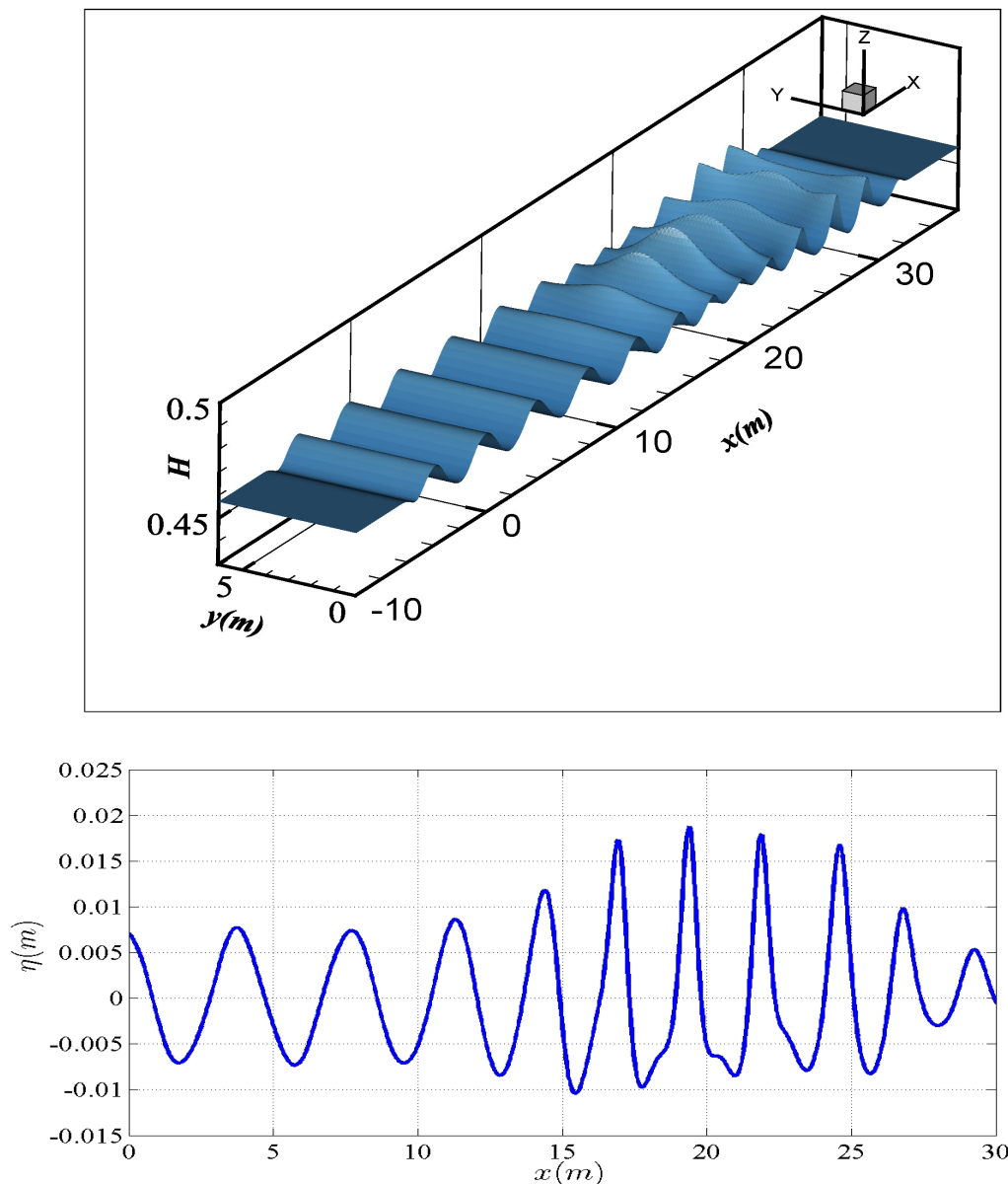


Figure 7.16: Shoaling of regular waves: perspective view of the free surface (top) and surface elevation along the centerline at $t = 48.5s$ for $T = 2s$

The wave focusing phenomenon is again evident. The harmonic analysis presented in Fig. 7.19 shows that the numerical results overestimate the first harmonic amplitude and underestimate the second and third harmonics. This same trend has been presented also in most previous studies, we refer for example in [114, 103, 60, 163? ?]. These discrepancies between numerical results and laboratory data were attributed to the shorter evolution distance for this test case or to the presence of free reflected waves.

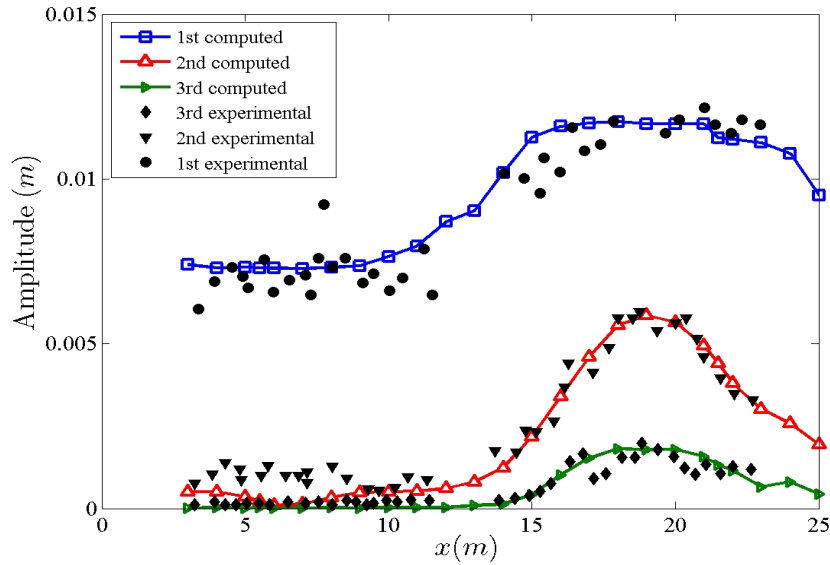


Figure 7.17: Shoaling of regular waves: comparison of the computed and experimental results for the wave amplitudes for the first, second and third harmonics along the centerline for $T = 2s$

7.6 Wave propagation over an elliptic shoal

In this test we study monochromatic wave propagation over a shoal. Berkhoff et al. [16] carried out an experiment to study the refraction and diffraction of 2D monochromatic waves over a complex bathymetry. Many researchers have used this test to validate their Boussinesq models, although this is a standard test to verify models based on the mild-slope equations. We refer for example to [179, 163, 138, 178, 132, 109]. The model set up and bottom geometry is shown in Fig. 7.20. The wave tank was 20m wide and 22m long, and the bottom topography consists of an elliptic shoal, over an inclined slope of $1/50$, forming a 20° angle with the x axis. The maximum water depth is $h = 0.45m$ at the wave maker, which is placed at $y = -10m$. The bathymetry is described by the formula $b = b_f + b_s$, where

$$b_f(x, y) = \begin{cases} (5.82 + y_r)/50, & \text{if } y_r \leq -5.82, \\ 0, & \text{otherwise} \end{cases} \quad (7.1)$$

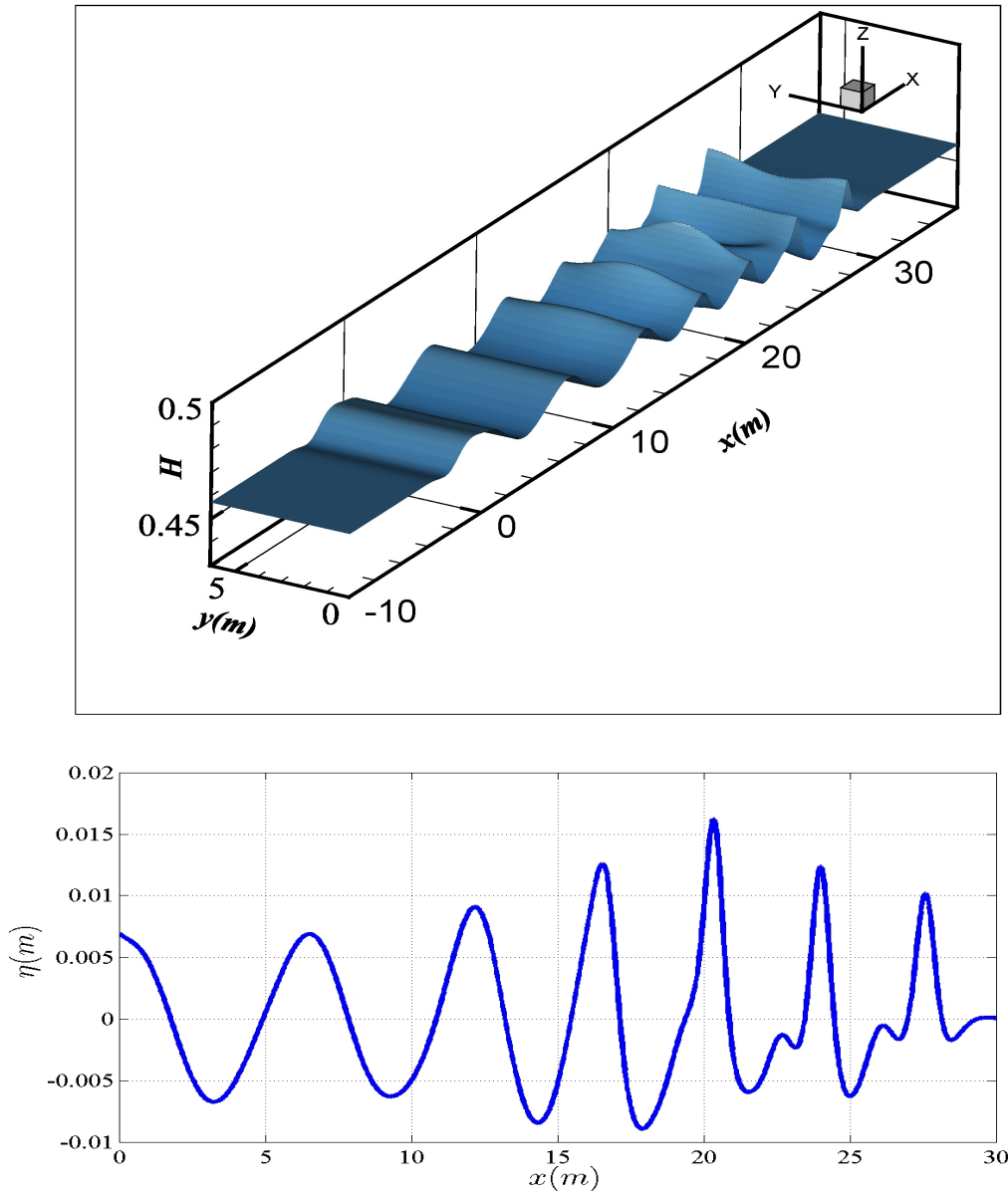


Figure 7.18: Shoaling of regular waves: perspective view of the free surface (top) and surface elevation along the centerline at $t = 48s$ for $T = 3s$

and

$$b_s(x, y) = \begin{cases} -0.3 + \frac{1}{2} \sqrt{1 - \left(\frac{x_r}{5}\right)^2 - \left(\frac{4y_r}{15}\right)^2}, & \text{if } \left(\frac{x_r}{4}\right)^2 + \left(\frac{y_r}{3}\right)^2 \leq 1, \\ 0, & \text{otherwise,} \end{cases} \quad (7.2)$$

where $x_r = x \cos(20^\circ) - y \sin(20^\circ)$, $y_r = x \sin(20^\circ) + y \cos(20^\circ)$. The incoming wave has period $T = 1s$ and amplitude $A = 0.0232m$ while nonlinearity is $\epsilon = 0.3$ and Stokes number is $S = 1.13$. Surface elevation was measured at sections $x_m = 0$ and $y_m =$

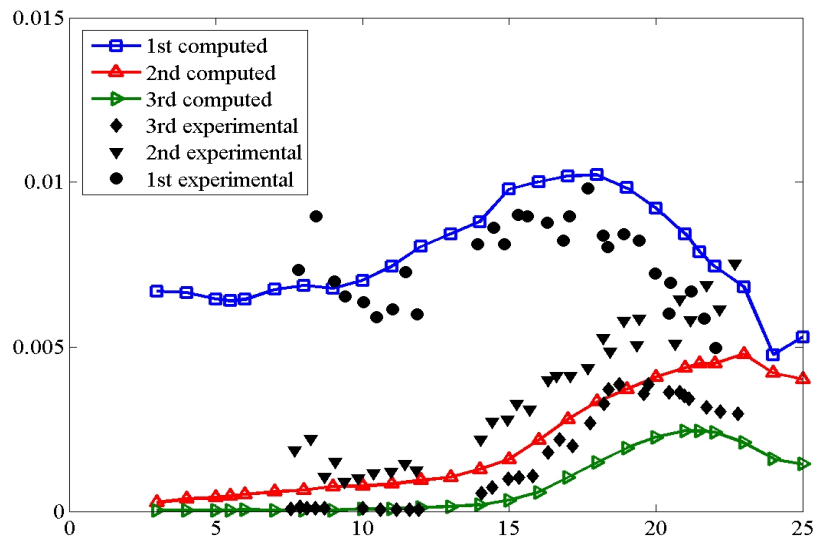


Figure 7.19: Shoaling of regular waves: comparison of the computed and experimental results for the wave amplitudes for the first, second and third harmonics along the centerline for $T = 3s$

[1.0, 3.0, 5.0, 7.0, 9.0] as shown in Fig. 7.20 and the mean wave height is computed.

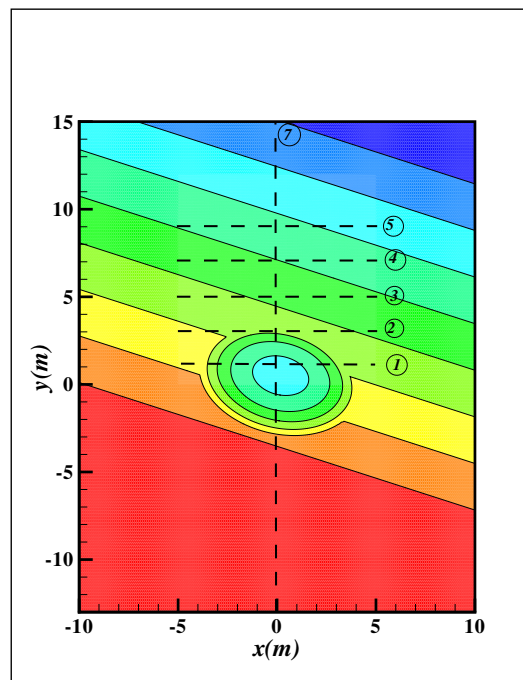


Figure 7.20: Bottom topography and position of experimental sections for the wave propagation over an elliptic shoal test case

The computational domain is $[-10, 10] \times [-13, 15]$. The grid consists of triangles

with edge size of $0.1m$ and has been refined in the region of the shoal with $h_N = 0.05$. The sponge layers of $2.5m$ width, are placed at the top and the bottom of the domain and a CFL value of 0.3 is used. The simulation period is $50s$ and the ten last waves are employed to estimate wave height, using the zero-up crossing technique.

The results normalized by the incoming wave amplitude are reported to Fig. 7.21. The agreement between the numerical results and the experimental data are quite satisfactory and comparable to the results found in the literature [179, 163, 138, 178, 132, 109]. Wave's focusing occurs behind the shoal, due to refraction and wave height is well reproduced. In section 5 (see Fig. 7.20) the maximum amplification factor is well predicted instead to other results in the literature [163, 179] which is underestimated. These results demonstrate that wave refraction and diffraction can be well simulated by the numerical model.

7.7 Solitary wave run-up on a plane beach

The below test cases are an extension of one dimensional test cases described in Section 4.4. The incident wave height for the case considered here is $A/h = 0.28$. As described before, the wave broke strongly both in the run-up and the run-down phases of the motion. The 2D topography of the problem in two dimension has the form

$$b(x, y) = \begin{cases} -x \tan \beta, & x \leq \cot \beta \\ -1, & x > \cot \beta \end{cases} \quad (7.3)$$

A solitary wave is placed at point that is located at half wavelength from the toe of the beach. The initial surface profile for η and velocity \mathbf{u} (with $v = 0$) was computed again with the semi-analytical solution from [179]. Also, a Manning coefficient of $n_m = 0.01$ is used in order to define the glass surface roughness used in the experiments. We consider a computational domain of $(x, y) \in [-20, 60m] \times [0, 0.8m]$. The numerical model use a triangular grid consisting of equilateral triangles with side length of $h_N = 0.05m$ leading to a mesh of $N = 30,428$ nodes, the CFL number is $C_r = 0.35$ and a sponge layer is applied offshore with length of $5m$. The threshold value is $\epsilon_{wd} = 1.d - 5$

Fig 7.22 and 7.23 compares the measured surface profiles and the models results for different non-dimensional times. Numerical results using the hybrid wave breaking model 6.6.2 (with $\partial_t \eta^{(I)} = 0.55 \sqrt{gh}$ and $\partial_t \eta^{(F)} = 0.15 \sqrt{gh}$) and the eddy viscosity model

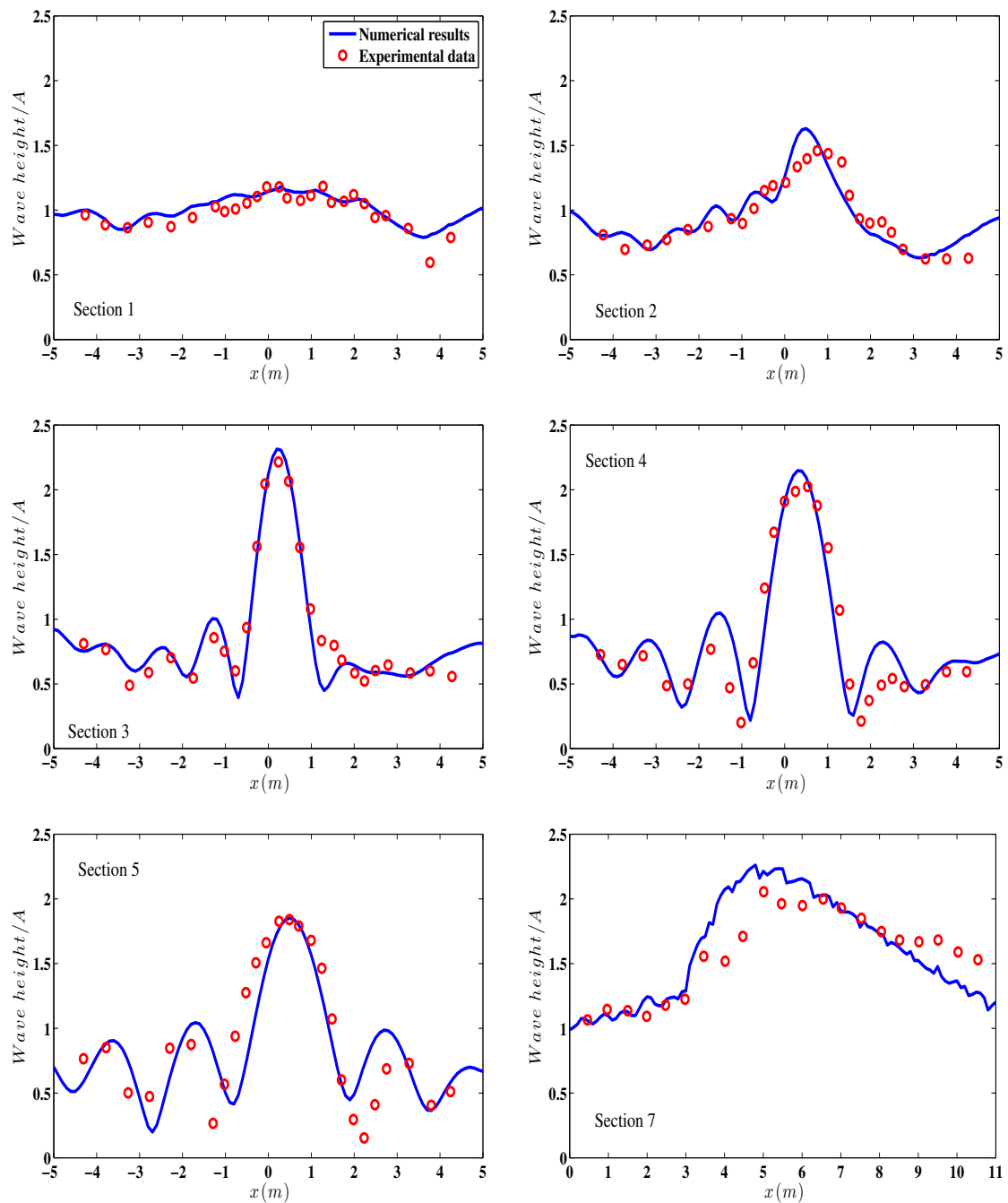


Figure 7.21: Wave diffraction over an elliptic shoal. Comparison of the computed average wave height with the experimental data [16] in sections 1-5 and 7

6.6.1 are simultaneously presented. Until time $t\sqrt{g/h} = 10$ the solitary propagates through the shore and the two models are identical, as expected, since wave breaking starts around $t\sqrt{g/h} = 15$. The experimental wave breaks around $t\sqrt{g/h} = 20$. The numerical solution for the new hybrid model, is represented like a bore storing the water

spilled from the breaking wave behind the front. We can see the different approaches of the two wave breaking models. In the eddy viscosity model the wave breaking is simulated as a triangular bore. The numerical results agree well with the experimental data. Similar behavior has been observed by other researchers too [189, 47, 108]. At time $t\sqrt{g/h} = 25$ the bore collapses at the shore and the results shows good qualitative agreement except the front face of the bore which is due to the different bore head at breaking time. After that the wave starts to run-up. The time of maximum runup occurs at $t\sqrt{g/h} = 45$. up to that time the computed solution fully recovers due to the volume conservation in both models. As the water recedes a breaking wave is created at $t\sqrt{g/h} = 55$ near the still water level. The numerical solution is approximated as a hydraulic jump. According to Kennedy et al. [93] the largest disadvantage of the eddy viscosity model is that, in some cases, such as stationary hydraulic jumps, breaking initiation is not recognized. For that reason oscillations at the numerical solution of the eddy viscosity model were observed after $t\sqrt{g/h} = 55$ and the solution became unstable. Thus, no results for this model are included in Fig. 7.23 for times $t\sqrt{g/h} = 70$ and $t\sqrt{g/h} = 80$. Zelt [189] has also mentioned that it might also be necessary to treat that backwash bore by a completely different breaking algorithm in place of the artificial viscosity model. On the other hand, the new hybrid breaking model has better agreement with the experimental data. Although the numerical scheme used is of third-order spatial accuracy, the numerical results are very similar to those obtained by the 1D FV/FD scheme (see Section 4.4) which is fourth order formally in space.

Figure 7.24 shows distinct runup regimes for breaking and non-breaking waves where maximum vertical runup is scaled by the water depth. Both measured and computed runup results along with the theoretical runup law of Synolakis [157] are depicted. The current predictions are in close agreement with the experimental data for breaking and non-breaking events. There is a distinct transition between the two events, with the data to the right of the transition representing spilling and plunging breakers. Our model simulates the runup of plunging breakers extremely well indicating that the proposed wave breaking treatment dissipates correctly the energy, associated to the wave breaking, providing stable results without implementing artificial smoothing or filtering.

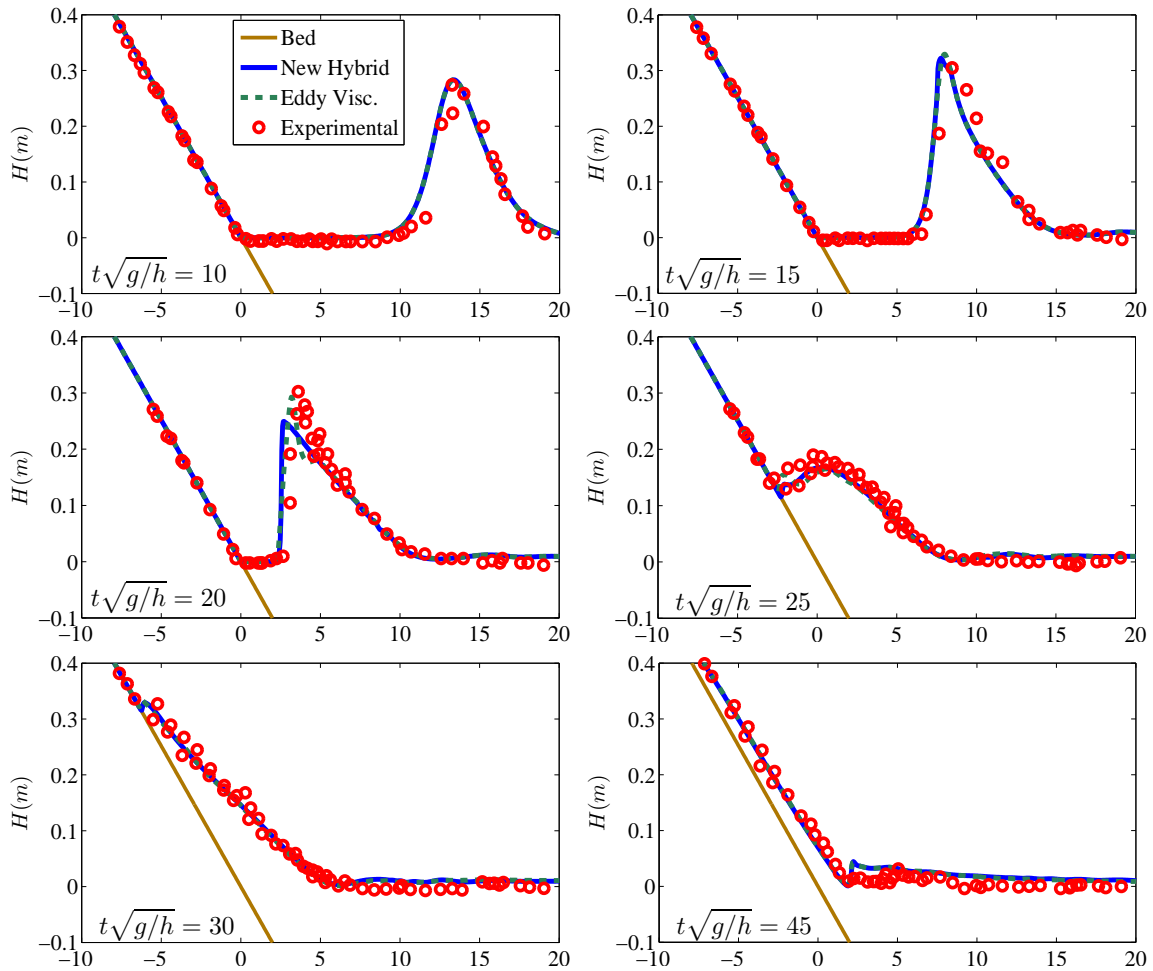


Figure 7.22: Free surface elevation of solitary wave run-up on a plane beach for $A/d = 0.28$ (cont)

7.8 Breaking waves on a sloping beach

Hansen and Svendsen [79] performed a number of regular wave test on plane slopes in order to study wave shoaling and breaking on a beach. Waves were generated over a $0.36m$ horizontal bottom, propagated shoaled and broke over a slope of $1 : 32.26$. Multiple tests were performed including plunging breakers, plunging-spilling breakers and spilling breakers and many authors have used the experimental data for model validation. We refer for example to [93, 164, 147, 90, 48, 175].

Two of these experiments, producing breaker types ranging from gentle spilling to strong plunging, are recreated numerically, described in Table 7.2. We consider $T(s)$ regular wave's period, $H(m)$ the incident wave height and S the corresponding Stokes number. The computational domain is $52m$ long and $1m$ wide were $(x, y) \in$

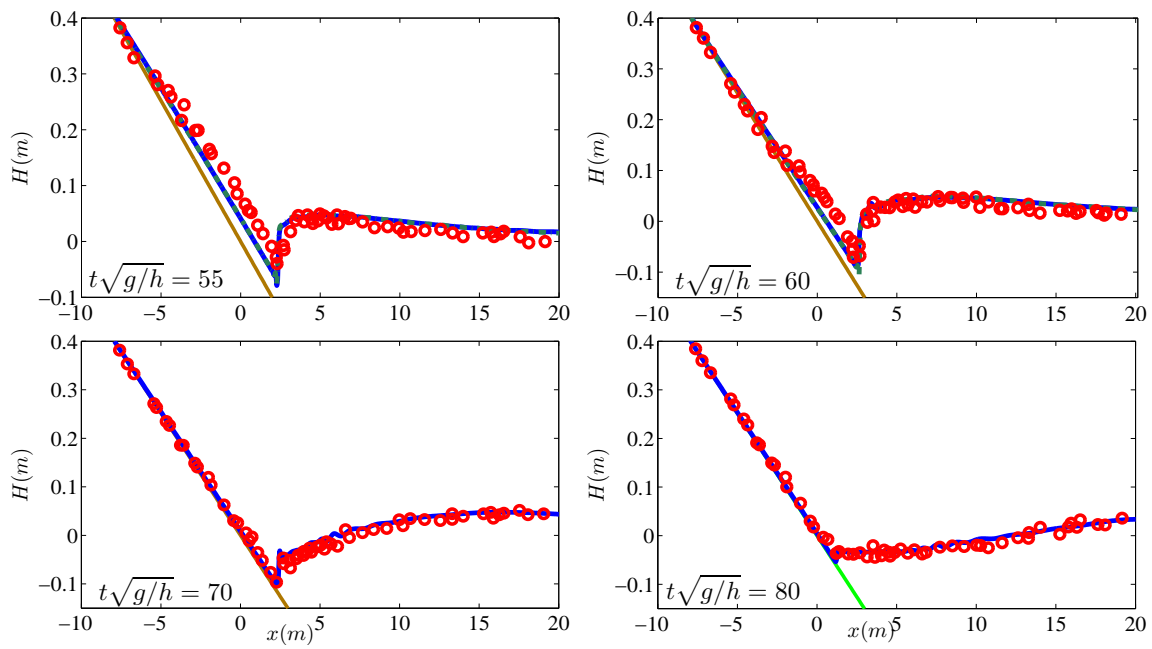


Figure 7.23: Free surface elevation of solitary wave runup on a plane beach for $A/d = 0.28$

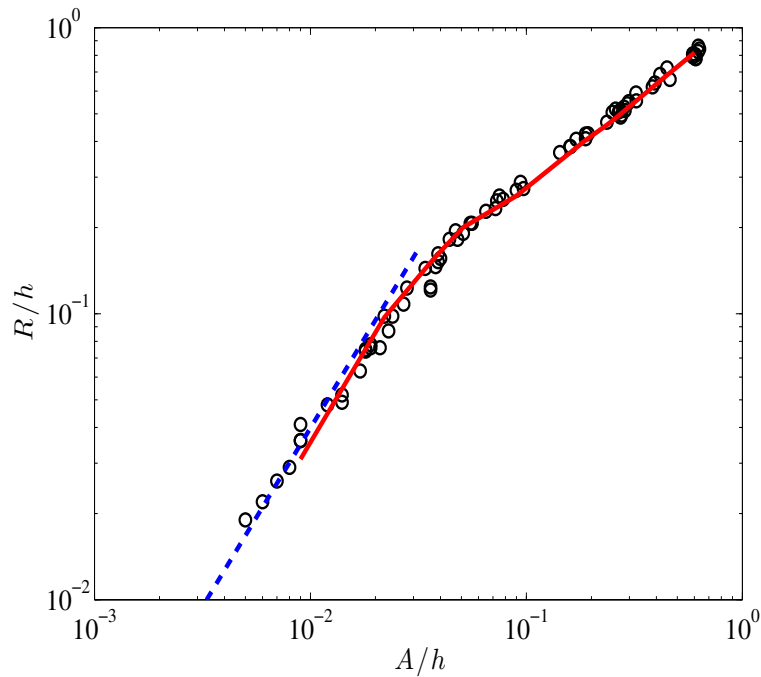


Figure 7.24: The normalized maximum runup of solitary waves up a 1:19.85 beach versus the normalized wave height. Solid line and circles denote computed and measured data. Dashed line denote the runup law.

$[-26, 26m] \times [0, 1m]$. For the computation a triangular grid was used, consisting of equilateral triangles with side length $h_N = 0.025$, leading to a mesh of $N = 49,956$ nodes. The CFL value used was 0.35 and $\gamma = 0.6$. A sponge layer of $L_s = 10m$ is applied at the offshore boundary of the domain and the wave-making internal source function is used at a distance $14.78m$ of the toe of the beach. Bottom friction is not considered in this test case. The free surface elevation is reordered at gauges which are placed every $0.1m$ along the center-line. The time series are analyzed evaluating the mean wave height and the position of the mean water level (MWL). The numerical results are compared to the experimental data. Figure ?? shows computed and measured wave heights and mean water level as the wave propagates up the slope.

Table 7.2: Experimental wave characteristics for Hansen and Svendsen Tests.

Test	$T(sec)$	$H(m)$	S	Breaking type
031041	3.333	0.043	17.5588	Spilling-plunging
051041	2.0	0.036	4.8077	Spilling

The computational domain is $52m$ long and $2m$ wide. The sloping beach starts at a distance of $26m$ from the offshore boundary and the internal wave generator has been placed at a distance of $14.78m$ from the toe of the beach (see Fig. 7.25). A sponge layer is placed in front of the offshore boundary and for the cases considered here $L_s = 10, 10.4m$ for Test 041041, 051041 respectively. For the computation a triangular grid was used, consisting of equilateral triangles with side length of $0.5m$, leading to a mesh of $N = 24,996$ nodes. The CFL number used was set to 0.3 and $\delta = 3.0$ in all cases.

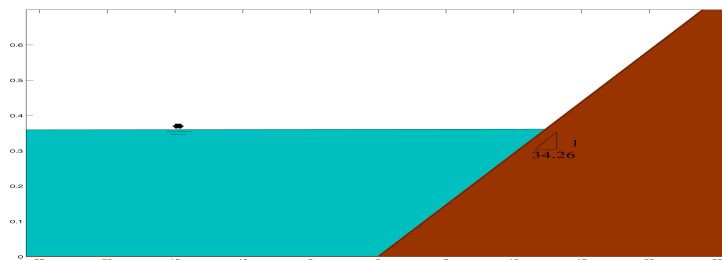


Figure 7.25: Definition sketch of the numerical domain for the test cases of Hansen and Svendsen [79]

Fig. 7.26 illustrates the wave-by-wave treatment and the l_{NSW} area along the centerline for our hybrid model and for test case 031041, at two time instances. As they

propagate shore-ward, the waves gradually steepen, due to shoaling, and the surface variation criterion flags for breaking first. After a while the waves are fully broken and energy is dissipated while propagating shore-ward leading to a progressive decrease of the wave breaker heights and front slopes. The surface variation criterion is active on each bore front until the fronts reach the shoreline. Individual breaking fronts can be seen as they are tracked by the model.

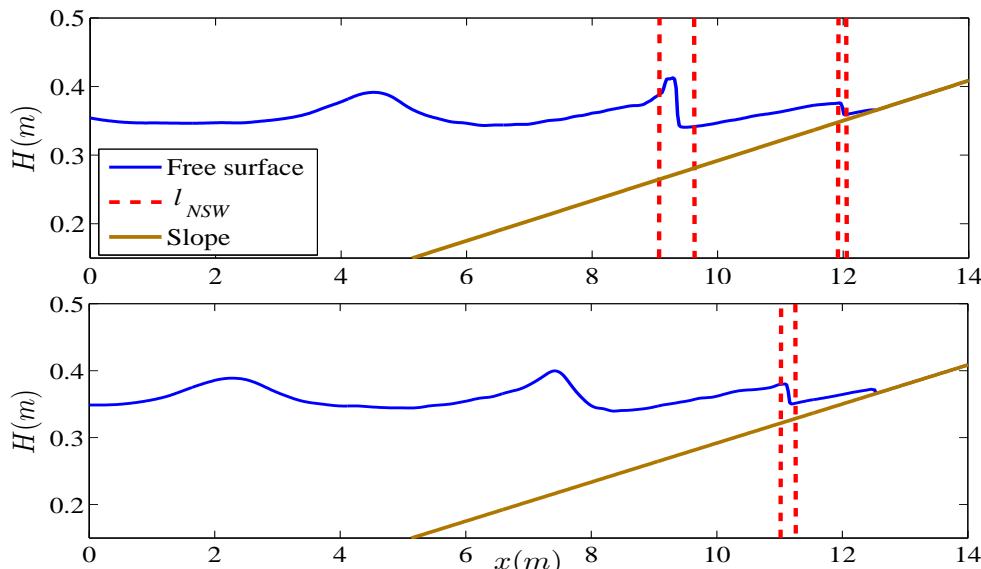


Figure 7.26: Spatial snapshots, along the centerline, of regular waves over a sloping beach with the flow between two consecutive vertical lines governed by the NSW equations

The numerical results of the hybrid model and the eddy viscosity one, using $\partial_t \eta^{(I)} = 0.5 \sqrt{gh}$ and $\partial_t \eta^{(F)} = 0.15 \sqrt{gh}$, are compared to the experimental data in Fig. 7.27 for case 031041. The results show the computed and measured wave heights and MWL as the wave propagates shoal and breaks up the slope. Both sets of wave breaking formulations predict reasonably well the location of the breaking event, that happens slightly earlier compared to the experimental data. This is due to the overshooting produced in the numerical wave, which is closely connected to the nature of the weakly nonlinear weakly dispersive BT model used here, [93]. The differences in the wave height prediction at the swash zone, between the two models is attributed to the different nature of the wave breaking mechanisms. The hybrid mechanism represents the breaking wave as a shock storing the water spilled from the breaking wave behind the front while the eddy viscosity formulation initiates a diffusion coefficient added to the momentum

equation which models the turbulent mixing and dissipation caused by breaking. Wave heights in the inner surf zone tend to be over predicted by the eddy viscosity model and this has also been observed in [93, 147]. In the wave set-up results, a small discrepancy between the measured data and the numerical results can be observed and its is due to the transformation of the regular wave, as expected, since the Stokes number in this case is 17.558 and is far away of the limits of the BT equations of Nwogu.

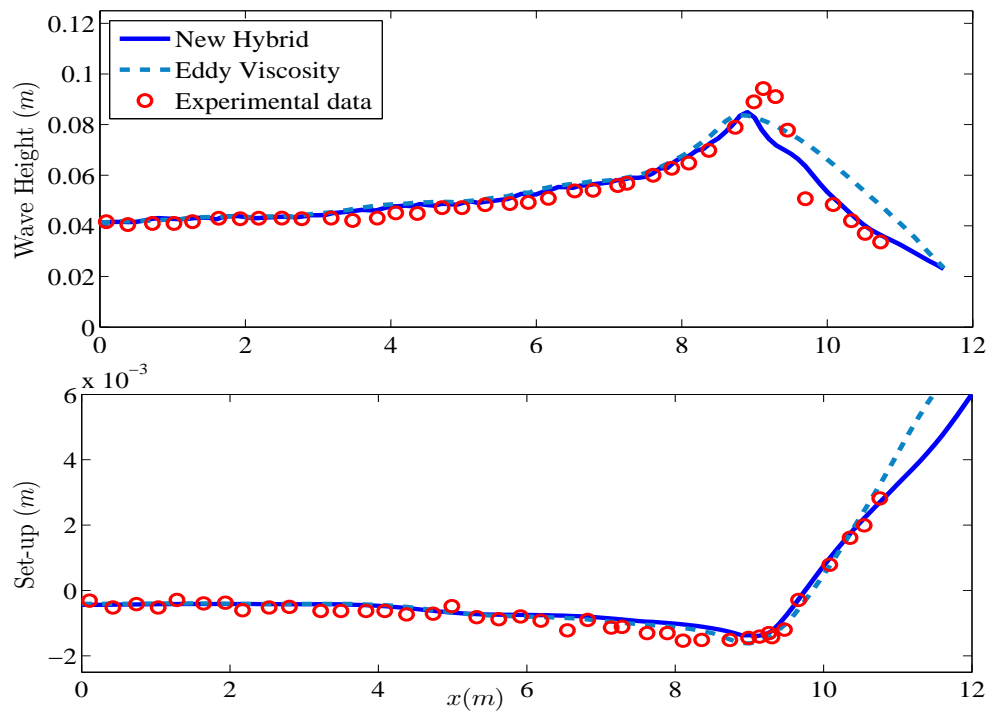


Figure 7.27: Computed and measured wave heights(top) and set-up (bottom) for the Hansen and Svendsen plunging breaker 031041

In Fig. 7.28, results of the hybrid model and the eddy viscosity one are compared to the experimental data in for case 051041. Wave shoaling is again predicted moderately well for both the hybrid and the eddy viscosity model, along with a somewhat premature breaking. Again, the numerical prediction of the wave height in the inner surf zone is better for the hybrid model compared to the eddy viscosity one. The same behavior can be observed on the set-up computations.

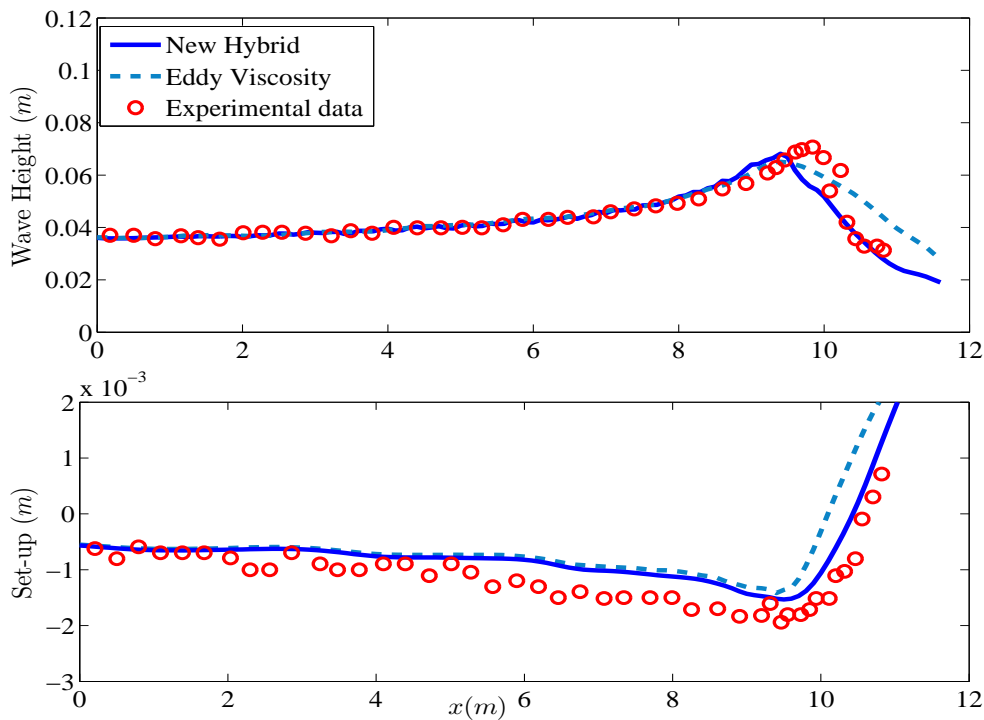


Figure 7.28: Computed and measured wave heights(top) and set-up (bottom) for the Hansen and Svendsen spilling breaker 051041

7.9 Regular wave propagation over a submerged bar

Next, and for 2D, the regular wave propagation over a submerged bar test is implemented. This test is extensively described (for 1D) in section 4.5 where test's configuration can be found. The experimental set-up was conceived to investigate the frequency dispersion characteristics and nonlinear interaction of complex wave propagation phenomena. As the wave propagates over a submerged bar multiple transformations occur, such as non-linear shoaling, amplification of bound harmonics and wave breaking. Two case are implemented using the 2D unstructured FV model. Case (a) and (c) (see section 4.5).

For the test case (a), and to be able to apply appropriate length sponge layers, upstream and downstream, as well as of using the wave-making internal source function from Section 6.5 at $x = 0m$, the dimensions of the computational domain were set to $(x, y) \in [-10, 30mm] \times [0, 0.8m]$. δ in the wave generation function is 0.8 and $L_s = 6.5m$. For the computation a triangular grid was used, consisting of equilateral triangles with side length of 0.05m, leading to a mesh of $N = 72,679$ nodes. The CFL number used was set equal to 0.4. The free-surface elevations are recorded at eight gauges over and

behind the bar as in the laboratory experiment. They have been placed along the flume at $x = 2.0, 5.7, 10.5, 13.5, 15.7, 19.0 \text{ m}$. The definition of the computational domain along the centerline as well as the wave gauge locations are shown in Fig. 4.15. In the wave evolution for the first non-breaking case (a) and, regular waves are generated and propagated without changing their shape, until they reach the front slope. On the slope the waves shoal since nonlinear effects cause the waves to steepen. The wave amplitude grows and the surface profile becomes asymmetric. The back slope causes the waves to breakup into independent waves traveling at their own speed. Hence, bound higher harmonics are developed along the front slope, which are then released from the carrier frequency on the lee side of the bar as the water depth parameter kh increases rapidly. Fig. shows the results for case (a). The numerical results provide good agreement with the experimental data for WG 4 and 5, reproducing the wave transformations over the front slope and immediately behind the front slope. The numerical results maintain relatively good agreement with the experimental data at WG 6-8 over the crest and the lee-slope, where the waveform undergoes significant transformation with high frequency dispersion. Discrepancies arise behind the bar over the flat bottom between numerical and experimental data for WG 9-11, where higher harmonics are released. As it was commented in [142], a spectral analysis shows evidence of fourth and fifth-order harmonics of $6 < kh < 10$, which cannot be (fully) resolved by the governing equations, but do not contain significant energy to affect the overall performance of the model.

For the test case (c) the dimensions of the computational domain were set to $(x, y) \in [-26, 26\text{m}] \times [0, 0.8\text{m}]$ with sponge layer widths is set to $L_s = 10\text{m}$ at both ends of the computational domain. For the computation a triangular grid was used, consisting of equilateral triangles with side length of $h_N = 0.014\text{m}$, leading to a mesh of $N = 25,078$ nodes. The CFL number used was set equal to 0.35 with the value of γ now set to 0.3. All other computational parameters are like before. Since we are interested only on the breaking behavior of the model and due to the inability of the BT model to fully resolve the higher harmonics released at the lee side of the bar [92], only four wave gauges were placed at $x = 6, 12, 13$ and 14m respectively as shown in Fig. ??, along with the problem's geometry along the centerline.

In the wave evolution, waves shoal along the front slope, since nonlinear effects cause the waves propagating along this slope to steepen and broke at the beginning of

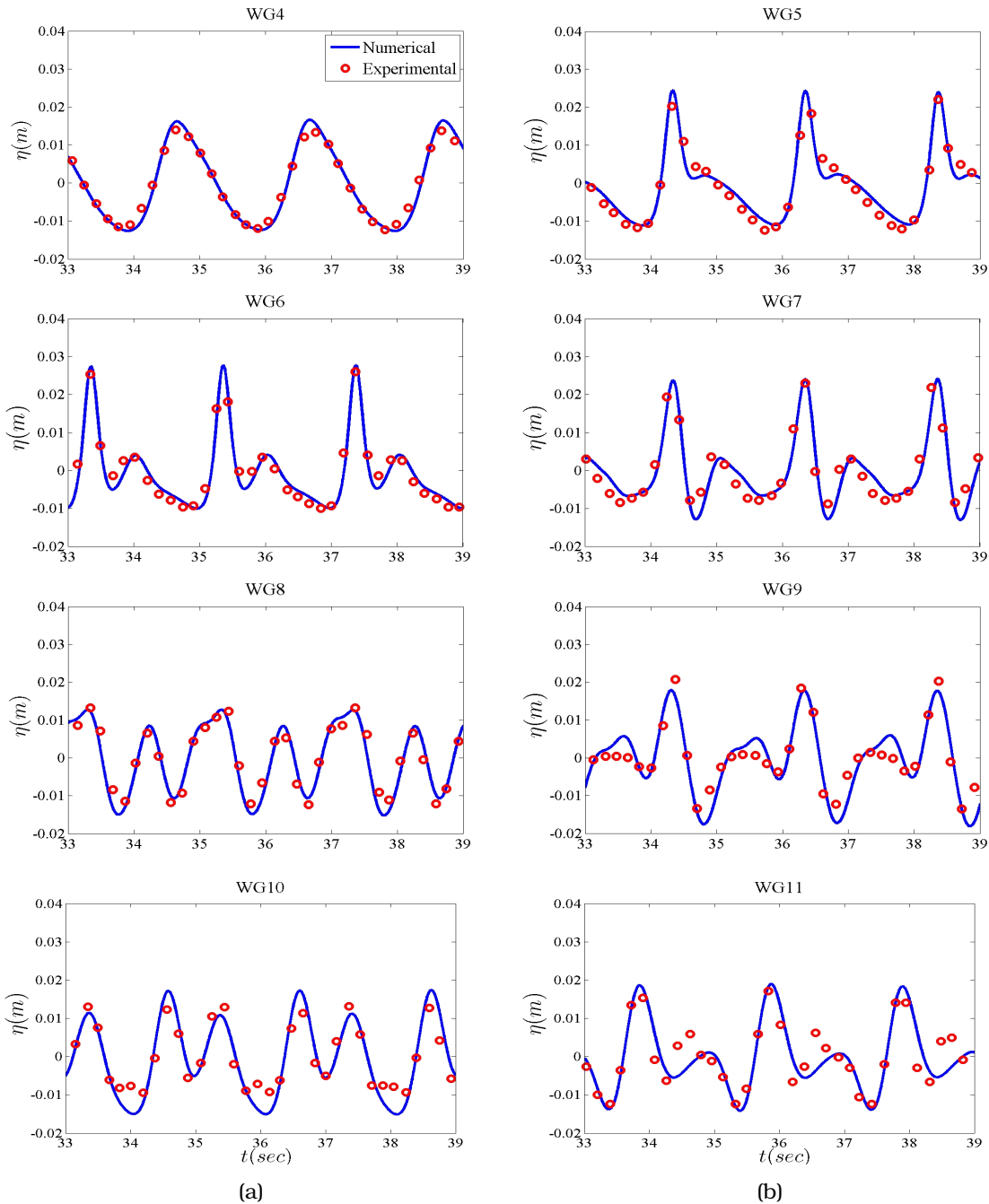


Figure 7.29: Time series of surface elevation at wave gauges for periodic wave propagation over a submerged bar

the bar crest. Breaking is classified as plunging. In the lee side, the back slope causes the wave train to breakup into independent waves traveling at their own speed. Hence, bound higher harmonics are developed along the front slope, which are then released from the carrier frequency on the lee side of the bar as the water depth parameter kh increases rapidly. Fig. 7.30 illustrates the wave-by-wave treatment and the l_{NSW} area

along the centerline for our hybrid model at different time instances (covering roughly one wave period). The onset of breaking is correctly predicted close to the beginning of the bar crest and continues along the flat of the bar leading to a wave height decay. Individual breaking fronts can be seen again as they are tracked by the model.

Fig. 7.31 shows the computed and recorded wave forms at the four wave gauges of interest. The numerical results of the new hybrid model are compared with those produce by the Hybrid(ϵ) model and the experimental ones. The wave shape is well-reproduced by the new hybrid model for all wave gauges. The wave height decay on the top of the bar compare very well with the experimental data. The results obtained with the Hybrid(ϵ) model, although they are in phase with the experimental data, overestimate the predicted wave height resulting in a different wave shape at the last gauge. These results are due to the inability of this model to dissipate correctly the wave energy of the broken waves on the top of the bar, since wave breaking ceases before all the wave energy is dissipated as discussed in section 6.6.2. One way to overcome this problem would have been to pre-specify the region on the bar top to be governed by the NSW model but this can not be consider as a universal approach in the application of this model.

7.10 Solitary wave propagation over a two dimensional reef

The next experimental test case initially presented in [142] is on solitary wave transformations over an idealized fringing reef and examines the model's capability in handling nonlinear dispersive waves along with wave breaking and bore propagation. It is an extension of the 1d test case presented in Section 4.6.2. The 2D test presented here, include a steep slope along with a reef crest in order to represent fringing reefs, found in tropical environments. The computational domain is $(x, y) \in [0, 83.7m] \times [0, 1.1m]$ and the topography includes a fore reef slope of 1/12 a 0.2m reef crest and a water depth $h = 2.5m$. The reef crest is then exposed by 6cm and submerges the flat with $h = 0.14m$. This test case involves a 0.75m high solitary wave which gives a dimensionless wave high of $A/h = 0.3$. The computational mesh used has $h_N = 0.05$ leading to $N = 43,563$ mesh nodes. A CFL number of 0.35 was used, the wet/dry threshold parameter $\epsilon_{wd} = 1.d - 6$ and $\gamma = 0.6$. Wall boundary conditions were placed at each

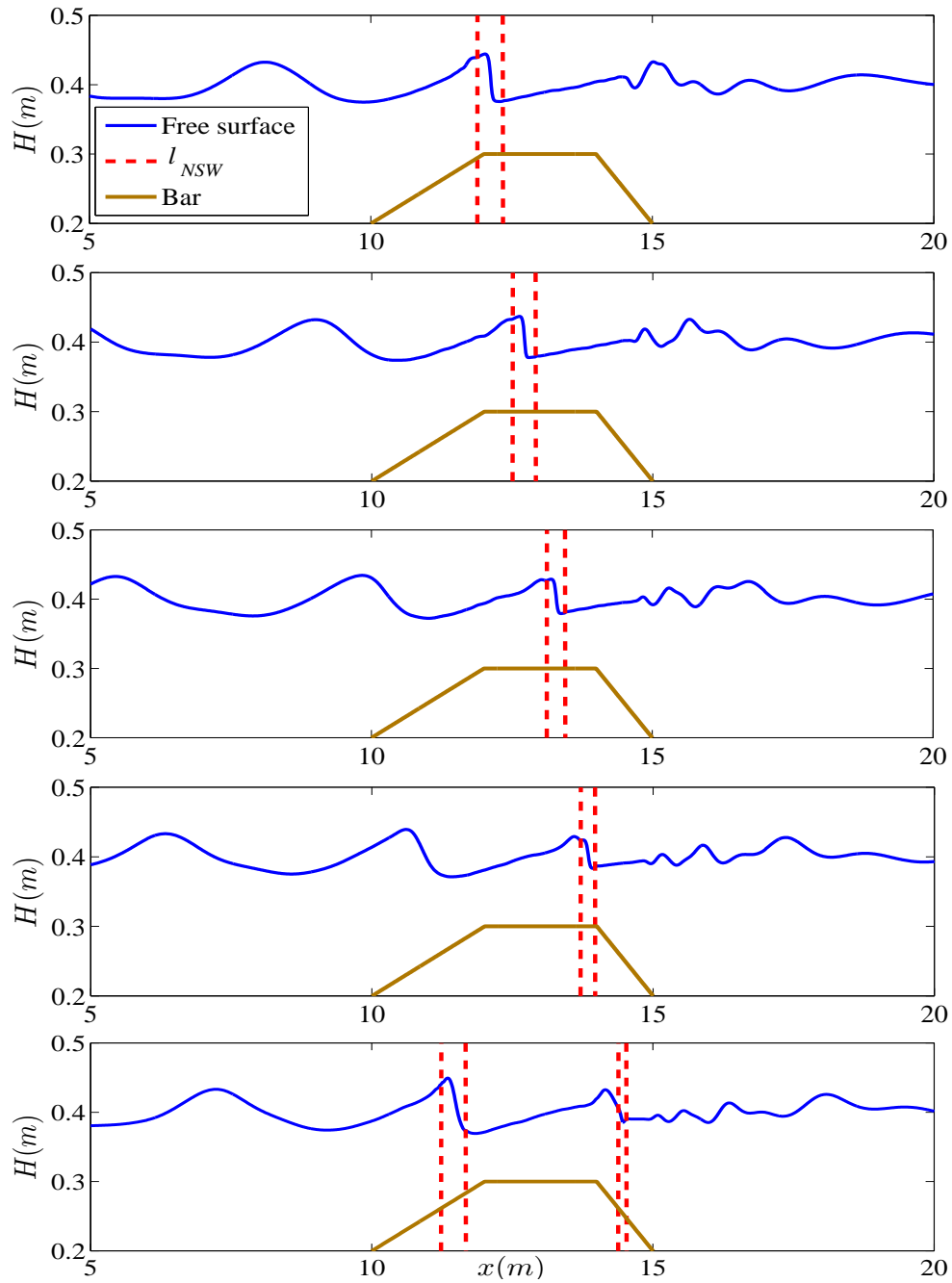


Figure 7.30: Spatial snapshots along the centerline of regular waves breaking over a bar with the flow between two consecutive vertical lines governed by the NSW equations

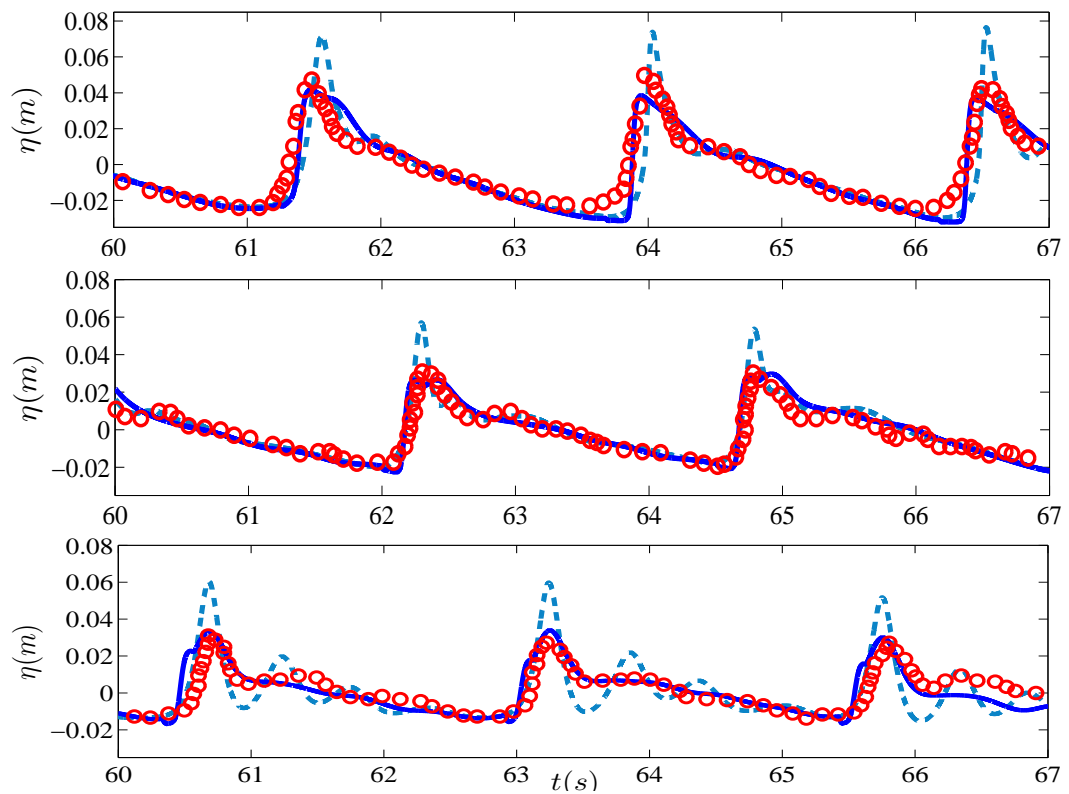


Figure 7.31: Time series of surface elevation at wave gauges for periodic wave breaking over a bar

boundary of the computational domain and as suggested in [141] a Manning coefficient $n_m = 0.012s/m^{1/3}$ was used, to define the roughness of the concrete surface of the reef. Experimental results for the free surface elevation were recorded at 14 wave gauges [142] along the centerline of the computational domain.

Figs 7.32 and 7.33 compare the measured and computed wave profiles as the numerical solitary wave propagates. The numerical solutions of the new hybrid BT model is compared also with that of the NSW equations. As the initially symmetric solitary wave shoals across the toe of the slope at $x = 25.9m$, it begins to skew to the front with the NSW equations forming a vertically-faced propagating bore. Experimentally the wave begins to break around $t = 33s$ developing a plunging breaker on the top of the reef crest that collapsed around $t = 34.5s$. Both models are mimicking the breaker as a collapsing bore that slightly underestimates the wave height but conserved the total mass. By time $t = 35.5s$ the broken wave begins to travel down the back slope of the reef crest generating a supercritical flow that displaces the initially stagnant water, generating a hydraulic jump off the back reef and a downstream propagating bore fueled by the supercritical flow mass and momentum transfer. Laboratory observations indicated this generation of the hydraulic jump and an overturning of the free surface off the back reef along with a turbulent bore propagating down stream. Around $t = 40s$ the momentum flux balances at the flow discontinuity and the hydraulic jump becomes stationary momentarily, while the bore continues to propagate downstream. The hybrid model predicts correctly the phase and amplitude of the discontinuities indicating the correct energy dissipation during wave breaking.

At subsequent times, the end wall reflects a bore back that by time $t = 54s$ has overtopped the reef crest generating a hydraulic jump on the fore reef and a reflected bore at the back of the reef that travels again downstream. At this point, and as the water rushes down the fore reef, the flow transitions from flux to dispersion-dominated through the hydraulic jump. The hydraulic jump generates an offshore propagating undular bore, which transforms into a train of dispersive waves over the increasing water depth. The created bore at the fore reef propagates as a shock for the NSW equations offshore due to the hyperbolic character of the equations, as can be seen in Figure 7.33. The NSW model totally smooths the results with an additional phase shift. On the other hand, the BT model reproduces correctly the decaying undular bore as well as the subsequent higher harmonics released at later times.

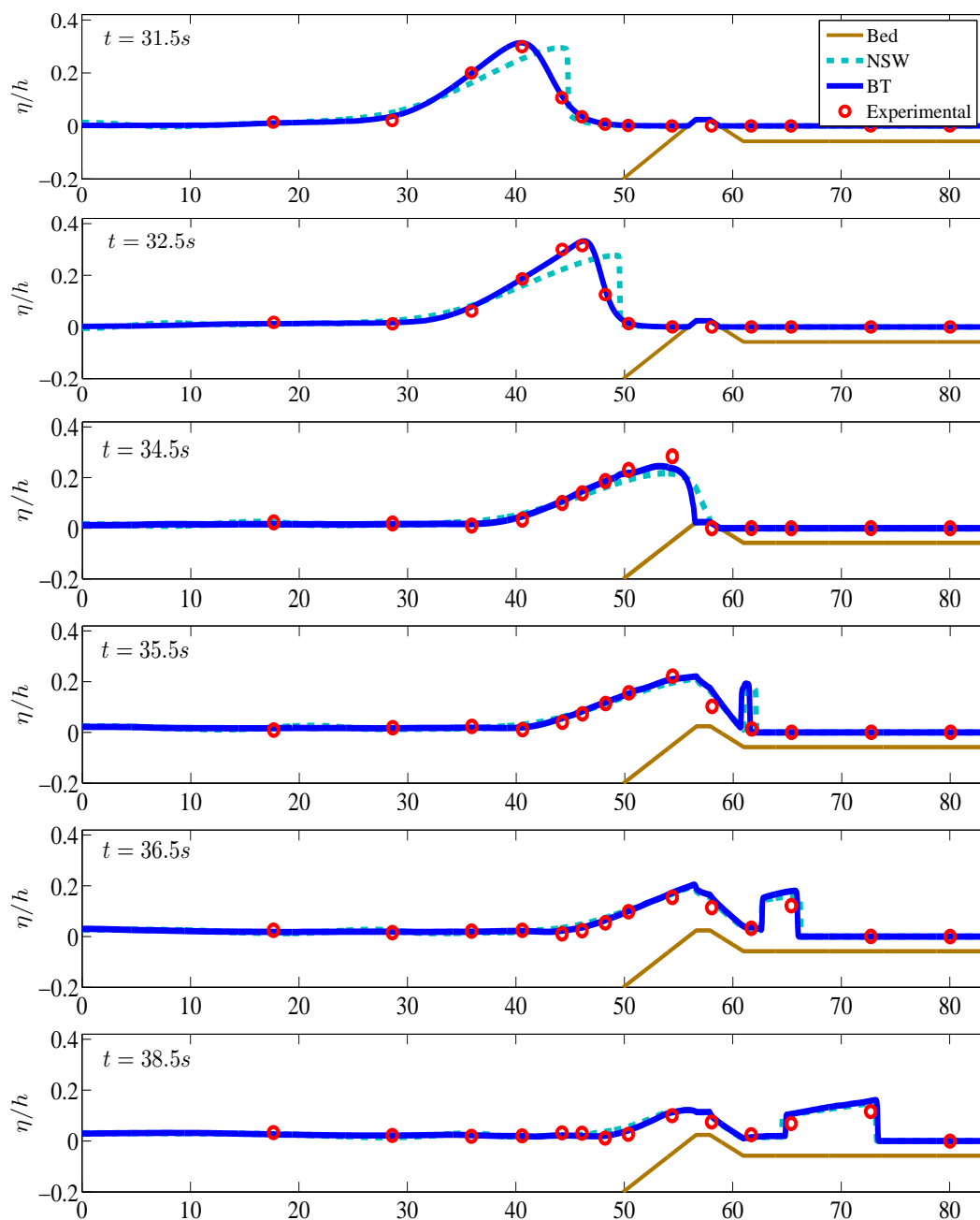


Figure 7.32: Evolution of surface profiles and wave transformations over an exposed reef for $A/h = 0.3$ and $1/12$ slope

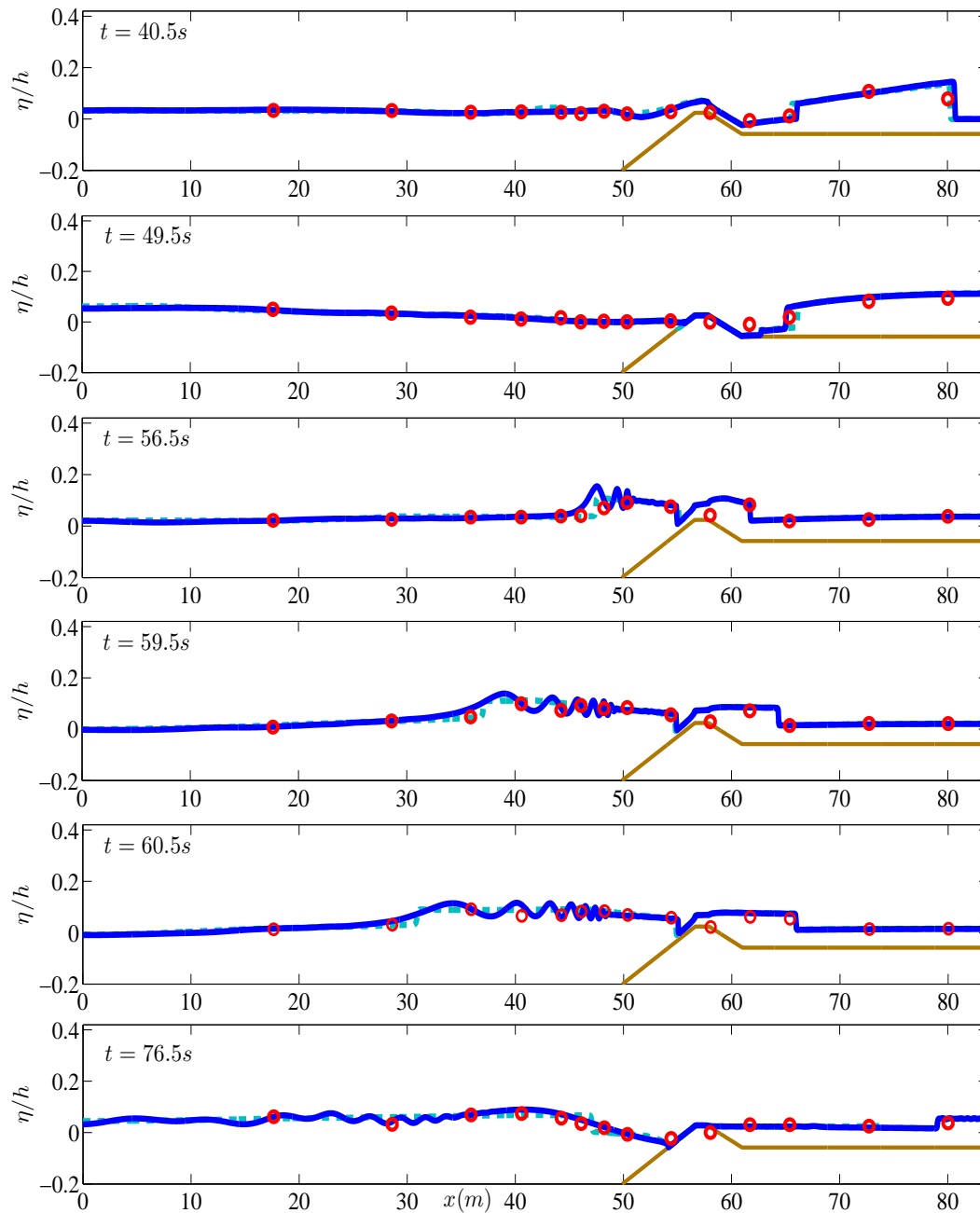


Figure 7.33: Evolution of surface profiles and wave transformations over an exposed reef for $A/h = 0.3$ and $1/12$ slope

The use of the proposed breaking criteria is critical, in this particularly challenging test case, in order to capture the stationary and nearly stationary jumps and reflected bores on the flow profile. The evolution of the breaking regions can be seen in Fig. 7.34. Stationary hydraulic jumps are correctly recognized by the local slope angle criterion in all instances. The development of an undular bore in the flow justifies the use of the critical Froude termination criterion which correctly recognizes the non-breaking undular bore which is resolved by the BT model as it travels in deeper waters.

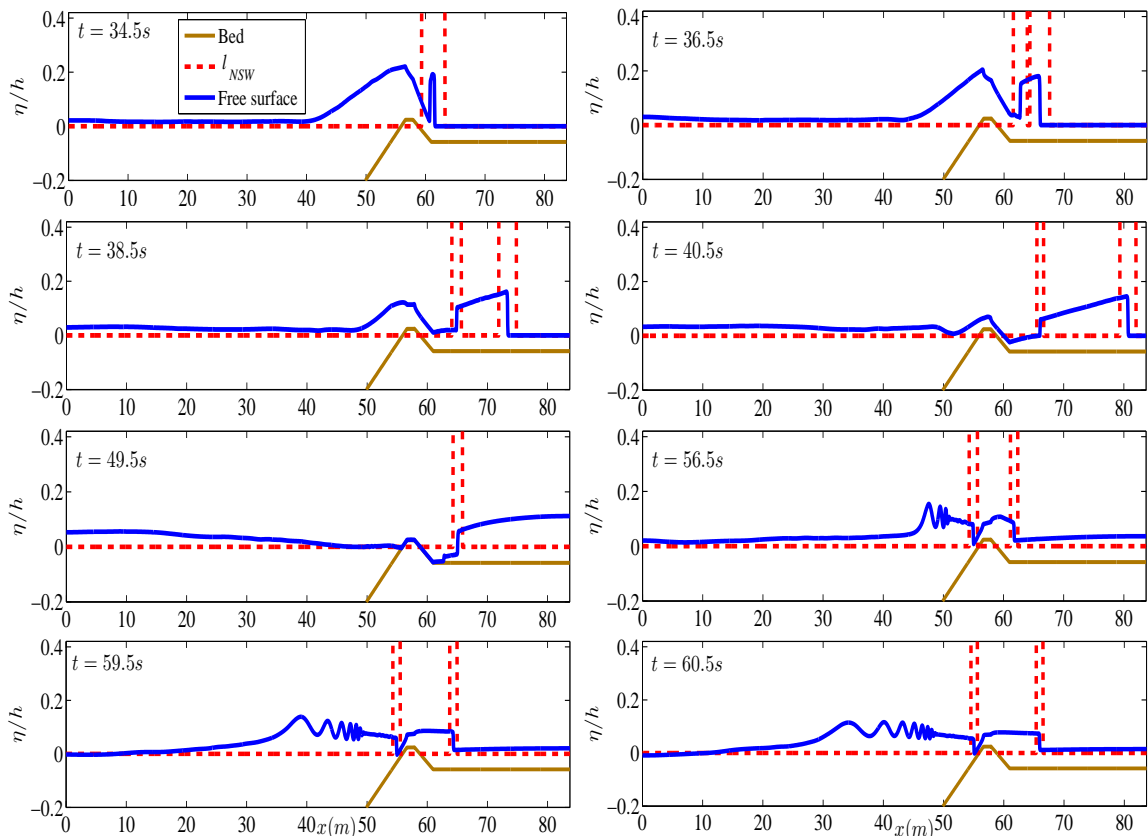


Figure 7.34: Spatial snapshots along the centerline of a solitary wave propagation over a two-dimensional reef with the flow between two consecutive vertical lines governed by the NSW equations

Figs 7.35 and 7.36 compare the computed and recorded surface elevation time series at specific wave gauges. Fig. 7.35 compares the computed and recorded surface elevation time series at the wave gauges before the reef and Fig. 7.36 after the reef. The recorded data from the wave gauges at $x \leq 50.4m$ shows the effect of the dispersive waves on the free surface. The produced train of waves over the increasing water depth and the resulting undulations were intensified as higher harmonics were released. As

a matter of fact, wave gauges near the toe of the slope recorded highly dispersive waves of $kd > 30$ [142]. The hybrid BT model managed to reproduce these highly dispersive waves with the correct phase and height strengths. The computational results are comparable to those obtained by the 1D FV/FD model (see Section 4.6.2). The 2D New Hybrid breaking model, seems to be more efficient recognizing and handling undular bores due to the 2D nature of the solver. More over the efficiency of the wet/dry front treatment is confirmed from the time series of the WG which is placed on the reef (at $x = 58.05m$).

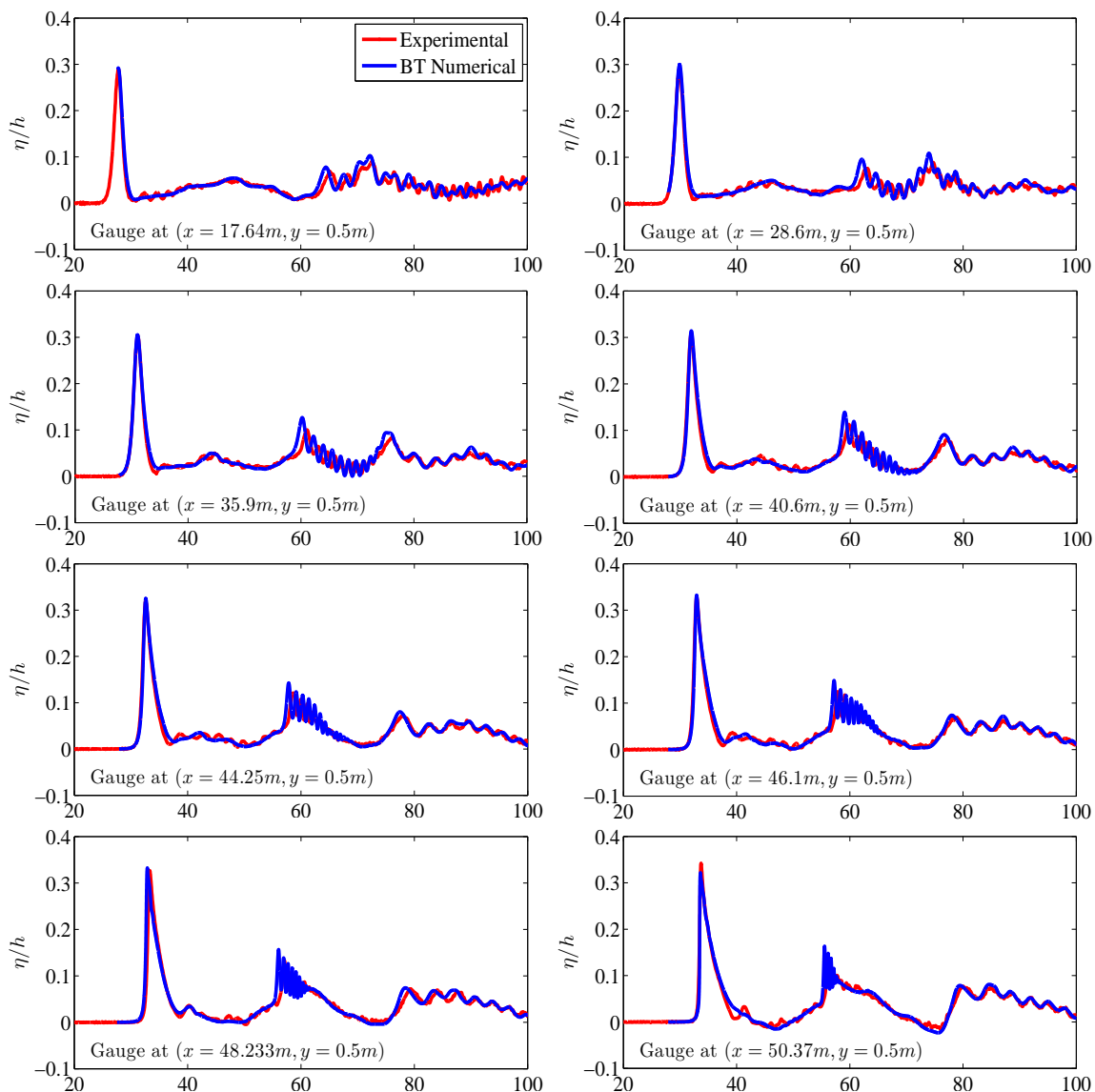


Figure 7.35: Time series of the normalized free surface at the wave gauges before the reef

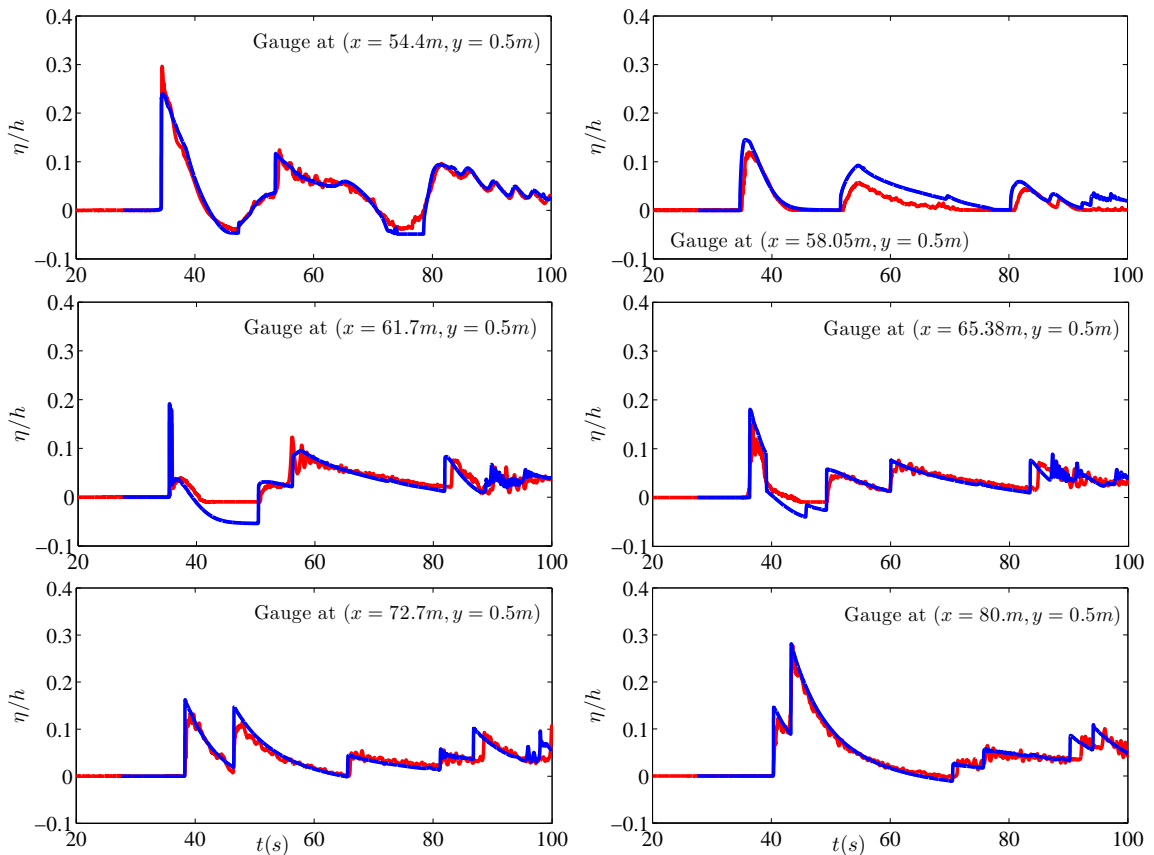


Figure 7.36: Time series of the normalized free surface at the wave gauges on top and after the reef

7.11 Solitary wave propagation over a three-dimensional reef

Swing and Lynett [156] performed two laboratory experiments at the O.H Hinsdale Wave Research Laboratory of Oregon State University, to study specific phenomena, that are known to occur when solitary waves approach a shoreline, such as shoaling, refraction, breaking and turbulence. The basin is 48.8m long 26, 5m wide and 2.1m deep.

7.11.1 Case I.

For the first benchmark case, a complex bathymetry from $x = 10.2m$ to $x = 2.5m$ consisting of a 1 : 30 is connected with a triangular reef flat submerged between 7.5cm and 9cm below the still water level. The offshore shelf edge has an elevation of 0.71m with the apex located at $x = 12.6m$. The steepest slope of the shelf is at the apex and

becomes milder moving along the shelf edge toward the basin side walls. The planar beach continues to $x = 31m$ and then becomes level until the back of the basin.

Seventeen wave gauges which measure the free surface elevation, three of them are also Acoustic Doppler Velocimeters (ADV), in alongshore and cross-shore arrays which measure the velocity. Gauges 1 – 7 are located at $y = 0m$ and $x = 7.5, 11.5, 13, 15, 17, 21, 25m$, gauges 8–13 are located at $y = 5m$ and $x = 7.5, 11.5, 13, 15, 17, 21, 25$ and gauges 14–17 are located along $x = 25m$ and $y = 2, 5, 7, 10m$. ADV 1-3 are placed at $(13.0, 0.0)m$, $(21.0, 0.0)$ and $(21.0, 5.0)m$. An unstructured mesh refined along the shelf with $N = 87,961$ nodes has been created for this problem with $h_N = 0.1m$ at the refined region. The CFL value used was 0.4 and $\gamma = 0.6$. A solitary wave of $0.39m$ in height is placed along $x = 5m$ at time $t = 0s$. Fig 7.37 shows a series of snapshots of the free surface which propagates over the shallow water shelf, creating a strongly plunging breaker. At time $t = 3s$ the solitary propagates unchanged since the topography is flat until $x = 10m$. As the wave approaches the shelf apex, breaking begins along the center-line. The bore front propagates onshore, while the wave along the sides shoals. Up to time $t = 8s$ a plunging wave has been developed along the entire length of the reef edge and a new bore has been developed at the apex of the shelf, which propagates over and away from the sill. The flow transition into a surge moving up the initially dry slope propagating over the reef and slope complex. At $t = 16s$ a third bore-front is visible further onshore and it is a portion of the first bore which has been reflected off the top of the planar beach generating an offshore flow. Six seconds later the third bore-front converges at the apex of the shelf as a refraction phenomenon, while the flow at the top continues to move forward. At $t = 35s$ and along the self edge, the offshore flow leads to the formation of a nearly stationary hydraulic jump. The last snapshot shows the reflection from the downstream boundary which has propagate on the slope and a second run-up is observed.

The solitary wave as it propagates on the 3D reef is presented in Fig 7.37. Fig. 7.38 shows the time series of the computed surface elevation recorded measurements at WG 1-7, located along the center-line. The first two wave gauges show the solitary wave as it travels in the constant depth portion of the tank and the arrival of the wave is almost correctly predicted. Moving onshore, at WG 3, the front face of the bore-front is approaching in a vertical shape, just prior to breaking. By the time $t = 6s$ the bore-front has reached WG 4 and wave breaking has begun as revealed by the decay in wave

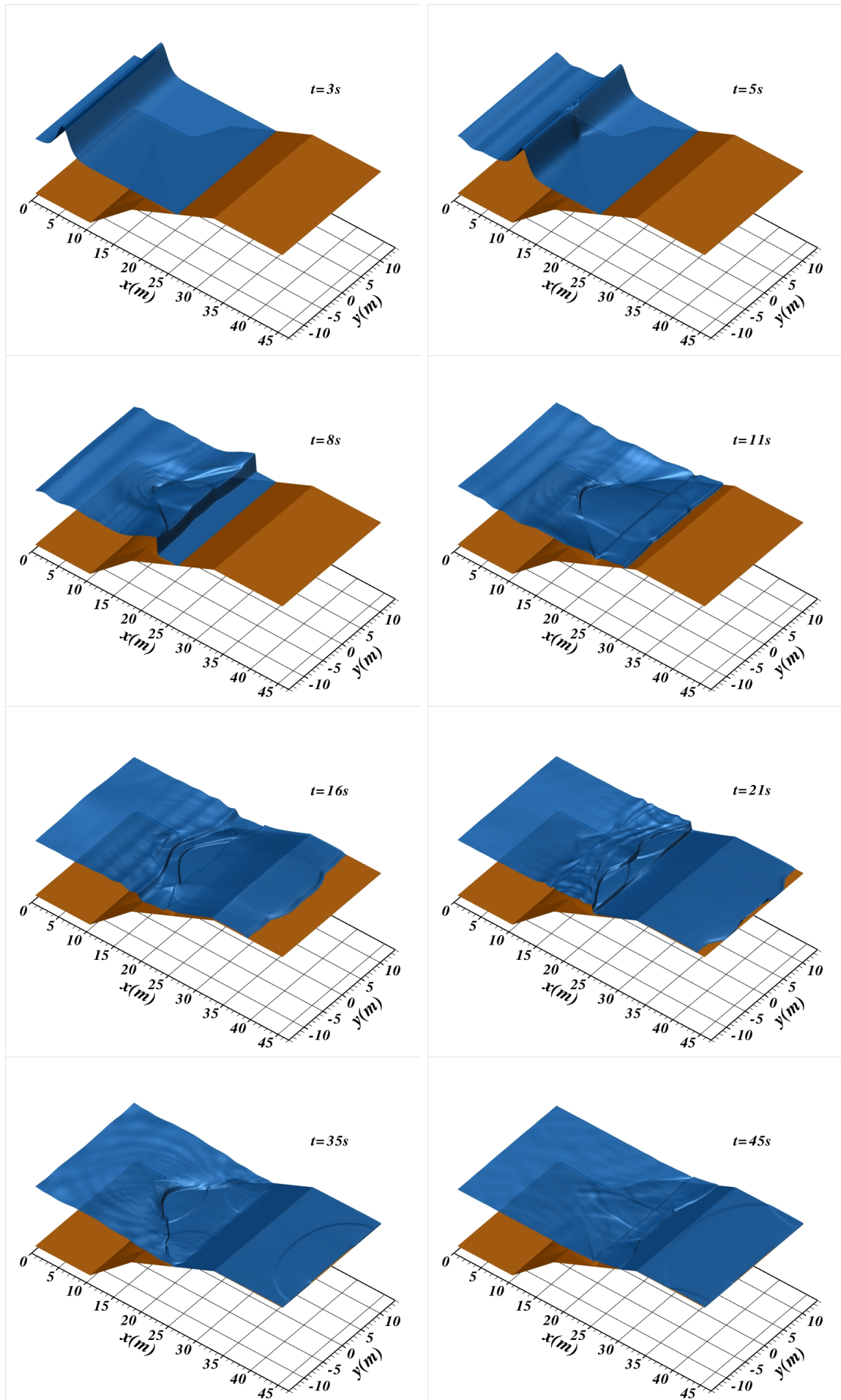


Figure 7.37: Water surface for solitary wave propagation on a 3D reef at different times

height. At the next two gauges the height of the bore-front has decreased significantly as it travels further onshore. The second bore-front created at the apex of the reef is depicted in WG 3 around $t = 10s$ and can be seen as it travels onshore and interacts with the third one at WG 6 around $t = 20s$. The third bore-front is a reflected bore created on the reef slope and then travels off-shore. The model agrees equally well with the measurements at the remaining wave gauges.

Fig. 7.39 shows the time series of the surface elevation for the wave gauges located along $y = 5m$, while Fig. 7.40 shows the same for the wave gauges located at the edge of the reef flat. Finally Fig. 7.41 compares recorder and computed velocity components in the x and y directions at three of the gauges.

7.11.2 Case II.

The second benchmark case utilizes the same topography as the previous case but with a conical cone of $6m$ diameter and $0.45m$ height fitted to the apex of the reef between $x = 14m$ and $20m$. Nine wave gauges were placed to measure the free surface elevation along with three ADVs alongshore and cross-shore to measure the velocity as shown in Fig. 7.42. Gauges 1, 2, 3, 7 were located at $y = 0m$ and at $x = 7.5, 13.0, 21.0, 25m$ respectively, while gauges 4, 5, 6, 8 were located at $y = 5m$ and $x = 7.5, 13, 21, 25m$. ADVs 1-3 are placed at $(13.0, 0.0)m$, $(21.0, 0.0)$ and $(21.0, -5.0)m$ respectively. The computational domain is extended from $x = 0m$ to $x = -5m$ with a constant water depth of $0.78m$. The same unstructured mesh, with the first benchmark case, was used. The CFL value used was 0.4 and $\gamma = 0.6$. A solitary wave of $0.39m$ in height is placed along $x = 5m$ at time $t = 0s$. It should be mentioned that, $A/h = 0.5$ in this problem which constitutes a particular demanding case for the BT model used due to its high nonlinearity. Fig. 7.43 shows the computed water surfaces at various times. At the initial stages the wave front becomes very steep as the solitary wave advances on the shelf. The solitary wave begins to break along the centerline around $t = 5s$, when it crosses the shelf's apex. By time $t = 6.5s$ the resulting surge completely overtops the cone while the wave along the basin's sides continues to shoal. By time $t = 8.5s$ the refracted waves and the diffracted waves collide on the shelf. The refracted waves collide at the lee side of the cone as edge waves which propagate around the two sides of the cone. The water withdraws from the cone and the borefront from the diffracted wave propagates onshore and reinforces the refracted waves from the reef edge. A new bore is created from the

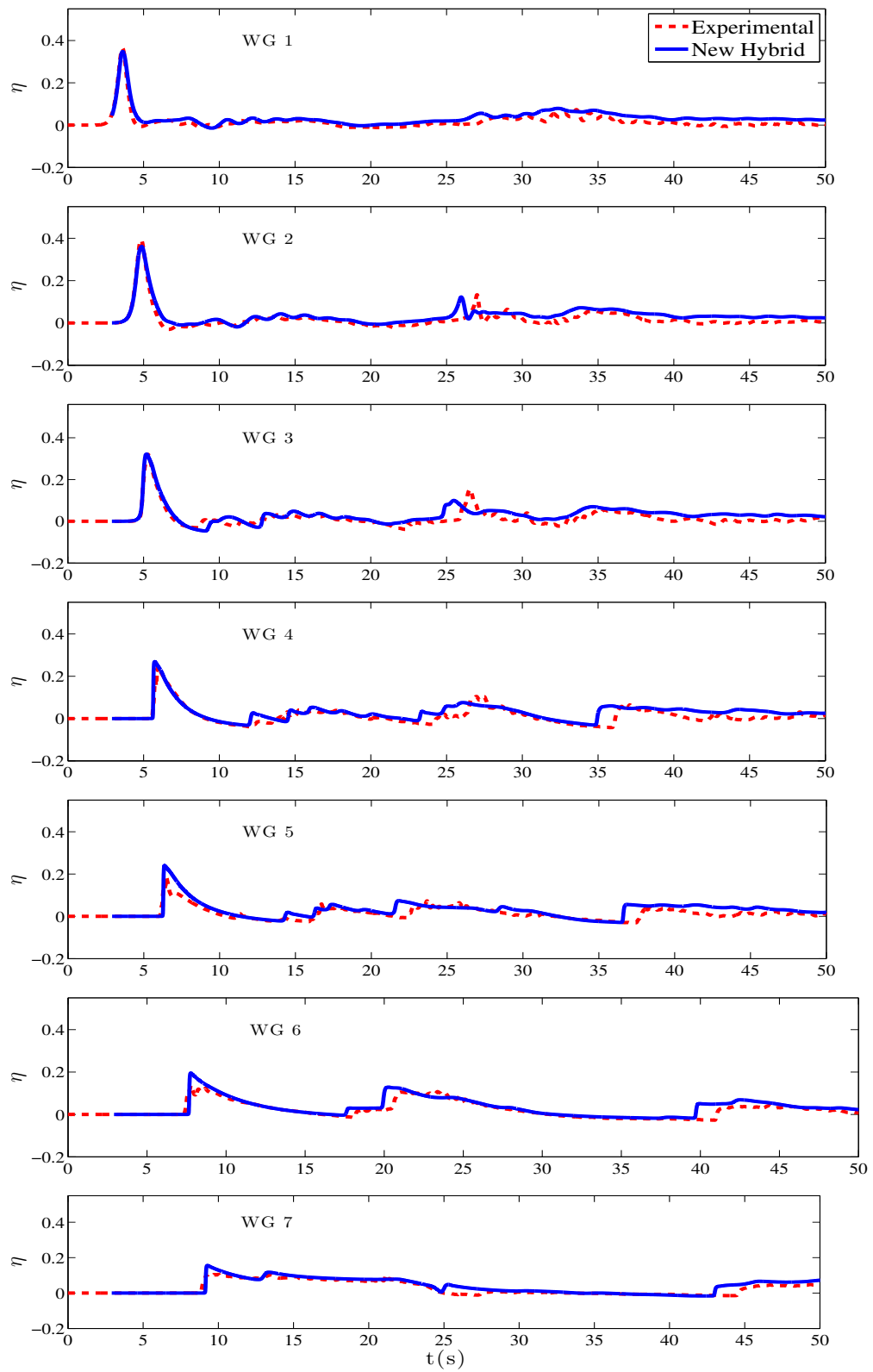


Figure 7.38: Time series of surface elevation for solitary wave propagation on a 3D reef along the centerline

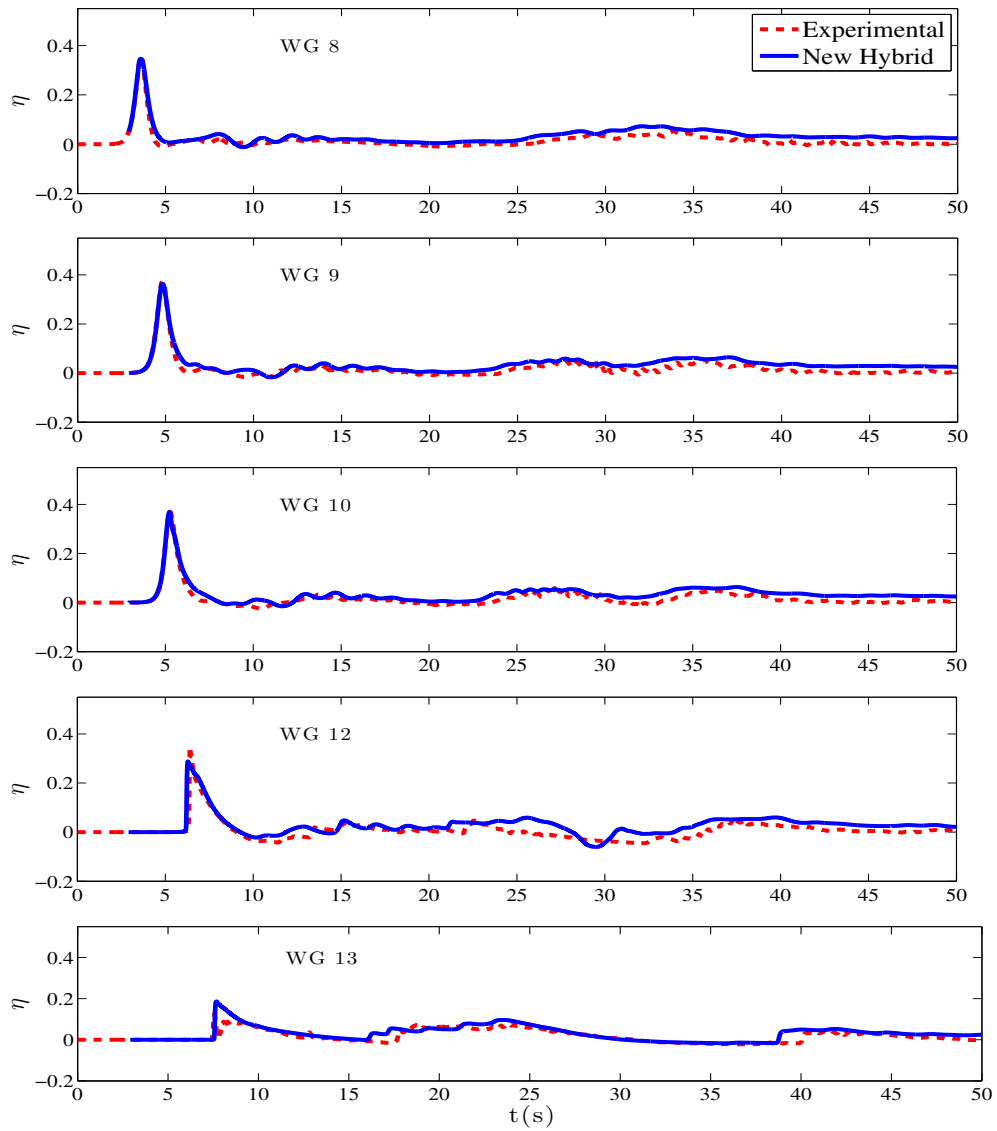


Figure 7.39: Time series of surface elevation for solitary wave propagation on a 3D reef along $y = 5m$.

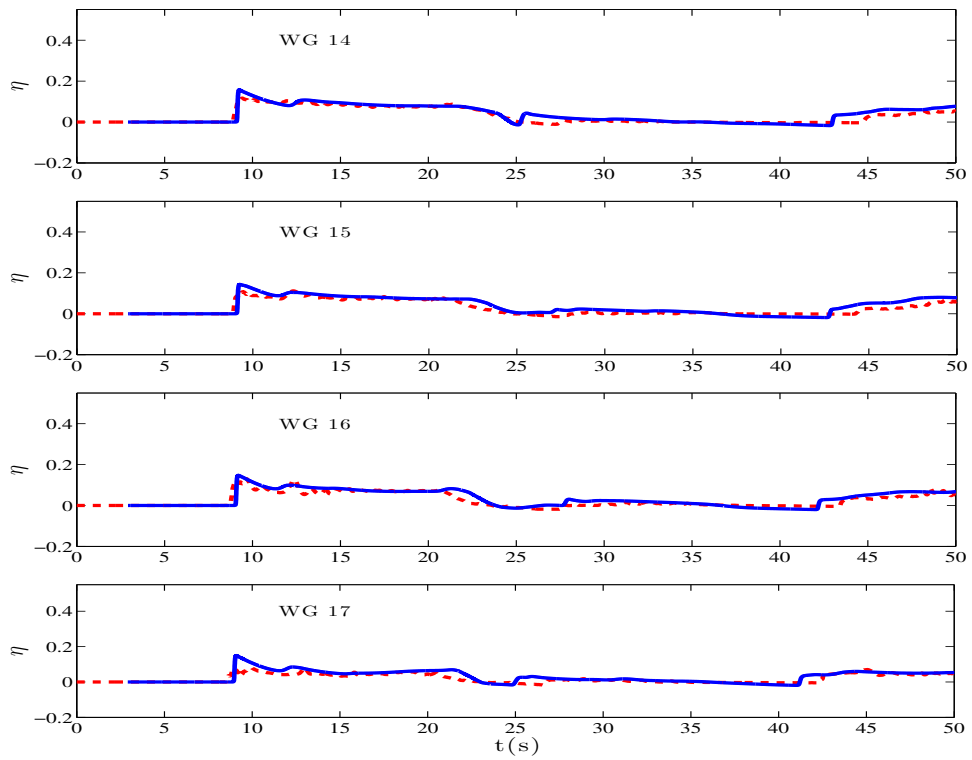


Figure 7.40: Time series of surface elevation for solitary wave propagation on a 3D reef for the wave gauges located at the edge of the reef flat.

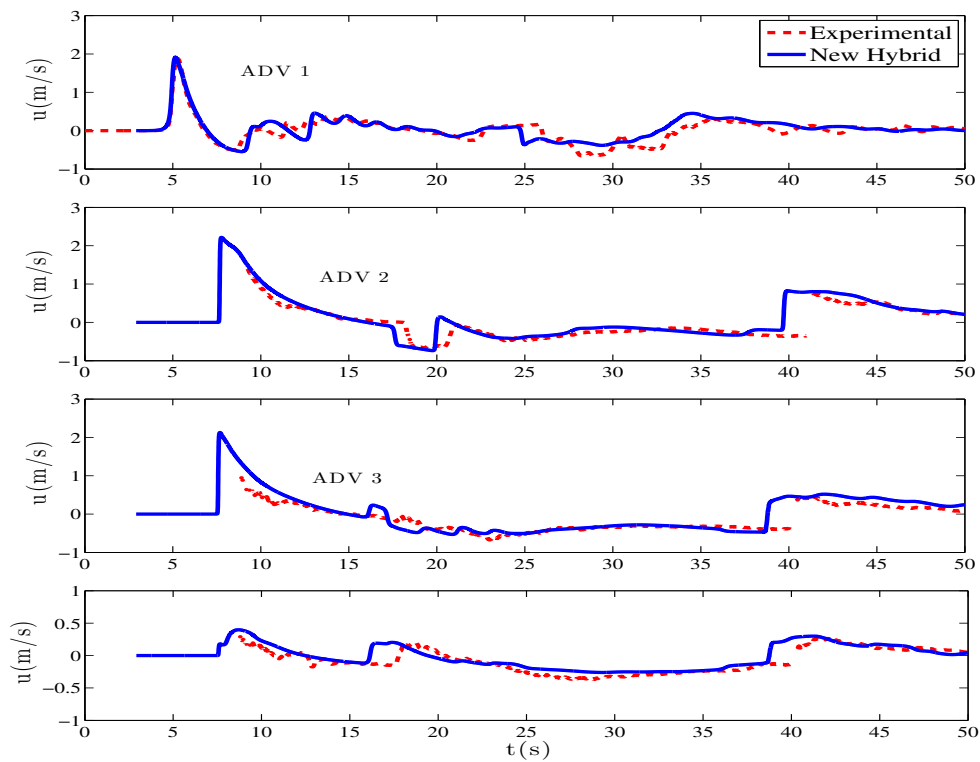


Figure 7.41: Time series of cross-shore and long-shore velocity for benchmark1.

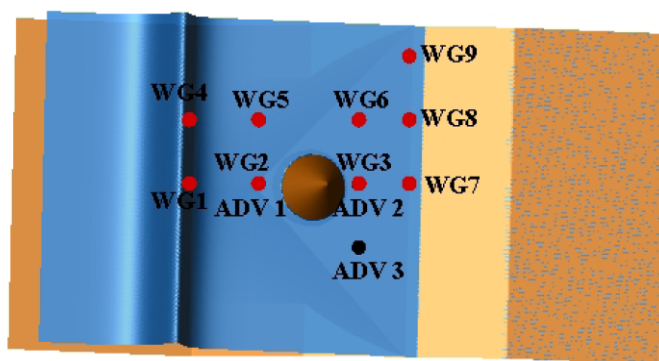


Figure 7.42: Three-dimensional reef problem geometry along with wave gauges's and ADVs's locations

drawdown of the water and collides with the refracted waves.

Fig. 7.44 presents the time series of the computed surface elevation recorded measurements at WGs 1-9. At the first two gauges the arrival of the wave is almost correctly predicted. WG 2 is located at the point where wave breaking is initiated. The collision of the refracted and diffracted waves at the lee side of the cone is almost exactly computed by the model without an over-prediction of the the wave height as can be seen from the results in WG 3 around time $t = 8s$. The data and model comparisons at WGs 4, 5, 6, 8 and 9, located at the north side of the shelf, indicate that the numerical model predicts wave shoaling, refraction and breaking on the shelf accurately. The onshore propagation of the diffracted waves and the subsequent water recession is well predicted as indicated by the results at WG 7. We note her that, after time $t = 40s$ the numerical results start to deviate from the measurements due to late arrival of the numerical reflected waves from the extended computational domain.

Finally, in Fig. 7.45 the velocity time series measurements are compared with the numerical ones at the different ADVs locations. The hybrid BT model matches the u -components of the velocity reasonably well by predicting correctly peak velocities as well as the entire trend in time of the u - velocity profiles. The v - velocity results where not compared with measurements from ADV 1 and ADV 2 since the measurement values were too small, a similar observation has been made in [147]. The production of the v -component of the velocity is well predicted by the numerical model at the location of ADV 3. It is noted that, the measurements at ADV 3 record the initial wave's shoaling, breaking and refraction.

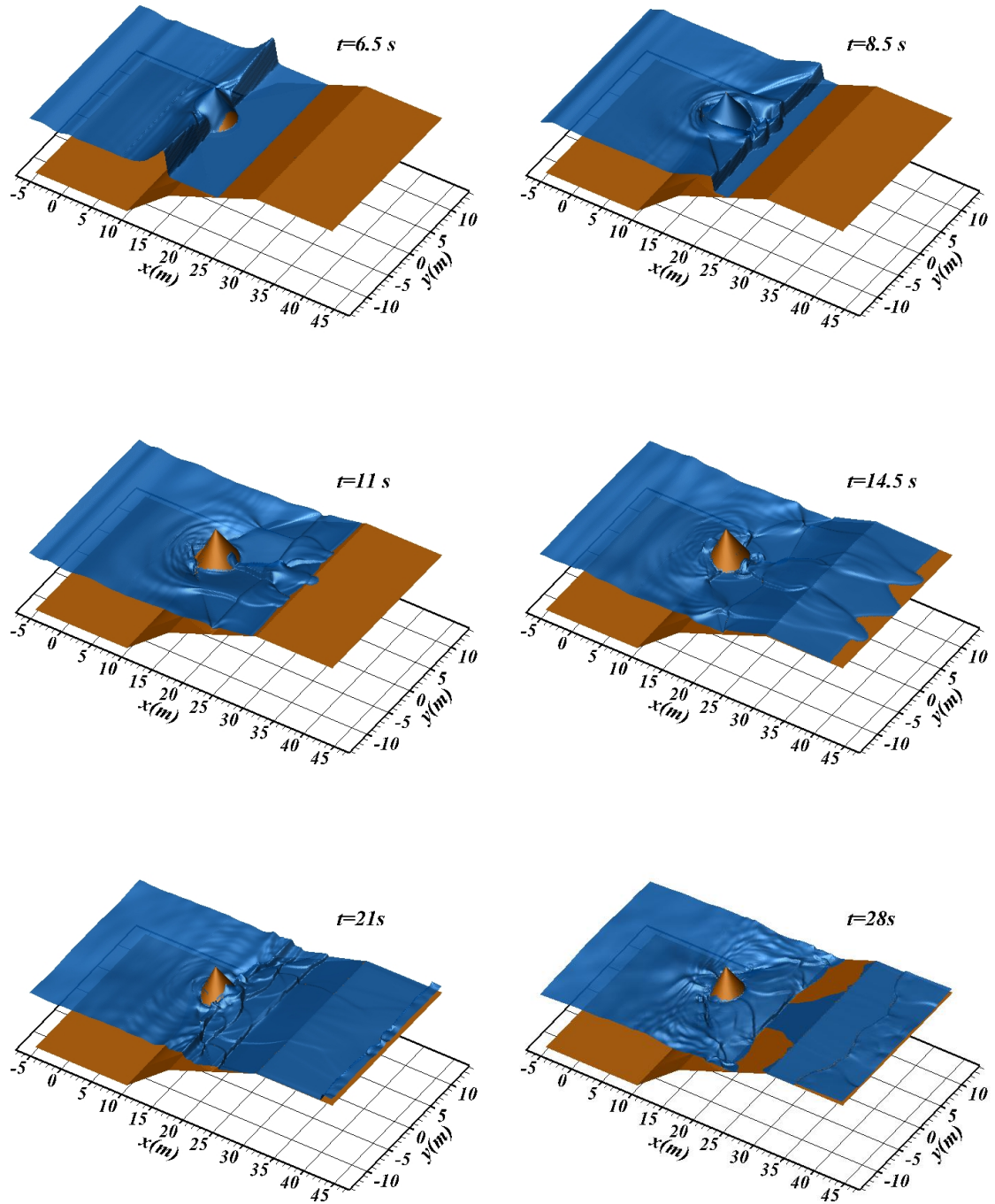


Figure 7.43: Water surface for solitary wave propagation on a 3D reef at different times

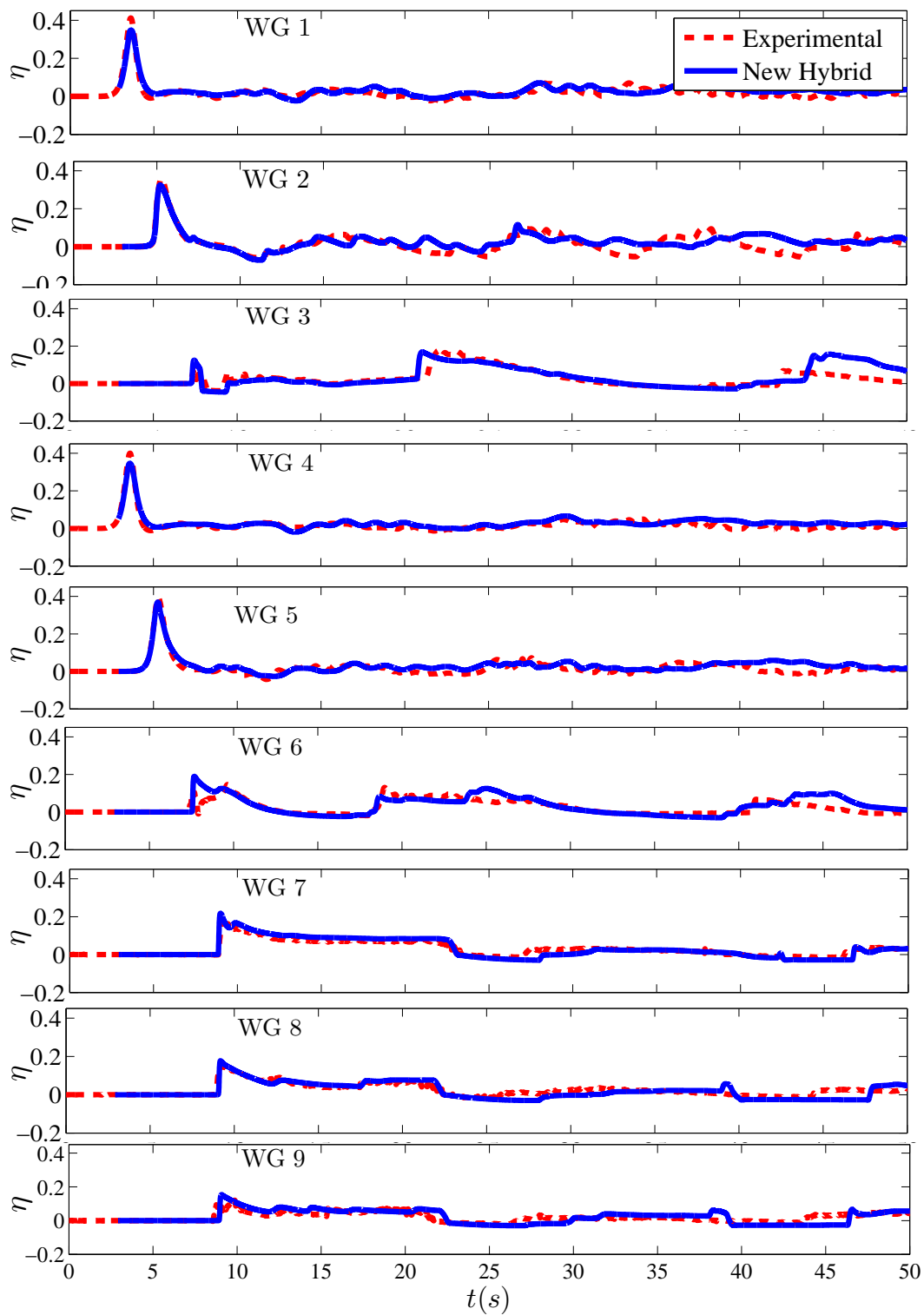


Figure 7.44: Time series of surface elevation for solitary wave propagation on a 3D reef

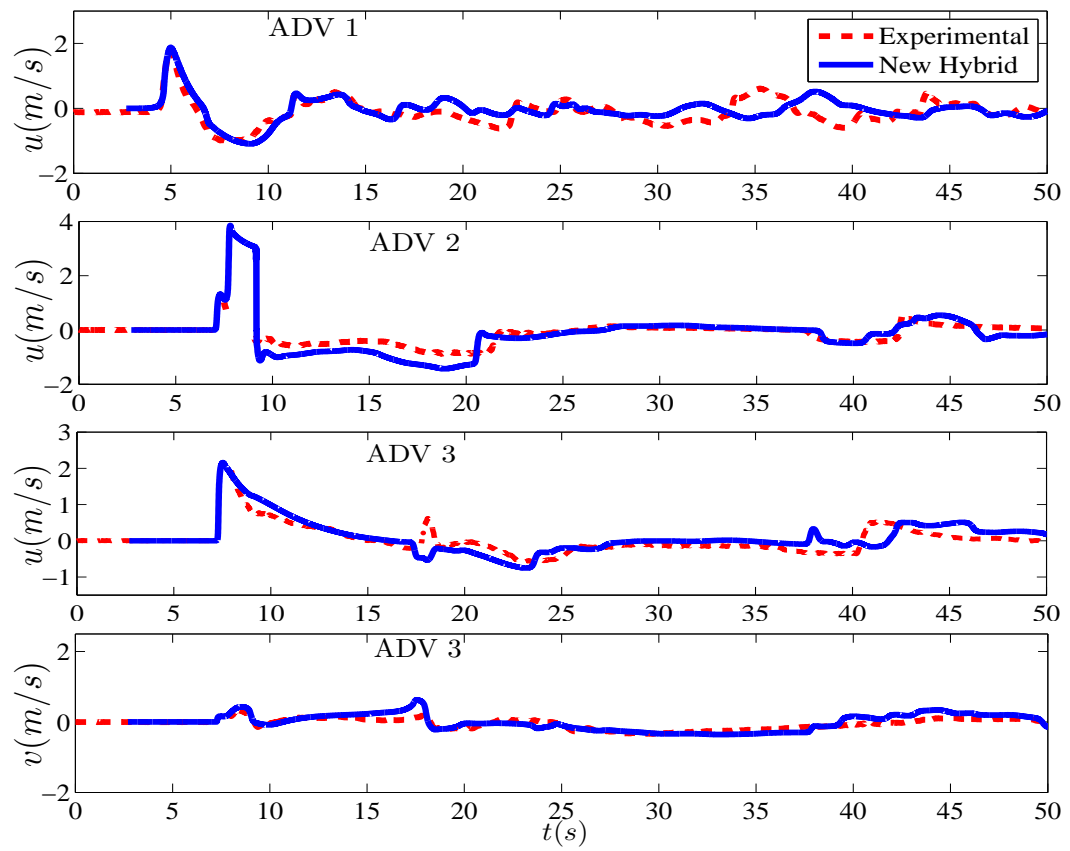


Figure 7.45: Time series of velocity components at the different ADVs for solitary wave propagation on a 3D reef

Chapter 8

Conclusions

As a wide number of topics have been touched upon, the conclusions from this thesis are many. This thesis has three main parts each of them providing different concluding remarks. The most important of these are highlighted in Section 8.1. Some recommendations for further research are also provided in Section 8.2

8.1 Summary and concluding remarks

The first part of this thesis describes the development of an 1D alternative hybrid FV/FD conservative numerical model with shock-capturing capabilities for solving Nwogu's and MS equations, formulated as to have identical flux terms as to the NSWE. The application of a fourth-order conservative Godunov-type FV method for the evaluation of the advective fluxes makes the proposed scheme shock-capturing. An improved numerical treatment for the topography source terms and the conservative computation of wet/dry fronts results to a well-balanced scheme. Further multiple wave breaking models for the BT equations presented, introducing also a new more stable hybrid BT/NSWE modeling for breaking waves. This new approach is of the hybrid-type meaning that the strategy proposed is that of switching to NSWE, by locally suppressing the dispersion terms in the vicinity of a breaking wave. A stable methodology is developed for the smooth transition between the two models within our FV framework, when wave breaking occurs in a numerical simulation. With this methodology, any non-physical mix of the two models is avoided and there is no need for any numerical filtering to be applied.

Special attention was paid to comparing both BT models to the NSWE confirming

that for long wave's that don't break, differences between NSWE and BT models were small. Although the NSWE can be sufficient in some cases to predict maximum runup values and the general characteristics of propagating waves, the two BT models provided considerable more accurate results for highly dispersive waves over increasing water depth. The two models showed a good agreement with "challenging" experimental data, with Nwogu's equations to slightly perform better behavior than MS equations.

The second part of this work consists of comparing two types of FV schemes for the 2D NSWE. A CCFV and a NCFV one. Both FV approaches are widely used nowadays individual advantages of each of the two approaches have been extensively presented in the literature but except [51] and this work there exists no consensus about which approach offers more advantages. We compare these two FV schemes and study their relative performance, robustness and effectiveness, with a controlled environment for a fair and extensive comparison. Both schemes compared to analytical solutions and convergence studies have been performed along with grid refinement studies. Concluding remarks from this comparison can be found in Section 5.7.4. The most advantageous of them is that for the CCFV approach different convergence behavior is exhibited (with an order reduction) for grids where the center of the face does not coincide with the reconstruction location, while the NCFV scheme exhibited identical convergence behavior on all grids. Further, the effects of the grid's geometry at the boundary can lead to order reduction for the CCFV scheme (if the center of the face does not coincide with the reconstruction location), even for good quality grids.

Thereafter and using the BT equations of Nwogu and the NCFV approach, a new 2D unstructured FV numerical model has been developed for the aforementioned BT equations. To the best of our knowledge this is the first time that this FV approach is applied in extended BT equations for unstructured triangular meshes. The edge-based structure adopted can provide computational efficiency, since most of the geometric quantities needed can be calculated in a pre-processing stage. The BT equations formulated as to have identical flux terms as to the NSWE. The conservative formulation and the higher order FV scheme enhance the applicability of the model without altering its dispersion characteristic. The well-balanced topography and wet/dry front discretizations provided accurate, conservative and stable wave propagation and run-up. Using the NCFV formulations we impose boundary conditions through weak formulation and no ghost cells have to be used.

The numerical model was validated against standard test cases of non-breaking/breaking wave propagation over variable topographies with emphasis to comparisons with experimental results. We observed that the 2D numerical problems presented in Chapter 7 have similar or better results than the 1D problems presented in Chapter 4. We must keep in mind that the numerical scheme in 1D is of fourth-order accurate while the one in 2D is of third-order accurate. In all test cases, the presented results were in good agreement with experimental data and previously published solutions within the limits of applicability of the equations.

Different types of wave breaking mechanisms have implemented for the BT model presented. The New Hybrid model has been extended to 2D and was proved more stable and accurate than others applied in this work. A certain combination of criteria is established to characterize the initiation of wave breaking based on the free surface elevation and the local slope angle, with only few parameters needing to be calibrated depending on the test case. More precisely, in the test cases considered in this work, only the parameter that governs the surface variation criterion had to be adjusted and only for the case of regular waves propagating over a submerged bar. The complementary nature of these two criteria was proven efficient and robust in tracking broken wave fronts as well as stationary breaking or partially breaking hydraulic jumps. In addition the methodology for the smooth transition between the two models, when wave breaking occurs is extended in 2D. Like before no numerical filtering is applied. In conclusion it is relatively straight forward to extend existing SWE codes that use (unstructured) FV schemes as to include dispersion characteristics for deeper water simulations.

8.2 Future Work/Recommendations

We conjecture that the present approach can be applied to other BT models (w.g. Madsen and Sørensen [112], standard Boussinesq). Furthermore, it would be relatively straight forward to extend existing SWE codes that use (unstructured) FV schemes as to include dispersion characteristics for deeper water simulations. The conservative form of the equations along with a conservative FV scheme is ideal for shock capturing when moving from deeper to shallow water.

For deeper water the weakly nonlinear, weakly dispersive equations (like Nwogu's and MS) can be prove inadequate. See for example the performance of the equations

in the test cases 4.5 and 7.9 (wave propagation over a submerged bar), at the back of the bar where kh grows and its out of the range of the equations. So extension of the proposed methodology to highly nonlinear BT models can be performed.

Further the quest for extending to even higherorder spatial accuracy for FV schemes that combine state of the art techniques for the leading order terms such as, Riemman solvers, higher order reconstruction, well-balanced discretizations and wet/dry front treatment is an ongoing process.

The algorithms presented here and all the test cases executed as a single process (on a single core) on a 2.5Gz Intel Core i5 processor. Ideally, they could be implemented on parallel platforms, allowing more rapid calculations, especially for real life problems, in which the computational domains are large.

Appendix A

Initial conditions

Some solitary wave solutions for extended Boussinesq models are presented next. These solutions have been used as initial conditions from the numerical models presented in this work, since no-analytical solutions for the equations of Nwogu [127] or for those of MS [114] exist.

Wei et al. [179] have derived an approximate solitary wave solution for the BT equations of Nwogu [127]. Using the 1D Nwogu's equations in dimensionless form in constant depth h we denote $\mu = kh$ and $\epsilon = A/h$. Substituting the velocity potential to the equations, retaining terms that are consistent with the BT equations and after some calculations we obtain:

$$\eta = A_1 \operatorname{sech}^2(B(x - Ct)) + A_2 \operatorname{sech}^4(B(x - Ct)) \quad (\text{A.1})$$

$$u_a = A \operatorname{sech}(B(x - ct)) \quad (\text{A.2})$$

where

$$A = \frac{C^2 - 1}{\epsilon C}, \quad (\text{A.3})$$

$$B = \left\{ \frac{C^2 - 1}{4\mu [(\alpha + 1/3) - \alpha C^2]} \right\}^{1/2}, \quad (\text{A.4})$$

$$A_1 = \frac{C^2 - 1}{3\epsilon^2 [(\alpha + 1/3) - \alpha C^2]}, \quad (\text{A.5})$$

$$A_2 = -\frac{(C^2 - 1)^2 [(\alpha + 1/3) + 2\alpha C^2]}{2\epsilon C^2 [(\alpha + 1/3) - \alpha C^2]}, \quad (\text{A.6})$$

C can be found solving the equation:

$$2\alpha(C^2)^3 - (3\alpha + 1/3 + 2\alpha\epsilon)(C^2)^2 + 2\epsilon(\alpha + 1/3)(C^2) + \alpha + 1/3 = 0. \quad (\text{A.7})$$

The corresponding dimensional expressions for A, B, A_1, A_2 are:

$$A = \frac{C^2 - gh}{C}, \quad (\text{A.8})$$

$$B = \left\{ \frac{C^2 - gh}{4[(\alpha + 1/3)gh^3 - \alpha h^2 C^2]} \right\}^{1/2}, \quad (\text{A.9})$$

$$A_1 = \frac{C^2 - gh}{3[(\alpha + 1/3)gh - \alpha C^2]} h, \quad (\text{A.10})$$

$$A_2 = -\frac{(C^2 - gh)^2 [(\alpha + 1/3)gh + 2\alpha C^2]}{2ghC^2 [(\alpha + 1/3)gh - \alpha C^2]} h. \quad (\text{A.11})$$

Synolakis [157] used the following surface profile to derive a result for the maximum runup of a solitary wave climbing up a sloping beach. A solitary wave centered at $x = X_1$ at $t = 0$ has the following surface profile:

$$\eta(x, 0) = \frac{A}{h} \operatorname{sech}^2(\gamma(x - X_1)), \quad (\text{A.12})$$

where

$$\gamma = \sqrt{\frac{3A}{4h^3}}$$

and using the lowest-order approximation, the horizontal depth-averaged velocity is given as:

$$u = \frac{\sqrt{gh}}{h} A \operatorname{sech}^2(\gamma(x - X_1)). \quad (\text{A.13})$$

This approximation has been used by [163] as an initial condition to validate their model.

Bibliography

- [1] M. B. Abbott, A. McCowan, and I. R. Warren. Accuracy of short wave numerical models. *J. Hydraul. Eng.*, 110(10):1287–1301, 1984.
- [2] M. Aftosmis, D. Gaitone, and T.S. Tavares. On the accuracy, stability and monotonicity of various reconstruction algorithms for unstructure meshes. 1994.
- [3] M. Aftosmis, D. Gaitone, and T.S. Tavares. Behavior of linear reconstruction techniques on unstructured meshes. *AIAA Journal*, 33:2038, 1995.
- [4] J. S. Antunes do Carmo, F. J. Seabra-Santos, and E. Bathélamy. Surface waves propagation in shallow water: A finite element model. *Int. J. Num. Meth. Fluids*, 16:447, 1993.
- [5] E. Audusse and M.-O. Bristeau. A well-balanced positivity preserving second order scheme for shallow water flows on unstructured meshes. *J. Comp. Phys.*, 206:311, 2005.
- [6] F. Aureli, P. Maranzoni, and C. Ziveri. A weighted surface-depth gradient method for the numerical integration of the 2D shallow water equations with topography. *Advances in Water Resources*, 31:962, 2008.
- [7] T. J. Barth. Aspects of unstructured grids and finite volume solvers for the Euler and Navier-Stokes equations. In Special Course on Unstructured Grid Methods for advection Dominated Flows, AGARD report 787, 1992.
- [8] T. J. Barth. *Numerical Methods and Error Estimation for Conservation laws on Structured and Unstructured Meshes*. VKI Computational Fluid Dynamics Lecture Series, 2003.
- [9] T. J. Barth and D. C. Jespersen. The design and application of upwind schemes on unstructured meshes. *AIAA paper 89-0366*, 1989.

- [10] T. J. Barth and M. Oehlberger. Finite volume methods: foundation and analysis. In E. Stein, R. de Borst, and T.R. Hudges, editors, *Encyclopedia of Computational Mechanics*. John Wiley and Sons Ltd., 2004.
- [11] E. Barthélemy. Nonlinear shallow water theories for coastal waves. *Surveys in Geophysics*, 25(3-4):315-337, 2004.
- [12] D. R. Basco and I. A. Svendsen. Modeling turbulent bore propagation in the surfzone. In *Proceedings of the 19th International Conference on Coastal Engineering*, 1984.
- [13] P. Batten, C. Lambert, and D. M. Causon. Positively conservative high-resolution convection schemes for unstructured elements. *Int. J. Num. Meth. Fluids*, 39:1821, 1996.
- [14] L. Begnudelli and B. F. Sanders. Adaptive Godunov-based model for flood simulation. *J. Hydraul. Eng.- ASCE*, 134:714, 2008.
- [15] M. Berger, M. J. Aftosmis, and S. M. Murman. Analysis of slope limiters on irregular grids. *AIAA paper 2005-0490*, 43rd AIAA Aerospace Sciences Meeting and Exhibit:Reno, Nevada, 2005.
- [16] J. C. E. Berkhoff, N. Booy, and A. C. Radder. Verification of numerical wave propagation models for simple harmonic linear water waves. *Coast. Eng.*, 6:255-279, 1982.
- [17] A. Bermudez, A. Dervieux, J. A. Desideri, and M. E. Vázquez. Upwind schemes for the two-dimensional shallow water equations with variable depth using unstructured meshes. *Comput. Methods Appl. Mech. Eng.*, 155:49, 1998.
- [18] A. Bermudez and M. E. Vázquez-Cendón. Upwind methods for hyperbolic conservation laws with source terms. *Computers and Fluids*, 23:1049, 1994.
- [19] S. Betji and J. A. Battjes. Experimental investigations of wave propagation over a bar. *Coastal Engineering*, 19:151, 1993.
- [20] S. Betji and K. Nadaoka. A formal derivation and numerical modelling of the improved Boussinesq equations for varying depth. *Ocean Engineering*, 23-8:691-704, 1996.

- [21] H. B. Bingham, P. A. Madsen, and D. R. Fuhrman. Velocity potential formulations of highly accurate Boussinesq-type models. *Coast. Eng.*, 56:467, 2009.
- [22] J. Blazek. *Computational Fluid Dynamics*. Elsevier, Amsterdam, 2006.
- [23] P. Bonneton, E. Barthelémy, J. D. Carter, F. Chazel, and S. T. Cien. Recent advances in Serre-Green naghdi modelling for wave transformation, breaking and runup processes. *European Journal of Mechanics - B/Fluids*, 30:589–597, 2011.
- [24] A. G. L. Borthwick, M. Ford, B. P. Weston, P. H. Taylor, and P. K. Stansby. Solitary wave transformation, breaking and run-up at a beach. In *Proceedings of the institution of Civil Engineers, Maritime Engineering 159*, Issue MA3, September 2006.
- [25] A. G. L. Borthwick, M. Ford, B. P. Weston, P. H. Taylor, and P. K. Stansby. Solitary wave transformation, breaking and run-up at a beach. *Maritime Engineering*, 159:97–105, 2006.
- [26] S. F. Bradford and B. F. Sanders. Finite-volume model for shallow-water flooding of arbitrary topography. *J. Hydraul. Eng.-ASCE*, 128:289, 2002.
- [27] R. Briganti and N. Dodd. Shoreline motion in nonlinear shallow water coastal models. *Coast. Eng.*, 56:495, 2009.
- [28] M. J. Briggs, C. E. Synolakis, G. S. Harkins, and D. R. Green. Laboratory experiments of tsunami runup on a circular island. *Pure Appl. Geophys.*, 144:569, 1995.
- [29] M. O. Bristeau and B. Coussin. Boundary conditions for the shallow water equations solved by kinetic schemes. Rapport de Recherche No 4282, INRIA, 2001.
- [30] M. Brocchini, R. Bernetti, A. Mancinelli, and G. Albertini. An efficient solver for nearshore flows based on the WAF method. *Coastal Eng.*, 43:105, 2001.
- [31] M. Brocchini and N. Dodd. Nonlinear shallow water equations modeling for coastal engineering. *J. Waterway, Port, Coastal, Ocean Eng.*, 134:104, 2008.

- [32] M. Brocchini, R. S. Svendsen, R. S. Prasad, and G. Bellotti. A comparison of two different types of shoreline boundary conditions. *Comput. Methods Appl. Mech. Eng.*, 191:4475–4496, 2002.
- [33] P. Brufau, P. García-Navarro, and M. E. Vázquez-Cendón. Zero mass error using unsteady wetting-drying conditions in shallow flows over dry irregular topography. *Int. J. Num. Meth. Fluids*, 45:1047–1082, 2004.
- [34] P. Brufau, M. E. Vázquez-Cendón, and P. Gracia-Navarro. A numerical model for the flooding and drying of irregular domain. *Int. J. Num. Meth. Fluids*, 39:247, 2002.
- [35] S. Bunya, E.J. Kubatko, J.J. Westerink, and C. Dawson. A wetting and drying treatment for the Runge-Kutta discontinuous Galerkin solution to the shallow water equations. *Comput. Methods Appl. Mech. Eng.*, 198:1548, 2009.
- [36] J. Burguete, J. Murillo, and P. Garcia-Navarro. Numerical boundary conditions for globally mass conservative methods to solve shallow-water equations and applied to river flow. *Int. J. Num. Meth. Fluids*, 51:585, 2006.
- [37] G. F. Carrier and H.P. Greenspan. Water waves of finite amplitude on a sloping beach. *J. Fluid Mech.*, 4:97–109, 1958.
- [38] M. J. Castro, A. M. Ferreiro, J. A. García-Rodríguez, J. M. González-Vida, J. Macías, C. Parés, and M. E. Vázquez-Cendón. The numerical treatment of wet/dry fronts in shallow flows: Application to one-layer and two-layer systems. *Mathematical and Computer Modelling*, 42:419, 2005.
- [39] M. J. Castro, J. M. González-Vida, and C. Parés. Numerical treatment of wet/dry fronts in shallow flows with a modified Roe scheme. *Math. Models and Meth. in Ap. Sc.*, 16:897, 2006.
- [40] V. Casulli and P. Zanolli. Comparing analytical and numerical solution of non-linear two and three-dimensional hydrostatic flows. *Int. J. Num. Meth. Fluids*, 53:1049, 2007.
- [41] L. Cea, J. R. French, and M. E. Vázquez-Cendón. Numerical modelling of total flows in complex estuaries including turbulence: an unstructured finite volume solver and experimental validation. *Int. J. Numer. Methods Eng.*, 67:1909, 2006.

- [42] L. Cea, J. Puertas, and M. E. Vázquez-Cendón. Depth averaged modelling of turbulent shallow water flow with wet-dry fronts. *Arch. Comput. Methods Eng.*, 14:303, 2007.
- [43] Q. Chen. Fully nonlinear Boussines-type equations for waves and currents over porous beds. *J. Eng. Mech.*, 132:220–230, 2006.
- [44] J. M. Chidaglia. Flux schemes for solving nonlinear systems of conservation laws. In J.J Chattot and M. Hafez, editors, *Proceedings of the meeting in honor of P.L. Roe*, Arcachon, July 1998.
- [45] B. H. Choi, D. C. Kim, E. Pelinovsky, and S. B. Woo. Three-dimensional simulation of tsunami run-up around conical island. *Coast. Engineering*, 54:618, 2007.
- [46] R. Cienfuegos, E. Barthélemy, and P. Bonneton. A fourth-order compact finite volume scheme for fully nonlinear and weakly dispersive Boussinesq-type equations. Part I: Model development and analysis. *Int. J. Num. Meth. Fluids*, 51:1217–1253, 2006.
- [47] R. Cienfuegos, E. Barthélemy, and P. Bonneton. A fourth-order compact finite volume scheme for fully nonlinear and weakly dispersive Boussinesq-type equations. Part II: Boundary conditions and validation. *Int. J. Num. Meth. Fluids*, 53:1423–1455, 2007.
- [48] R. Cienfuegos, E. Barthélemy, and P. Bonneton. Wave-breaking model for Boussinesq-type equations including roller effects in the mass conservation equation. *J. Waterway, Port, Coastal, Ocean Eng.*, 136:10–26, 2010.
- [49] F. D’Alessandro and G. Tomasicchio. The BCI criterion for the initiation of breaking process in Boussinesq-type equations wave models. *Coast. Eng.*, 55:1174–1184, 2008.
- [50] A. I. Delis, M. Kazolea, and N. A Kampanis. A robust high resolution finite volume scheme for the simulation of long waves over complex domain. *Int. J. Num. Meth. Fluids*, 56:419, 2008.

- [51] A. I. Delis, I. A. Nikolos, and M. Kazolea. Performance and comparison of cell-centered and node-centered unstructured finite volume discretizations for shallow water free surface flows. *Arch. Comput. Methods Eng.*, 18:57, 2011.
- [52] A. I. Delis and C. P. Skeels. TVD schemes for open channel flow. *Int. J. Num. Meth. Fluids*, 26:791, 1998.
- [53] M. W. Dingemans. Verification of numerical wave propagation models with laboratory measurements. Report, H228 Part 1. Delft Hydraulics. 400pp, 1987.
- [54] B. Diskin, J. L. Thomas, E. J. Nielsen, and H. Nishikawa. Comparison of node-centered and cell-centered unstructured finite volume discretizations. Part I: viscous fluxes. *AIAA paper 2009-597*, 47th AIAA Aerospace sciences meeting including the New Horizons Forum and Aerospace Exposition:Orlando, Florida, 2009.
- [55] B. Diskin and J.L. Thomas. Comparison of node-centered and cell-centered unstructured finite volume discretizations: inviscid fluxes. *AIAA paper 2010-1079*, 48th AIAA Aerospace sciences meeting including the New Horizons Forum and Aerospace Exposition:Orlando, Florida, 2010.
- [56] V. A. Dougalis and D. E. Mitsotakis. Theory and numerical analysis of Boussinesq systems: A review. In N. A. Kampanis, V. A. Dougalis, and J. A. Ekaterinaris, editors, *Effective Computational Methods in Wave Propagation*. CRC Press, 2008.
- [57] D. Dutykh, T. Katsaounis, and D. E. Mitsotakis. Finite volume schemes for dispersive wave propagation and runup. *J. Comp. Phys.*, 230:3035–3061, 2011.
- [58] D. Dutykh, R. Poncet, and F. Dias. The VOLNA code for the numerical modeling of tsunami waves: Generation, propagation and inundation. *European Journal of Mechanics - B/Fluids*, 30:598–615, 2011.
- [59] W. El Asmar and O. Nwogu. Finite volume solution of Boussinesq-type equations on an unstructured grid. In J. McKee Smith, editor, *Proceedings of the 30th International Conference on Coastal Engineering*, pages 73–85, San Diego, CA, USA, 2006.

- [60] A. P. Engsig-Karup, J. S. Hesthaven, H. B. Bingham, and T. Warburton. DG-FEM solution for nonlinear wave structure interaction using Boussinesq-type equations. *Coast. Eng.*, 55:197, 2008.
- [61] K. S. Erduran. Further application of hybrid solution to another form of Boussinesq equations and comparisons. *Int. J. Num. Meth. Fluids*, 53:827–849, 2007.
- [62] K. S. Erduran, S. Ilic, and V. Kutija. Hybrid finite-volume finite-difference scheme for the solution of Boussinesq equations. *Int. J. Num. Meth. Fluids*, 49:1213–1232, 2005.
- [63] C. Eskilsson and S. J. Sherwin. Spectral/*hp* discontinuous Galerkin methods for modelling 2D Boussinesq equations. *J. Comp. Phys.*, 210:566, 2006.
- [64] C. Eskilsson, S. J. Sherwin, and L. Bergdahl. An unstructured spectral/*hp* element model for enhanced Boussinesq-type equations. *Coast. Eng.*, 53:947, 2006.
- [65] J. H. Ferziger and M. Peric. *Computational methods for Fluid Dynamic, 3rd edition*. Springer-Verlag, Berlin, Heidelberg, New York, 2002.
- [66] S. S. Frazao and Y. Zech. Undular bores and secondary waves-experiments and hybrid finite-volume modelling. *J. of Hydraulic Res.*, 40:33–43, 2002.
- [67] D. R. Fuhrman and H. B. Bingham. Numerical solutions of fully non-linear and highly dispersive Boussinesq equations in two horizontal dimensions. *Int. J. Num. Meth. Fluids*, 44:231, 2004.
- [68] D. R. Fuhrman and P. A. Madsen. Simulation of nonlinear wave run-up with a high-order Boussinesq model. *Coast. Eng.*, 55:139–154, 2008.
- [69] M. Gaitani. Numerical solution of sparse linear systems resulting from the discretization of Boussinesq type equations using the finite volume method. Master Thesis, (in Greek), 2013.
- [70] J. M. Gallardo, C. Parés, and M. Castro. On a well-balanced higher-order finite volume scheme for shallow water equations with topography and dry areas. *J. Comp. Phys.*, 227:574, 2007.

- [71] T. Gallouet, J.-M. Herard, and N. Seguin. Some approximate Godunov schemes to compute shallow water equations with topography. *Computers and Fluids*, 32:479, 2003.
- [72] A. George and J. W. H. Liu. *Computer solution of Large Sparce Positive Definite Systems*. Prentice Hall, Englewood Cliffs, N.J, 2008.
- [73] D. L. George. Augmented Riemann solvers for the shallow water equations over variable topography with steady states and inundation. *J. Comp. Phys.*, 227:3089, 2008.
- [74] M. F. Gobbi, J. T. Kirby, and G. Wei. A fully nonlinear Boussinesq model for surface waves. Part 2. Extension to $O(kh^4)$. *J. Fluid Mech.*, 405:181, 2000.
- [75] E. Godlewski and P. A. Raviart. *Hyperbolic systems of conservation laws, Applied Mathematical Sciences, vol. 118*. Springer, Berlin, 1995.
- [76] S. K. Godunov. Finite difference methods for the computation of discontinuous solutions of the equations of fluid dynamics. *Math. Sb.*, 47:271–306, 1959.
- [77] S. Gottlieb, C. W. Shu, and E. Tadmor. Strong stability-preserving high-order time discretization methods. *SIAM Review*, 43:89, 2001.
- [78] V. Guinot. Riemann solvers and boundary conditions for two-dimensional shallow water simulations. *Int. J. Num. Meth. Fluids*, 41:1191, 2003.
- [79] J. B. Hansen and I. A. Svendsen. Regular waves in shoalling water: experimental data. Technical Report, ISVA Series Paper 21, 1979.
- [80] A. Harten. Upwind difference schemes for hyperbolic conservation laws. *J. Comp. Phys.*, 49:1–, 1980.
- [81] A. Harten and P. Hyman. Self-adjusting grid methods for one-dimensional hyperbolic conservation laws. *J. Comp. Phys.*, 50:235, 1983.
- [82] A. Harten, P. D. Lax, and B. van Leer. On upstream differencing and Godunov-Type schemes for hyperbolic conservation laws. *SIAM Review*, 25:35–61, 1983.
- [83] K. L. Heitner and G. W. Housner. Numerical model for tsunami run-up. *Journal of Waterw. Harbors Coastal Eng. Div.*, 96 (WW3):701–719, 1970.

- [84] C. Hirsch. *Numerical Computation of Internal and External Flows*. J. Wiley and Sons Ltd., Chichester, England, 1990.
- [85] M. E. Hubbard. Multidimensional slope limiters for MUSCL-type finite volume schemes on unstructured grids. *J. Comp. Phys.*, 155:54, 1999.
- [86] M. E Hubbard and N. Dodd. A 2D numerical model of wave runup and overtopping. *Coast. Eng.*, 47:1–26, 2002.
- [87] M. E. Hubbard and P. García-Navarro. Flux difference splitting and the balancing of source terms and flux gradients. *J. Comp. Phys.*, 165:89–125, 2000.
- [88] U. Kânoğlu and C. E. Synolakis. Long wave runup on piecewise linear topographies. *J. Fluid Mech.*, 374:1, 1998.
- [89] Th. V. Karambas. Nonlinear wave energy modeling in the surf zone. *Nonlinear Process. Geophys.* 3, pages 127–134, 1996.
- [90] Th. V. Karambas and C. Koutitas. A breaking wave propagation model based on the Boussinesq equations. *Coast. Eng.*, 18:1–19, 1992.
- [91] M. Kazolea and A. I. Delis. A well-balanced shock-capturing hybrid finite volume-finite difference numerical scheme for extended 1D Boussinesq models. *Applied Numerical Mathematics*, 67:167–186, 2013.
- [92] M. Kazolea, A. I. Delis, I. A. Nikolos, and C. E. Synolakis. An unstructured finite volume numerical scheme for extended 2D Boussinesq-type equations. *Coast. Eng.*, 69:42–66, 2012.
- [93] A. B. Kennedy, J. T. Chen, Q. Kirby, and R. A. Dalrymple. Boussinesq modeling of wave transformation, breaking and runup. Part I: 1D. *J. Waterway, Port, Coastal, Ocean Eng.*, 126:39–47, 2000.
- [94] D-H. Kim, P. J. Lynett, and S. A. Socolofsky. A depth-integrated model for weakly dispersive, turbulent, and rotational fluid flows. *Ocean Modelling*, 27:198–214, 2009.
- [95] V. P. Kolgan. Application of the principle of minimizing the derivative to the construction of finite-difference schemes for computing discontinuous solutions of

- gas dynamics. *Transactions of the Central Aerohydrodynamics Institute*, 3(6):63, 1972.
- [96] V. P. Kolgan. Application of the principle of minimizing the derivative to the construction of finite-difference schemes for computing discontinuous solutions of gas dynamics. *J. Comp. Phys.*, 230:2384, 2011.
- [97] C. A. Lacor, S. A. Smirnov, and M. Baelmans. A finite volume formulation of compact central schemes on arbitrary structured grids. *J. Comp. Phys.*, 198:535–566, 2004.
- [98] M. H. Lallemand. Etude de schémas Runge-Kutta á 4 pas pour la résolution multigrille des équations d'Euler 2D. Rapport de Recherche, INRIA, 1988.
- [99] M. H. Lallemand. Dissipative properties of Runge-Kutta schemes with upwind spatial approximation for the Euler equations. Rapport de Recherche No 1173, INRIA, 1990.
- [100] P. D. Lax and B. Wendroff. System of conservation laws. *Comm. Pure Appl. Math.*, 13:217–237, 1960.
- [101] C. Lee, Y.-S. Cho, and S. B. Yoon. A note on linear dispersion and shoaling properties in extended Boussinesq equations. *J. Waterway, Port, Coastal, Ocean Eng.*, 30:1849–1867, 2002.
- [102] R. J. LeVeque. *Finite-Volume Methods for Hyperbolic Problems*. Cambridge University Press, 2004.
- [103] Y. S. Li, Y.-X. Liu, S.-X. amd Yu, and G.-Z. Lai. Numerical modeling of Boussinesq equations by finite element method. *Coast. Eng.*, 37:97, 1999.
- [104] P. L.-F. Liu, Y.-S. Cho, M. J. Briggs, U. Kanoglou, and C. E. Synolakis. Runup of solitary wave on a circular island. *J. Fluid Mech.*, 302:259, 1995.
- [105] N. D. Lopes, P. J. S. Pereira, and L. Trabucho. A numerical analysis of a class of generalized Boussinesq-type equations using continuous/discontinuous FEM. *Int. J. Num. Meth. Fluids*, 69:1186, 2012.
- [106] P. J Lynett. Nearshore Wave Modelling with High-Order Boussinesq-Type Equations. *J. Waterway, Port, Coastal, Ocean Eng.*, 132:348–357, 2006.

- [107] P. J. Lynett and P. L. F. Liu. A two-layer approach to wave modeling. *Proceedings of the Royal Society of London Series A*, 460:2637, 2004.
- [108] P. J. Lynett, T.-R. Wu, and P. L.-F. Liu. Modeling wave runup with depth-integrated equations. *Coastal Engineering*, 46:89–107, 2002.
- [109] G. Ma, F. Shi, and J. T. Kirby. Shock-capturing non-hydrostatic model for fully dispersive surface wave processes. *Ocean Modelling*, 43-44:22–35, 2012.
- [110] P. A. Madsen, H. Bingham, and H. Liu. A new Boussinesq method for fully nonlinear waves from shallow to deep water. *J. Fluid Mech.*, 462:1, 2002.
- [111] P. A. Madsen, H. B. Bingham, and H. A. Schaffer. Boussinesq type formulations for fully nonlinear and extremely dispersive water wave: derivation and analysis. *Proceedings of the Royal Society of London Series A*, 459:1075, 2003.
- [112] P. A. Madsen, D. R. Fuhrman, and B. Wang. A Boussinesq-type formulations for fully nonlinear waves interacting with rapidly varying bathymetry. *Coast. Eng.*, 53:487, 2006.
- [113] P. A. Madsen and O. R. Sørensen. A new form of the Boussinesq equations with improved linear dispersion characteristics. *Coast. Eng.*, 15:371–388, 1991.
- [114] P. A. Madsen and O. R. Sørensen. A new form of the Boussinesq equations with improved linear dispersion characteristics. Part 2: A slowly varying bathymetry. *Coast. Eng.*, 18:183–204, 1992.
- [115] P. A. Madsen, O. R. Sørensen, and H. A. Schaffer. Surf zone dynamics simulated by a Boussinesq-type model: Part I. Model description and cross-shore motion of regular waves. *Coast. Eng.*, 32:255–288, 1997a.
- [116] P. A. Madsen, O. R. Sørensen, and H. A. Schaffer. Surf zone dynamics simulated by a Boussinesq-type model: Part II. Surf beat and swash oscillations for wave groups and irregular waves. *Coast. Eng.*, 32:289–319, 1997b.
- [117] F. Marche. A simple well-balanced model for two-dimensional coastal engineering applications. In *Hyperbolic problems: theory, numerics, applications*, Springer Berlin Heidelberg, 271–283 2008.

- [118] F. Marche, P. Bonneton, P. Fabrie, and N. Seguin. Evaluation of well-balanced bore-capturing schemes for 2D wetting and drying processes. *Int. J. Num. Meth. Fluids*, 53:867–894, 2007.
- [119] D. J. Mavriplis. Unstructured mesh discretizations and solvers for computational aerodynamics. 18th AIAA Computational Fluid Dynamics Conference, AIAA 2007-3955, 2007.
- [120] C. C. Mei. *The applied dynamics of ocean surface waves*. Wiley, New York, N.Y., 1983.
- [121] K. W. Morton and T. Sonar. Finite volume methods for hyperbolic conservation laws. *Acta Numerica*, 16:155, 2007.
- [122] J. Murillo, P. Garcia-Navarro, and J. Burguete. Time step restrictions for well-balanced shallow water solutions in non-zero velocity steady states. *Int. J. Num. Meth. Fluids*, 60:1351, 2009.
- [123] J. Murillo, P. Garcia-Navarro, J. Burguete, and P. Brufau. The influence of source terms on stability, accuracy and conservation in two-dimensional shallow flow simulation using triangular finite volumes. *Int. J. Num. Meth. Fluids*, 54:543, 2007.
- [124] R. J. Murray. Short wave modelling using new equations of Boussinesq type. In *Proc. 9th Australasian Conf on Coast. and Oc. Engrg.*, Adelaide, Australia, July 1989.
- [125] I. A. Nikolos and A. I. Delis. An unstructured node-centered finite volume scheme for shallow water flows with wet/dry fronts over complex topography. *Comput. Methods Appl. Mech. Engrg.*, 198:3723–3750, 2009.
- [126] D. Z. Ning, Liang Q., P. H. Taylor, and A. G. L. Borthwick. Boussinesq cut-cell model for nonlinear wave interaction with coastal structures. *Int. J. Num. Meth. Fluids*, 57:1459, 2008.
- [127] O. Nwogu. An alternative form of the Boussinesq equations for nearshore wave propagation. *J. Waterway, Port, Coastal, Ocean Eng.*, 119:618–638, 1994.

- [128] O. Nwogu and Z. Demirbilek. BOUSS-2D: A Boussinesq wave model for coastal regions and harbors. ERDC/CHL TR-01-25. Vicksburg,MS: Coastal and Hydraulics Laboratory, USACOE Engineering Research and Development Center, 2001.
- [129] T. Okamoto and D. R. Basco. The Relative Trough Froude Number for initiation of wave breaking: Theory, experiments and numerical model confirmation. *Coast. Eng.*, 53:675–690, 2006.
- [130] J. Orszaghova, A. G. L. Borthwick, and P. H. Taylor. From the paddle to the beach - A Boussinesq shallow water numerical wave tank based on Madsen, and Sørensen's equations. *jcf*, 231:328–344, 2012.
- [131] S. Osher and F. Solomon. High resolution schemes for hyperbolic conservation laws. *Math. Comp*, 38:339–374, 1982.
- [132] L. Pengzhi and M. Chaunjian. A staggered-grid numerical algorithm for the extended Boussinesq equations. *Applied Mathematical Modelling*, 31:349–368, 2007.
- [133] D. H. Peregrine. Long waves on a beach. *J. Fluid Mech.*, 27:815–882, 1967.
- [134] D. H. Peregrine and I. A. Svendsen. Spilling breaker, bores and hydraulic jumps. In *Proceeding of the 16th International Conference on Coastal Engineering*, 1978.
- [135] M. Ricchiuto, R. Abgrall, and H. Deconinck. Application of conservative residual distribution schemes to the solution of the shallow water equations on unstructured meshes . *J. Comp. Phys.*, 222:287, 2007.
- [136] M. Ricchiuto and A. Bollerman. Stabilized residual distribution for shallow water simulations. *J. Comp. Phys.*, 1071:1115, 2009.
- [137] M. Ricchiuto and A. Bollermann. Accuracy of stabilized residual distribution for shallow water flows including dry beds. In *Proceedings of the 12th international conference on hyperbolic problems : theory, numerics, applications (HYP08)*, Maryland, USA, June 2008.

- [138] M. Ricchiuto and A.G. Fiippini. Upwind residual discretization of enhanced boussinesq equations for wave propagation over complex bathymetries. Research Report, *N^o 8311*, Project-Teams BACCHUS, Inria, 2013.
- [139] P. L. Roe. Approximate Riemann solvers, parameter vectors, and difference schemes. *J. Comp. Phys.*, 43:357–372, 1981.
- [140] P.L. Roe. Sonic flux formulae. *SIAM Journal of Scientific and Statistical Computing.*, 13:611, 1992.
- [141] V. Roeber and K. F. Cheung. Boussinesq-type model for energetic breaking waves in fringing reef environment. *Coast. Eng.*, 70:1–20, 2012.
- [142] V. Roeber, K. F. Cheung, and M. H. Kobayashi. Shock-capturing Boussinesq-type model for nearshore wave processes. *Coast. Eng.*, 57:407, 2010.
- [143] Y. Saad. *Iterative methods for Sparse Linear Systems*. PWS, 1996.
- [144] H. A. Schaffer, P. A. Madsen, and R. Deigaard. A Boussinesq model for waves breaking in shallow water. *Coast. Eng.*, 20:185–202, 1993.
- [145] A. Serrano-Pacheco, J. Murrillo, and P. Garcia-Navarro. Finite volume method for the simulation of the waves generated by landslides. *Journal of Hydrology*, 373:273, 2009.
- [146] F. Shi, R. A. Dalrymple, J. T. Kirby, Q. Chen, and A. Kennedy. A fully nonlinear Boussinesq model in generalized curvilinear coordinates. *Coastal Engineering*, 42:337–358, 2001.
- [147] F. Shi, J. T. Kirby, J. C. Harris, J. D. Geiman, and S. T. Grilli. A high-order adaptive time-stepping TVD solver for Boussinesq modeling of breaking waves and coastal inundation. *Ocean Modelling*, 43-44:36–51, 2012.
- [148] J. B. Shiach and C.G. Mingham. A temporally second-order accurate Godunov-type scheme for solving the extended Boussinesq equations. *Coast. Eng.*, 56:32–45, 2009.
- [149] T. M. Smith, M. F. Barone, and R. B. Bond. Comparison of reconstruction techniques for unstructured mesh vertex centered finite volume schemes. *18th AIAA Computational Fluid Dynamics Conference*, pages 1–22, 2007.

- [150] S. Soares-Frazaio and V. Guinot. A second order semi-implicit hybrid scheme for one-dimensional Boussinesq-type waves in rectangular channels. *Int. J. Num. Meth. Fluids*, 58:237-261, 2008.
- [151] O. R. Sørensen, H. A. Schaffer, and P. A. Madsen. Surf zone dynamics simulated by a Boussinesq type model: Part III. Wave-induced horizontal nearshore circulations. *Coastal Eng.*, 33:155-176, 1998.
- [152] O. R. Sørensen, H. A. Schaffer, and L. S. Sørensen. Boussinesq-type modelling using an unstructured finite element technique. *Coast. Eng.*, 50:182, 2004.
- [153] R. J. Spiteri and S. J. Ruuth. A new class of optimal high-order strong-stability-preserving time discretization methods. *SIAM Journal of Numerical Analysis*, 40:469, 2002.
- [154] I. A. Svendsen. Mass flux and undertow in a surf zone. *Coastal Eng.*, 8:347-365, 1984.
- [155] P. K. Sweby. High resolution schemes using flux limiters for hyperbolic conservation laws. *SIAM J. Numer. Anal.*, 21:995, 1984.
- [156] D. Swigler and P. J. Lynett. Laboratory study of the three-dimensional turbulence and kinematic properties associated with a solitary wave travelling over an alongshore-variable, shallow self. submitted for publication, 2011.
- [157] C. E. Synolakis. The run-up of solitary waves. *J. Fluid Mech.*, 185:523-545, 1987.
- [158] W.C. Thacker. Some exact solutions to the nonlinear shallow water wave equations. *J. Fluid Mech.*, 107:499, 1981.
- [159] J. L. Thomas, B. Diskin, and C. L. Rumsey. Towards verification of unstructured-grid solvers. *AIAA paper 2008-666*, 46th AIAA Aerospace sciences meeting and exhibit:Reno, Nevada, 2008.
- [160] M. Tissier, P. Bonneton, F. Marche, F. Chazel, and D. Lannes. A new approach to handle wave breaking in fully non-linear boussinesq models. *Coastal Engineering*, 67:54-66, 2012.

- [161] V. V. Titov and C. E. Synolakis. Modeling of breaking and nonbreaking long-wave evolution and runup using VTCS-2. *J. Waterway, Port, Coastal, Ocean Eng.*, 121:308–316, 1995.
- [162] V. V. Titov and C. E. Synolakis. Numerical modeling of tidal wave runup. *J. Waterway, Port, Coastal, Ocean Eng.*, 124:157–171, 1998.
- [163] M. Tonelli and M. Petti. Hybrid finite-volume finite-difference scheme for 2DH improved Boussinesq equations. *Coast. Eng.*, 56:609–620, 2009.
- [164] M. Tonelli and M. Petti. Finite volume scheme for the solution of 2d extended boussinesq equations in the surf zone. *Ocean Engineering*, 37:567–582, 2010.
- [165] M. Tonelli and M. Petti. Shock-capturing Boussinesq model for irregular wave propagation. *Coast. Eng.*, 61:8–19, 2012.
- [166] M. Tonelli and M. Petti. Numerical simulation of wave overtopping at coastal dikes and low-crested structures by means of a shock-capturing Boussinesq model. *Coast. Eng.*, 79:75–88, 2013.
- [167] E. F. Toro and P. Garcia-Navarro. Godunov-type methods for free-surface shallow flows: A review. *J. of Hydraulic Res.*, 45:736, 2007.
- [168] E. F. Toro, M. Spurce, and W. Speares. Restoration of the contact surface in the HLL-Riemann solver. *Shock Waves*, 4:25–34, 1994.
- [169] E. F. Toro and V. Titarev. Derivative Riemann solvers for systems of conservation laws and ADER methods. *J. Comp. Phys.*, 212:150, 2006.
- [170] E.F. Toro. *Shock-Capturing Methods for Free-Surface Shallow Flows*. Wiley, 2000.
- [171] E.F. Toro. *Riemann Solvers and Numerical Methods for Fluid Dynamic, A Practical Introduction*. Springer, 2009.
- [172] G. D. Van Albada, B. Van Leer, and W.W. Roberts. A comparative study of computational methods in cosmic gas dynamics. *Astron. Astrophysics*, 108:46–84, 1982.

- [173] B. van Leer. Towards the ultimate conservative difference scheme III. Upstream Centered Finite Difference Schemes for Ideal Compressible Flow. *J. Comp. Phys.*, 23:263-275, 1977.
- [174] B. van Leer. Towards the ultimate conservative difference scheme V. A second order sequel to Godunov's method. *J. Comp. Phys.*, 32:101-136, 1979.
- [175] J. Veeramony and I. A. Svendsen. The flow in surf-zone waves. *Coastal Eng.*, 39:92-122, 2000.
- [176] V. Venkatakrisnan. On the accuracy of limiters and convergence to steady state solutions. *AIAA paper 1993-0880*, 1993.
- [177] M. Walkley. *A numerical method for extended Boussinesq Shallow-water wave equations*. PhD thesis, The University of Leeds, School of Computer Studies., 1999.
- [178] M. Walkley and M. Berzins. A finite element method for the two-dimensional extended Boussinesq equations. *Int. J. Num. Meth. Fluids*, 39:865, 2002.
- [179] G. Wei and J. T. Kirby. A time-dependent numerical code for extended Boussinesq equations. *J. Waterway, Port, Coastal, Ocean Eng.*, 120:251-261, 1995.
- [180] G. Wei and J. T. Kirby. A coastal processes model based on time-domain Boussinesq equations. Research report no. CACR-96-01, Center for applied and coastal research, 1996.
- [181] G. Wei, J. T. Kirby, and A. Sinha. Generation of waves in Boussinesq models using a source function method. *Coastal Engineering*, 36:271-299, 1999.
- [182] R. W. Whalin. The limit of applicability of linear wave refraction theory in a convergence zone. Research report H-71-3, U.S. Army Corps of Engineers, WES, Vicksburg, Mi, Res. Rep., 1971.
- [183] J. M. Witting. A unified model for the evolution of nonlinear water waves. *J. Comp. Phys.*, 56 (2):203-239, 1984.
- [184] S. B. Woo and P. L. Liu. Finite-element model for modified Boussinesq equations: I, Model development. *J. Waterway, Port, Coastal, Ocean Eng.*, 130:1, 2004.

- [185] T.-R. Wu. *A numerical study of three dimensional breaking waves and turbulence effects*. PhD thesis, Cornell University, 2004.
- [186] S. Yamamoto, S. Kano, and H. Daiguji. An efficient CFD approach for simulating unsteady hypersonic shock-shock interface flows. *Computers and Fluids*, 27:571–580, 1998.
- [187] Y. Yamazaki, Z. Kowalik, and K. F. Cheung. Depth-integrated, non-hydrostatic model for wave breaking and run-up. *Int. J. Num. Meth. Fluids*, 61:473, 2009.
- [188] H. Yeh, P. L. Liu, and C .E. Synolakis, editors. *Long Wave Runup Models*. World Scientific Publishing Co., Friday Harbor, USA, 1996.
- [189] J. A. Zelt. The run-up of nonbreaking and breaking solitary waves. *Coastal Eng.*, 15:205–246, 1991.
- [190] Z. Zhong and K. H. Wang. Time-accurate stabilized finite-element model for weakly nonlinear and weakly dispersive water waves. *Int. J. Num. Meth. Fluids*, 57:715, 2008.
- [191] J. G. Zhou, D. M. Causon, Mingham C. J, and D. M Ingram. The surface gradient method for the treatment of source terms in the shallow water equations. *J. Comp. Phys.*, 168:1–25, 2001.